Analysis and Design of Propulsive Guidance for Atmospheric Skip Entry Trajectories

by

Garrett Oliver Teahan

B.S., Aeronautical and Astronautical Engineering
University of Washington (2004)

Submitted to the Department of Aeronautics and Astronautics
in partial fulfillment of the requirements for the degree of

Master of Science in Aeronautics and Astronautics

at the

MASSACHUSETTS INSTITUTE OF TECHNOLOGY

May 2006
[June 2006]

Author: _____
Department of Aeronautics and Astronautics
May 26, 2006

Certified by: _____
Stephen C. Paschall II
Member of Technical Staff
The Charles Stark Draper Laboratory, Inc.
Technical Supervisor

Certified by: _____
Richard H. Battin, Ph.D.
Senior Lecturer in Aeronautics and Astronautics
Thesis Advisor

Accepted by: _____
Jaime Peraire
Professor of Aeronautics and Astronautics
Chair, Committee on Graduate Students

Analysis and Design of Propulsive Guidance for Atmospheric Skip Entry Trajectories

by

Garrett Oliver Teahan

Submitted to the Department of Aeronautics and Astronautics
on May 26, 2006, in partial fulfillment of the
requirements for the degree of
Master of Science in Aeronautics and Astronautics

Abstract

A study of the ability to use propulsive guidance for atmospheric skip entry trajectories was completed. The analysis centered itself around the proposed design of NASA's Crew Exploration Vehicle. The primary aerodynamic guidance system must execute an atmospheric skip maneuver when attempting to reach distant landing sites. These maneuvers result in the loss of aerodynamic control authority during the skip phase. The physics of the problem were studied through an analysis of the minimum impulsive ΔV. This analysis was completed for a number of different trajectories with varying energies. The framework of the propulsive guidance algorithm, derived from the Powered Explicit Guidance law of the Space Shuttle, was presented and the augmented design was explained. The sensitivity of the propulsive guidance solution to a given trajectory was explored as well as its response to altitude constrained maneuverability. The robustness of the algorithm is measured using Monte Carlo techniques. The results showed that the current design of the Crew Exploration Vehicle and the current implementation of the primary aerodynamic guidance system are inadequate for a precise, long range, crewed return from the Moon. It was also shown that the lower energy trajectories are more favorable given the altitude reorientation constraint. It was recommended that the skip phase be redefined such that it does not begin until the altitude reorientation constraint is met. It was shown that a combination of increasing the total amount of thrust available, ΔV allowance, and the entry guidance precision are necessary to bring the success rate to acceptable levels for a precise, long range, crewed return from the Moon.

Technical Supervisor: Stephen C. Paschall II
Title: Member of Technical Staff
The Charles Stark Draper Laboratory, Inc.

Thesis Advisor: Richard H. Battin, Ph.D.
Title: Senior Lecturer in Aeronautics and Astronautics

Acknowledgments

There are a number of people without which this thesis would not have been completed. I would like to thank my technical supervisor, Steve Paschall. His insight and understanding were invaluable. It has been great working with him and I would hope it will be possible to work with him again in the future. I would also like to thank Gregg Barton, Sarah Bairstow, Roberto Pileggi, and Sungyung Lim whose work has led to the problem discussed in this thesis. Sean George was very helpful in understanding the aerodynamics of capsules in rarefied flow. Peter Neirinckx was my advisor during the early part of my graduate studies and his guidance was rewarding. Brooke Marquardt and the library staff were great at helping me dig up old references about the Soviet space program. I would also like to thank George Schmidt and The Charles Stark Draper Laboratory for giving me the opportunity to study at the Massachusetts Institute of Technology while working with some of top engineers in this field.

I would also like to show my appreciation to Zach Putnum, Melanie Miller, and Geoff Huntington (the officemate that never was) for sharing an office with me and keeping me entertained when I needed it most. I would also like to thank the Friday Morning Donuts Crew for allowing to me consume more than my fair share of the dozen.

My greatest thanks is given to my family whose love, support, and encouragement has made me who I am today. I'm looking forward to finally joining the rest of you in the real world. I would especially like to thank my mother for having the courage and patience to raise me from my day one to day 8943. You've always been there for me ever since my first days in that tiny loft in San Francisco and I can't thank you enough.

This thesis was prepared at The Charles Stark Draper Laboratory, Inc., under Internal Research and Development, Project GCDLF-Support, 20340:001.

Publication of this thesis does not constitute approval by Draper or the sponsoring agency of the findings or conclusions contained herein. It is published for the exchange and stimulation of ideas.

_____

Garrett Teahan

Contents

List of Figures

List of Tables

List of Symbols

Subscripts

$()_I$	Earth-centered, inertial frame	$()_T$	Total quantity
$()_F$	Earth-centered, Earth-fixed frame	$()_{\mathrm{D}}$	Drag quantity
		$()_{\mathrm{L}}$	Lift quantity
$()_L$	Local vertical/local horizontal frame	$()_0$	Initial quantity
		$()_f$	Final quantity
$()_S$	Stability frame	$()_{go}$	Quantity-to-go
$()_{ref}$	Reference variable	$()_d$	Desired quantity
$()_g$	Gravity quantity	$()_r$	Radial quantity
$()_a$	Aerodynamic quantity	$()_h$	Horizontal quantity
$()_t$	Thrust quantity	$()_e$	Error quantity

Superscripts

$()^{-1}$	Inverse	$()^{\mathrm{T}}$	Transpose

Accents

$\dot{()}$	First time derivative	$\hat{()}$	Unit vector
$\ddot{()}$	Second time derivative	$\tilde{()}$	Normalized variable

Coordinate Triads

$\hat{\mathbf{i}}$	First coordinate vector	$\hat{\mathbf{k}}$	Third coordinate vector
$\hat{\mathbf{j}}$	Second coordinate vector		

Physical Parameters

t	Time
r	Radial distance
v	Speed
a	Acceleration
x	Downrange distance
h	Altitude
ρ	Atmospheric density
m	Mass
S	Surface area
F_t	Thruster force
ΔV	Change in velocity
I_{sp}	Specific impulse
α	Angle of attack
γ	Flight path angle
θ_b	Bank angle
β	Thrust direction angle
$\hat{\boldsymbol{\lambda}}_t$	Thrust direction vector
$\mu_\oplus$	Gravitational parameter of Earth
$r_\oplus$	Radius of Earth
$\omega_\oplus$	Rotational frequency of Earth
C_L	Lift coefficient
C_D	Drag coefficient
$^L/_D$	Lift-to-drag ratio
B_N	Ballistic number
$\mathcal{T}_A^Z$	Transformation from frame A to frame Z
θ	Longitude
J_2	Second gravitational harmonic
a_s	Semimajor axis
μ	Mean
σ	Standard deviation
$\mathcal{L}$	Thrust integral
$\mathcal{J}$	Thrust integral
$\mathcal{S}$	Thrust integral
$\mathcal{Q}$	Thrust integral
$\frac{\partial A}{\partial Z}$	Partial derivative of A with respect to Z

Chapter 1

Introduction

Exploration has long been a part of the human endeavor. The latest incarnation of this quest has been the manned exploration of our solar system. What began in the early 1960s under the inauspicious haze of the Cold War with the Soviet Vostok and Voskhod missions and the American Mercury and Gemini missions has, in the past decade, turned toward more multinational cooperation as demonstrated with the International Space Station. This massive space structure has brought together the once competing Soviet/Russian and American space agencies along with those of Canada, Japan, Brazil and the eleven member nations of the European Space Agency. However, with completion of the ISS on the horizon and retirement of the Space Shuttle eminent, NASA has once again been steered towards the target of putting humans back on the Moon. The plan is to return to the Moon but with the intention of setting up a permanent presence and developing needed experience to further the footprint of human civilization to other planets in the Solar System, namely Mars.

It may seem that returning to the Moon would be pointless and relatively easy considering that this was done nearly forty years ago. That assumption proves to be incorrect as the forty year hiatus has caused a loss of capability in designing human-based exploration missions throughout the industry. In addition, there are much broader mission goals for the modern system that weren't present or considered during the design of the Apollo spacecrafts. Among these is the requirement for the

entry vehicle to be capable of performing extended range landings during a return to Earth from the Moon. This requirement is necessitated by an increased attention to safety and the desire to allow the astronauts to return safely to the surface of Earth at any time during a mission without the need to wait for precise alignment between the Moon launch site and the Earth landing site. However, a capsule shape complicates this process because it has a low lift-to-drag ratio which reduces the range capability of the spacecraft for direct entries. Therefore, some sort of maneuver must be performed during entry to extend its capability to the desired ranges. This is what has brought about the concept of performing skipping entries as a method to achieve the required capability. These maneuvers form the basis of this thesis and the work herein.

1.1 Presidential Vision

On January 14, 2004 President George W. Bush laid the groundwork for the future of NASA and American space exploration in what he called his "New Vision for the Space Exploration Program" [1]. In his speech he made public a plan to put America back on the Moon by 2020. This includes the completion of the International Space Station to fulfill our responsibility to that project and the fifteen international partners. It also entails retiring the Space Shuttle after 30 years of service to make room for the next generation of launch vehicles. The next spacecraft, named the Crew Exploration Vehicle (CEV), will be tested beginning in 2008, during the final days of the Space Shuttle. This vehicle will assume the role of ferrying astronauts to the International Space Station but will also be capable of transporting them beyond Earth orbit. He proposed how the experience gained by living and working on the Moon for extended periods of time will enable humans to extend their reach to Mars as well. The establishment of a lunar base could produce significant reductions in the cost of future space exploration. It might be possible to process the lunar soil for useful applications like rocket fuel or breathable air. He emphasized that this progress will be steady and made one step at a time.

The speech draws upon historical references to pre-industrial exploration by adventurers such as Meriweather Lewis and William Clark. He goes on to explain that America's adventure into space is a modern version of Lewis and Clark expedition. He continues to state that exploration is a part of the American character and that it has brought tangible improvements to the American life. Even with all the successes of NASA with the Space Shuttle, robotic exploration of the solar system, and numerous telescopes such as the Hubble Space Telescope; no human has been further than 386 miles upward since 1974. This is roughly equivalent to the distance between Boston and Washington, D.C. or between San Francisco and Los Angeles. The future of space exploration will use these robotic trailblazers to send images and scientific data that will lay the foundation for the arrival of humankind.

Since this announcement there has been a lot of engineering put into designing a system that can take humans to the Moon and beyond while maintaining a level of safety that is demanded in the wake of the Columbia tragedy. The current preliminary design of the CEV is documented in detail in "NASA's Exploration System Architecture Study" [2]. A key aspect of this design is a move away from the Shuttle-like lifting bodies with delta wing planforms to an Apollo derived capsule shape with a large heat shield belly. This design was chosen for a variety of reasons not the least of which are safety and efficiency. The conic shape allows the capsule to be placed atop a launch vehicle which improves the safety of the crew and allows for a method of escape in the event of an accident during launch. It is also a more efficient use of structural material because the wings of the Shuttle are essentially dead weight beyond the atmosphere and therefore ill-suited for interplanetary travel. Another key design element is the separation of cargo lifting operations and crew transportation. This adds another factor of safety because the crew launch vehicle can be designed specifically its intended purpose. This will also reduce cost of launching cargo because the launch vehicle does not need to carry as stringent of a safety rating as the crewed launch vehicle.

Perhaps the aspect of the design most relevant to this thesis is that the CEV is designed to perform an atmospheric skip entry. An atmospheric skip entry trajectory

is defined, for the purpose of this thesis, to be a trajectory that upon entering the atmosphere has enough energy that the trajectory effectively lofts the spacecraft upwards momentarily before returning to back to Earth. A skip is traditionally defined to begin and end the entry interface which for Earth is approximately 120 km altitude. The atmospheric skip entry trajectory concept is illustrated in Figure 1-1. A common analog that is frequently stated is that of skipping a stone off the surface of a pond. If the skip is properly controlled, it can be used to increase the range capability of the entering spacecraft. This proves to be very advantageous for low lift-to-drag ratio vehicles such as the CEV concept. The trajectories created by skip entry maneuvers form the basis of this thesis.

1.2 Background

The concept of atmospheric skip entry trajectories is not entirely new. The idea has been around since the beginning of manned space exploration. The Apollo program used a guidance algorithm that was designed to perform such a maneuver [3]. However, the documentation doesn't show any evidence that this capability was ever tested beyond the feasibility stage and subsequent testing has shown that the performance of the entry guidance algorithm is less than satisfactory when attempting to perform this maneuver. The Soviets performed the first successful skip entry with the Zond 6 circumlunar spacecraft [4] [5] [6]. It was decided to perform such a maneuver for two reasons. The first was to reduce the excessive g-loads placed on the crew during a ballistic entry from the moon. The other, and perhaps more politically driving, factor was that it wasn't possible to land in Soviet territory from a lunar ballistic return. The Zond 6 return was completed with spacecraft reaching an altitude of 45 km during its first entry while decelerating from 11 $^{km}/_{s}$ to 7.6 $^{km}/_{s}$ and experiencing g-loads of only 4 to 7 g's. Unfortunately, a pressure sensor onboard the spacecraft failed and it crashed after the parachutes deployed too early [7]. It is interesting to note that until the U.S.S.R. opened up under *Glasnost*, the fact that the Zond 6 mission ended in disaster was not known because a few photographs that were recovered

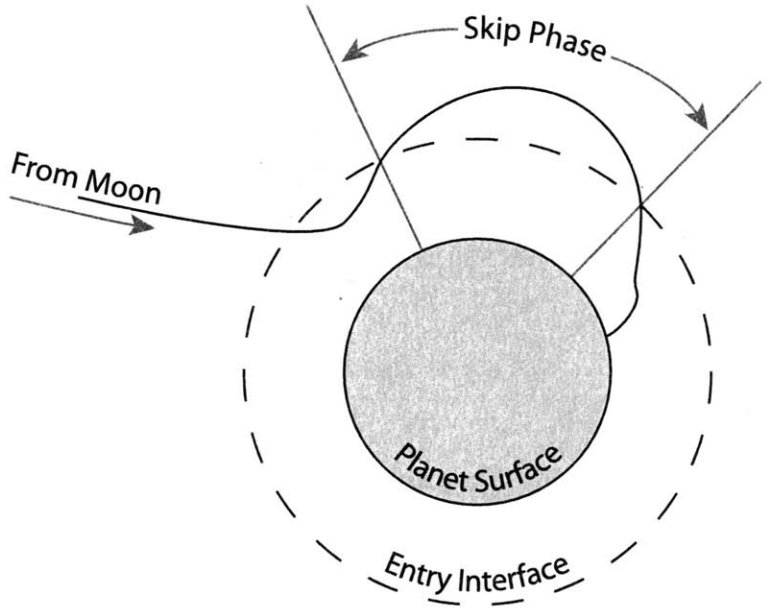

(a) Polar view of a skip trajectory

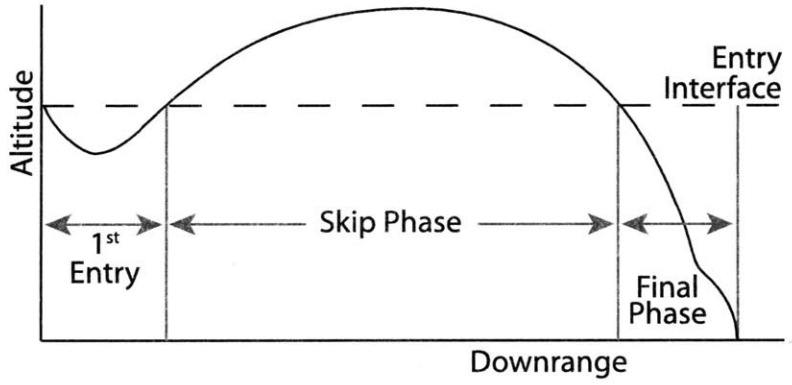

(b) Skip trajectory phase definitions

Figure 1-1: An example of an atmospheric skip entry trajectory

from the wreckage were shown to the public and was assumed to be proof of success. The next attempt at a circumlunar mission was made a few weeks after Apollo 8 in January of 1969. There was some debate within the Soviet space command over whether or not to place a crew on this mission. It was decided against placing a crew onboard since a simple fly-by of the Moon would not look good compared to the ten orbits achieved by Apollo 8. This decision proved to be fortuitous for the possible cosmonauts as the launch failed when the second stage exploded and thus the mission remained unnamed. The next Zond mission, Zond 7, was the only Russian mission which could have carried humans successfully around the Moon and landed safely back on Earth. Despite public claims by the Soviet cosmonauts that a manned lunar landing would take place by early 1970, it was decided to continue testing the Zond spacecraft unmanned. Zond 7, launched on August 8, 1969, a couple weeks after the Americans' historic landing on Moon with Apollo 11. It followed the trajectory of Zond 6 and likewise performed a skip entry but landed successfully in what is now Kazakhstan south of the town of Kostanai (then spelled Kustanai) six days after it launched [4] [5] [7]. There have been a few subsequent papers that focus on guidance algorithms for such a maneuver.

Reference [8] discusses a rudimentary guidance algorithm for the "skipout" phase of a skip trajectory. The "skipout" phase was defined at the latter half of the first entry as defined in Figure 1-1b. The optimal guidance solution is found using a conjugate gradient method to converge to a reference trajectory. The simulation used was straightforward and relatively simple; it is essentially a point design and does not include any sensitivity analysis. The skip phase target range of the trajectory considered is 16,924 nmi (approximately 31,000 km) or more than three quarters around the globe. This is substantially larger than the skip considered by other references or this thesis.

Reference [9] proposes using skip trajectories for aeroassisted orbital transfer. The guidance algorithm proposed uses an analytic predictor-corrector which solves for the final state of the vehicle using a closed form expression. This expression is an approximation of the flight dynamics derived from using the method of matched asymptotic

expansions. It shows good performance for a Martian aerocapture trajectory. However, this technique does not appear to be well suited for the aeroassisted transfer trajectories discussed in the paper as it seems as though this maneuver would require more fuel to enter and exit the transfer orbit than an equivalent Hohmann transfer. This solution would clearly require less time than a Hohmann transfer but time is generally unconstrained for these types of missions and fuel mass is a system driver.

Perhaps the most recent addition to the literature and certainly the most pertinent to this thesis is Reference [10]. The work presented covers an aerodynamic guidance algorithm developed for a low lift-to-drag ratio spacecraft such as the CEV. A key feature of this work is the ability to perform a skip maneuver to allow a low L/D vehicle to achieve the extended range landings. This is done by augmenting the Apollo guidance algorithm with a numeric predictor-corrector to increase the landing accuracy. A numeric predictor-corrector solves for the final state of the spacecraft by integrating the equations of motion forward in time. This method is generally more accurate than an analytic predictor-corrector but can take substantially more computational effort.

Reference [10] covers quite a bit of the entry problem and is an excellent reference on the inner workings of the original Apollo guidance algorithm. While it presents an algorithm for reaching a wide variety of targets, it also offers a look in the physics of a skip entry. Besides extending the landing range capability, another advantage with skip entries is that the maximum g-load can be reduced. This benefit arises because the spacecraft is able to extend the deceleration over a longer period of time. This effect creates a gentler entry environment for the astronauts onboard that may be injured or simply weak from spending an extended period of time in a reduced gravity environment. One problem with skip trajectories is that they tend to increase the total heat load due to their extended flight time through the atmosphere. However, the maximum heat rate is achieved during the first entry and, therefore, is independent of the desired range.

1.3 Motivation

The resulting algorithm designed in Reference [10] performs very well for the set of landing ranges that was examined. One caveat to this is the simulation was performed using only translational dynamics. The problem is that this neglects the effects of the rotational dynamics which enhance the fidelity of the model. The performance of the algorithm actually degrades because the inclusion of rotational dynamics complicates the guidance problem and results in poorer precision performance.

Some preliminary follow-up to Reference [10] using a six degree-of-freedom simulation has shown that in fact large errors can occur when targeting the farthest of the landing ranges. These errors can be caused by problems within the algorithm design itself but it is more likely that they are the result of imperfect control and the uncertainties in the newly included rotation axes. Regardless of the cause of the errors, a method for correcting them without the use of aerodynamic control is needed. This need can be met by the addition of a propulsive guidance algorithm performing a ΔV maneuver during the skip portion of the entry. This complements the aerodynamic guidance perfectly because they operate in separate regimes. The bank-to-steer guidance proposed in Reference [10] works extremely well when the atmosphere is thick and the entering spacecraft can exchange energy and momentum with the atmosphere. This unfortunately creates a problem when the atmosphere is thin as it is during the skip portion of a long range trajectory. A propulsive algorithm compliments this because it works best when the atmosphere is thin since it is necessary to reorient the vehicle to point the thrusters in the right direction for a propulsive maneuver. Figure 1-2 qualitatively shows this distinction between aerodynamic and propulsive guidance.

The algorithm from Reference [10] also demonstrates the capability to choose a "high loft" or "low loft" trajectory. The main difference between these types of trajectories is that the "high loft" trajectories reach a higher maximum altitude during the skip phase of the entry than those of the "low loft" variety. However, there are other differences between the trajectories which point to differences in their individual

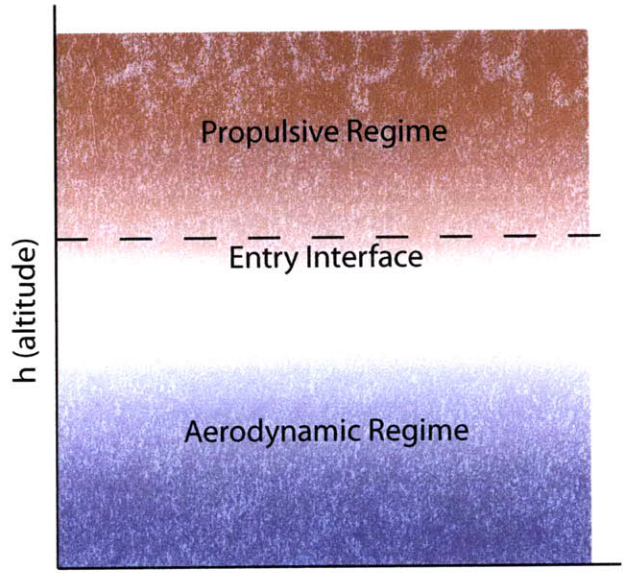

Figure 1-2: Effective regimes for aerodynamic and propulsive guidance

energy levels and flight path angles. The reasons for choosing one type of trajectory over the other are discussed but the primary reason is to reduce the range sensitivity of the skip phase due to aerodynamic effects that exist in the "low loft" trajectories as will be discussed later. This, in actuality, exacerbates the problem of using only bank-to-steer guidance during the skip phase because a "high loft" trajectory spends more time in the uppermost regions of the atmosphere. This accentuates the need for a propulsive guidance algorithm during the skip phase because without it the spacecraft is essentially flying open-loop and can very easily drift off course. One advantage to using the high loft trajectories is that they allow for more time perform the propulsive maneuver. The reason for this is because the spacecraft will likely need to reorient and point the thrusters in some other direction to achieve the desired change in velocity. However, for a reasonable thruster size, it will not be possible to reorient whenever it might be necessary. This means that the aerodynamic moments must drop below some specified level, depending on the size of the thrusters, before it

is possible to reorient the spacecraft. This only occurs when either the atmospheric density or velocity becomes small enough. The velocity is near orbital speed so the prerequisite that remains is the density which becomes small when the spacecraft is high in the atmosphere.

The aforementioned problem and its intricacies lay the foundation for the work encompassed by this thesis. That being the design of a propulsive guidance algorithm to correct for errors during the skip portion of the trajectory that would otherwise create large landing inaccuracies.

1.4 Objective

The objective of this thesis is to implement and evaluate a propulsive guidance algorithm for use during the skip phase of a lunar return trajectory. The skip phase becomes increasingly prominent as the landing range is increased, therefore the longest landing ranges are considered. The vehicle will be based upon the CEV design concept which is a low lift-to-drag ratio capsule similar in shape to the Apollo capsule.

The guidance algorithm will be based upon the Powered Explicit Guidance (PEG) law that was developed for the Space Shuttle in the 1970s. It was originally developed for ascent and later revised to perform exoatmospheric maneuvers such as plane changes and orbit raising and lowering as well as deorbit targeting for the descent phase. It has the advantage that it has been verified and validated through its many uses in the Space Shuttle program. Although none of the current implementations are completely appropriate for the problems encountered by a spacecraft in a skip trajectory, all contain certain elements that are crucial to this new derivative. The operating regime of this problem is most clearly related to that of the orbital maneuvering version. However, this version does not contain the ability to target a specified downrange location and it does not account for any atmospheric effects. The ascent version of PEG does account for the atmospheric effects but it, too, has no ability to specify the downrange termination condition and its operational regime is not appropriate. The deorbit targeting version does allow for the targeting of a landing site but

its operating regime is inappropriate as well. Clearly each version of the algorithm works very well for its intended purpose. However, it is not a trivial task to include the atmospheric effects from the ascent version with the targeting capability of the deorbit version into the operating regime of the orbital maneuvering version.

The first step is to define a set of nominal reference trajectories representative of a reasonable range of atmospheric exit conditions produced by the initial aerodynamic guidance. This set is separated into several different "classes" of trajectories. The term "classes" is used because the skip phase of the entry can be shaped depending on a number of parameters. This idea is very similar to the "high" and "low" loft trajectories mentioned earlier but it will be necessary to explore what happens between these two extremes. It is clear that there are many possible trajectories to reach a desired landing target. These trajectories can be classified in terms of their individual energy levels during the skip phase. The higher energy trajectories are ones that enter the skip phase with a greater velocity and a shallower flight path angle. Conversely, the low energy trajectories enter the skip phase with a lower velocity and a high flight path angle. The high energy trajectories are more desirable from a pure capability standpoint because they allow for more variation in the final phase entry condition and thus a broader range of correction. However, the low energy trajectories are more desirable from a feasibility standpoint since it allows for more time to perform the corrective maneuver because they travel higher out of the atmosphere. Both high and low energy trajectories offer advantages over the other and these will be examined along with a number of the "shades of gray" in between.

A preliminary analysis is completed using an impulsive ΔV. This gives a good lower bound on the amount of ΔV (and hence fuel) needed to correct for a given amount of error. The problem with getting realistic approximations from impulsive analysis solutions is that they require extremely high thrust levels to achieve the specified ΔV in a very short amount of time. Therefore, using more reasonably sized thrusters makes the time (and hence the ΔV) required to perform the necessary corrections increase when compared to the impulsive case. The result of this analysis will include a way of determining the thruster size and/or number needed depending

on vehicular and environmental constraints.

Once the guidance algorithm has been developed and tested against a representative set of skip trajectories it is necessary to quantify the performance under a variety of conditions. This will require defining a set of vehicle and environmental uncertainties. A Monte Carlo analysis will then be performed to test the sensitivity of the algorithm to unanticipated variations in the vehicle and environment. This defines the robustness of the design and is a measure of the quality of the design.

1.5 Overview

This chapter gives a broad overview of using skip trajectories during entry and provides an introduction to the topic of the thesis. Chapter 2 provides an explanation of the physics of the problem and the design of the spacecraft used during this thesis. Chapter 3 covers the results of a preliminary analysis using an impulsive ΔV to find a lower bound to the problem. Chapter 4 discusses the design of the guidance algorithm and an overview of the Powered Explicit Guidance algorithm that forms the basis of the algorithm presented here. Chapter 5 presents the results of a Monte Carlo analysis using the newly designed guidance algorithm. Finally, Chapter 6 summarizes the work presented in this thesis and gives some suggestions for future avenues of study.

Chapter 2

Simulation Environment

In order to begin the analysis, a number of parameters must be defined. This will bound the scope of the thesis to validity only in the neighborhood of where the assumptions hold. To that end, it is important that the assumptions be as broad and unrestrictive as possible so the solutions are not a point design. However, making the assumptions too broad will make the problem too complicated to be solved with one thesis. Therefore, assumptions are tuned for a scope that produces a result that is significant and useful.

Many tools can be used when designing a simulation. The tool of choice for this problem is MATLAB version 7.2 produced by The MathWorks, Inc. MATLAB contains a complete development environment with many included functions and the ability to extend its capability to specific areas of interest through the use of toolboxes and user-defined libraries of functions. One such toolbox is Simulink. It allows the designer to develop dynamic models of systems using an intuitive graphical interface to represent the various components of the system and their connections. Once a system has been developed, the designer can simulate the dynamics of the system with the press of a button. A designer can then see how the system behaves and how that behavior compares to the nominal design. This capability of being able to rapidly design and test an idea is invaluable in engineering and science.

2.1 Coordinate Frames

There exist multiple ways to formulate any given problem depending on the coordinate frame desired. However, the choice of the coordinate frame can greatly reduce the complexity of a problem and allow for deep insights into the dynamics of the system. For the purpose of this thesis, four different coordinate frames are used: an inertial frame, an Earth-fixed frame, a local vertical/local horizontal frame, and a stability frame. To disambiguate a vector in each frame the subscripts $()_I$, $()_F$, $()_L$, and $()_S$ are used; respectively. Due to their similarities, the coordinate frames are presented in two groups based upon where the origin is located. The first group is the Earth-centered frames which include the inertial and Earth-fixed frames. The other group is the spacecraft-centered frames which include the local vertical/local horizontal frame and the stability frame.

2.1.1 Earth-centered

The Earth-centered inertial frame is used primarily for the integration of the equations of motion presented later in Section 2.4. It is represented by the unit vectors $\hat{\mathbf{i}}_I$, $\hat{\mathbf{j}}_I$, and $\hat{\mathbf{k}}_I$. The $\hat{\mathbf{i}}_I$ axis points to the intersection of the equator and the prime meridian (zero latitude and longitude) at $t = 0$. The $\hat{\mathbf{k}}_I$ axis points toward the North Pole (90° North latitude) and $\hat{\mathbf{j}}_I$ completes the frame in a right-handed sense (zero latitude and 90° East longitude). A vector $\mathbf{u}$ can then be expressed as

$$\mathbf{u} = x\hat{\mathbf{i}}_I + y\hat{\mathbf{j}}_I + z\hat{\mathbf{k}}_I. \tag{2.1}$$

This vector $\mathbf{u}$ can be any quantity that has magnitude and direction such as position or velocity.

The Earth-centered Earth-fixed frame is used to measure the spacecraft's position and velocity relative to a fixed point on the Earth. This is needed when discussing the range to a landing site and calculating the speed of the spacecraft relative to the atmosphere used in aerodynamic calculations. It is related to the Earth-centered

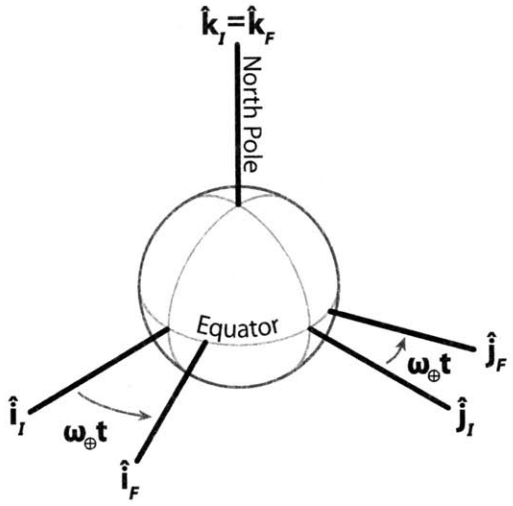

Figure 2-1: Earth-centered coordinate frames

inertial frame by a rotation about the polar axis, $\hat{\mathbf{k}}_F$, with a period identical to that of the Earth. The $\hat{\mathbf{i}}_F$ and $\hat{\mathbf{j}}_F$ axes stay fixed to the Earth as it rotates. This is distinguished from the Earth-fixed inertial frame by the following relations

$$\hat{\mathbf{i}}_I(t=0) = \hat{\mathbf{i}}_F \tag{2.2}$$

$$\hat{\mathbf{j}}_I(t=0) = \hat{\mathbf{j}}_F \tag{2.3}$$

$$\hat{\mathbf{k}}_I = \hat{\mathbf{k}}_F. \tag{2.4}$$

It should be clear that the Earth-fixed and inertial frames are identical at the beginning of the simulation, after that they oscillate with a period identical to Earth's rotational period. The inertial and Earth-fixed frames are shown in Figure 2-1 at some time, t, where $\omega_\oplus$ is the Earth's rotational frequency.

2.1.2 Spacecraft-centered

The local vertical/local horizontal is centered on the spacecraft and used to define the direction of motion of the spacecraft. This is defined as the flight path angle and is the angle above the local horizontal and in the direction of the velocity vector. The

local vertical is defined to be in the direction of the position vector so

$$\hat{\mathbf{j}}_L = \hat{\mathbf{i}}_r \tag{2.5}$$

where $\hat{\mathbf{i}}_r$ is the unit position vector. The local horizontal is defined to be in the downrange direction. Before this position can be defined it is necessary to define the crossrange direction as

$$\hat{\mathbf{k}}_L = -\hat{\mathbf{i}}_h = \frac{\hat{\mathbf{i}}_v \times \hat{\mathbf{i}}_r}{\left|\hat{\mathbf{i}}_v \times \hat{\mathbf{i}}_r\right|} \tag{2.6}$$

where $\hat{\mathbf{i}}_v$ is the unit velocity vector and $\hat{\mathbf{i}}_h$ is the unit angular momentum vector. Therefore, the local horizontal is defined to complete the right-handed coordinate frame as

$$\hat{\mathbf{i}}_L = \hat{\mathbf{j}}_L \times \hat{\mathbf{k}}_L = \hat{\mathbf{i}}_h \times \hat{\mathbf{i}}_r. \tag{2.7}$$

Then the flight path angle, γ, is defined as

$$\gamma = \cos^{-1}\left(\hat{\mathbf{i}}_v \cdot \hat{\mathbf{i}}_L\right) \operatorname{sign}\left(\hat{\mathbf{i}}_r \cdot \hat{\mathbf{i}}_v\right) \tag{2.8}$$

where sign is a real-valued function which is defined such that

$$z = |z| \operatorname{sign} z. \tag{2.9}$$

Therefore, the flight path angle is defined such that

$$\operatorname{sign} \dot{h} = \operatorname{sign} \gamma, \quad \forall \gamma \in (-\pi, \pi) \tag{2.10}$$

where $\dot{h}$ is the altitude rate.

The stability frame is also centered on the spacecraft and is used to define the directions in which the aerodynamic and propulsive forces are acting. The unit vector triad can be defined arbitrarily with respect to the body as long as they are kept fixed thereafter. For the purpose of this thesis it is beneficial to define this with respect to the velocity and the aerodynamic forces created by the velocity. Therefore, the $\hat{\mathbf{i}}_S$ axis

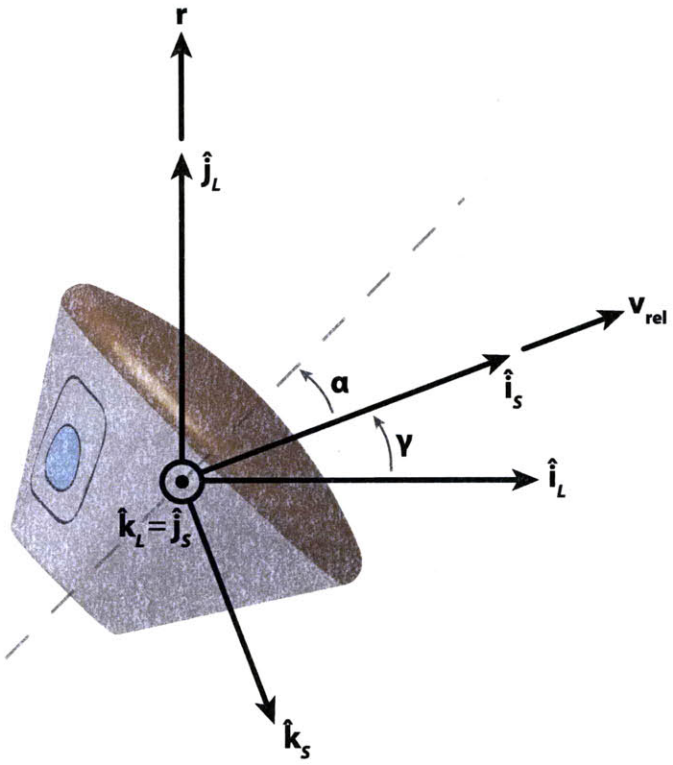

Figure 2-2: Spacecraft-centered coordinate frames

is defined into the wind (assuming no sideslip) so it is aligned with the Earth relative velocity and in the negative direction of the drag vector. The $\hat{\mathbf{k}}_S$ axis is defined in the negative direction of the lift vector (assuming straight and level flight) in the **r-v** plane. The $\hat{\mathbf{j}}_S$ axis completes the frame in a right-handed sense. This definition gives a positive angle of attack when the vehicle is pitched up.

The local vertical/local horizontal and stability frames are shown with respect to each other and the position and velocity vectors in Figure 2-2.

2.1.3 Coordinate Transformations

The definitions of the coordinate frames establish a convenient basis for analyzing the dynamics of the spacecraft under a variety of different conditions. A problem with using separate frames is that it isn't immediately clear what the spacecraft is doing in another frame. In addition, the equations of motion must be specified in a frame that

is non-accelerating and non-rotating in order for Newton's Second Law to be valid. The inertial frame is by definition one such frame. Therefore, it is necessary to define a method for transforming vectors from their natural frame to an inertial frame. To perform this operation, a transformation matrix, $\mathcal{T}$, from frame A to frame Z such that

$$\mathbf{r}_Z = \mathcal{T}_A^Z \mathbf{r}_A. \tag{2.11}$$

A transformation matrix has the benefit of being an orthonormal basis. This means that the reverse transformation can be computed by taking the transpose of $\mathcal{T}$ instead of requiring its inverse. Therefore, the reverse transformation from frame Z to frame A is

$$\mathbf{r}_A = \left(\mathcal{T}_A^Z\right)^{-1} \mathbf{r}_Z = \left(\mathcal{T}_A^Z\right)^{\mathrm{T}} \mathbf{r}_Z = \mathcal{T}_Z^A \mathbf{r}_Z. \tag{2.12}$$

It is also possible to perform a series of transformations consecutively. Therefore, it is possible to transform $\mathbf{r}$ from frame A to frame Z through frame M with

$$\mathbf{r}_Z = \mathcal{T}_M^Z \mathcal{T}_A^M \mathbf{r}_A. \tag{2.13}$$

One should note that serial transformations are non-commutative so that

$$\mathcal{T}_M^Z \mathcal{T}_A^M \neq \mathcal{T}_A^M \mathcal{T}_M^Z. \tag{2.14}$$

With the rules of coordinate transformations defined, it is now possible to establish the transformations needed for this thesis. The transformation from Earth-fixed to inertial is a simple rotation about their $\hat{\mathbf{k}}$ axes so that $\mathcal{T}_I^F$ is

$$\mathcal{T}_I^F = \begin{bmatrix} \cos\theta & \sin\theta & 0 \\ -\sin\theta & \cos\theta & 0 \\ 0 & 0 & 1 \end{bmatrix} \tag{2.15}$$

where $\theta = \omega_\oplus t$ for some time t and is the commonly known as the longitude.

The transformation from the local vertical/local horizontal frame to the inertial

frame, $\mathcal{T}_L^I$, is established by some key unit vectors as

$$\mathcal{T}_L^I = \left[\begin{array}{ccc} \left(\hat{\mathbf{i}}_L\right)_I & \left(\hat{\mathbf{j}}_L\right)_I & \left(\hat{\mathbf{k}}_L\right)_I \end{array} \right] \tag{2.16}$$

where

$$\left(\hat{\mathbf{i}}_L\right)_I = \left(\hat{\mathbf{j}}_L\right)_I \times \left(\hat{\mathbf{k}}_L\right)_I \tag{2.17}$$

$$\left(\hat{\mathbf{j}}_L\right)_I = \left(\hat{\mathbf{i}}_r\right)_I \tag{2.18}$$

$$\left(\hat{\mathbf{k}}_L\right)_I = -\left(\hat{\mathbf{i}}_h\right)_I = \left(\frac{\hat{\mathbf{i}}_v \times \hat{\mathbf{i}}_r}{\left|\hat{\mathbf{i}}_v \times \hat{\mathbf{i}}_r\right|} \right)_I . \tag{2.19}$$

The transformation from the stability frame to the local vertical/local horizontal frame is a series of rotations starting with a rotation about $-\hat{\mathbf{k}}_L$ through γ, the flight path angle followed by a 90 degree rotation about $\hat{\mathbf{i}}_L$ such that

$$\mathcal{T}_S^L = \begin{bmatrix} 1 & 0 & 0 \\ 0 & 0 & 1 \\ 0 & -1 & 0 \end{bmatrix} \begin{bmatrix} \cos\gamma & -\sin\gamma & 0 \\ \sin\gamma & \cos\gamma & 0 \\ 0 & 0 & 1 \end{bmatrix} = \begin{bmatrix} \cos\gamma & -\sin\gamma & 0 \\ 0 & 0 & 1 \\ -\sin\gamma & -\cos\gamma & 0 \end{bmatrix} . \tag{2.20}$$

With these three transformations defined and the transformation properties represented by Equations (2.12) and (2.13), all possible transformations can be found between the four coordinate frames discussed in this chapter.

2.2 Environment Model

The environment includes all things that are generally thought to be a part of Nature. This means that anything outside of the vehicle that can interact with it should be included within the simulation to maximize its fidelity. This might include things such as the atmosphere of Earth, the Earth's gravity field, the Earth's magnetosphere, or even the solar wind. The dominating components of the environment for this problem are the atmosphere and gravity. The magnetosphere only affects objects with

high electromagnetic properties such as charge or current and even still this is only significant while in orbit. The solar wind tends to dominate when things have a high surface area and are in interplanetary space. For these reasons the magnetosphere and solar wind are assumed to be negligible and are thus ignored.

2.2.1 Atmosphere Model

The atmosphere used for this thesis is based upon the 1962 U.S. Standard Atmosphere [11]. It gives a prediction of the expected value for physical atmospheric properties such as temperature, pressure, and density. The model extends up to 700 km which is easily encloses the operational regime of the problem presented in this thesis.

The wind is assumed to be negligible at the altitudes of interest, because even though the winds may be high, the density is small enough to safely ignore the effects of wind on the spacecrafts trajectory. The atmosphere is assumed to be fixed relative to the surface of the Earth therefore it remains coincident with the Earth-centered Earth-fixed frame.

The atmosphere is also assumed to be entirely in the continuum flow regime. While the trajectories do spend a substantial portion of time in the transitional regime between those of continuum and free molecular flow, the effects have shown to be minimal over the relatively short period of time of the skip phase. Therefore, the rarefied atmospheric effects and the required adjustments to the aerodynamic coefficients are assumed to be negligible.

2.2.2 Gravity Model

The gravity model used in this thesis is a simple Newtonian gravity field with its familiar inverse-squared relation. The acceleration due to gravity in a Newtonian gravity field is

$$\mathbf{a}_g = -\frac{\mu_\oplus}{r^2}\hat{\mathbf{i}}_r \tag{2.21}$$

where $\mu_\oplus$ is a constant known as the gravitational parameter of Earth (398,600 $^{km^3}/_{s^2}$), r is the distance between the spacecraft and the center of Earth, and $\hat{\mathbf{i}}_r$ is the unit vector pointing in the direction of the spacecraft.

A more complicated model for the gravity is unnecessary for the level of fidelity needed for this thesis because the next higher order model includes J_2, the second gravitational harmonic. Its magnitude is on the order of 10^{-3} and only has a significant effect on spacecraft that orbit for long periods of time. Given that the problem presented in this thesis is less than one orbit it is safe to assume that the effects of J_2 are negligible.

2.3 Vehicle Model

The vehicle chosen for the basis of this thesis is the current Crew Exploration Vehicle (CEV) design concept documented in Chapter 5 of Reference [2]. This chapter includes all the relevant information necessary to define a simplified model of the vehicle. It also includes the details of some interesting trade studies that were completed to define the shape and capabilities of the CEV. The shape that was shown to be the best overall design was a design that is essentially an enlarged Apollo Command Module. The shape is shown in Figure 2-3. It shows a 5.5 m diameter blunt body with a 32.5° sidewall. The original Apollo Command Module had 3.9 m diameter and a 32° sidewall. The purpose for enlarging the shape is to increase the pressurized volume by nearly a factor of three. This allows for larger crews but also more volume per crew member which is necessary for long duration missions.

The mass of the CEV on a return from the Moon is assumed to be 9600 kg which includes a 100 kg margin allotted to sample returns from the lunar surface. The cross-sectional area of the of the CEV is easily calculated from the diameter stated above, to be 23.76 m^2 ($S = \frac{1}{4}\pi d^2$). For comparison, the Apollo Command Module weighed in between 5500 kg and 5900 kg, depending on the mission, and had a cross-sectional area of 11.95 m^2.

The skip phase of an entry trajectory should always be in the hypersonic flight

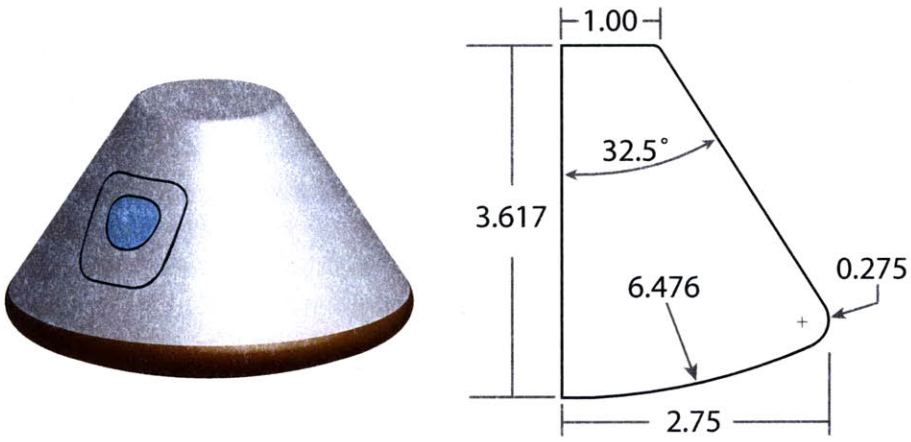

Figure 2-3: CEV shape [2]

Table 2.1: CEV aerodynamic properties during hypersonic flight [10]

M	α_{trim} (deg)	C_{D}	C_{L}	L/D	B_N (kg/m^2)
4	27.20	1.1444	0.50069	0.43751	353.08
6	26.68	1.1651	0.47066	0.40397	346.81
10	25.94	1.1886	0.46326	0.38975	339.95
18	24.18	1.2307	0.44825	0.36422	328.32
25	23.68	1.2446	0.43760	0.35160	324.66
32.2	23.22	1.2507	0.43513	0.34791	323.07

regime ($M > 5$) and initial tests have shown the Mach number to be at the upper end of that regime ($M > 15$). This is expected given that a skip occurs when the velocity is near orbital speeds. It should also be noted that it is assumed that the spacecraft maintains flight at a trim angle angle of attack (α_{trim}) when not performing a propulsive maneuver. A vehicle's lift-to-drag ratio is driven by a number of factors. One such factor is the location of the center of gravity. The center of gravity for the CEV model used in this thesis is chosen in accordance with Reference [10] where it was selected to establish a trim lift-to-drag ratio of 0.35 during the hypersonic regime. The aerodynamic properties of the CEV in the hypersonic regime are shown in Table 2.1 where M is the Mach number, α_{trim} is the trim angle of attack, C_{D} is

the drag coefficient, C_{L} is the lift coefficient, $^{L}/_{D}$ is the lift-to-drag ratio, and B_N is the ballistic number. These values are slightly different from those of the Apollo Command Module but this is due to a difference in the location of the center of gravity.

The CEV will also have the ability to perform a propulsive maneuver during the skip phase. The propulsion system design is also discussed in Reference [2]. It states that the assumed ΔV for entry maneuvering is 10 $^{m}/_{s}$ and for the skip phase correction burn is 40 $^{m}/_{s}$. The thrusters are chosen to be two 100 lbf (445 N) liquid fuel rockets with an I_{sp} of 274 s. It is assumed that these thrusters are positioned in such a way to provide only a translational force without any resultant moment.

2.4 Equations of Motion

The equations of motion are a set of equations that describe the dynamics of the system. They can vary depending on the accuracy of the model and the complexity of the problem. In the case of the propulsive entry problem the equations are non-linear and differential. The most basic representation of the equations of motion is

$$\ddot{\mathbf{r}} = \mathbf{a}_T = \mathbf{a}_g + \mathbf{a}_a + \mathbf{a}_t \tag{2.22}$$

where $\ddot{\mathbf{r}}$ is the second time derivative of the position, $\mathbf{a}_T$ is the total acceleration, $\mathbf{a}_g$ is the acceleration due to gravity, $\mathbf{a}_a$ is the aerodynamic acceleration, and $\mathbf{a}_t$ is the acceleration from the thrusters.

The acceleration due to gravity is already shown in Equation (2.21) but written in terms of the local vertical/local horizontal frame it becomes simply

$$\mathbf{a}_g = -\frac{\mu_{\oplus}}{r^2}\hat{\mathbf{j}}_L. \tag{2.23}$$

The aerodynamic acceleration is the vector sum of the drag and lift accelerations

$$\mathbf{a}_a = \mathbf{a}_{\mathrm{D}} + \mathbf{a}_{\mathrm{L}} \tag{2.24}$$

where the magnitude of $\mathbf{a}_{\mathrm{D}}$ is calculated from

$$a_{\mathrm{D}} = \frac{q}{B_N} \tag{2.25}$$

and the magnitude of $\mathbf{a}_{\mathrm{L}}$ is simply

$$a_{\mathrm{L}} = \frac{L}{D} a_{\mathrm{D}}. \tag{2.26}$$

The variable q in Equation (2.25) is known as the dynamic pressure and is the apparent pressure from moving through a fluid. It is defined as

$$q = \tfrac{1}{2}\rho v_{rel}^2 \tag{2.27}$$

where ρ is a function of altitude as defined in Subsection 2.2.1 and v_{rel} is the atmospheric relative speed.

The acceleration from drag always acts opposite the direction of motion relative to the wind, $-\hat{\mathbf{i}}_S$, and the lift acceleration is defined to be in the $\hat{\mathbf{j}}_S$-$\hat{\mathbf{k}}_S$ plane so it is perpendicular to the drag. The bank angle, θ_b, is defined such that when it is zero the lift vector points in the $-\hat{\mathbf{k}}_S$ direction. Therefore, in the stability frame, the combined aerodynamic acceleration becomes

$$(\mathbf{a}_a)_S = \frac{q}{B_N} \begin{bmatrix} -1 \\ \frac{L}{D}\sin\theta_b \\ -\frac{L}{D}\cos\theta_b \end{bmatrix}. \tag{2.28}$$

The thrust acceleration is defined as

$$\mathbf{a}_t = \frac{F_t}{m}\hat{\boldsymbol{\lambda}}_t \tag{2.29}$$

where F_t is the magnitude of the force applied by all the thrusters firing (in this case $2 \times 100\ lbf$), m is the spacecraft mass, and $\hat{\boldsymbol{\lambda}}_t$ is the unit vector in the direction of the thrusters.

For this thesis it is assumed that the thrusters remain in the **r**-**v** plane and thus no side force is created. Therefore, it is convenient to define the vector $\hat{\boldsymbol{\lambda}}_t$ in terms of the local vertical/local horizontal frame by simply breaking the vector into its components.

$$\left(\hat{\boldsymbol{\lambda}}_t\right)_L = \begin{bmatrix} \cos\beta \\ \sin\beta \\ 0 \end{bmatrix} \tag{2.30}$$

where β is the thrust direction angle which is the angle between $\hat{\boldsymbol{\lambda}}_t$ and the local horizontal. It uses the same sign convention as the flight path angle.

By combining Equations (2.21), (2.28), and (2.31), the total acceleration becomes

$$(\mathbf{a}_T)_I = \mathcal{T}_L^I \left(\frac{\mu_\oplus}{r^2} \begin{bmatrix} 0 \\ -1 \\ 0 \end{bmatrix}_L + \mathcal{T}_S^L \frac{q}{B_N} \begin{bmatrix} -1 \\ \frac{L}{D}\sin\theta_b \\ -\frac{L}{D}\cos\theta_b \end{bmatrix}_S + \frac{F_t}{m} \begin{bmatrix} \cos\beta \\ \sin\beta \\ 0 \end{bmatrix}_L \right) \tag{2.31}$$

and the position and velocity vectors are defined by

$$\mathbf{v} = \mathbf{v}_0 + \int_0^{t_f} \mathbf{a}_T \, dt \tag{2.32}$$

$$\mathbf{r} = \mathbf{r}_0 + \int_0^{t_f} \mathbf{v} \, dt \tag{2.33}$$

where $\mathbf{r}_0$ and $\mathbf{v}_0$ are the initial position and velocity, respectively, and t_f is the final time.

2.5 Boundary Conditions

The initial conditions and the final termination condition must be defined before the equations of motion can be integrated. These are represented in Equations (2.32) and (2.33) as $\mathbf{r}_0$, $\mathbf{v}_0$, and t_f.

The initial conditions $\mathbf{r}_0$ and $\mathbf{v}_0$ are the position and velocity at the start of the skip phase. The skip phase is defined in accordance with the Apollo guidance

algorithm that forms the basis of the algorithm developed in Reference [10]. The skip phase begins when the aerodynamic acceleration drops below 6 $^{ft}/_{s}$ (approximately 1.83 $^{m}/_{s}$ or 0.186 g's). The skip phase guidance proceeds until the aerodynamic acceleration rises above 6.5 $^{ft}/_{s}$ (approximately 1.98 $^{m}/_{s}$ or 0.202 g's) at which point it transitions to the final phase. The reason for the discrepancy between these two values is that it guarantees that the final phase isn't triggered before the actual skip has occurred. This definition of the skip phase boundary conditions is in contrast to the standard methodology that defines the skip phase based upon reaching a specific altitude that is known as the entry interface (approximately 120 km). This ends up being a conservative definition for the bounds of the skip phase because, as will be seen, the Apollo definition generally starts at a much lower altitude.

The initial position can be any vector (outside the surface of the Earth of course). However, for ease of implementation the initial position is defined to be entirely along one axis of the inertial frame. For this thesis the initial position will be defined to be along the $\hat{\mathbf{i}}_I$ axis (zero latitude and longitude). Therefore it is only necessary to define the initial altitude of the spacecraft to get the initial position vector as

$$(\mathbf{r}_0)_I = \begin{bmatrix} r_\oplus + h_0 \\ 0 \\ 0 \end{bmatrix} \tag{2.34}$$

where $r_\oplus$ is the equatorial radius of the Earth and h_0 is the initial altitude.

Once the initial position vector is defined, this constrains the initial velocity vector so as to enable the spacecraft to perform a skip. That range of velocities is very narrow. If the speed is too slow or the flight path angle too negative, the spacecraft will perform a direct entry. Likewise, if the speed is too fast or the flight path angle too positive, the spacecraft can skip away from Earth and out into interplanetary space. Following the simplifications made for the initial position, it will be assumed that the velocity will place the spacecraft in an equatorial orbit (azimuth = 90°) heading due East. It is generally more helpful to think about the velocity in terms of speed and flight path angle which define its magnitude and direction, respectively.

Given that the spacecraft is an equatorial orbit and heading due East, the speed and direction define the velocity by breaking it into components as

$$(\mathbf{v}_0)_I = v_0 \begin{bmatrix} \sin\gamma_0 \\ \cos\gamma_0 \\ 0 \end{bmatrix} \tag{2.35}$$

where v_0 is the initial speed and γ_0 is the initial flight path angle. It should be noted that the initial speed and flight path angle should be in a relationship that gives a periapsis that is low enough in the atmosphere so that the spacecraft is guaranteed to return to the Earth.

The value of t_f is not fixed and depends on a number of factors that are very non-linear in their nature. The first factor has already been discussed and that is the magnitude of the aerodynamic acceleration that is used to transition to the final phase. The other factor is the method of targeting the entry condition for specified landing site as shown in Figure 2-4. Figure 2-4 illustrates in, a rough sense, how a guidance algorithm might correct for a certain amount of overshoot or undershoot during the skip phase. An undershoot is defined as a trajectory that will fall short of the target by some amount, whereas an overshoot is defined as a trajectory will go beyond the target by a given amount. The dashed lines represent the trajectory that would occur without any propulsive correction. The solid lines represent the corrected trajectories that enter the final phase at the target conditions.

Two methods for targeting a specified landing range are used in this thesis. The first is the most straightforward and perhaps the easiest method to understand. It is known as "downrange targeting" and is defined as targeting a specified skip phase range that will place the spacecraft at the desired location for the transition to the final phase. The problem with this type of target is that it says nothing about the velocity and flight path angle at termination of the skip phase. This can be problematic if the guidance solution produces a result that places the spacecraft at the correct location but without the proper energy to reach the landing site (i.e. too slow or too steep). To counteract this problem another method of targeting was created. This method

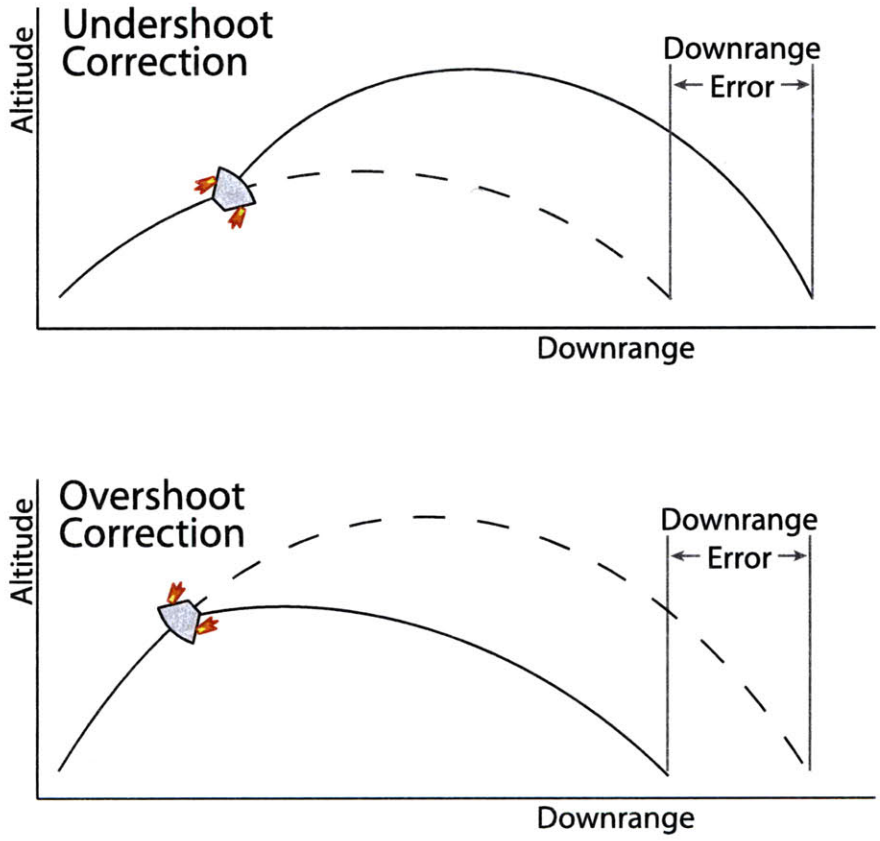

Figure 2-4: Propulsive guidance range corrections

Table 2.2: Summary of simulation parameters

Parameter	Description	Value	Unit
m	spacecraft mass	9600	kg
S	spacecraft surface area	23.758	m^2
L/D	spacecraft lift-to-drag ratio	≈ 0.37	–
B_N	spacecraft ballistic number	≈ 330	kg/m^2
F_t	thruster force	890	N
I_{sp}	thruster specific impulse	274	s
ΔV_{max}	thruster maximum velocity change	40	m/s
$\mu_\oplus$	gravitational parameter of Earth	398600	km^3/s^2
$r_\oplus$	equatorial radius of Earth	6378140	m
$\omega_\oplus$	rotational frequency of Earth	7.2921×10^{-5}	rad/s
a_{a_0}	initial magnitude of aero acceleration	0.186	g's
a_{a_f}	final magnitude of aero acceleration	0.202	g's

is know as "manifold targeting" and it offers a more accurate way of guaranteeing that the spacecraft will be able to reach the landing site at the end of the skip phase. It uses the velocity and flight path angle at the end of skip phase to calculate an estimate of the final phase range. It then adds the estimate to the skip phase range and checks to see if that sum equals the range-to-go at the initialization of the skip phase to within some finite tolerance. This guarantees that the spacecraft will reach the landing site to within the accuracy of the skip range tolerance and estimate of the final phase range. The concept of targeting a manifold will be discussed further in the next chapter.

Table 2.2 summarizes the values given to key parameters discussed in this chapter and used in the simulation of this problem.

Chapter 3

Impulsive Analysis

A good first step when approaching any problem is to bound the problem by performing a simplified analysis that is accurate to first-order in some respect. This allows the designer to become familiar with the physics of the problem and the underlying sensitivities of the solution to various parameters of problem. The simplification made here is that of using an impulsive ΔV to correct for a specific error. An impulsive analysis is generally the first step taken when approaching the design of a propulsive guidance algorithm. By using an impulsive ΔV it is possible to examine how its magnitude and direction change as a function of the initial conditions, time of thruster firing, and the amount of correction needed. Another advantage is that it provides a lower bound to the problem since an impulsive ΔV assumes that the thruster applies a force in an infinitesimal amount of time. As the impulsive assumption is loosened, the thrust is applied for a longer period of time and the state of the vehicle is no longer exactly at the location where the magnitude and direction were calculated. This knowledge can also be used as a "sanity check" for more accurate analysis to make certain that it is in fact valid. These reasons necessitate the inclusion of an impulsive analysis in this thesis and is presented in this chapter.

Table 3.1: Skip trajectory initial conditions

Class	h_0 (m)	v_0 $(^m/_s)$	γ_0 (deg)
1	79400.0	7780.00	1.3000
2	79437.5	7803.75	1.1625
3	79475.0	7827.50	1.0250
4	79512.5	7851.25	0.8875
5	79550.0	7875.00	0.7500

3.1 Trajectory Classification

The boundary conditions discussed in Section 2.5 fix the endpoints of the trajectory. However, it should be clear that there exist many possible trajectories that can satisfy the boundary conditions. In order to completely examine the problem presented in this thesis it is necessary to explore the space spanned by the reasonable trajectories.

This topic was touched upon in Reference [10] with the ability to select two different types of trajectories: "high loft" or "low loft." The trajectory classifications were so named because the "high loft" cases have a higher maximum altitude during the skip phase than their "low loft" counterparts. This effect is brought about by changing the time the numeric predictor-corrector is turned on. The predictor-corrector is turned on earlier to create the "high loft" trajectories. There are however multiple variations in between these two trajectories that can be generated by varying the time the predictor-corrector guidance scheme is turned on. This will produce a number of different trajectories that need to be examined to understand the effects of varying the skip phase initial conditions on the magnitude of the impulsive ΔV.

A set of possible initial conditions were created using a version of the simulation created in Reference [10]. Then five trajectories were chosen to represent the span of possible initial conditions. The initial conditions are shown in Table 3.1. The first and last initial conditions (classes one and five) were chosen because they give the highest and lowest maximum altitude during the skip phase, respectively. The middle three were then created by linearly interpolating between the first and last trajectories to give a smooth variation in initial altitude, speed and flight path angle.

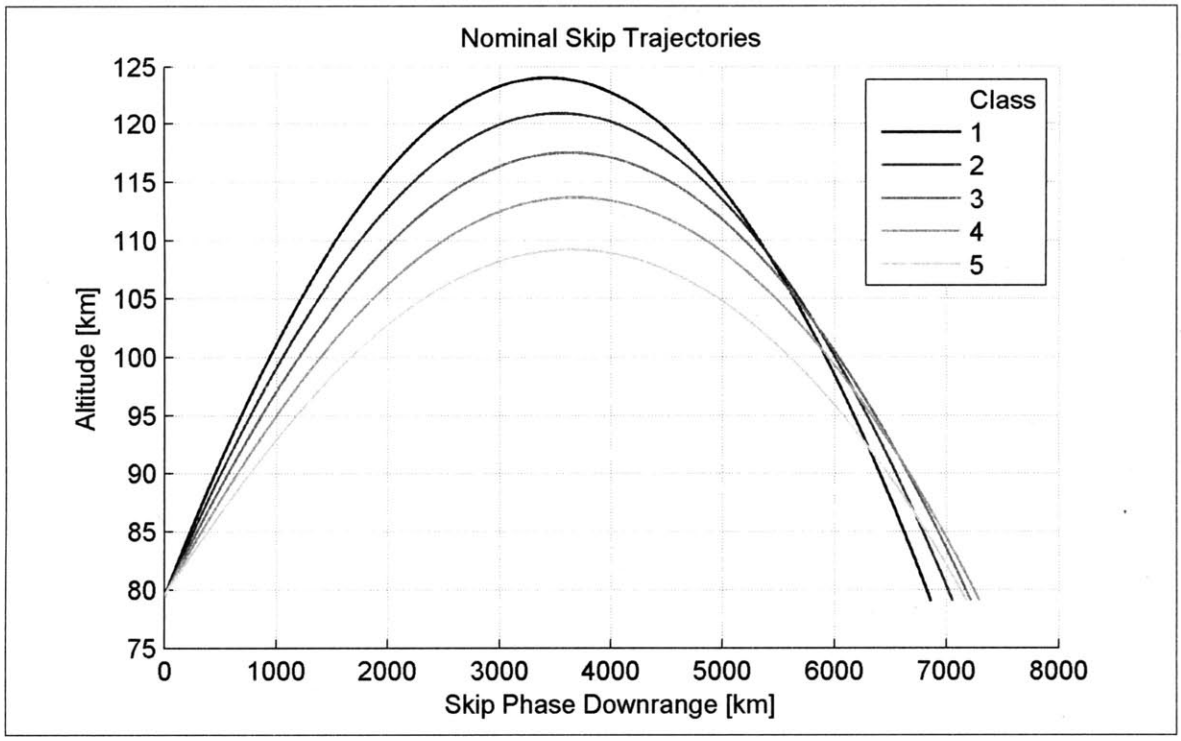

Figure 3-1: Nominal skip trajectories

The trajectories are given a generic "class" number as a way to reference each one individually but one should also note that the larger class numbers have higher initial total energies than those of the smaller class numbers. This means that the "low loft" trajectory had more energy at the start of the skip phase than the "high loft" trajectory. Figure 3-1 shows the skip trajectories created by the initial conditions displayed in Table 3.1. The reason that the skip trajectories in Figure 3-1 do not all end at the same location is because the skip phase exit conditions are dependent on the total range-to-go to the landing site as will be discussed later in Section 3.5. They might not start at the exact same location either as is shown in Figure 3-1. The trajectories all start from the zero downrange because it is strictly representing the downrange during the skip phase. Figure 3-1 is merely presented to give a feel for the shape of each trajectory relative to each other. Thus, now it should be clear what is meant by "high loft" (class one) and "low loft" (class five) trajectories. With the initial conditions shown in Table 3.1 it is now possible to begin analyzing their effect on the amount of ΔV required for a specific corrective maneuver.

3.2 Aerodynamic Effects

Most previously published work defines a skip starting and ending once it reaches the atmospheric entry interface which is defined as 120 km (approximately 400,000 ft) for Earth. However, the Apollo guidance algorithm and the extension presented in Reference [10] define it differently. It is defined once the vehicle experiences a given level of atmospheric acceleration. This method was mentioned briefly in Section 2.5. This definition is appropriate for guidance schemes that use energy management in its decision tree as the Apollo algorithm does. What is not clear is how this is different from the more common altitude definition. The energy definition means that the skip phase initial conditions are a function of the dynamic pressure, q, shown in Equation (2.27). This in turn is a function altitude and speed because density is a function of altitude. This coupling of speed and altitude creates boundary conditions that cause the skip phase to start lower than entry interface. In addition, since the skip phase is lower in the atmosphere, its range is likely to have some significant dependence on the aerodynamic forces created by the vehicle.

A number of open loop simulations were run to analyze the effects of aerodynamic forces on the skip phase range. The initial speed was varied between the 7500 $^m/_s$ and 8000 $^m/_s$ and the initial flight path angle was varied between zero and two degrees. The initial altitude was found by extrapolating a linear fit of the initial conditions presented in Table 3.1. Two sets of simulations were run: one with the lift vector pointed up ($\theta_b = 0°$) and one with the lift vector pointed down ($\theta_b = 180°$). If the trajectories are ballistic, there should be no difference between the lift-up and lift-down sets. However, if the trajectories are not entirely ballistic, the difference between the two sets will be significant and the lift-up and lift-down trajectories should give the maximum and minimum ranges, respectively. Figure 3-2 shows the difference between the range of the lift-up trajectories and that of the lift-down trajectories for varying initial conditions. Figure 3-2 demonstrates that the skip phase is in fact not ballistic. In the best case the range difference is more than 1500 km and it could be closer to 5500 km as in the worst case. This difference is very large considering

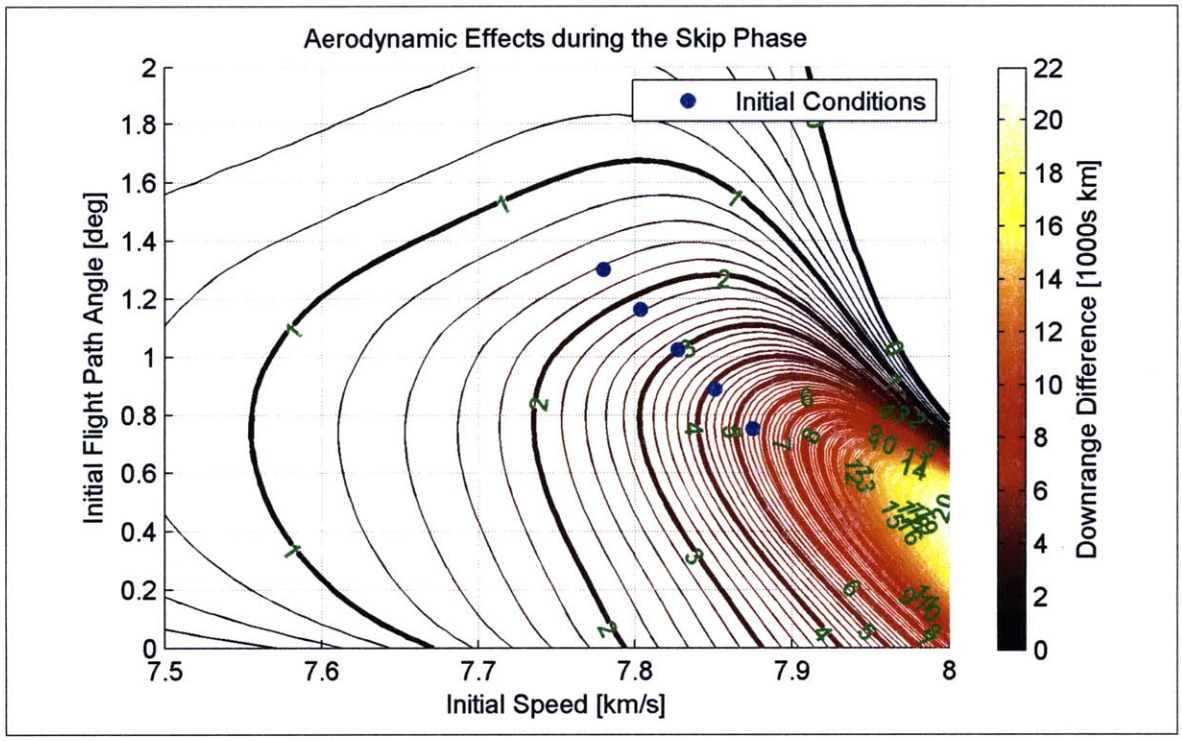

Figure 3-2: Range control authority of lift during the skip phase

the entire skip phase only has a range near 7000 km. Assuming that the skip phase is ballistic while using the boundary conditions discussed earlier would prove to be disastrous. For this reason, from this point further, the lift force is set to be out of the plane of motion (i.e. $\theta_b = 90°$). This negates any effect lift would have on the skip phase range and greatly simplifies the complexity of the problem by removing one variable, namely the bank angle, θ_b.

3.3 Downrange Targeting

The most straightforward way to analyze the sensitivity of a corrective maneuver to a given amount of error is to target a specific downrange location. This idea was illustrated earlier in Figure 2-4. The method used to calculate the minimum magnitude and the appropriate direction of a ΔV burn is brute force in nature with only a couple simplifying assumptions. The first assumption is that an error in either speed or flight path angle can be characterized in terms of an equivalent downrange

error. This assumption is made to reduce the dimensionality of the problem and is valid when the errors are reasonable. The other assumption is that the minimum ΔV direction can be found by using a polynomial fit of a given number of data points found instead of needing to search the entire solution space. The reasoning for and validity of this assumption will be discussed more later, but in order to understand that a discussion of the search method needs to be completed.

To start, the initial conditions are biased for a given amount of range error. The range error is limited between $-1000\ km$ and $1000\ km$ for this analysis and is evaluated in steps of $200\ km$. Remember that the skip phase has a range around $7000\ km$ so this amounts to approximately ± 14 percent error. Starting at the initialization of the skip phase, the ΔV is calculated to correct for the amount of range error. The ΔV is found by bounding the burn direction by finding the angles that will correct for the given error with a maximal amount of ΔV. Then the angle is incremented by one degree in between these bounds all the while finding the correct magnitude at each angle. The magnitude is found by comparing the residual error between two subsequent magnitudes and successively dividing the magnitude in half until it is accurate to within $0.01\ {}^{m}/_{s}$. Once the correct magnitude has been found for a given angle, the magnitude is found for the next angle. When all the directions between the bounds have been exhausted, the minimum ΔV can be found by choosing the minimum magnitude and its corresponding direction. Once this value has been found the minimum ΔV is found for the next point along the biased trajectory. In order to limit the number of points analyzed along a trajectory, the trajectory is discretized by normalizing it with respect to the inertial angle and the minimum ΔV is found for each tenth percentile along the trajectory. Then, when the minimum ΔV has been found for an entire biased trajectory, the error is incremented to the next amount of range bias. All this must be completed for each trajectory shown in Figure 3-1. The dimensionality of the problem is summarized in Table 3.2.

The process described above can be simplified by fitting one of the dimensions with a polynomial instead of finding each ΔV for each point. The dimension that was chosen for fitting was the ΔV direction. The reason for this is that it may be

Table 3.2: Minimum ΔV search dimensionality

Dimension	Resolution	Range	Unit
Class	1	$[1, 5]$	n/a
Range Error	200	$[-1000, 1000]$	km
Location	10	$[0, 90]$	%
ΔV Direction	1	$[0, 360]$	deg
ΔV Magnitude	0.01	$[0, 50]$	m/s

necessary to iterate for close to 180 different directions. Using a sixth order polynomial fit reduces the maximum number of iterations to seven. This vastly improves the computational efficiency with a negligible hit to accuracy. So instead of finding the ΔV direction bounds and iterating between them in one degree increments, the ΔV is found for seven equally spaced interior directions which is then fit with a polynomial. Once the polynomial has been defined it is trivial to find the minimum ΔV magnitude and direction. To demonstrate the accuracy of this method Figure 3-3 shows the brute force method and the polynomial fit results for each trajectory and various amounts of range error with the ΔV burn applied at the initiation of the skip phase.

It should be clear from Figure 3-3 that a sixth order polynomial fit to the ΔV direction is relatively good considering the shape created. Table 3.3 summarizes the mean and standard deviations of the percent differences between the two methods which are very small. Perhaps the biggest advantage to the polynomial fit method is that the computational time was reduced by more than ninety percent compared to that of the brute force method. Some others interesting features in Figure 3-3 are the asymmetries between correcting for an overshoot (positive range error) and an undershoot (negative range error) and decreasing trend for trajectories with higher class numbers. These features and the reasoning behind them will be discussed later.

Now that the efficiency of the minimum ΔV search algorithm has been increased by nearly an order of magnitude, it is economical to extend the results presented in Figure 3-3 to locations further along the trajectory. This will allow one to see how much ΔV is required the longer one might need to wait to perform the maneuver.

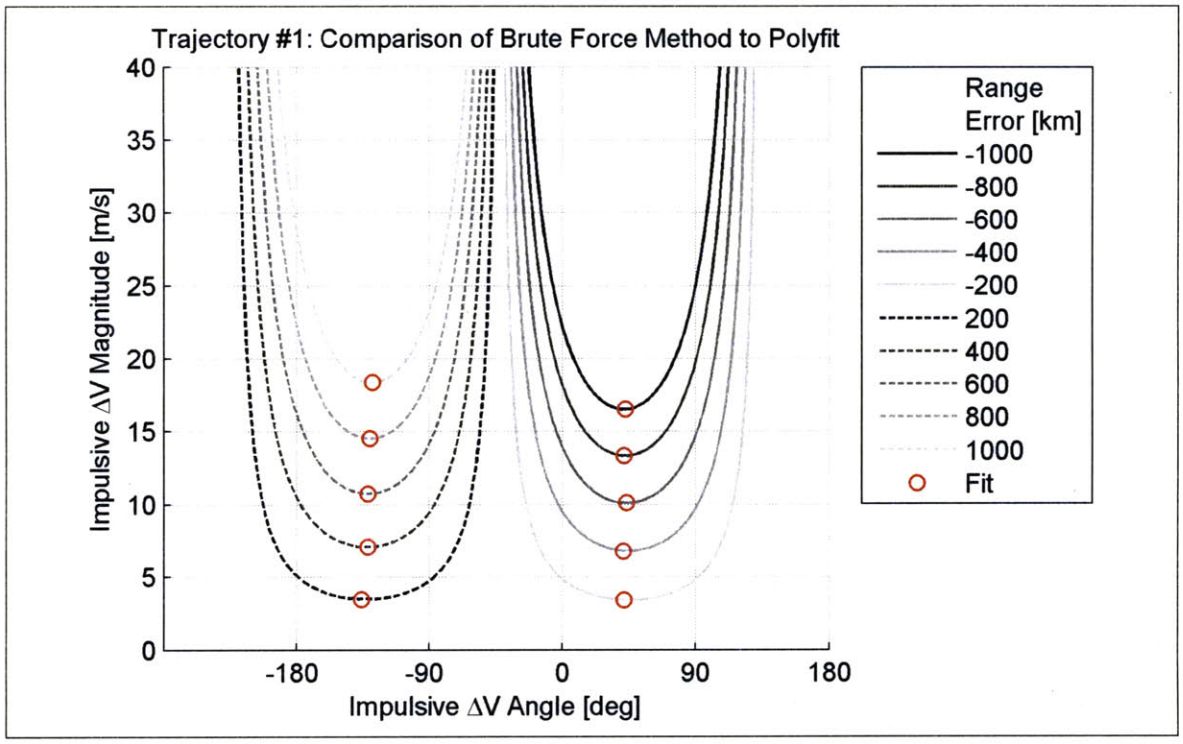

(a) Trajectory #1

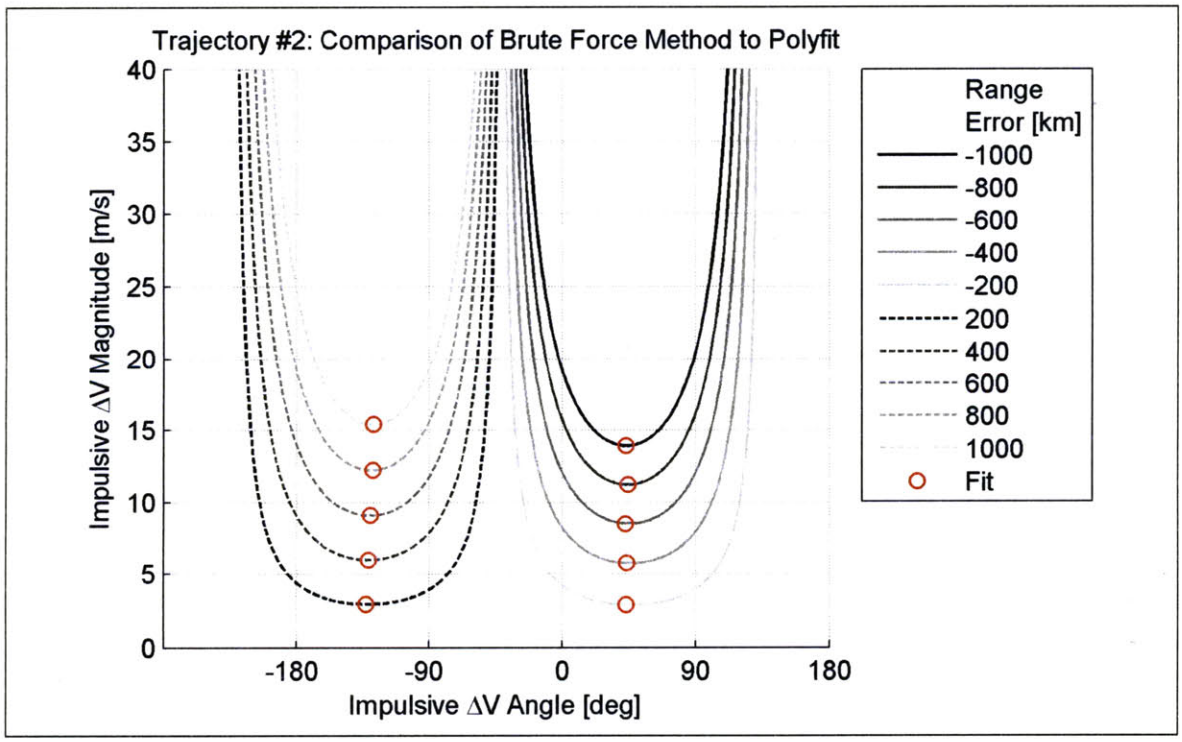

(b) Trajectory #2

Figure 3-3: Impulsive ΔV at the initiation of the skip phase

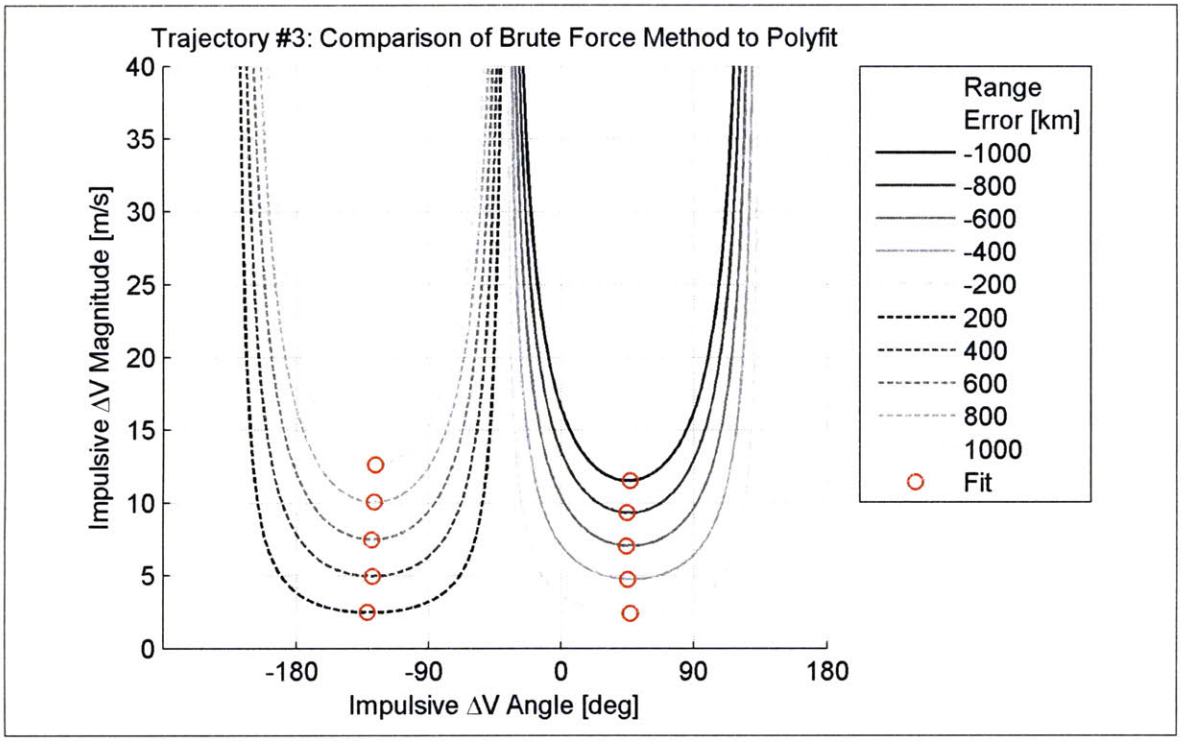

(c) Trajectory #3

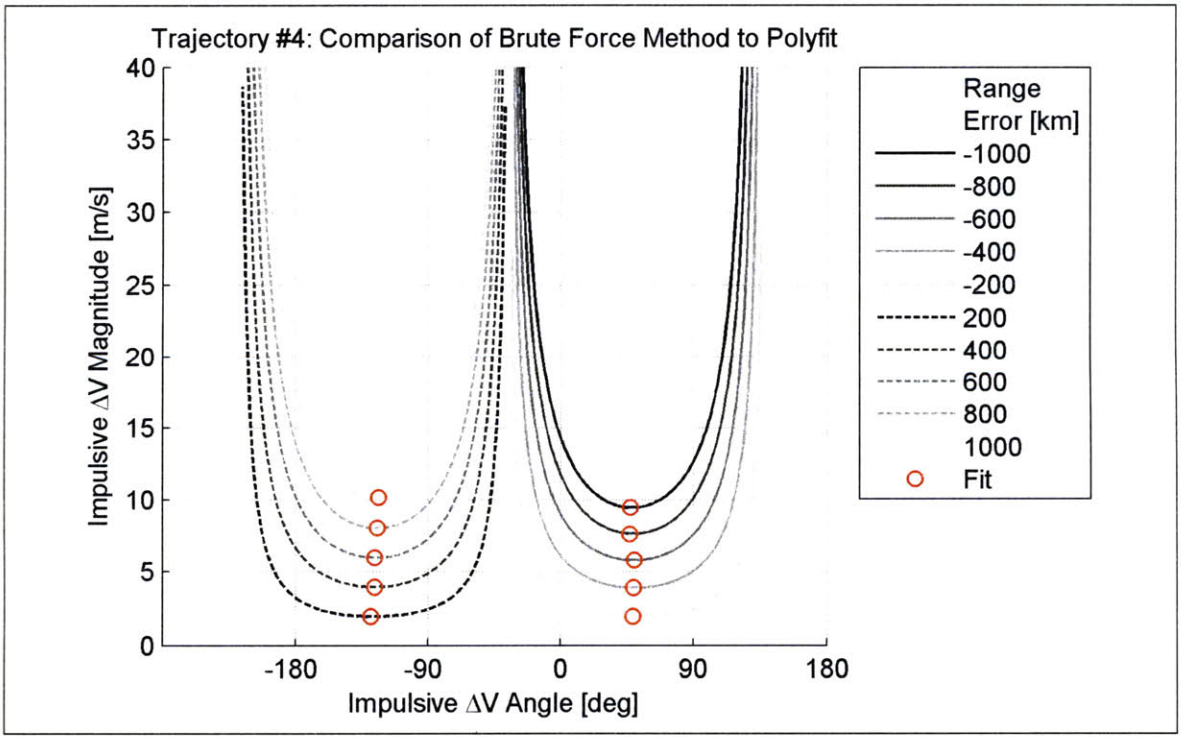

(d) Trajectory #4

Figure 3-3: Impulsive ΔV at the initiation of the skip phase (cont'd)

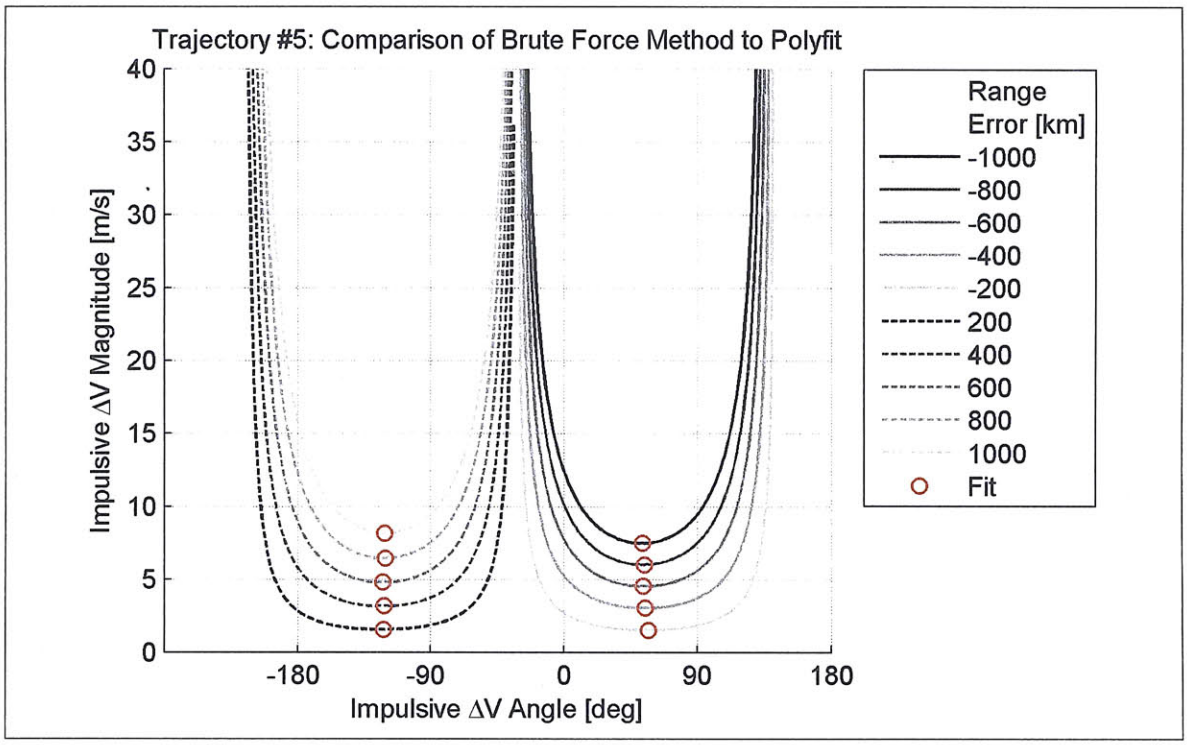

(e) Trajectory #5

Figure 3-3: Impulsive ΔV at the initiation of the skip phase (cont'd)

Table 3.3: Percent differences between minimum ΔV search methods

Class	Δ(ΔV Magnitude) [%]		Δ(ΔV Direction) [%]	
	μ	σ	μ	σ
1	0.14465	0.21388	0.55833	0.59669
2	0.10594	0.15867	0.43830	0.37447
3	0.10585	0.11988	0.68433	0.58821
4	0.07028	0.09032	0.46227	0.41074
5	0.06254	0.08534	0.45740	0.35722

The need to wait to perform the ΔV burn could be caused for a multitude of reasons, not the least of which is the need to reorient the vehicle to the specified ΔV direction. This effect will also play into results for a non-impulsive ΔV burn since it will require a finite time to perform the burn all the while the spacecraft is moving closer towards the end of the skip phase. To demonstrate the effect of location on the magnitude of the ΔV, Figure 3-4 shows contours of ΔV for various amounts of range error, locations and trajectories. The directions of the corresponding ΔV maneuvers are shown in Section A.1 of Appendix A.

Figure 3-4 shows a number of interesting trends. The first, and probably most evident, is that more ΔV is required for locations that are closer to the end of the skip phase. This is a result of the fact that the range-to-go is constantly decreasing and thus less range error can be corrected by a given amount of ΔV. Notice in Figure 3-1 that the total range of the skip phase is roughly 7000 km therefore ten percent of the range is 700 km which is within the bounds of the range error examined here. This means that it would be impossible to correct for more than 700 km of range error at the ninety percent location without either completing another orbit or completely reversing the velocity which would require tens of $^{km}/_{s}$ of ΔV. Neither option is possible within the bounds of this thesis since the maximum ΔV considered for this problem is 40 $^{m}/_{s}$.

Another trend shown in Figure 3-4 is the asymmetry along the range error axis. For instance, examine Figure 3-4a along the thirty percent normalized inertial angle vertical. To correct for 1000 km of initial range error (an overshooting trajectory), it will require about 37.5 $^{m}/_{s}$. To perform a similar maneuver with an undershooting trajectory (-1000 km of initial range error), it will require 28.5 $^{m}/_{s}$. The reason for this discrepancy is similar to the reason behind the previously discussed trend. With 1000 km of overshoot, the trajectory has just become 1000 km shorter and less time is available to perform the maneuver and more ΔV is required to correct for the error. Similarly, a trajectory with 1000 km of undershoot is that much longer and thus smaller changes have bigger effects at the end of the skip phase. Figure 3-5 graphically demonstrates this asymmetry by plotting contours of the difference of the

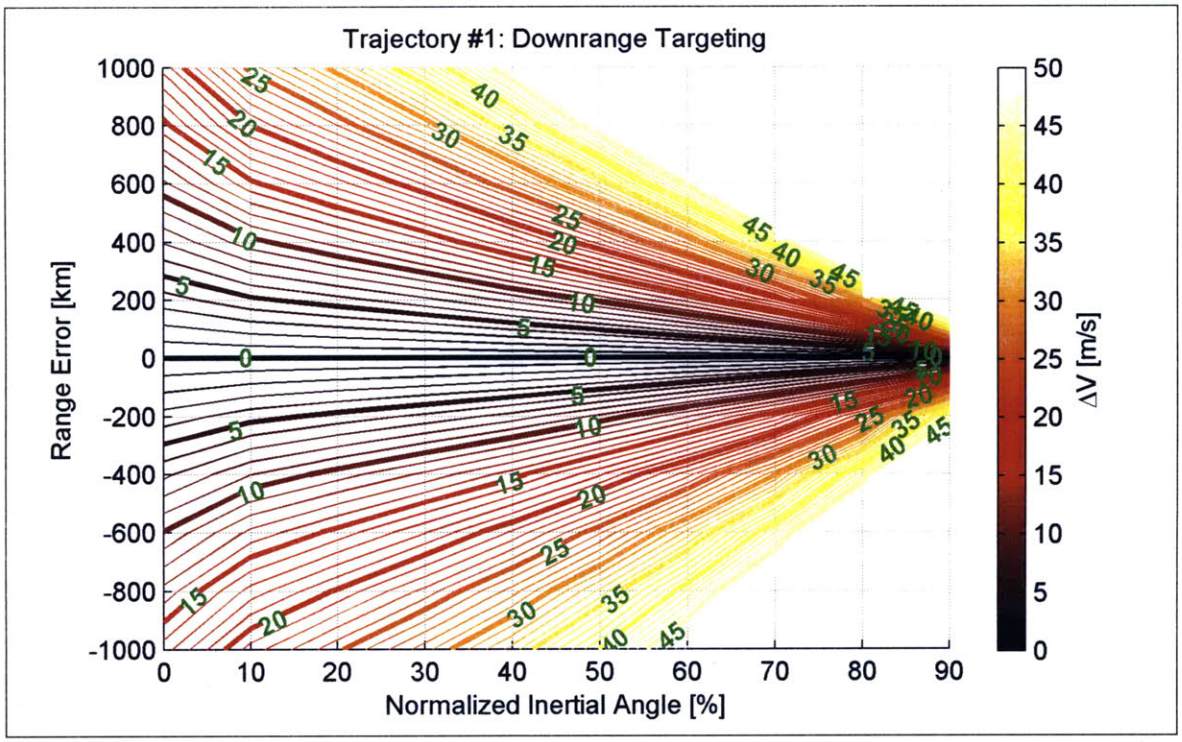

(a) Trajectory #1

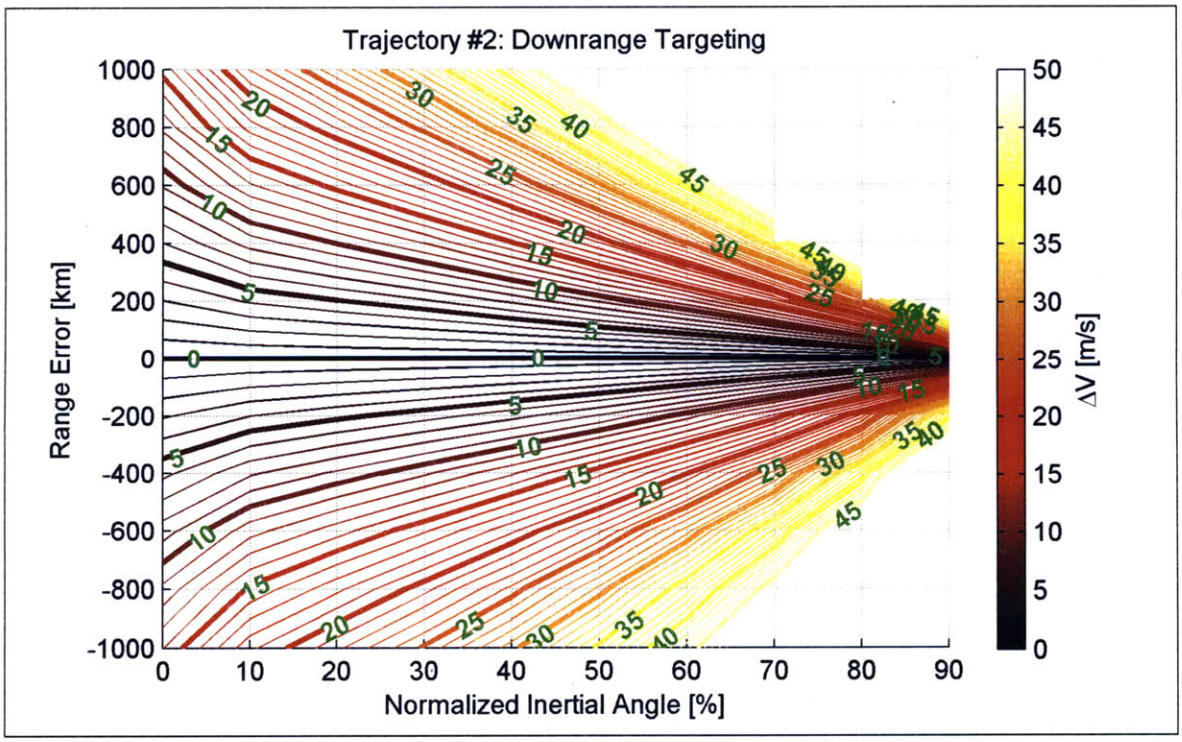

(b) Trajectory #2

Figure 3-4: Minimum impulsive ΔV to target a downrange location

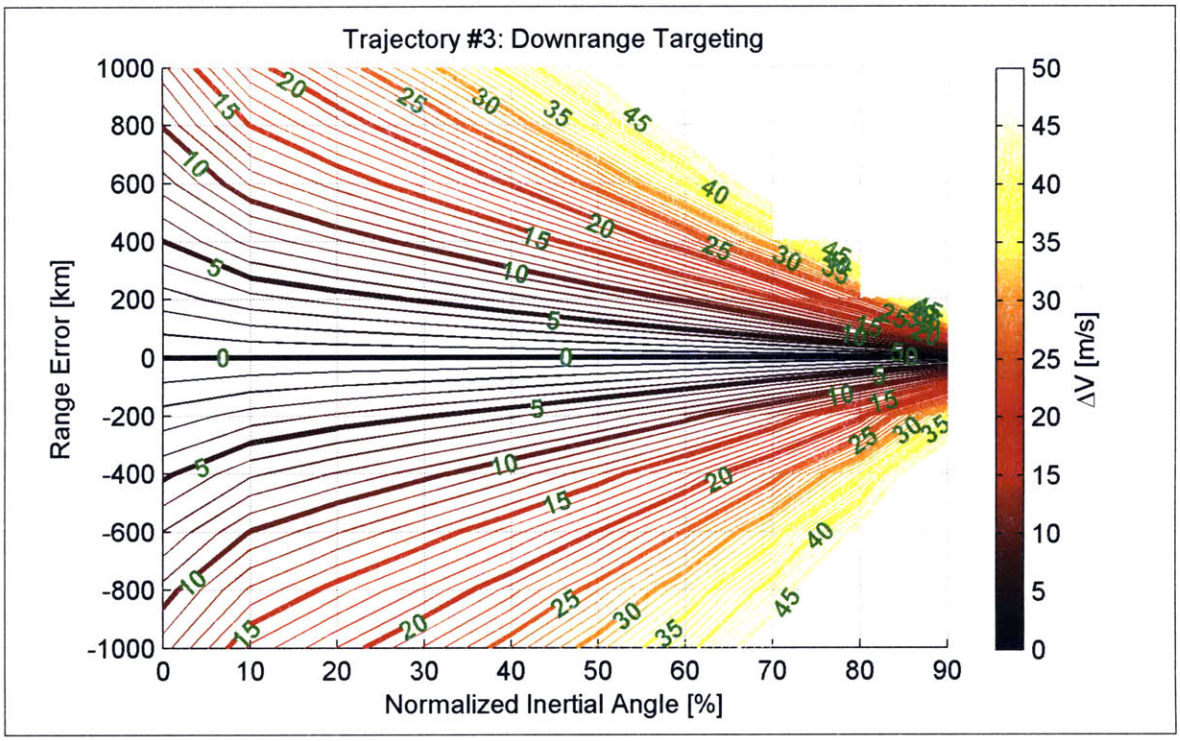

(c) Trajectory #3

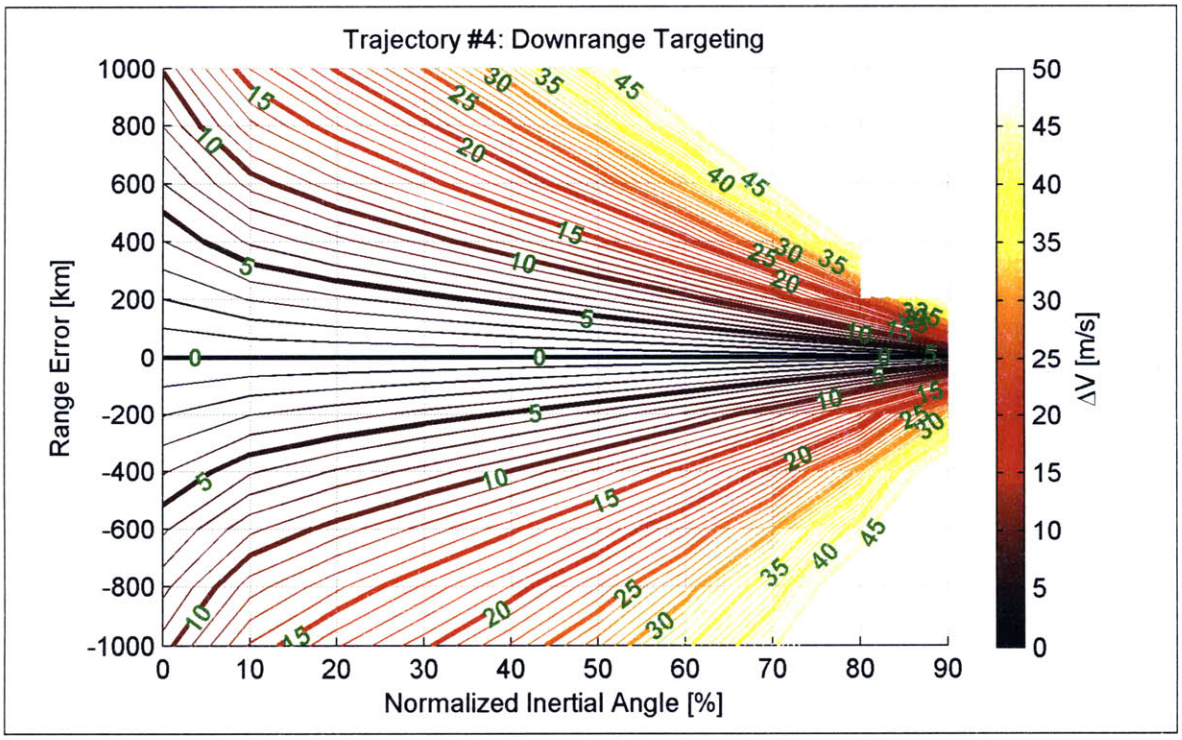

(d) Trajectory #4

Figure 3-4: Minimum impulsive ΔV to target a downrange location (cont'd)

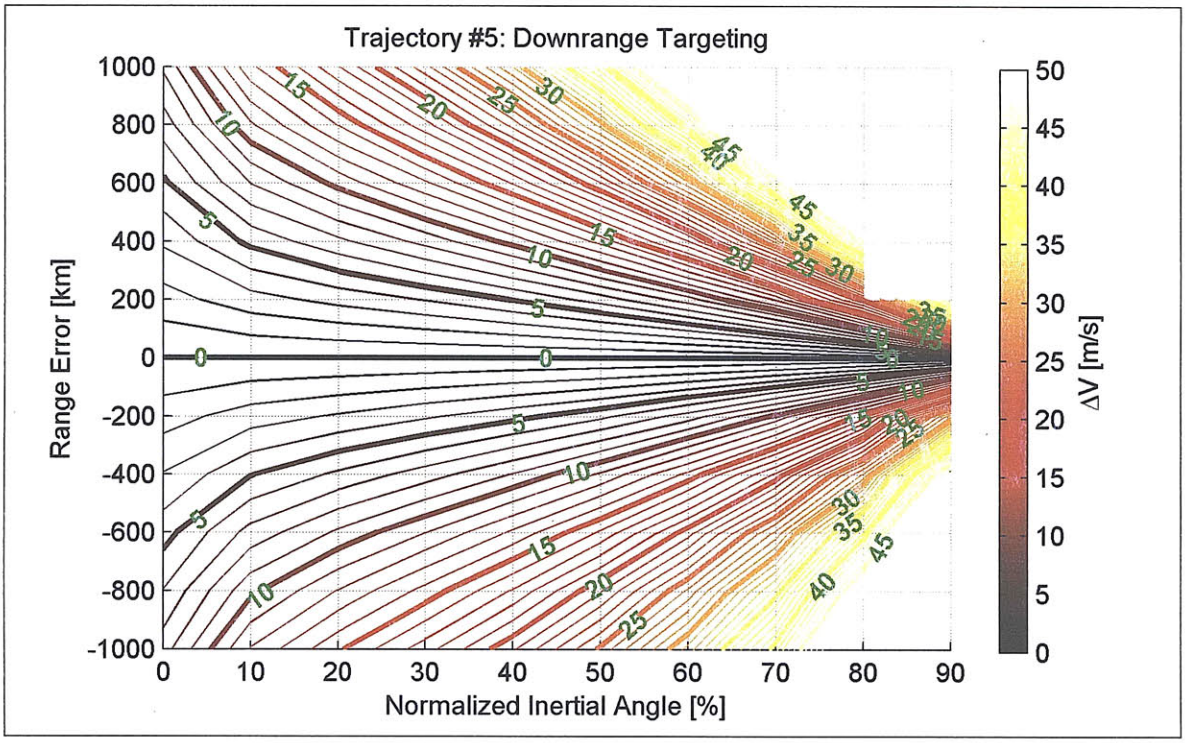

(e) Trajectory #5

Figure 3-4: Minimum impulsive ΔV to target a downrange location (cont'd)

minimum ΔV required to correct for symmetrical amounts of initial range error. It should be noted that the apparent missing data in the right-hand corners of previous figures and those presented in the future is due to the resolution of the analysis.

The final trend to make special note of is the topic of the next section as it represents a significant result and forms the basis of an important trade.

3.4 Correction Capability

The results from the previous section showed a couple interesting trends that occur while varying the initial range error or the location the impulsive burn is performed. However, another trend exists between the different trajectories. Careful examination of Figure 3-4 shows that the contours constrict in towards Figure 3-4a and spread out towards Figure 3-4e. This shows trajectories like the higher energy class 5 trajectory are more beneficial with respect to ΔV and hence fuel used, than those like the lower energy class 1 trajectory. Figure 3-6 shows the difference of the minimum impulsive

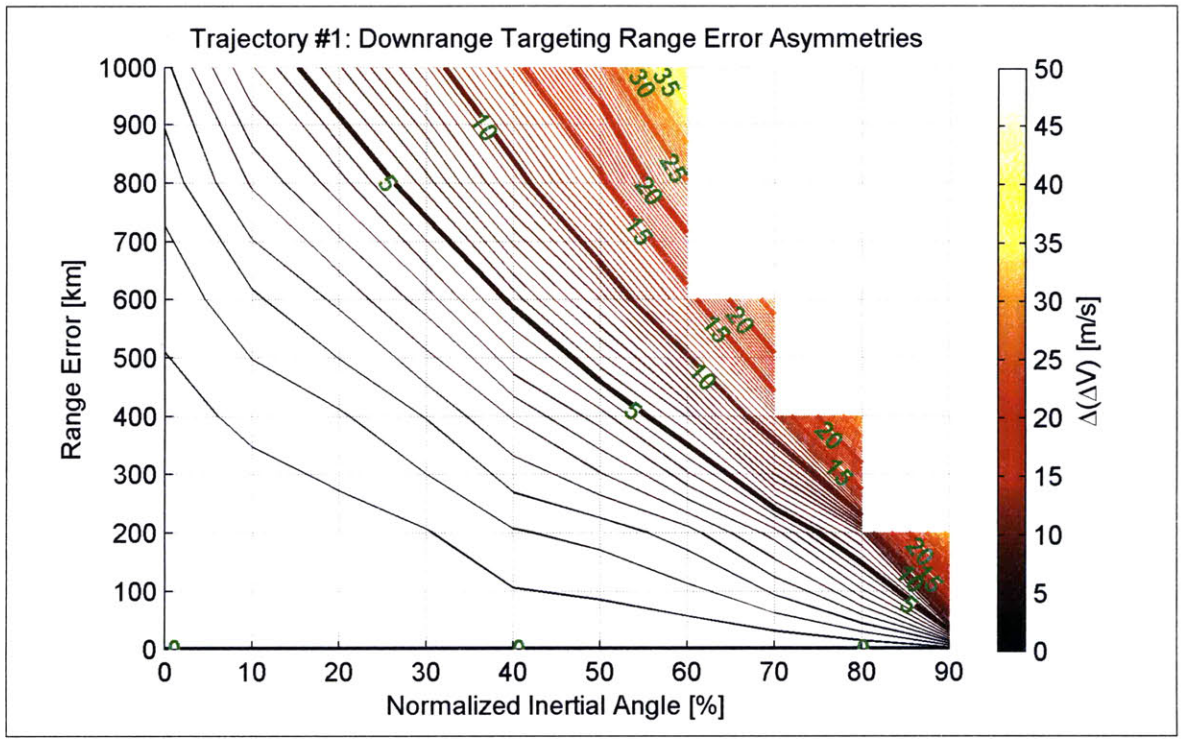

Figure 3-5: Asymmetrical minimum impulsive ΔV with respect to range error

ΔV between the class 1 and class 5 trajectories. These two trajectories were chosen to represent this trend because they show greatest difference between each other.

The differences between the trajectories used to create Figure 3-6 arise from differences between the initial conditions as is shown in Table 3.1. At first glance the difference in initial conditions might seem subtle, but the difference becomes amplified if the energy of the trajectory is represented as the semimajor axis, a_s, as in Equation (3.1), a form of the vis-viva integral.

$$a_s = \left(\frac{2}{r} - \frac{v^2}{\mu_\oplus} \right)^{-1} \tag{3.1}$$

The semimajor axis at the initiation of the skip phase for each trajectory is shown in Table 3.4 along with the difference between the semimajor axis and the radius of Earth. Table 3.4 clearly shows that the energy increases rather smoothly (by about 38 km) between each trajectory from class 1 to class 5. This difference in energy is the reason for the variation between trajectories in Figure 3-4. It also plays a direct

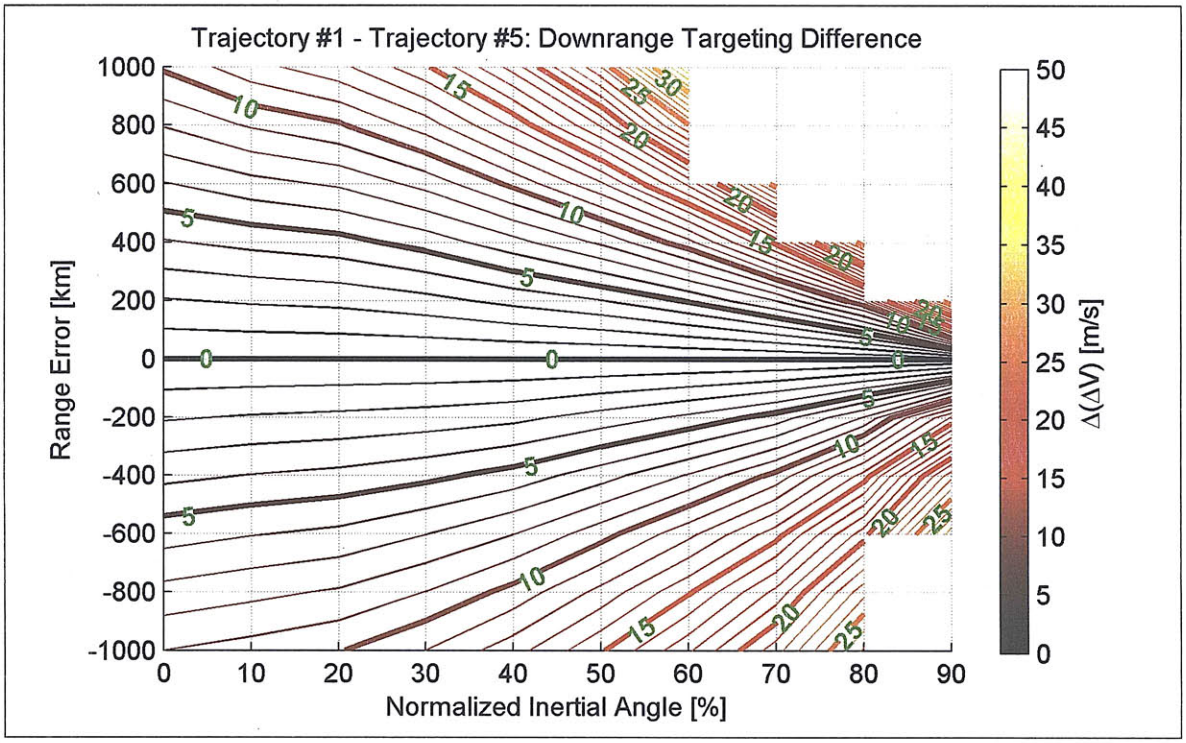

Figure 3-6: Difference between class 1 and class 5 trajectories

Table 3.4: Initial semimajor axis of each trajectory

Class	a_{s_0} (m)	$a_{s_0} - r_{\oplus}$ (m)
1	6334601	-43539
2	6372154	-5986
3	6410271	32130
4	6448964	70824
5	6488247	110106

role in the maximum amount of error a maneuver is capable of correcting with a given ΔV burn size. The correction capability of each trajectory will be examined further a little later in this section.

One should also note that Table 3.4 gives the values for the initial semimajor axis. This value is not constant as can be derived with the Calculus of Variations. The following derivation follows one in Reference [12]. Beginning with the vis-viva integral

$$\mu_{\oplus}\left(\frac{2}{r}-\frac{1}{a_s}\right)=v^2=\mathbf{v}\cdot\mathbf{v} \tag{3.2}$$

Therefore, the partial derivative with respect to the velocity, $\mathbf{v}$, is

$$\frac{\mu_{\oplus}}{a_s^2}\frac{\partial a_s}{\partial \mathbf{v}}=2\mathbf{v}^{\mathrm{T}} \tag{3.3}$$

It can be shown that the time derivative of any orbital element is

$$\frac{\mathrm{d}\xi}{\mathrm{d}t}=\frac{\partial \xi}{\partial \mathbf{v}}\mathbf{a}_{disturb} \tag{3.4}$$

where ξ a generic orbital element and $\mathbf{a}_{disturb}$ is a disturbing acceleration. This gives

$$\frac{\mathrm{d}a_s}{\mathrm{d}t}=\frac{\partial a_s}{\partial \mathbf{v}}\mathbf{a}_{disturb} \tag{3.5}$$

so that the variational equation for the semimajor axis becomes

$$\frac{\mathrm{d}a_s}{\mathrm{d}t}=\frac{2a_s^2}{\mu_{\oplus}}\mathbf{v}\cdot\mathbf{a}_{disturb} \tag{3.6}$$

Equation (3.6) shows that the rate of change of the semimajor axis is directly proportional to the inner product of the spacecraft's velocity with a disturbing acceleration such as atmospheric drag or a ΔV maneuver. This means that given the equations for the aerodynamic acceleration in Equation (2.28) it is clear that drag from the atmosphere makes this rate always negative since the disturbing acceleration in this case is antiparallel to the velocity by definition. This is intuitive since atmospheric drag is a form of friction which is always non-conservative and thus causes the energy

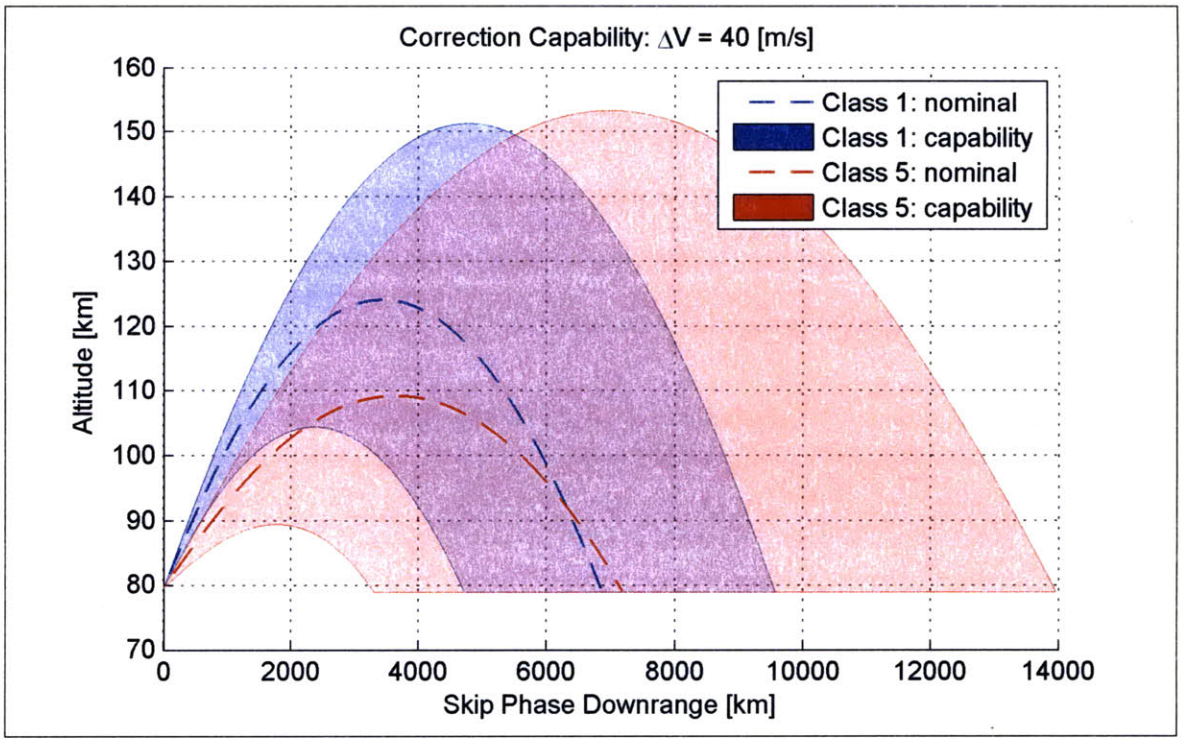

Figure 3-7: Range correction capability for high and low energy trajectories

to decrease. Unfortunately, the same analysis cannot be performed for the ΔV burn with the thrust direction vector, $\hat{\boldsymbol{\lambda}}_t$, because it can be oriented anywhere in the **r**-**v** plane.

The results shown in Figure 3-6 and the subsequent analysis above represent an interesting trend in the minimum impulsive ΔV when varying the trajectory. It appears to be cheaper to correct for a given amount of range error when a trajectory reaches a lower maximum altitude than one that lofts higher out of the atmosphere. Another more explicit way of representing this variation is shown in Figure 3-7 and summarized in Table 3-7.

Figure 3-7 shows the maximum and minimum ranges that are achievable with 40 $^m/_s$ of ΔV for the lowest energy trajectory (class 1: blue) and the highest energy trajectory (class 5: red). Table 3.5 shows the nominal range without a maneuver being performed and the maximum and minimum ranges achievable with 40 $^m/_s$ of ΔV for all five trajectories. It is clear from Figure 3-7 and Table 3.5 that the high energy trajectories give more than double the amount of variation in the achievable

Table 3.5: Range correction capability with 40 $^{m}/_{s}$ of ΔV

Class	x_{nom} (km)	x_{max} (km)	x_{min} (km)	Δx (km)
1	6859	9553	4713	4840
2	7051	10325	4532	5793
3	7215	11286	4242	7044
4	7292	12481	3825	8656
5	7186	13936	3306	10631

range at the end of the skip phase than the low energy trajectories. The reason for this variation relies on the fact that the high energy trajectories remain lower in the atmosphere but with a higher initial speed. Since the high energy trajectory is lower in the atmosphere, it can shorten its range by using a thicker atmosphere to create more drag. In addition, if the range needs to be lengthened, a high energy trajectory can rely on its higher velocity to carry the spacecraft further downrange before entering the final phase. The main drawback to using high energy trajectories is the decreased amount of time that is available to perform ΔV maneuver. While this is not a problem given the analysis presented here that uses an impulsive ΔV, it will be a problem when the impulsive assumption is removed and it takes a finite amount of time to perform a maneuver. This creates a trade that needs to be made between the amount of time required to perform a ΔV maneuver and the maximum amount of error the system will be able to correct for.

3.5 Manifold Targeting

As mentioned earlier, the problem with strictly targeting a downrange location during the skip phase is that there is no guarantee that the initial conditions of the final phase will allow the spacecraft to reach the desired landing target. This non-guarantee arises because the speed and flight path angle at the end of the skip phase are left unconstrained. While this might be a greater problem with a ΔV an order of magnitude larger than the maximum ΔV considered in this thesis, it is nonetheless important to explore a targeting solution that gives greater control over the spacecraft's capability

Table 3.6: Manifold parameters

Parameter	Value	Unit
x_{ref}	2175600	m
$\frac{\partial x}{\partial v}$	1452.192	s
v_{ref}	7700	m/s
$\frac{\partial x}{\partial \gamma}$	637225.4	m/deg
γ_{ref}	-1	deg

to reach the desired landing target which is after all the ultimate goal of any reentry guidance algorithm. This section concerns such a method; more specifically, one that targets downrange location based on the range-to-go and a prediction of the final phase range derived from the final conditions of the skip phase.

The targeting method employed here is known as manifold targeting as it targets a manifold of final conditions of the skip phase that are known to reach a specified landing range. This method was derived and used by the Apollo guidance algorithm and an excellent in-depth discussion of the method can be found in chapter 5 of Reference [10]. The equation governing the relationship between the three variables is a Taylor expansion about a reference point as shown in Equation (3.7)

$$x = x_{ref} + \frac{\partial x}{\partial v}(v - v_{ref}) + \frac{\partial x}{\partial \gamma}(\gamma - \gamma_{ref}) \tag{3.7}$$

where x is the final phase range-to-go and the $()_{ref}$ subscripted variables are the conditions at which the Taylor expansion is made. The partial derivatives are linear gains weighting the errors in velocity and flight path angle. They are found by integrating the adjoint equations of motion backwards in time from the desired landing point to the initialization of the final phase. The reference values and gains are given in Table 3.6.

The parameters in Table 3.6 allow for a first order prediction of the final phase

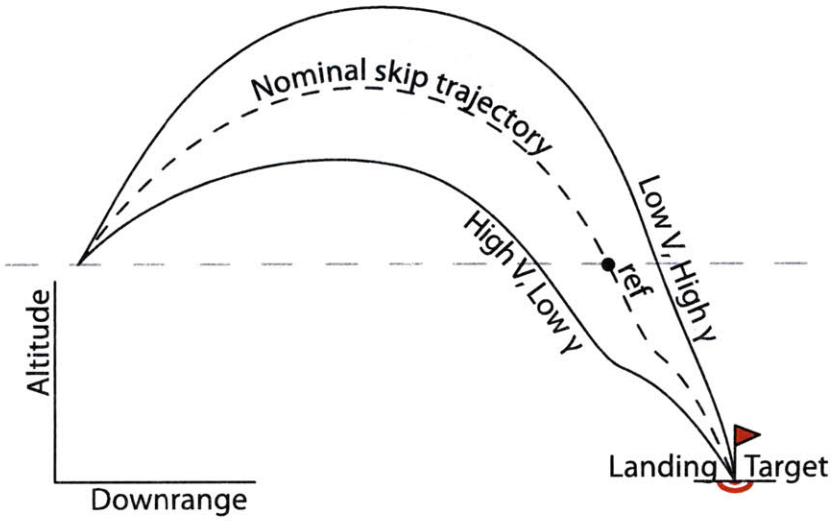

Figure 3-8: Manifold targeting to achieve a landing target

range to be made. These parameters along with Equation (3.7) define a manifold of ranges, speeds, and flight path angles that will enable the spacecraft to reach the desired landing point if they are achieved at the end of the skip phase. This is precisely the target needed to guarantee (at least to first order) that the final condition of the skip phase is desirable. To use this target another operation is added to the algorithm described in the previous section. Instead of comparing the downrange at the end of the skip phase to the targeted downrange, the downrange at the end of the skip phase is added to the final phase range predicted by the manifold and that value is compared to the total range-to-go. Therefore, when the actual range converges to the range predicted by the manifold, the ΔV ensures that the spacecraft will reach the desired target. This concept is illustrated in Figure 3-8. Figure 3-8 shows three trajectories that are all capable of achieving the desired landing target given a guided final phase. The dashed trajectory is the nominal trajectory and the point marked "ref" along it is the point about which Equation (3.7) is linearized. The lower trajectory is one whose range is shortened for one reason or another and therefore has a higher velocity and shallower flight path angle than the nominal trajectory. However, these final phase initial conditions still allow it to reach the landing target. Inversely, the upper trajectory is one whose range is lengthened for

one reason or another. This results in a lower velocity and higher flight path angle when compared to the nominal trajectory. Similarly, this trajectory is still able to reach the target. Enabling a guidance scheme to target these trajectories as well is beneficial since it will loosen constraints on the terminal condition slightly.

The minimum impulsive ΔV that can be used while targeting the manifold are shown in Figure 3-9. The same initial conditions were used as were the range errors and normalized inertial angles. The ΔV directions of the following maneuvers are shown in Section A.2 of Appendix A.

The results shown in Figure 3-9 are very similar to those in Figure 3-4. The same trends exist in Figure 3-9 that exist in Figure 3-4. It is still expensive to correct for a given amount of range error when a ΔV burn is performed later. Likewise, overshoots are more expensive than undershoots which result in the asymmetry about the x-axis, and the low energy trajectories result in larger ΔVs than a higher energy trajectory.

One interesting difference between Figure 3-4 and Figure 3-9 is that it appears

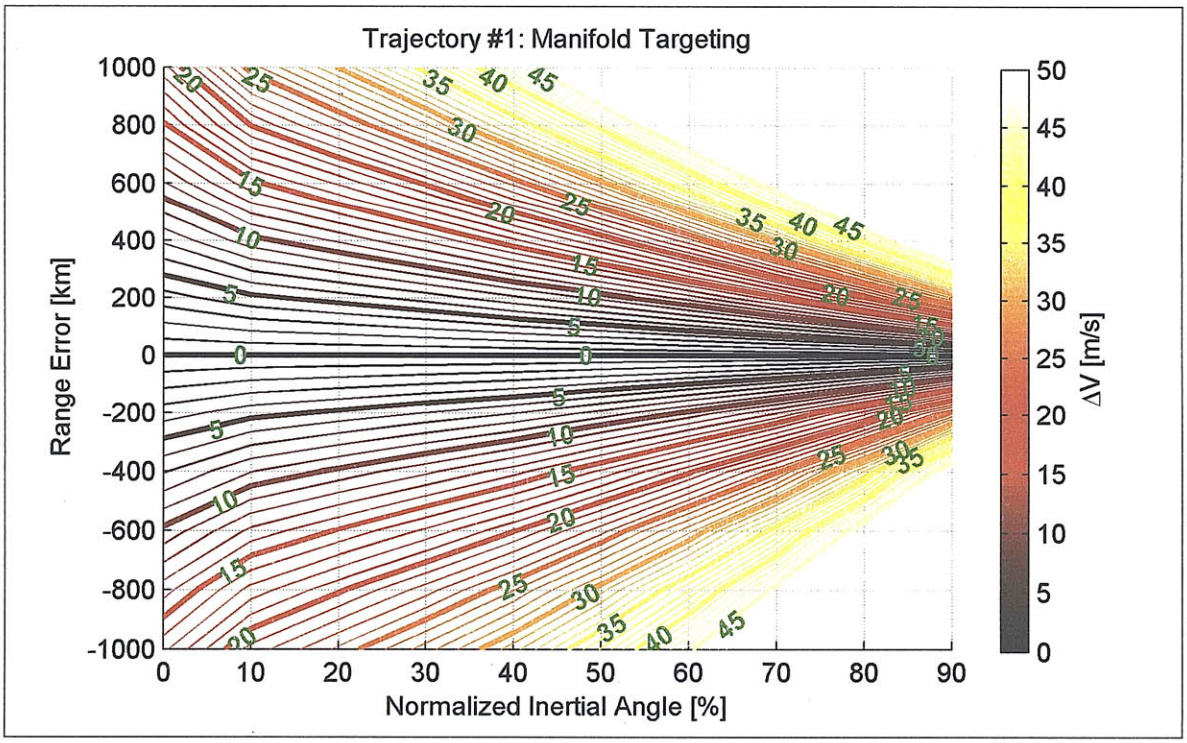

(a) Trajectory #1

Figure 3-9: Minimum impulsive ΔV to target a manifold

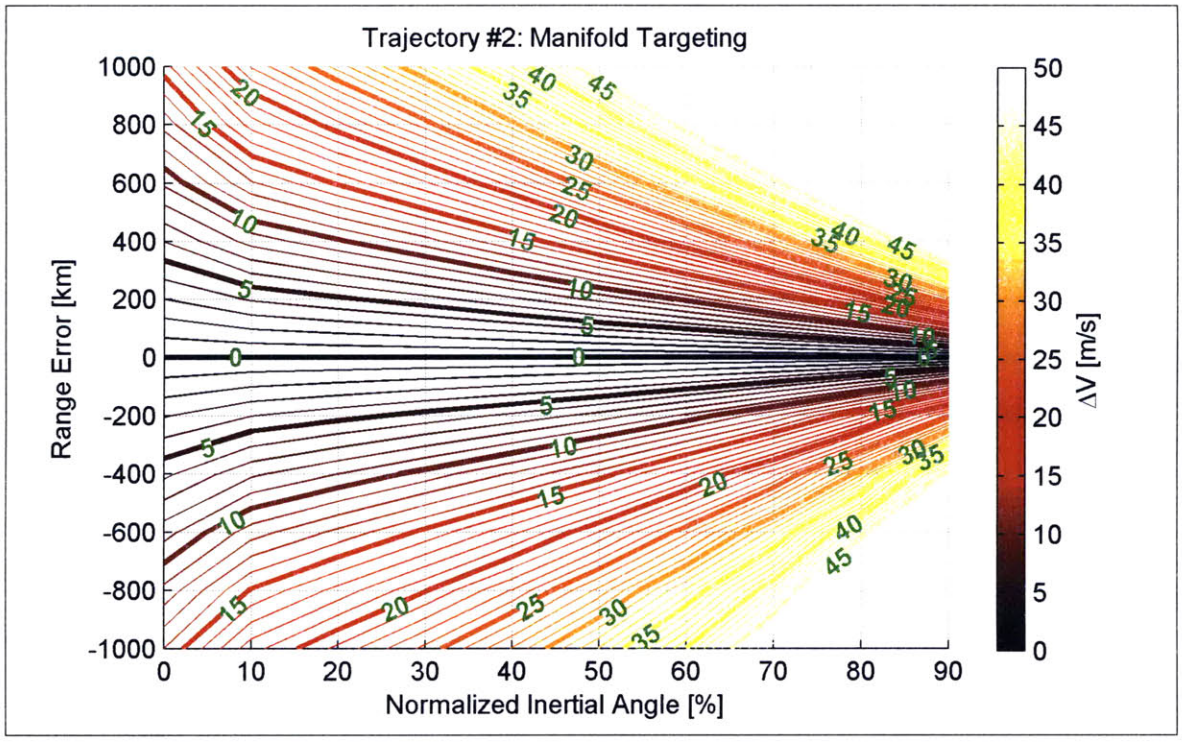

(b) Trajectory #2

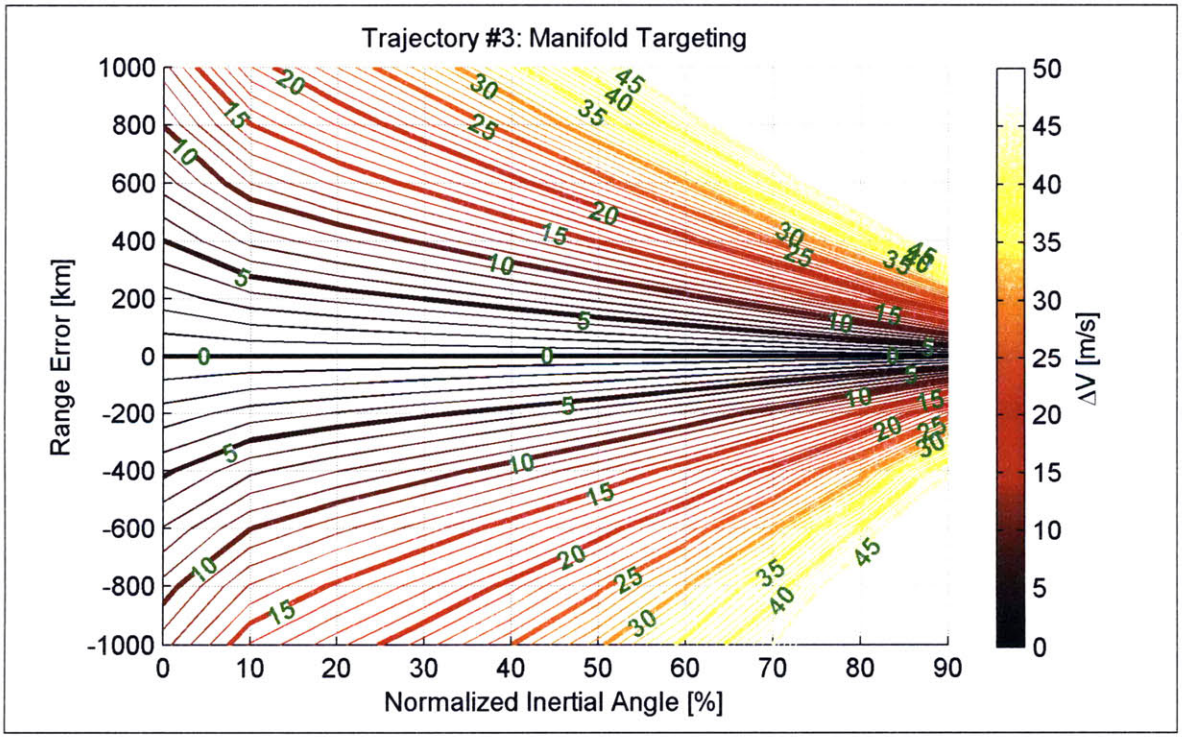

(c) Trajectory #3

Figure 3-9: Minimum impulsive ΔV to target a manifold (cont'd)

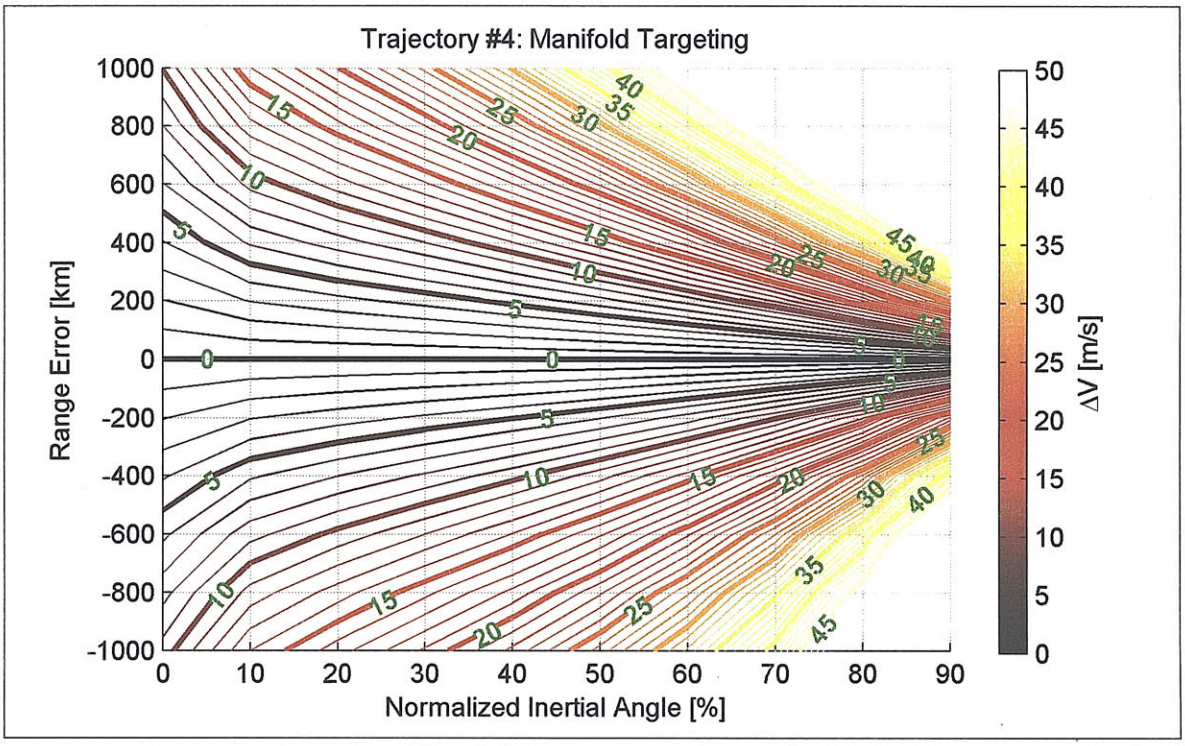

(d) Trajectory #4

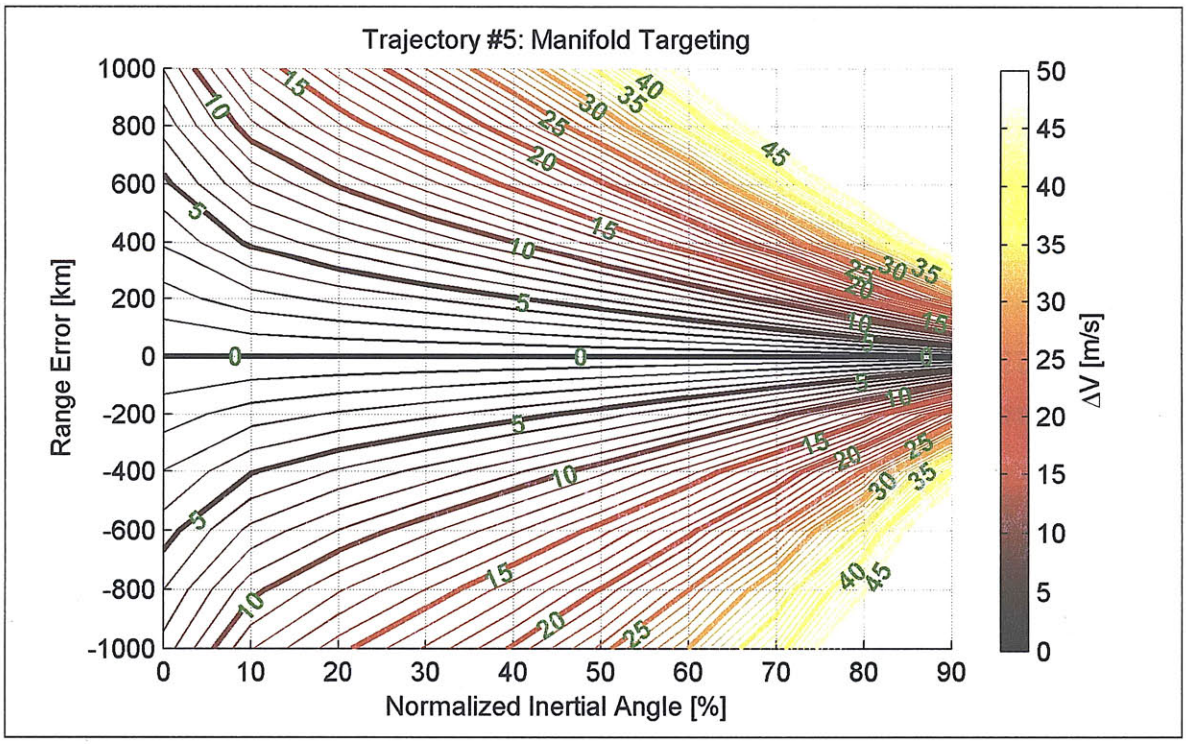

(e) Trajectory #5

Figure 3-9: Minimum impulsive ΔV to target a manifold (cont'd)

to be cheaper to target the manifold defined by Equation (3.7) and Table 3.6. This might be counterintuitive since it appears that Equation (3.7) will add more constraints than a strictly range targeting algorithm. However, this is not the case because Equation (3.7) adjusts the range targeted given the end conditions of the final phase. So if the skip phase ends with a steep flight path angle or a low speed, inclusively, the manifold equation adjusts the range targeted by increasing the skip phase range since the final phase range will be shortened with those initial conditions. The contrapositive is also true; that if the skip phase ends with shallow flight path or a high speed, inclusively, the final phase needs to be longer and thus the skip phase is shortened. This behavior makes physical sense and can be intuited from the sign of the gains in Table 3.6 and is illustrated in Figure 3-8. This also loosens the constraint on the final condition of the skip phase and thus reduces the ΔV required for a similar amount of range error when compared to only targeting a range location. Figure 3-10 shows the minimum impulsive ΔV differences ($\Delta V_{downrange}$ - $\Delta V_{manifold}$) between the two targeting methods explored here for the span of range errors and burn locations for both class 1 and class 5 trajectories.

Figure 3-10 shows that it is indeed cheaper to target a manifold but one also must remember that it is also more advantageous for the broader goal of the reentry guidance algorithm. The only disadvantage with targeting a manifold is the added complexity of determining the correct gains for Equation (3.7) since they are dependant on not only the trajectory as defined by the landing target but also on the vehicle itself.

As stated earlier in Section 3.4, the correction capability is highly dependant on the initial conditions. The result is that the high energy trajectories are favored based upon the fact the less ΔV is required to correct for a given amount of error. With the inclusion of targeting a manifold of acceptable entry conditions as opposed to a specific downrange location, this trend is amplified. One concern to be addressed is that the high energy trajectories are generally shorter in time. This is not only because they are faster but also because the total path length is shorter. The effect of this is inconsequential when considering an impulsive ΔV, but when the impulsive

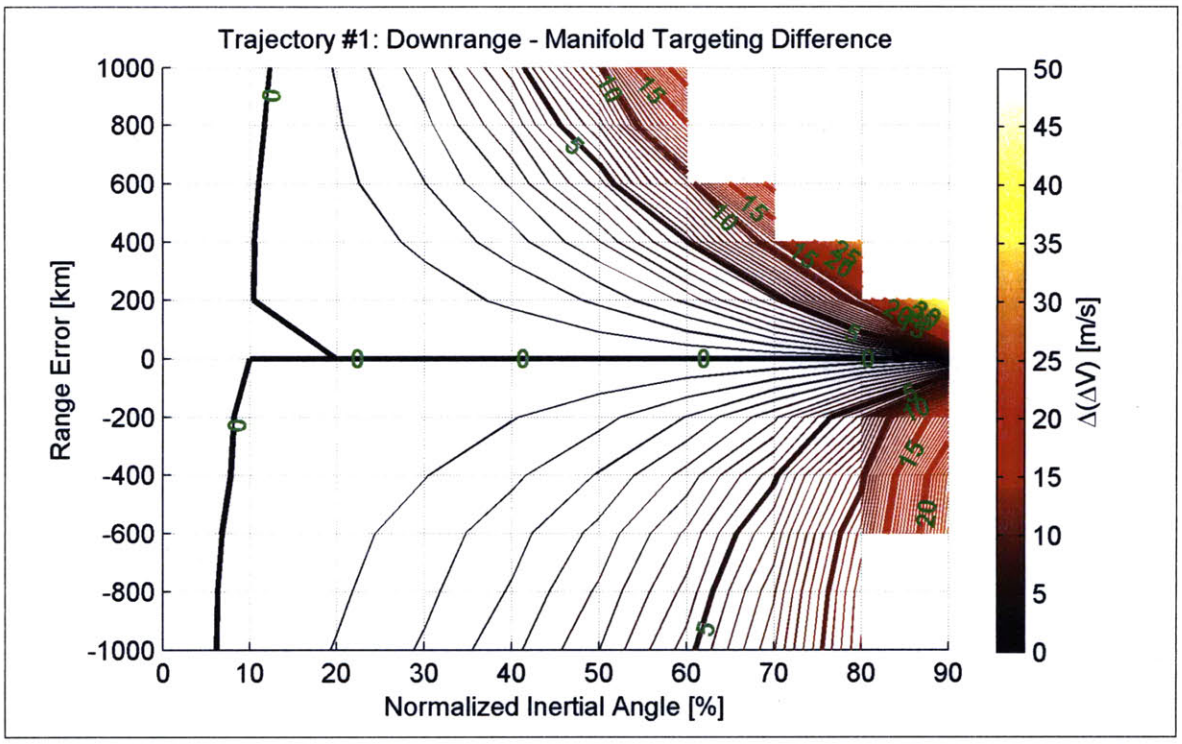

(a) Trajectory #1

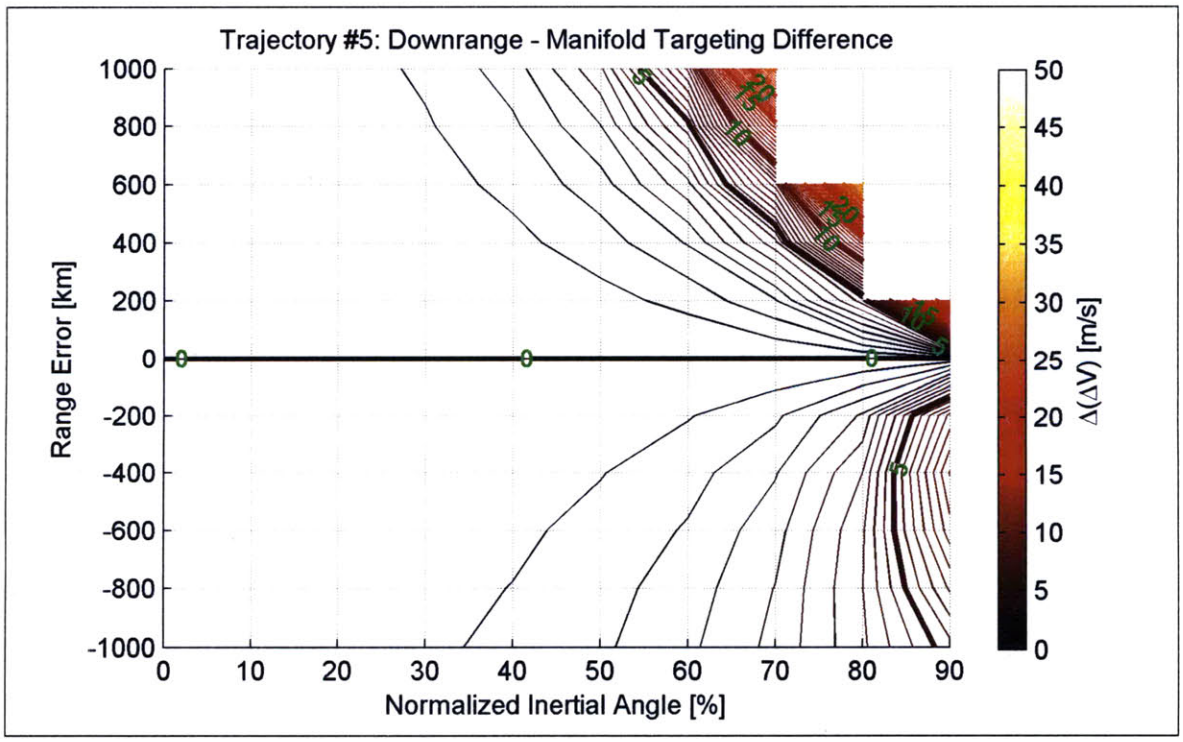

(b) Trajectory #5

Figure 3-10: Differences between targeting a downrange location versus a manifold

assumption is lifted, it can no longer be ignored as a finite burn time will require more ΔV than an impulsive one. This will result in a very important trade between the amount of time required to perform the non-impulsive burn and amount of ΔV required based upon the energy of the trajectory.

Chapter 4

Guidance Design

Up until now the analysis has been based upon the assumption that the thruster force has been impulsive, that is that it can supply a specified amount of force in an infinitesimal amount of time. It has already been stated that this is not physically realizable with any real propulsion system. Therefore, it is necessary to release the impulsive assumption and allow for a propulsive force to act for a finite amount of time. This adds another degree of freedom to the problem which does two things: increases the fidelity of the simulation and increases the complexity as well.

The fidelity of the simulation is increased because it is more accurately simulating what actually happens in reality. This is very beneficial and extremely necessary for any person that is looking to implement such a system in reality. The complexity is increased because the dynamics of the system change over time which couples into the amount of force required to perform the desired maneuvers. In addition to simply allowing a force to occur for a finite amount of time, the thrust direction is also free to point in any direction needed. While it is possible to design an algorithm around a fixed thrust direction, these solutions are not optimal and thus are excluded.

The algorithm presented in this chapter relies heavily upon the Powered Explicit Guidance (PEG) algorithm developed for the Space Shuttle and discussed in Reference [13].

4.1 Powered Explicit Guidance

The Powered Explicit Guidance (PEG) algorithm was developed in the 1970s and handles all powered flight phases of the Space Shuttle except for the first stage of launch. The first stage of the Shuttle ascent is flown open-loop and minimizes the structural loads in the high dynamic pressure region. PEG is based on the linear tangent steering law and provides guidance for a variety of different flight regimes with widely varying cutoff constraints and thrust-to-weight ratios.

PEG was derived from the solution to the minimum-time-to-orbit problem for a flat Earth with uniform gravity and no atmosphere. The problem is to find the thrust direction angle, β, to place a vehicle at a given altitude and desired velocity in the minimum amount of time. The final downrange position is left unconstrained and the optimal control law is

$$\tan\beta = c_1 + c_2 t. \tag{4.1}$$

The problem with outright using this control law is that the flat Earth, uniform gravity, and no atmosphere assumptions do not provide an accurate enough description of the dynamics of the problem. As a result, a guidance scheme is needed to automate the process of finding a near optimal solution that is valid without the assumptions and is computationally efficient.

Although a full explanation of all the details involved would be beneficial from the standpoint of completeness, the following subsections present only a brief introduction to the subject. A more thorough and extensive analysis can be studied in References [13] and [14].

4.1.1 Guidance Equations

Consider a vehicle of mass m with thrusters acting with a force F. The equation of motion of this simplified vehicle is

$$\ddot{\mathbf{r}} = \frac{F}{m}\hat{\boldsymbol{\lambda}}_t + \mathbf{a}_g. \tag{4.2}$$

The thrust direction vector, $\hat{\boldsymbol{\lambda}}_t$, is then restricted to a profile defined by

$$\hat{\boldsymbol{\lambda}}_t = \hat{\boldsymbol{\lambda}} + \dot{\boldsymbol{\lambda}}\,(t - t_{ref}) \tag{4.3}$$

where $\hat{\boldsymbol{\lambda}}$ is a vector pointing the direction of the velocity-to-be-gained, $\dot{\boldsymbol{\lambda}}$ is the time derivative of $\hat{\boldsymbol{\lambda}}_t$, and t_{ref} is a reference time. All three of the parameters in Equation (4.3) are constants. The resulting equation of motion becomes

$$\ddot{\mathbf{r}} - \mathbf{a}_g = \frac{F}{m}\left(\hat{\boldsymbol{\lambda}} + \dot{\boldsymbol{\lambda}}\,(t - t_{ref})\right). \tag{4.4}$$

The following four thrust scalar integrals and two gravity vector integrals are defined to integrate Equation (4.4).

$$\mathcal{L} = \int_0^{t_{go}} \frac{F}{m}\,\mathrm{d}t \tag{4.5}$$

$$\mathcal{J} = \int_0^{t_{go}} \frac{F}{m}\,t\,\mathrm{d}t \tag{4.6}$$

$$\mathcal{S} = \int_0^{t_{go}} \int_0^{t} \frac{F}{m}\,\mathrm{d}s\,\mathrm{d}t \tag{4.7}$$

$$\mathcal{Q} = \int_0^{t_{go}} \int_0^{t} \frac{F}{m}\,s\,\mathrm{d}s\,\mathrm{d}t \tag{4.8}$$

$$\mathbf{v}_g = \int_0^{t_{go}} \mathbf{a}_g\,\mathrm{d}t \tag{4.9}$$

$$\mathbf{r}_g = \int_0^{t_{go}} \int_0^{t} \mathbf{a}_g\,\mathrm{d}s\,\mathrm{d}t \tag{4.10}$$

where t_{go} is the time-to-go. Therefore, integrating Equation (4.4) over the length of the burn gives

$$\mathbf{v}_{go} = \mathbf{v}_d - \mathbf{v} - \mathbf{v}_g = \mathcal{L}\hat{\boldsymbol{\lambda}} + (\mathcal{J} - t_{ref}\mathcal{L})\,\dot{\boldsymbol{\lambda}} \tag{4.11}$$

where $\mathbf{v}_{go}$ is the velocity-to-be-gained and $\mathbf{v}_d$ is the desired final velocity. Integrating once more gives

$$\mathbf{r}_{go} = \mathbf{r}_d - \mathbf{r} - \mathbf{v}t_{go} - \mathbf{r}_g = \mathcal{S}\hat{\boldsymbol{\lambda}} + (\mathcal{Q} - t_{ref}\mathcal{S})\,\dot{\boldsymbol{\lambda}} \tag{4.12}$$

where $\mathbf{r}_{go}$ is the position-to-be-gained and $\mathbf{r}_d$ is the desired final position.

The result of Equations (4.11) and (4.12) is a system of five equations and seven unknowns. There are only five equations because the final downrange position is left unconstrained. The seven unknowns are the components of $\hat{\boldsymbol{\lambda}}$ and $\dot{\boldsymbol{\lambda}}$ and remaining burn time, t_{go}. The problem is clearly underdetermined at this stage. The unitization of Equation (4.3) adds one more equation. The final constraint needed to fully determine the system is one that enforces the orthogonality between $\hat{\boldsymbol{\lambda}}$ and $\dot{\boldsymbol{\lambda}}$, namely

$$\hat{\boldsymbol{\lambda}} \cdot \dot{\boldsymbol{\lambda}} = 0. \tag{4.13}$$

The constraint in Equation (4.13) can be used with Equations (4.11) and (4.12) to solve for the unknowns. First, $\hat{\boldsymbol{\lambda}}$ can be found by taking the dot product of $\hat{\boldsymbol{\lambda}}$ with Equation (4.11) to get

$$\hat{\boldsymbol{\lambda}} \cdot \mathbf{v}_{go} = \mathcal{L}. \tag{4.14}$$

Given that $\hat{\boldsymbol{\lambda}}$ is a unit vector, $\mathcal{L} = v_{go}$, and

$$\hat{\boldsymbol{\lambda}} = \frac{\mathbf{v}_{go}}{v_{go}}. \tag{4.15}$$

A similar manipulation can be used to find $\dot{\boldsymbol{\lambda}}$. The dot product of $\hat{\boldsymbol{\lambda}}$ with Equation (4.12) gives

$$\hat{\boldsymbol{\lambda}} \cdot \mathbf{r}_{go} = \mathcal{S}. \tag{4.16}$$

However, $\mathbf{r}_d$ has an unconstrained downrange component and thus the unknown component of $\mathbf{r}_{go}$ must be found using Equation (4.16). Once $\mathbf{r}_{go}$ is fully specified, Equation (4.12) is used to solve for $\dot{\boldsymbol{\lambda}}$ as

$$\dot{\boldsymbol{\lambda}} = \frac{\mathbf{r}_{go} - \mathcal{S}\hat{\boldsymbol{\lambda}}}{\mathcal{Q} - t_{ref}\mathcal{L}} \tag{4.17}$$

where t_{ref} is defined such that Equation (4.11) is consistent with Equation (4.15). This yields

$$t_{ref} = \frac{\mathcal{J}}{\mathcal{L}}. \tag{4.18}$$

In order for the guidance solution to converge to a near optimal solution a predictor-corrector algorithm is used. This requires one to make assumptions about the nature of Earth's gravity field and the vehicle's thrust profile. These assumptions allow one to calculate the thrust integrals given in Equations (4.5) through (4.8). Furthermore, by approximating the gravity integrals in Equations (4.9) and (4.10), one is able to predict what the position and velocity are at the end of the burn to first order as in Reference [14]. Reference [13] also gives two additional thrust integrals that allow one to approximate the velocity and position change due to thrust to second order. The predicted position and velocity are then used to update the desired position and velocity. If the predicted and desired position and velocity have converged to a reasonable tolerance, then the guidance loop is complete and the vehicle performs the calculated maneuver.

A salient feature that remains unresolved for the problem of targeting during a skip trajectory is that the final downrange position is unconstrained. One method of constraining the final position is through the use of a linear terminal velocity constraint and is the topic of the next subsection.

4.1.2 Linear Terminal Velocity Constraint

The addition of a downrange position constraint is required for many of the Shuttle's on-orbit operations and the deorbit maneuver. These maneuvers pose a different problem than that of an ascent maneuver because a coast phase is needed. This means that the position contraints are no longer imposed at cutoff and an additional calculation is required to find the velocity necessary to achieve a desired cutoff condition. This velocity can be found using the equations in Chapter 11 of Reference [12]. The calculation finds the velocity that enables the spacecraft to reach a desired location with a specified linear relationship between the radial and horizontal components of

velocity as

$$v_r = C_1 + C_2 v_h \tag{4.19}$$

where C_1 and C_2 are given.

Now that the terminal position of the thrusting phase is unconstrained, Equation (4.17) is no longer valid. It is also not acceptable to set this parameter to zero because a constant attitude is not fuel optimal for maneuvers that may traverse a large inertial angle. Reference [13] cites empirical studies in determining that a turning rate of 35 percent of the mean motion of a circular satellite is nearly optimal, so that the magnitude of $\dot{\boldsymbol{\lambda}}$ becomes

$$\left|\dot{\boldsymbol{\lambda}}\right| = 0.35\sqrt{\frac{\mu_\oplus}{r^3}}. \tag{4.20}$$

The algorithm for finding the cutoff velocity is mentioned in Reference [13]. It is a method for finding the solution to a second order system of equations where one equation is the linear relation between the radial and horizontal terminal velocities shown in Equation (4.19) and the other is a quadratic constraint created by the geometry of the trajectory

$$\left(\frac{r_f}{r_0} - \cos\theta\right) v_{h_f}^2 - \left(v_{r_f}\sin\theta\right) v_{h_f} - \frac{\mu_\oplus}{r_f}\left(1 - \cos\theta\right) = 0 \tag{4.21}$$

where subscripts $()_f$ and $()_0$ mean final and initial position or velocity, respectively. These constraints essentially describe the intersection of a line with the hyperbolic locus of velocity vectors as described in Chapter 6 of Reference [12]. Given Equations (4.19) and (4.21) it is clear that the system will have one, two, or no roots. Thus great care needs to be made in ensuring the correct solution is chosen if it exists.

What remains to be seen is the method of selecting of the coefficients of Equation (4.19), C_1 and C_2. These coefficients are chosen such that the relationship between the horizontal and radial components of velocity is achieved at the target point. For orbital maneuvers, they are set to zero and the target location is set to the desired apoapsis or periapsis. For a deorbit burn it is necessary to set C_1 and C_2

such that the desired speed and flight path angle is achieved at the initiation of entry.

The linear terminal velocity constraint (LTVC) method for targeting desired position is not the final solution to the guidance problem presented here. The issue is that it assumes no aerodynamic effects. While this is valid for the regime of flight it is used in (above 120 km), it was shown in Section 3.2 that for the problem presented here the aerodynamics effects cannot be ignored. The perturbing accelerations caused by atmospheric drag make the coefficients C_1 and C_2 in Equation (4.19) highly non-linear functions of time. Therefore, a different method must be devised that accounts for the atmospheric effects during the ballistic phase.

4.2 Augmented Algorithm

The algorithm in the previous section clearly works very well for its intended purpose and even under a wide variety of conditions as mentioned earlier. The problem with implementing PEG as is, for this problem is that it assumes a conic trajectory when doing any prediction or correction. This assumption is not-valid for this problem because of the highly non-linear effects of aerodynamic forces due to operating in the regime of a skip trajectory. A more accurate prediction is required during the skip phase because of the high sensitivity of the trajectory to the atmosphere. This sensitivity arises because the vehicle is traveling along the edge of the atmosphere and traveling faster than the satellite velocity for its altitude. If the trajectory is too high or too fast, the spacecraft will go into an orbit similar to an aerocapture or aerobraking maneuver. If the trajectory is too low or too slow, the spacecraft will reenter too far away from the desired location to reach the landing target. While PEG provides a very elegant and numerically very efficient solution to the on-orbit guidance problem, numerically integrating the equations of motion was chosen to circumvent this problem for implementation during a skip maneuver. This solution is neither elegant nor efficient, but it does guarantee that the resultant prediction and correction are accurate to within the tolerances specified.

The numerical integration for the predictor enters into the algorithm where Equa-

tions (4.5) to (4.10) would be approximated using a linear or quadratic fit to the acceleration profile and a conic state propagator. This means that instead of approximating the velocity and position changes due to the thrust and gravity, the actual dynamics of the spacecraft are simulated for a time, t_{go}. This has the advantage of being more accurate in general for a given a trajectory but unfortunately takes more computational effort since the state is calculated at each time step instead of only at the point of interest at t_{go}. This also has the advantage of being free to model other non-linear effects such as aerodynamic forces. A ΔV direction needs to be assumed for the thrusting phase of the skip trajectory. An angle of 45 degrees relative to the local horizontal is assumed for this based on the nearly flat nature of the results shown in Appendix A and given that the bottom of the curves in Figure 3-3 are also approximately flat for small changes in direction. The actual direction is chosen using the following relation

$$\left(\hat{\boldsymbol{\lambda}}_t\right)_L = \frac{-1}{\sqrt{2}} \operatorname{sign}\left(x_e\right) \begin{bmatrix} 1 \\ 1 \\ 0 \end{bmatrix}_L \tag{4.22}$$

where x_e is the downrange error. This points the thrust up and forward when the range error is negative (i.e. an undershoot) and down and back when the range error is positive (i.e. an overshoot). This direction is specified with respect to the local vertical/local horizontal frame.

In addition to the predictor, numerical integration is also used for the corrector portion of the algorithm. The corrector for this problem would have used LTVC routine discussed earlier. However, for the reasons mentioned above, the assumptions are no longer valid given the operational regime of the skip trajectory. Therefore, instead of using a conic state propagator to solve for the cutoff velocity for a given target, a numerical integration scheme is used. The algorithm finds the cutoff velocity by using a shooting method to determine the velocity that enables a coasting trajectory to hit the target to within 1 km of the desired target point. This velocity is then compared to the predicted velocity. If the difference between the two is small enough compared to the magnitude of the velocity remaining, then guidance has converged and the

thrust direction parameters are returned for execution. The convergence bound can be set relatively loose if the algorithm is called frequently. For the purpose of this problem, the tolerance was set to 0.1 with a period of 10 seconds. The tolerance is the ratio of the magnitude of the prediction error to the magnitude of the velocity-to-go. The period determines the iterative rate at which PEG is called throughout the trajectory to ensure the target is met despite disturbances to the system.

Now that a guidance algorithm has been defined it is possible to perform maneuvers over a finite amount of time as opposed to the results of Chapter 3 where an impulsive assumption is made.

Chapter 5

Results

The guidance algorithm described in Chapter 4 will enable the exploration of the problem with more fidelity because the impulsive assumption is no longer made. It is expected that removing the impulsive assumption will increase the ΔV requirement because it has already been shown that the ΔV increases for a given amount of error the closer the spacecraft gets to the target. An analysis similar to that performed on the nominal trajectories in Chapter 3 is presented to establish a comparison between an impulsive solution and the guided solution developed in Chapter 4. Then a robustness analysis is performed to measure the guidance solution's performance with an uncertain vehicle, environment, and initial conditions.

5.1 Trajectory Sensitivity

The analysis in Chapter 3 was preformed to get a lower bound on the amount of ΔV needed to perform a reasonable amount of correction to an off-nominal trajectory. In addition, a good grasp of the underlying physics of the problem can be gained from the data presented there. To review, the observed trends were:

- an overshooting trajectory requires more ΔV,
- an impulsive maneuver performed later in the trajectory requires more ΔV, and
- lower energy trajectories require more ΔV.

In order to measure the effects of removing the impulsive assumption and using PEG to calculate the required ΔV a similar analysis to that in Chapter 3 is to be performed. The initial range error is still between $-1000\ km$ and $1000\ km$ with steps of $200\ km$. In the previous analysis, the burn was applied at various points along the trajectory. With an impulsive assumption, it was possible to focus the maneuver at one instant in time but this is no longer possible using PEG. Therefore, PEG is turned on at the various normalized inertial angle locations that were analyzed before. PEG is then called with a period of 10 seconds with a convergence tolerance of 0.1 and allowed to run until either it will reach the target or it determines that it is not possible to reach the target given ΔV and time constraints.

The results of using PEG to target a manifold during the skip phase are shown in Figure 5-1. The results shown in Figure 5-1 show the same trends that were present with the impulsive results. Most notably, the penalty for performing the maneuver later in the trajectory is drastically increased. This is the reason for the contours

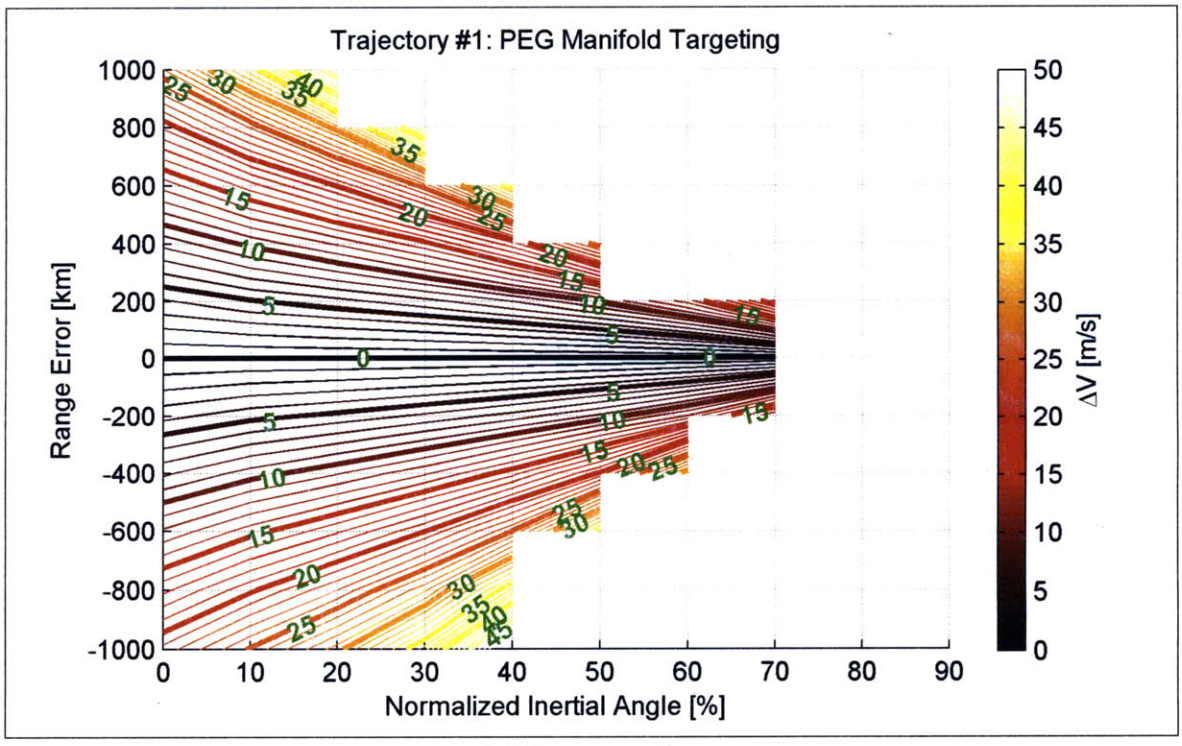

(a) Trajectory #1

Figure 5-1: PEG solution ΔV to target a manifold

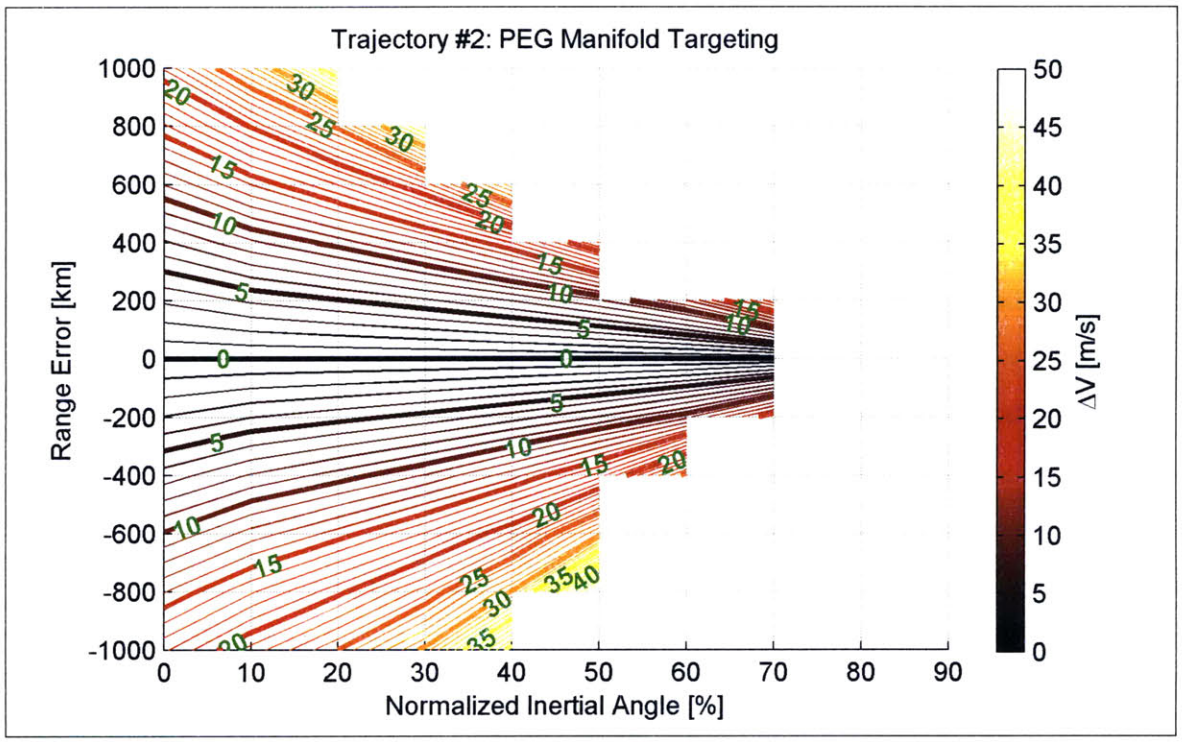

(b) Trajectory #2

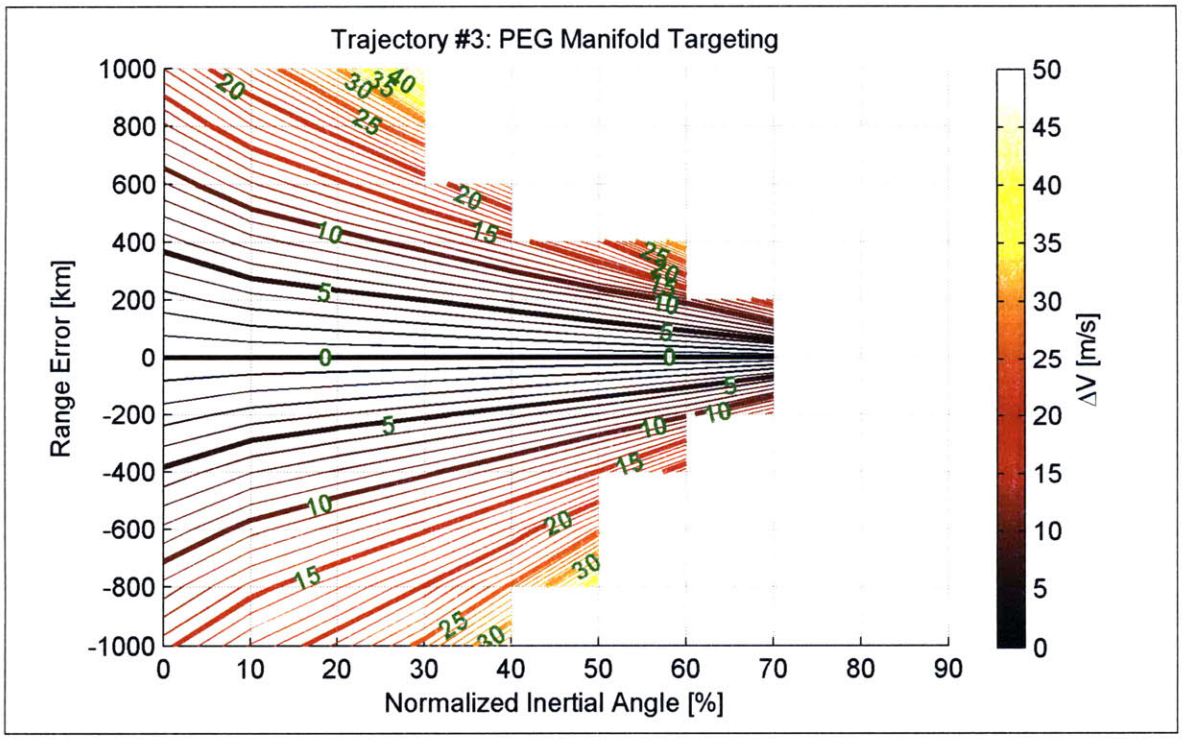

(c) Trajectory #3

Figure 5-1: PEG solution ΔV to target a manifold (cont'd)

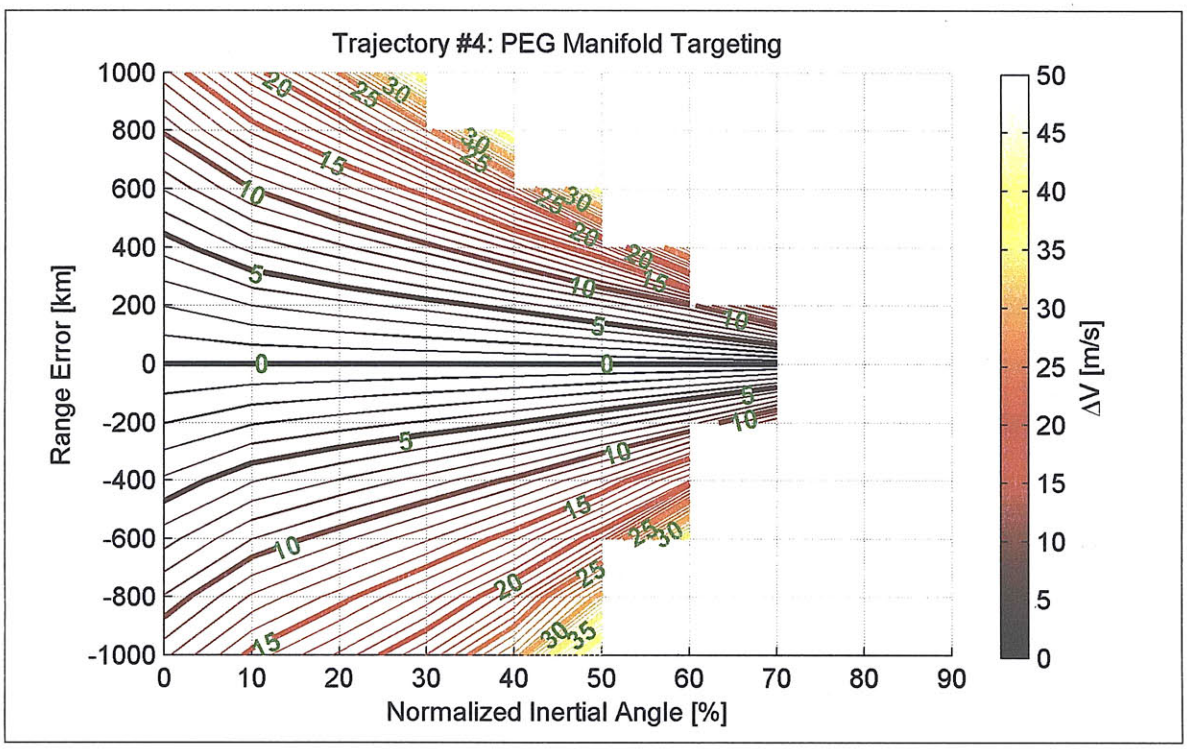

(d) Trajectory #4

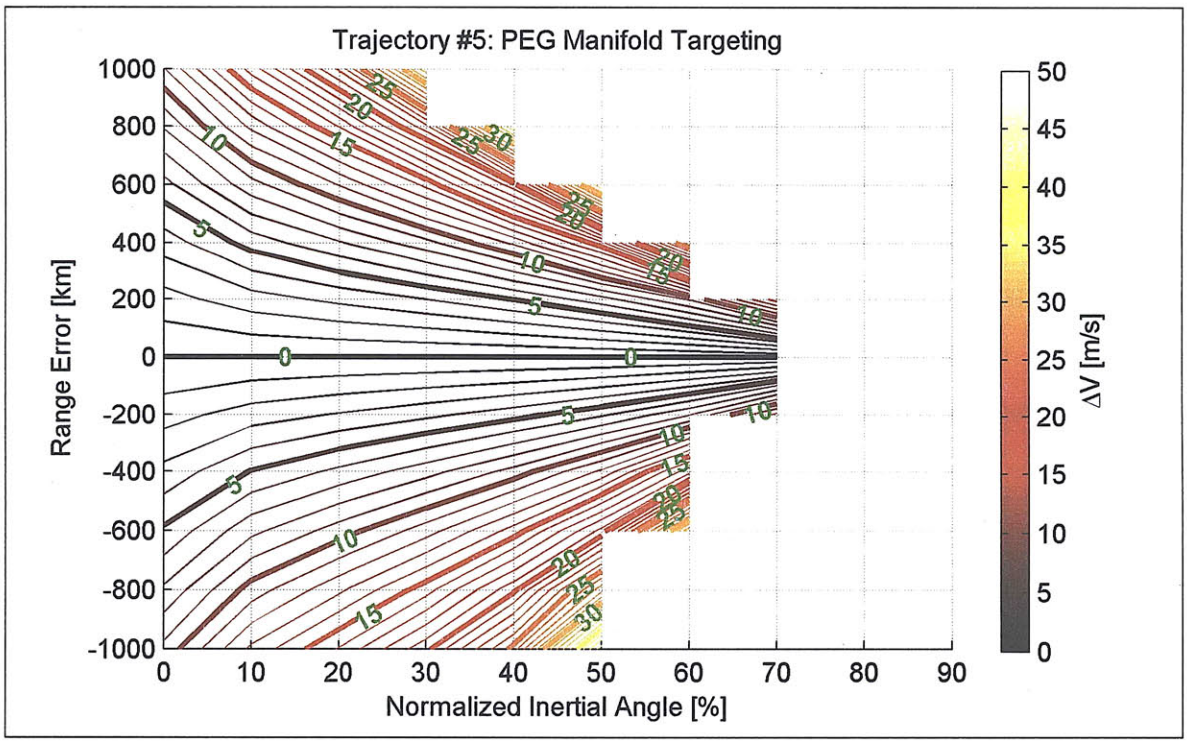

(e) Trajectory #5

Figure 5-1: PEG solution ΔV to target a manifold (cont'd)

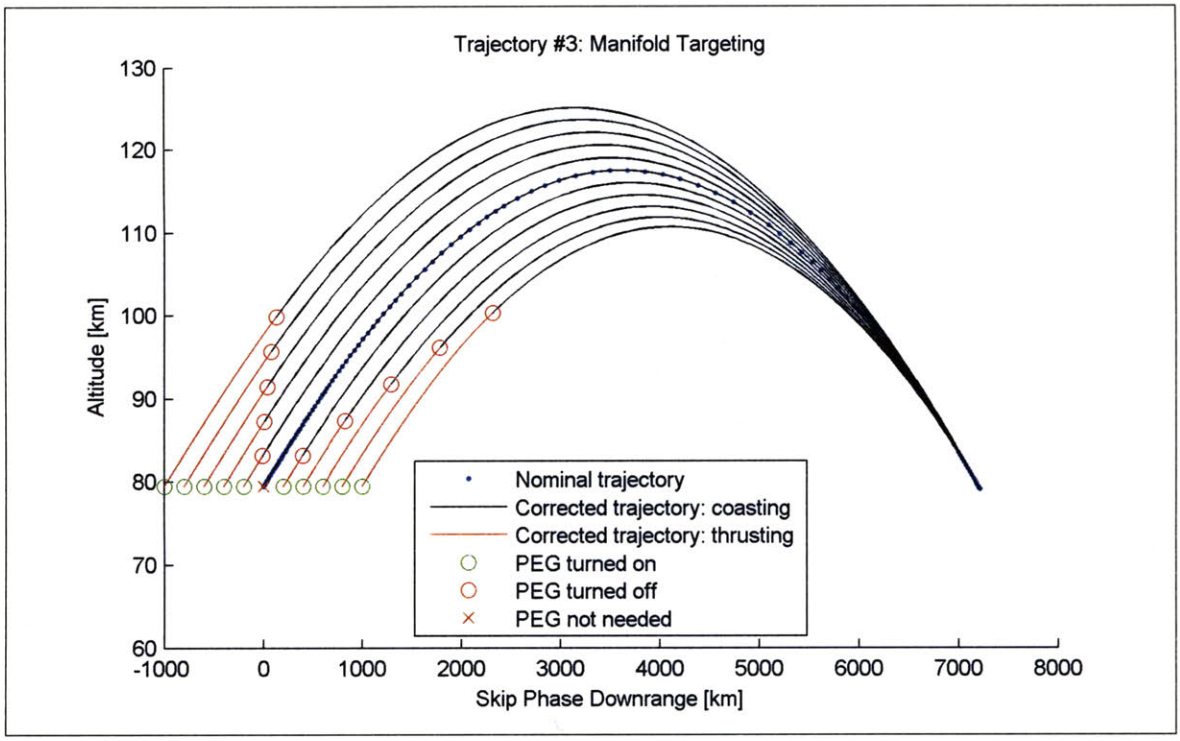

Figure 5-2: Example of corrected trajectories using PEG to target a manifold

ending at the 70 percent location, whereas before they extended all the way to 90 percent. The reasoning for this is intuitive. As the spacecraft moves along the skip trajectory with a given amount of error, the amount of ΔV required to correct for the error increases. However, when the impulsive assumption is removed, the amount of time required to perform a ΔV maneuver is proportional to its magnitude. Therefore, as the ΔV increases, the amount of time increases until the amount of time necessary to complete the correction is greater than the time remaining in the skip. The results in Figure 5-1, when compared to Figure 3-9, show the effect of removing the impulsive assumption. It is clear that the impulsive solution lower bounds the PEG solution. The ΔV are most similar when the magnitude is small because PEG more closely resembles an impulsive solution when the burn time approaches the simulation step size. The corrected trajectories along the first column of data in Figure 5-1c (varying range error while starting PEG at the initiation of the skip phase for trajectory 3) are shown in Figure 5-2. Figure 5-2 demonstrates quite a bit of information about using a non-impulsive guidance algorithm such as PEG to hit a target. It shows the range

error asymmetry demonstrated in Figure 3-5. It clearly demonstrates the correlation between burn time and total ΔV required to complete a correction. It also shows that corrections for small errors are nearly impulsive because of their relatively short burn times.

One concern that will exist for a full six degree-of-freedom model is the necessity to reorient to an attitude required to perform the burn in the direction required. Although the time to reorient to that attitude is finite, it was assumed to be negligible in Chapter 3 and that assumption exists here as well. Beyond that, one must also consider that ability of the thrusters to perform such a maneuver given the aerodynamic moments on the capsule. To simulate this effect, the altitude of 100 km is chosen define the boundary within the skip phase where it is possible to perform such a reorientation maneuver. This altitude was chosen merely to simulate the effect of having such a constraint. The actual altitude where this occurs depends on many things, some of which are beyond the scope of this thesis. The magnitudes of the aerodynamic moments depend on the atmospheric density, velocity, and the shape of the spacecraft. The propulsive torque depends on the size of the thrusters and their placement on the spacecraft. The moments and torques are ignored in this thesis given that the simulation itself assumes three degrees-of-freedom.

Figure 5-3 shows that result of constraining the altitude on the PEG solution presented earlier. The data displayed in Figure 5-3 show that an altitude constraint effectively establishes a constant ΔV requirement if PEG is started prior to reaching the constraint altitude. The ΔV increases because the start time of the burn is delayed further into the skip trajectory until the altitude constraint is met. Beyond this point, the same trends present in the previous figures remain. The effect of using an altitude constraint on the trajectories in Figure 5-2 is shown in Figure 5-4. Figure 5-4 shows the trajectories used to create the data in the first column of Figure 5-3c. One can clearly see the effect of the altitude constraint on the total burn time and the resultant ΔV. The trajectory with a 1000 km overshoot (far right trajectory) is now using a little more than half of the arc above 100 km to perform the correction. Whereas before, it was able to make the correction with approximately only a third of the arc

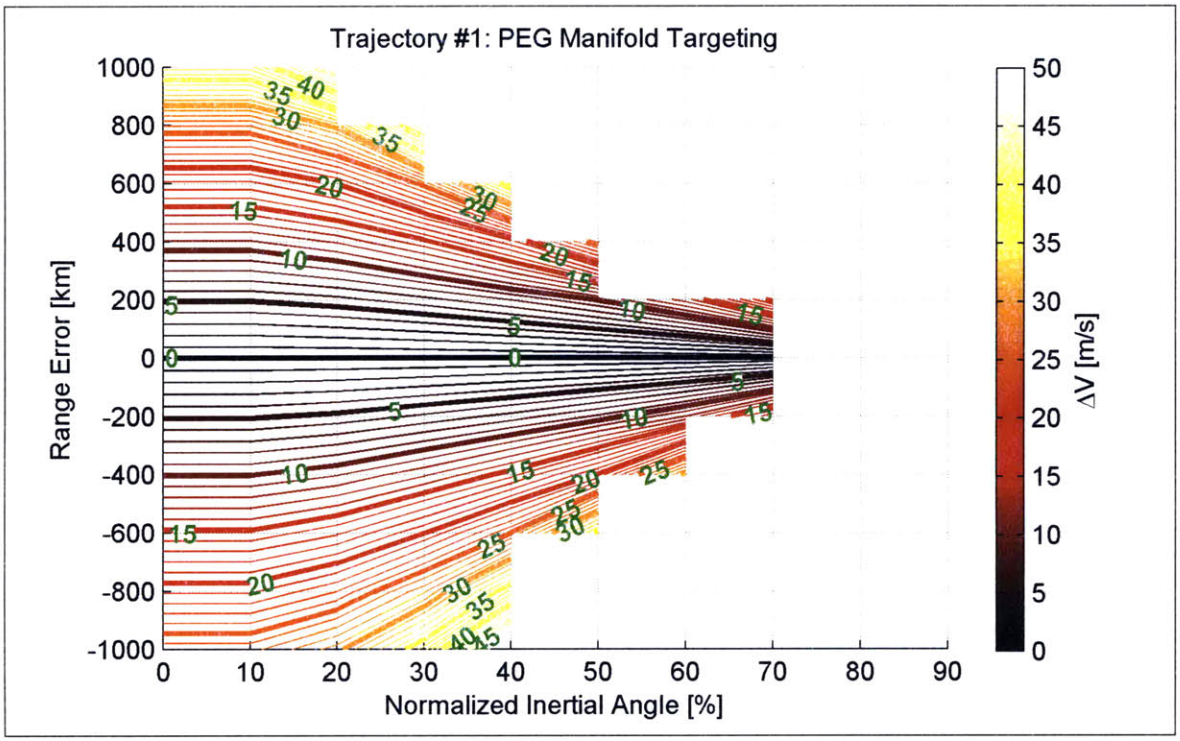

(a) Trajectory #1

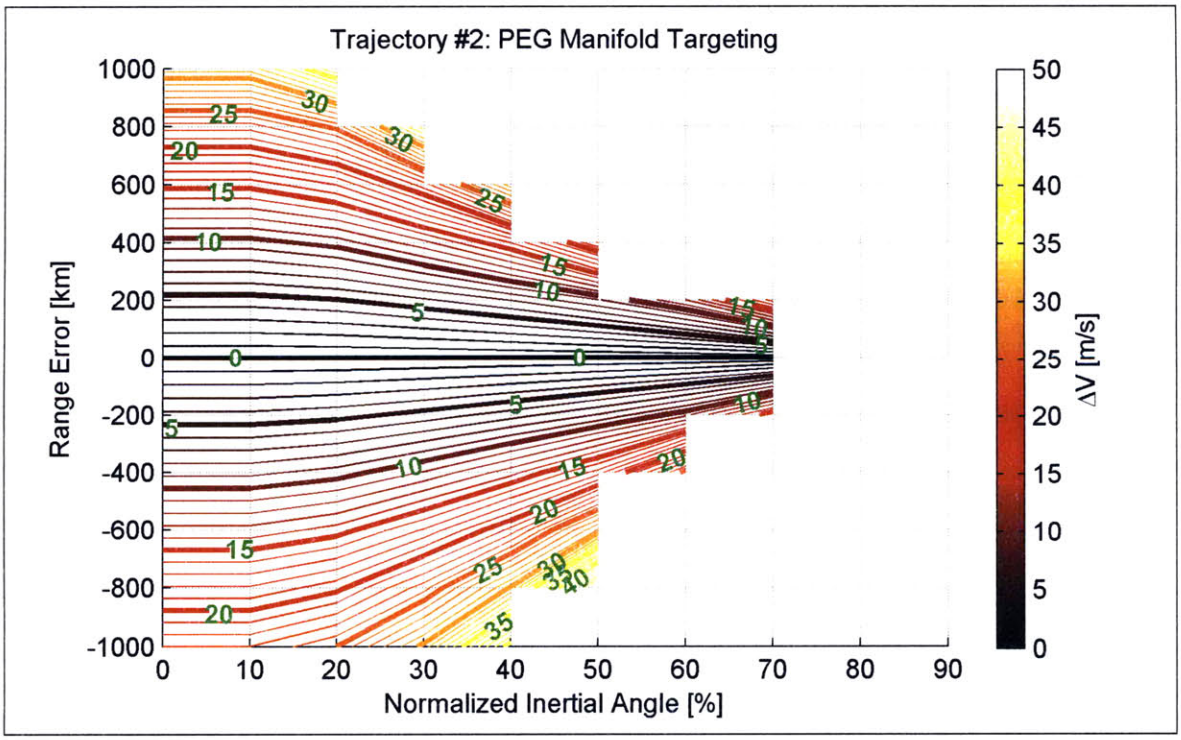

(b) Trajectory #2

Figure 5-3: PEG solution ΔV with a constrained altitude

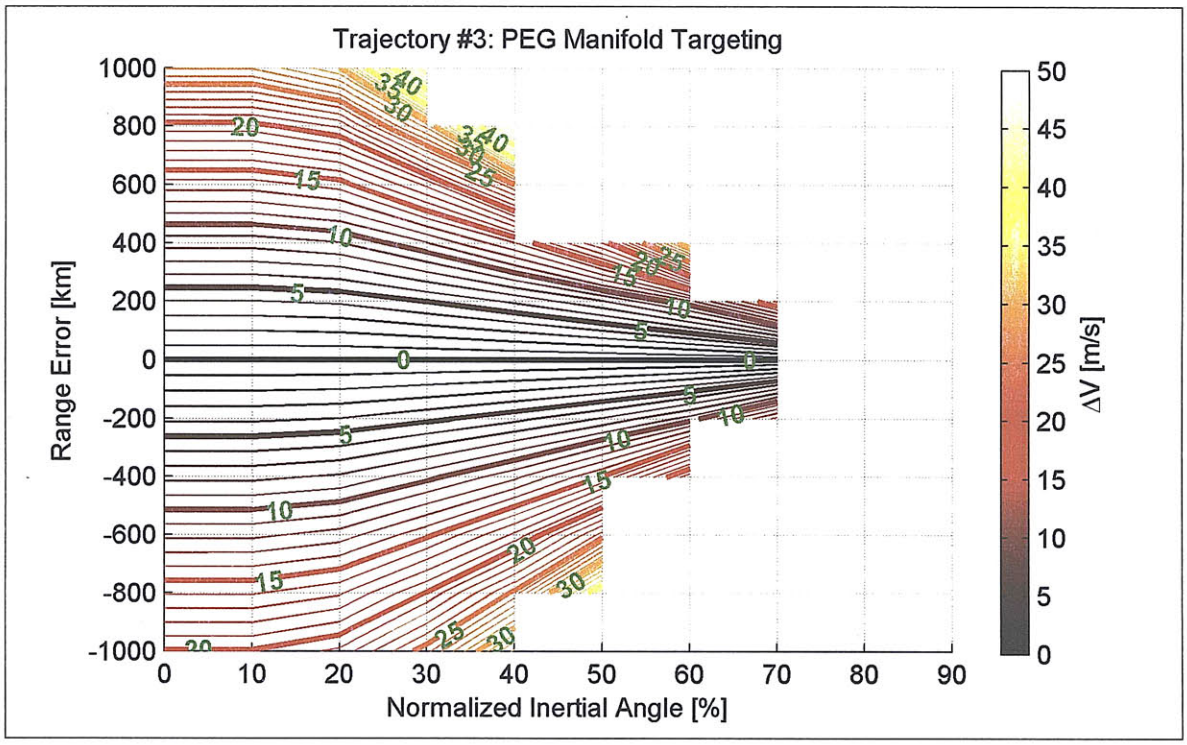

(c) Trajectory #3

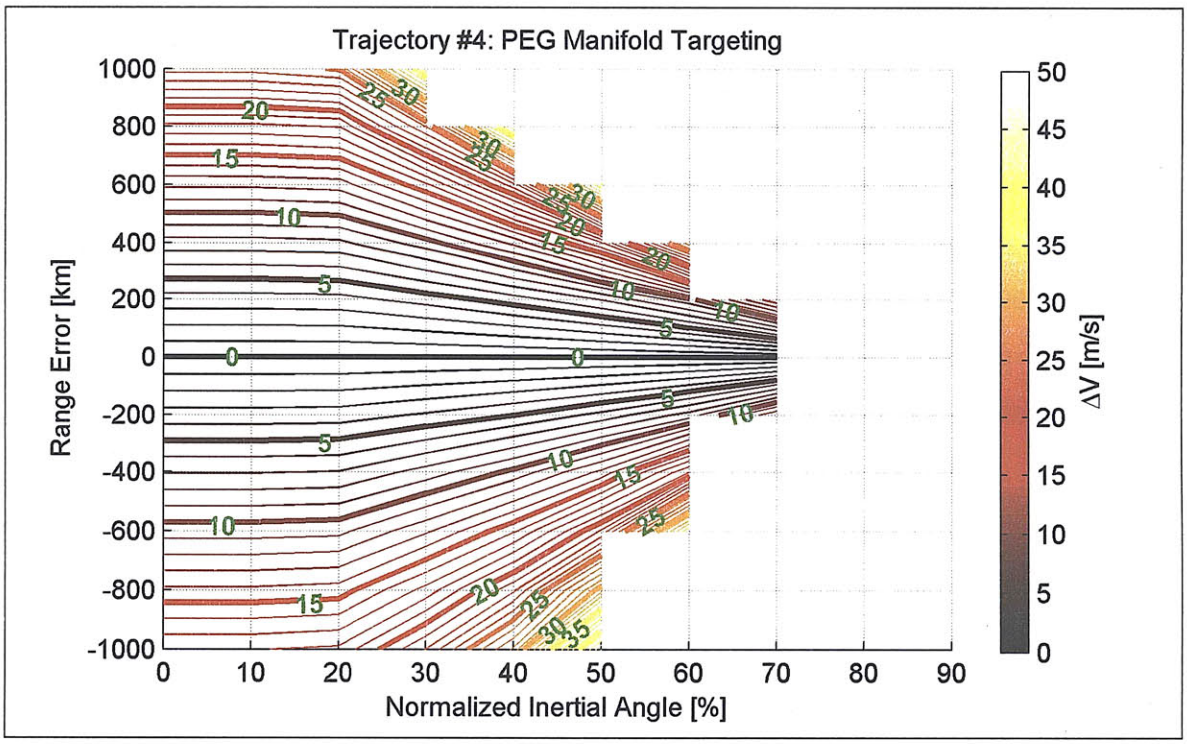

(d) Trajectory #4

Figure 5-3: PEG solution ΔV with a constrained altitude (cont'd)

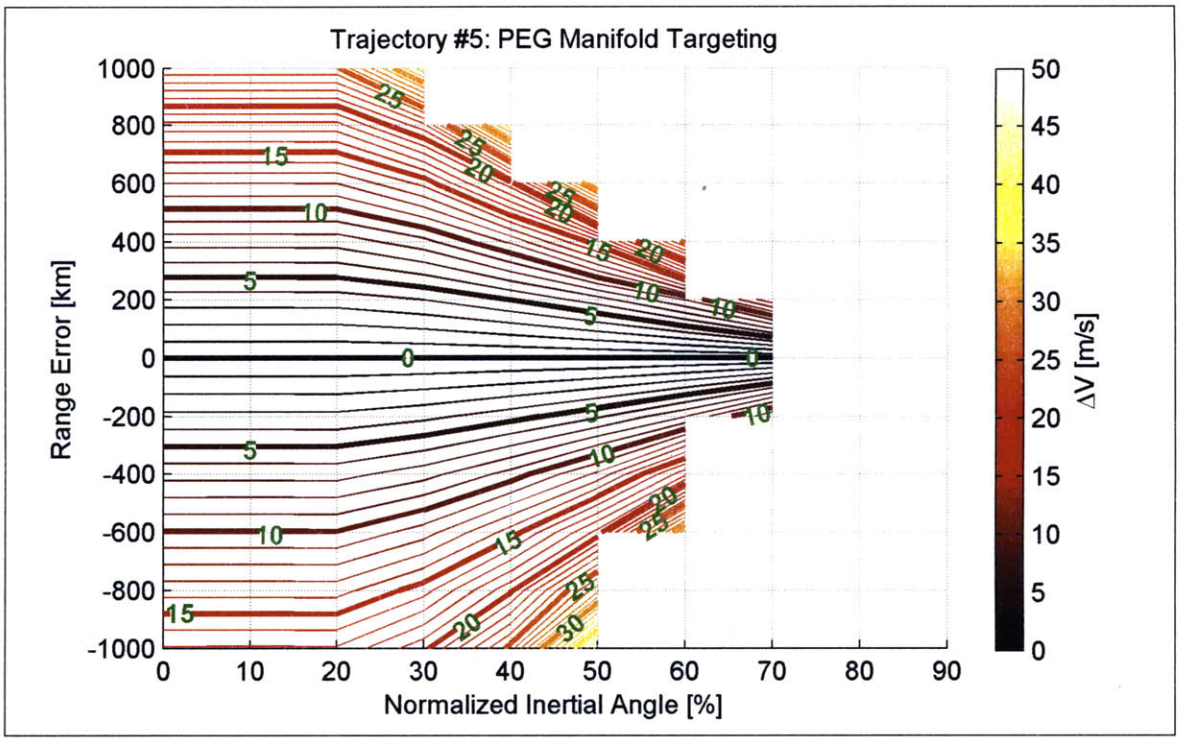

(e) Trajectory #5

Figure 5-3: PEG solution ΔV with a constrained altitude (cont'd)

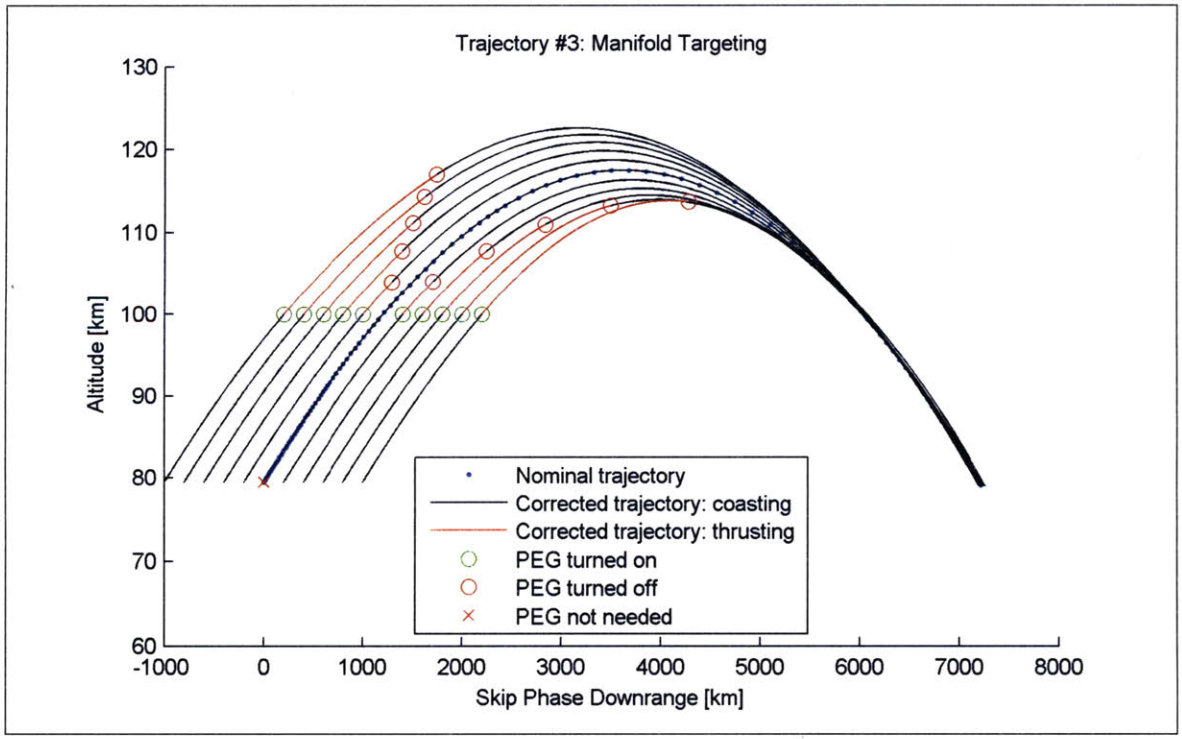

Figure 5-4: Example of corrected trajectories using PEG and a constrained altitude

available to it. It also demonstrates the increased asymmetry between trajectories that correct for similar magnitudes of range error.

Now that the ability to perform a guided maneuver during the skip phase has been demonstrated and the effect of including a constraint based upon the spacecraft's ability to maneuver to the correct orientation to perform the ΔV burn has been tested, it is necessary to test the design's robustness to uncertainties in the environment, vehicle, and initial state.

5.2 Environment, Vehicle, and State Uncertainties

To test the robustness of the guidance solution developed in Chapter 4 and introduced in Section 5.1, a Monte Carlo analysis must be performed. A Monte Carlo analysis allows one to gauge the performance of a system to uncertainties in any number of parameters of said system. It is performed by establishing a statistical variation in the parameters that are believed to be system drivers. There are three types of uncertainties that are considered for this problem. The uncertainties considered are environmental, vehicular, and the initial state. Perfect navigation is assumed and thus the guidance system is assumed to have perfect knowledge of the vehicle states throughout the skip maneuver. All the uncertainties for this analysis are assumed to be Gaussian distributed.

The environmental uncertainty is modeled as a density multiplier with unit mean and a standard deviation of 10 percent [10]. This means that the nominal atmosphere is represented as a multiplier of one. Therefore, a multiplier greater than one simulates a thicker atmosphere and a multiplier less than one simulates a thinner atmosphere.

The vehicular uncertainty is modeled by varying the mass, the aerodynamic coefficients, and the thrust level. These are all modeled as multipliers with a unit mean as well. The mass is modeled with a standard deviation of approximately 1.67 percent ($3\sigma = 5\% = 480\ kg$) [10]. The aerodynamic coefficients, C_{L} and C_{D}, are modeled with a standard deviation of approximately 3.33 percent ($3\sigma = 10\%$) [15]. The thrust uncertainty is modeled with a standard deviation of one percent. Reference [15]

states a 3σ value of 5 percent for relatively small thrusters and a robotic mission. It is assumed that given the size of the thrusters and the fact that the CEV must be crew-rated, that a 3σ variation of 3 percent is a reasonable amount of uncertainty.

Establishing the initial state uncertainty is not as straightforward as the environmental and vehicular uncertainties. This is primarily due to the fact that the initial conditions are dependant on a non-linear relationship between the altitude and the velocity. The relationship is defined such that the initial altitude and Earth-relative velocity are such that the aerodynamic acceleration is equal in magnitude to 0.186 g's. The altitude is found for a corresponding velocity by minimizing the error-squared term

$$a_{e_a}^2 = (9.81 \times 0.186 - a_a)^2 = \left(9.81 \times 0.186 - \sqrt{a_{\mathrm{D}}^2 + a_{\mathrm{L}}^2}\right)^2 \tag{5.1}$$

where a_{D} and a_{L} are defined by Equations (2.25) and (2.26), respectively. Another problem is that the trajectories are defined by the nominal initial conditions given in Table 3.1. These initial conditions are derived from the exit conditions of the guidance algorithm discussed in Reference [10]. Therefore, the dispersions of speed, flight path angle, and downrange location are inseparably linked to what the guidance algorithm can produce at the initialization of the skip phase. A set of six degree-of-freedom Monte Carlo runs of the algorithm defined by Reference [10] were used for the purpose of establishing a relationship between speed and flight path angle and between speed and downrange location. These runs gave a standard deviation of the speed to be 75 $^m/_s$. The flight path angle and downrange location were found to have nearly linear relationships with the speed as defined by

$$\gamma_0 = -0.4688\tilde{v} + 1.305 \tag{5.2}$$

$$\Delta x_0 = 141776\tilde{v} \tag{5.3}$$

where γ_0 is given in degrees and $\tilde{v}$ is a scaled velocity given by $\tilde{v} = \frac{1}{89}(v_0 - 7800)$. The initial downrange location is given as a delta because it is assumed to have a zero mean. These relationships are necessary because a skip trajectory is faster

Table 5.1: Monte Carlo dispersions

Parameter	μ	3σ
ρ	1	30%
m	1	5%
C_{L}	1	10%
C_{D}	1	10%
F_t	1	3%
v_0	see Table 3.1	225 $^m/_s$
h_0	see Table 3.1	see Eqn. (5.1)
γ_0	see Table 3.1	see Eqn. (5.2)
x_0	0	see Eqn. (5.3)

than the circular satellite speed $\left(\sqrt{\frac{\mu_\oplus}{h_0+r_\oplus}} \approx 7450^m/_s\right)$ for the initial altitudes given in Table 3.1. This fact truly shows the sensitivity of the skip trajectory and the challenge of designing a guidance algorithm for it. With these relationships it is now possible to define a variation in initial speed and get the corresponding range error and flight path angle associated with it. One final note to make is that Equations (5.2) and (5.3) must be centered for each trajectory being analyzed by finding the bias term to zero the relationship for zero speed perturbation.

Table 5.1 summarizes the mean and 3σ values used for the following Monte Carlo analysis.

5.3 Monte Carlo Results

For each trajectory a set of 250 trials were run while randomly varying the perturbation variables as prescribed by the dispersions defined in Table 5.1. The randomly generated Gaussian distributions are kept constant between each trajectory to provide a more direct comparison between each set of results. Each trial is setup by initializing the vehicle parameters and initial conditions as before. The dispersions are generated and applied to their respective variables. The simulation assumes perfect navigation, therefore the guidance algorithm receives a perfect state measurement. This is done to measure the algorithm's ability to reject disturbances since that is

the main focus of this thesis. Once the perturbed conditions have been initialized, an initial call to PEG is made. If this call to PEG returns a reasonable value, then the trajectory is simulated while maintaining the 100 km altitude constraint discussed in Section 5.1. Otherwise, if this results in a failure of convergence because there is not enough thrust to complete the maneuver before reentry, then the trajectory is flagged but not simulated.

The trials are categorized into successes and failures based upon whether they reach the target or not. The successes are further subdivided into two groups. The first subgroup of successes are those that succeed while staying within the prescribed ΔV limit (40 $^m/_s$) in the ESAS report [2]. The other subgroup of successes are trials that reached the goal but did not use less than the ΔV limit. The failures are subdivided into two groups as well. The first subgroup of failures are trials that failed because of the altitude constraint. These failures can either be due to the amount of time above 100 km is insufficient to achieve enough ΔV or because they simply do not even reach the minimum altitude necessary to perform the maneuver. The other subgroup of failures are those that would fail regardless of the altitude constraint. These trials create trajectories with so much error that there is not enough time during the entire skip phase to create enough ΔV to correct for the large amount of error. It should be noted that just because a failure does not reach the manifold target at the end of the skip phase does not mean that the spacecraft can not land safely at the desired landing target. The manifold is accurate to first order and thus some failures might still be able to reach the landing target despite missing the manifold target. However, this effect relies on the final phase guidance which is beyond the scope of this thesis and therefore cannot be measured.

A summary of the results for each trajectory are shown in Figure 5-5. Figure 5-5 shows the percentage of each set of trials that fall into the categories defined above. Note that the margin of error on these percentages is a couple percent based on the number of trails for each trajectory. One can infer quite a bit of information from Figure 5-5. It shows that trajectory three has the most number of trials that succeed under the ΔV limit. It also shows that trajectories two and three are nearly the same

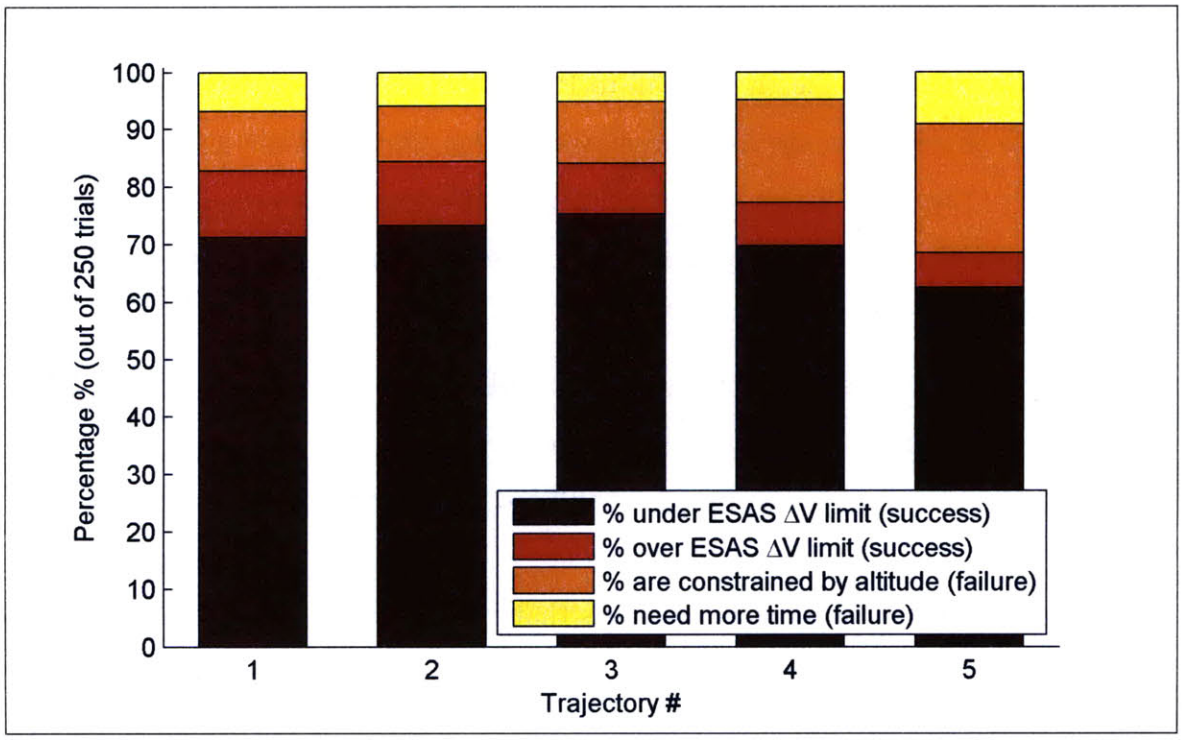

Figure 5-5: Summary of the Monte Carlo results

if the ΔV limit could be increased to include the other successes. The ability to turn some of the failures into successes will be discussed later. Figure 3-1 is duplicated here as Figure 5-6 for a reminder of the nature and shape of each trajectory.

Even though a great deal of information can be gained from Figure 5-5, a more in-depth analysis of the results will create a better understanding for the reason why successes reached the target and failures did not. To start, the histograms of ΔV required are shown in Figure 5-7. Figure 5-7 shows how the distribution changes depending on the nominal trajectory chosen. The shape is pretty consistent between all the trajectories and is what one would expect; the majority require a relatively small amount of ΔV whereas a long tail extends to ever greater values of ΔV. The legends in Figure 5-7 show the data that has been presented in Figure 5-5. It is compiled in Table 5.2 for clarity. The sum of each column in Table 5.2 should be 100 percent. In the columns where it doesn't add to 100 percent, this is due to rounding error. One can see some important trends in Figure 5-7 and Table 5.2. The first is that the number of successes under the 40 $^{m}/_{s}$ ΔV limit peaks with trajectory three. The

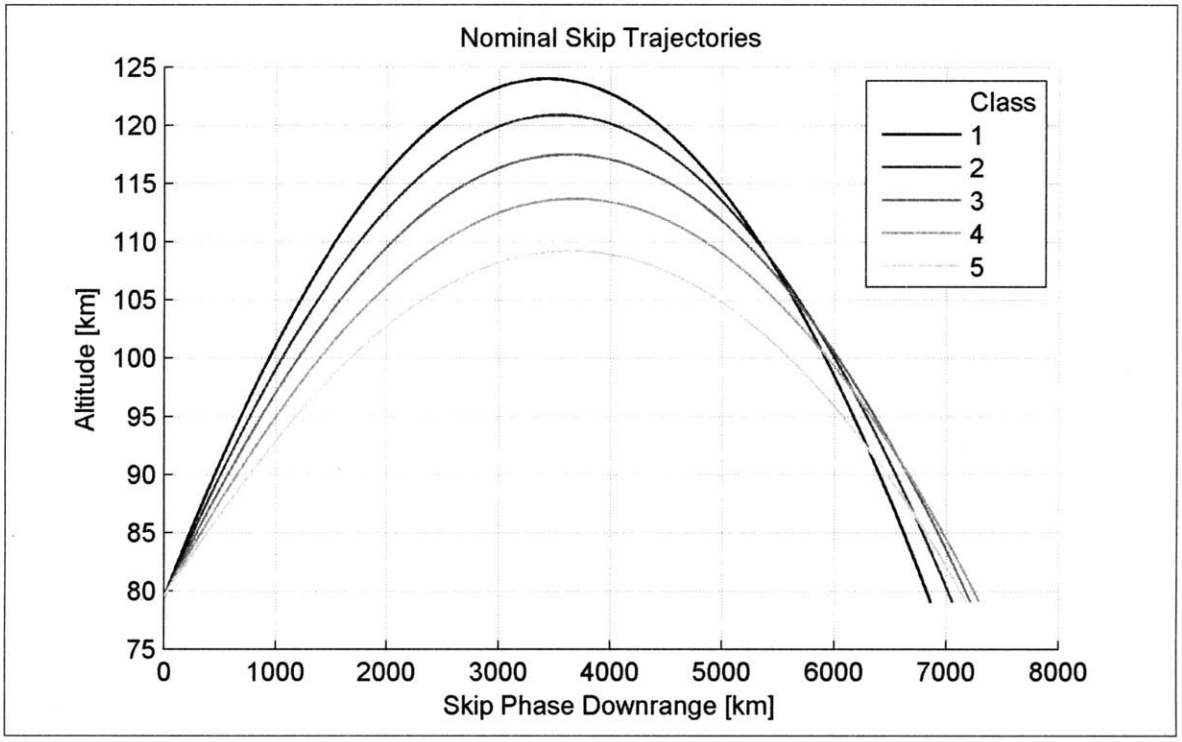

Figure 5-6: Nominal skip trajectories

Table 5.2: Monte Carlo success rate summary

Success or Failure	Remark	Trajectory #				
		1	2	3	4	5
Success	under ΔV limit	71%	73%	75%	70%	62%
	over ΔV limit	12%	11%	9%	8%	6%
Failure	altitude constraint	10%	10%	11%	18%	22%
	not enough time	7%	6%	5%	5%	9%

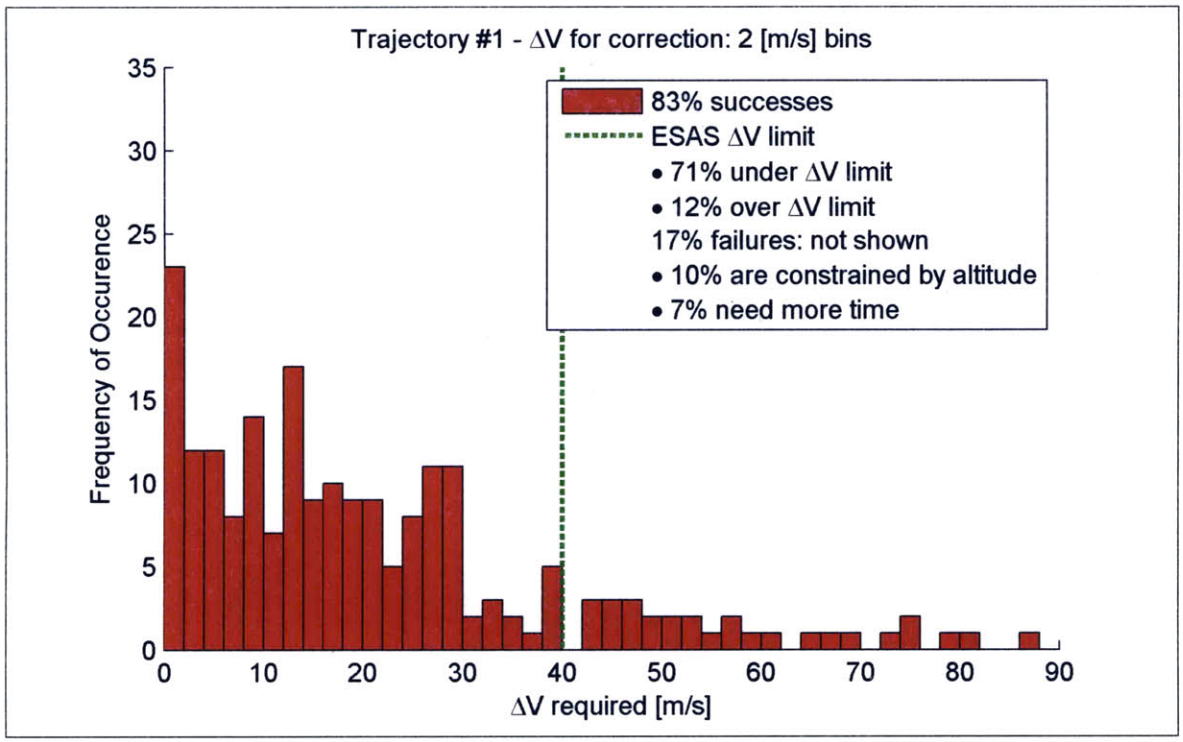

(a) Trajectory #1

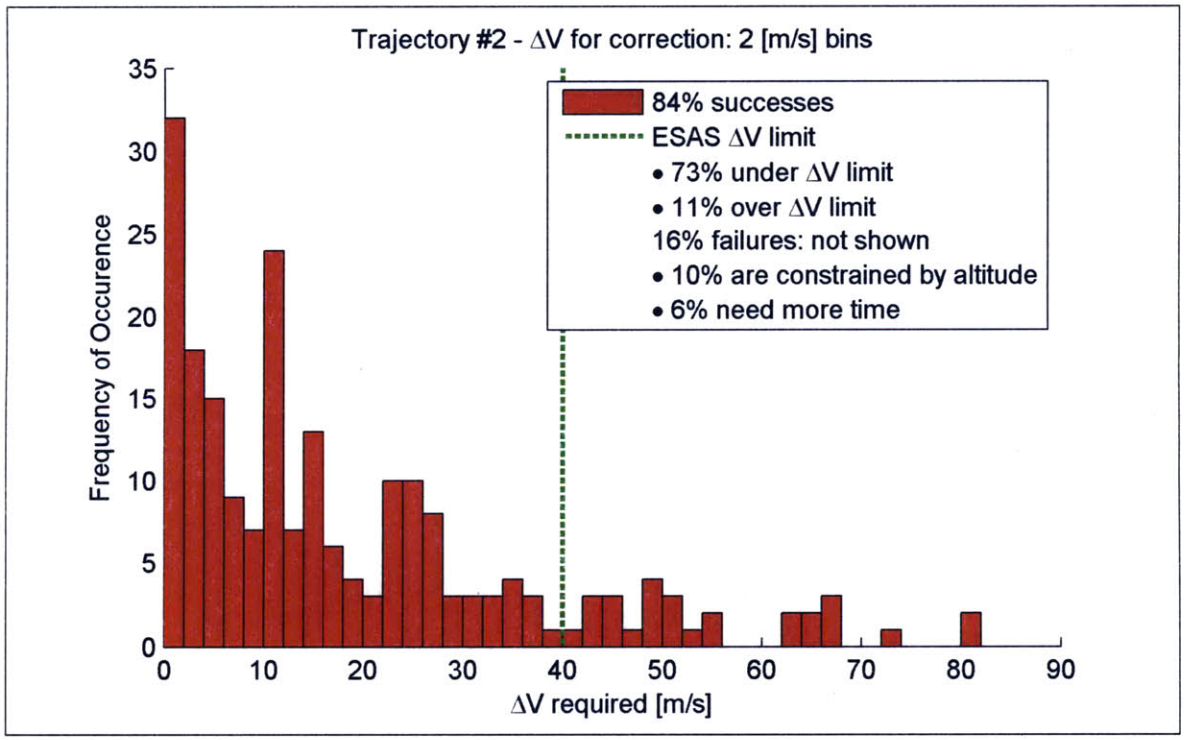

(b) Trajectory #2

Figure 5-7: Histogram of ΔV required

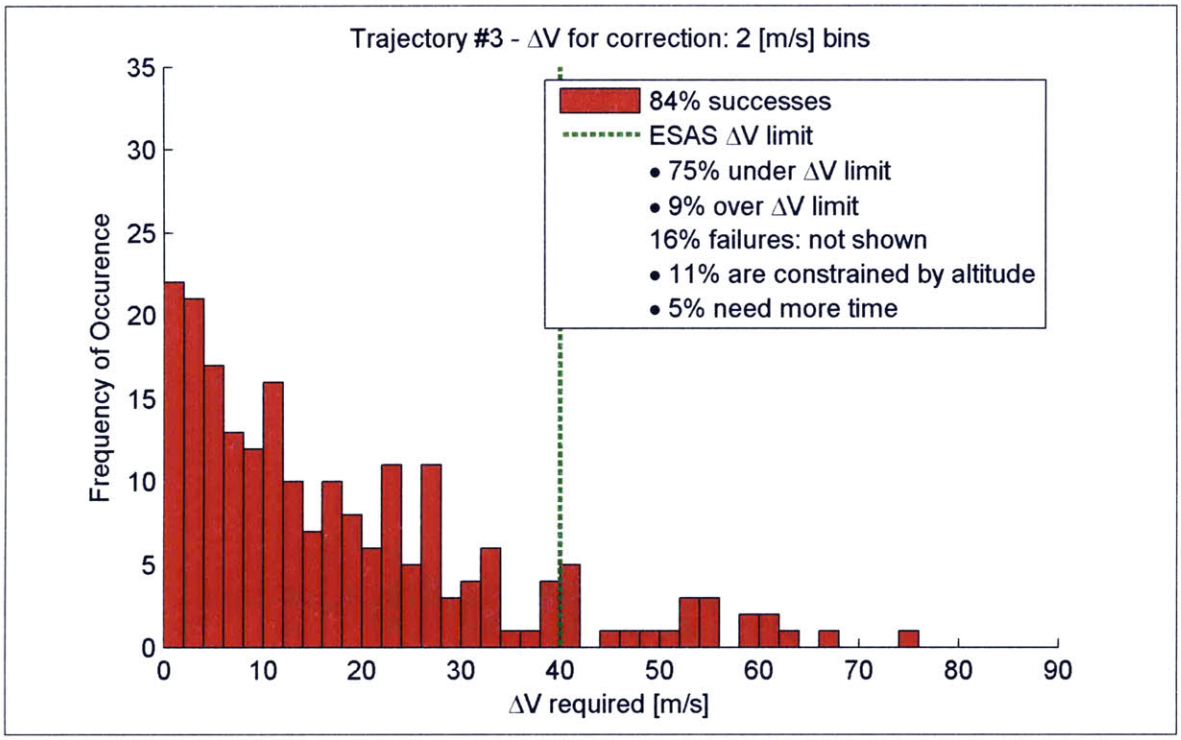

(c) Trajectory #3

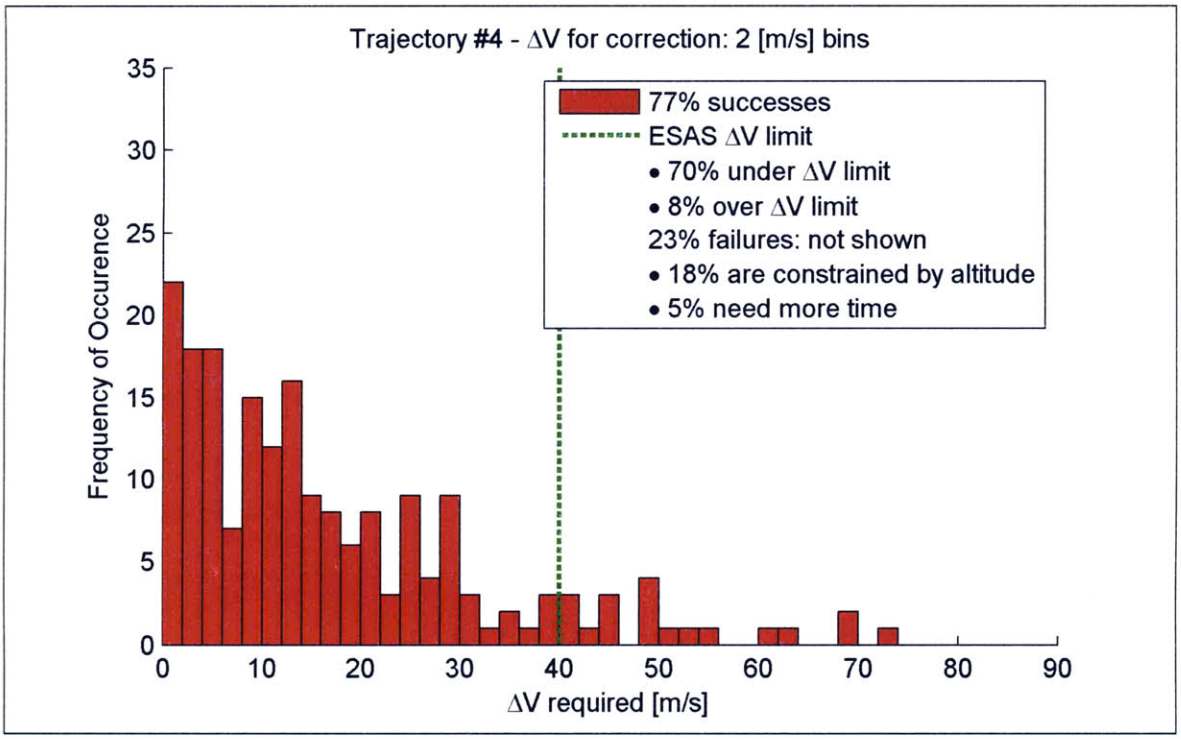

(d) Trajectory #4

Figure 5-7: Histogram of ΔV required (cont'd)

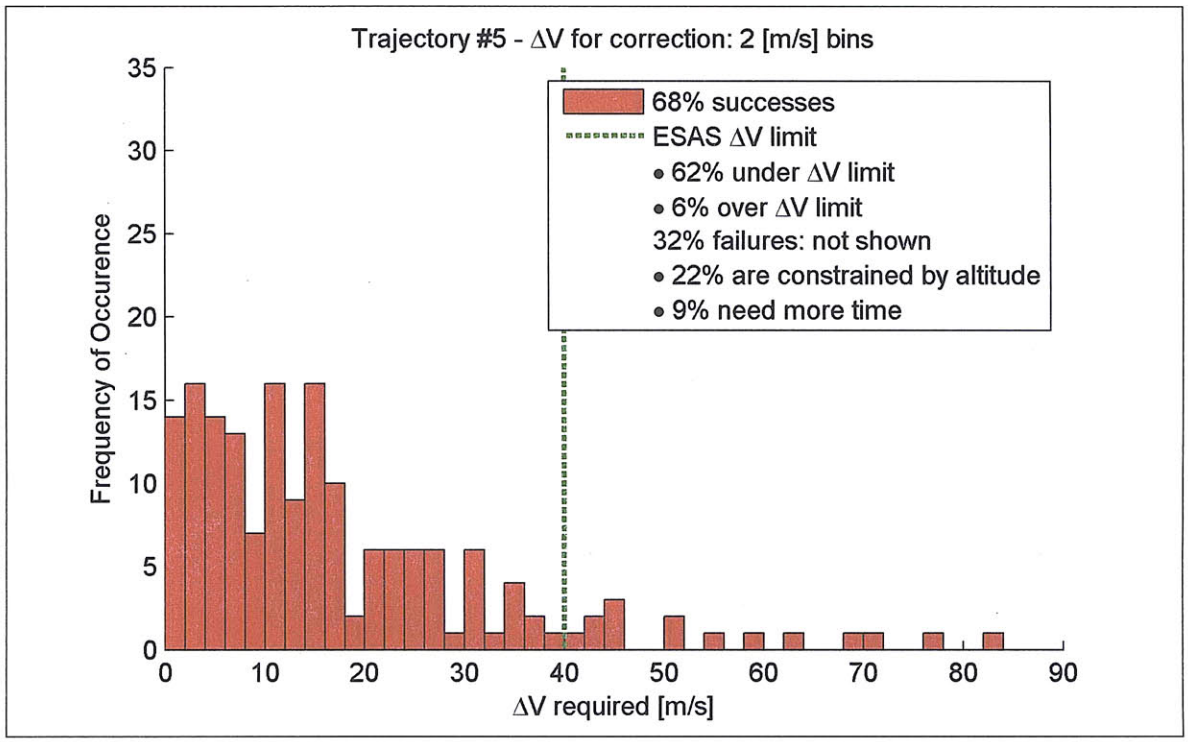

(e) Trajectory #5

Figure 5-7: Histogram of ΔV required (cont'd)

number of successes that occur while not meeting the ΔV limit steadily decline from trajectory one to five. Interestingly, the number of failures that are due the altitude constraint increases from trajectory one to five. This shows that maneuverability constraint dominates over the correction capability of the higher energy trajectories shown in Figure 3-7. These trends are most likely linked due to that fact that it has been shown that higher energy trajectories (larger trajectory number) remain lower in the atmosphere throughout the skip phase. So that if the altitude constraint was loosened (lower it to say 90 km) more of the high energy trajectories would become successes.

The reason for the outliers can be explored by examining the ΔV required as a function of the amount each dispersed variable was perturbed. The standard deviation of each dispersed variable is shown for trajectory three only in Figure 5-8. Figures for each variable and each trajectory are shown in Section B.1 of Appendix B. The circles in Figure 5-8 represent the successes. The red dashed line shows the ΔV limit

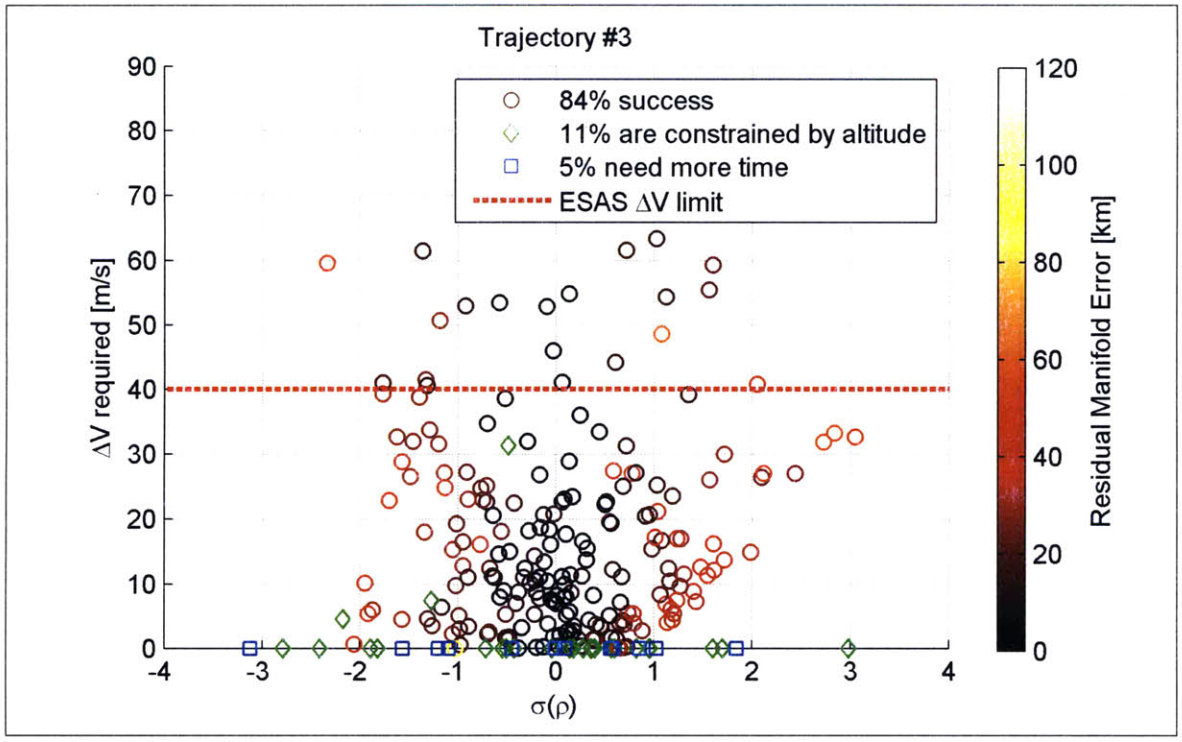

(a) Atmospheric density

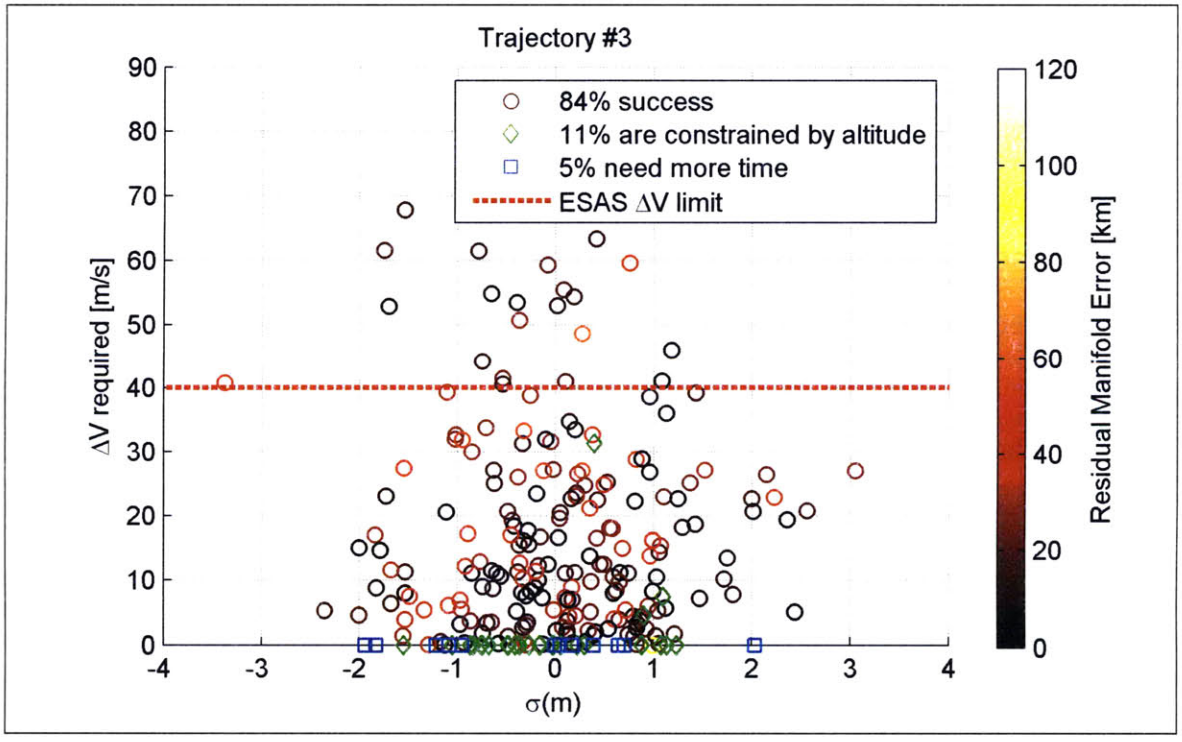

(b) Spacecraft mass

Figure 5-8: Scatter of ΔV required for trajectory #3

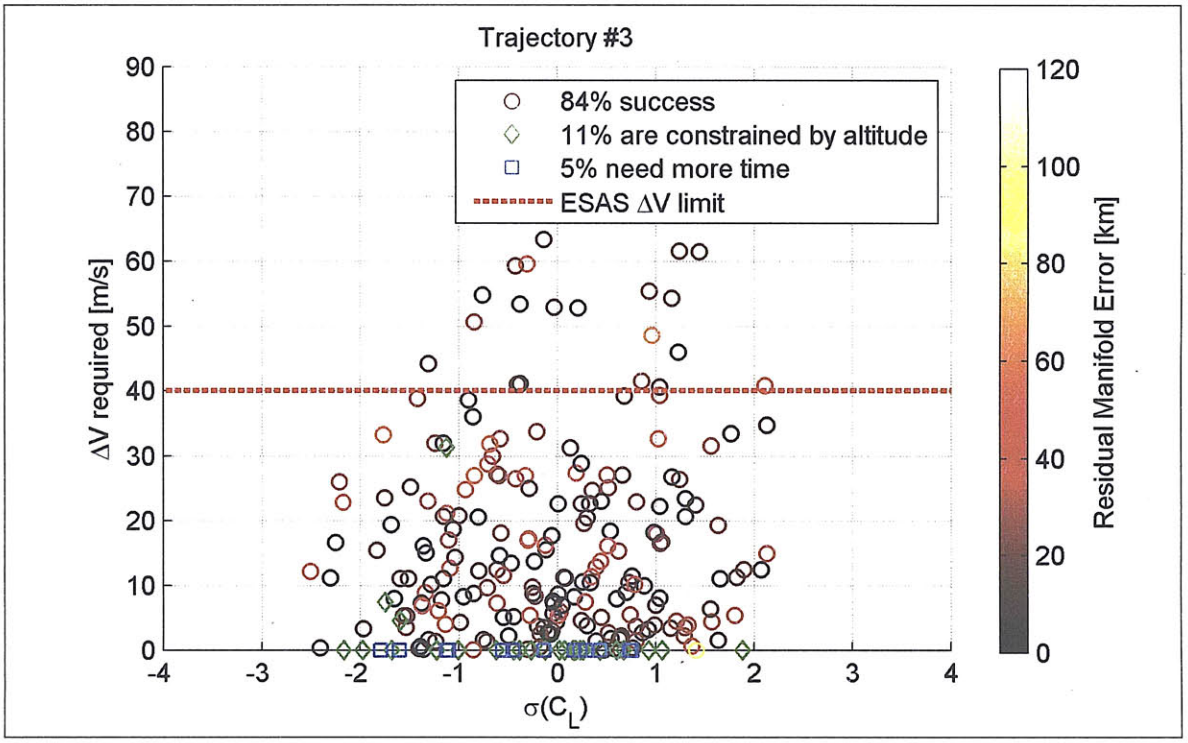

(c) Spacecraft lift coefficient

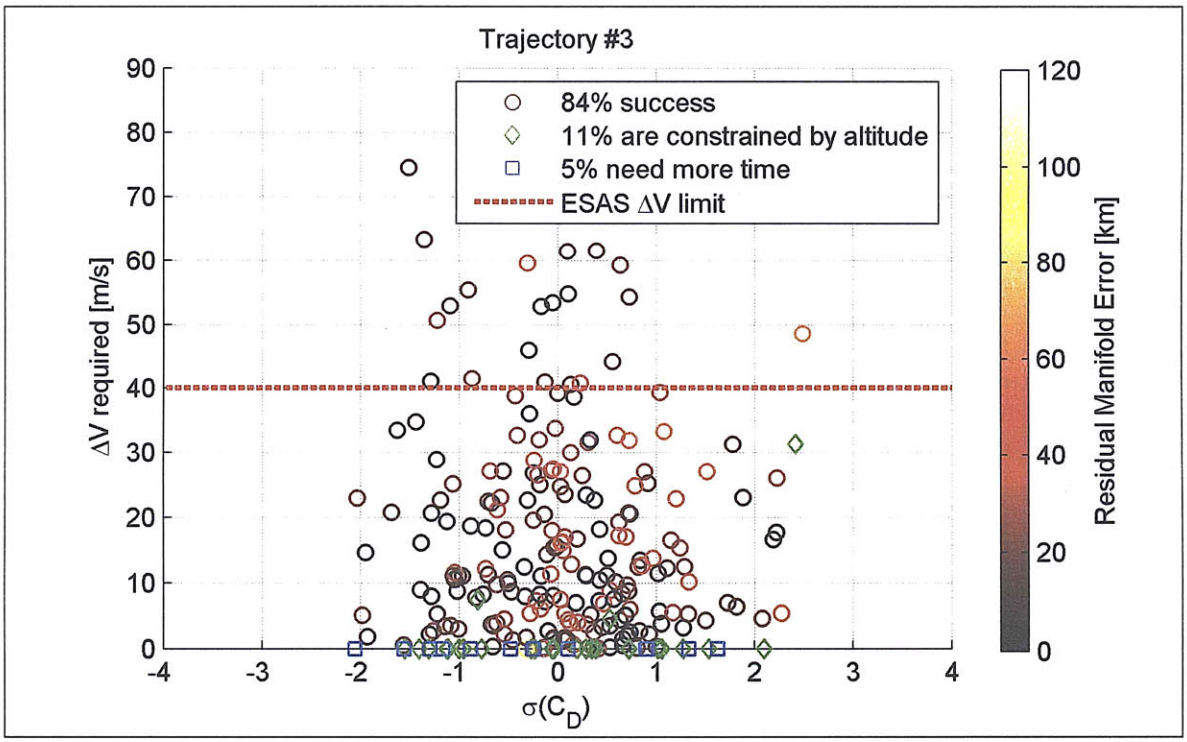

(d) Spacecraft drag coefficient

Figure 5-8: Scatter of ΔV required for trajectory #3 (cont'd)

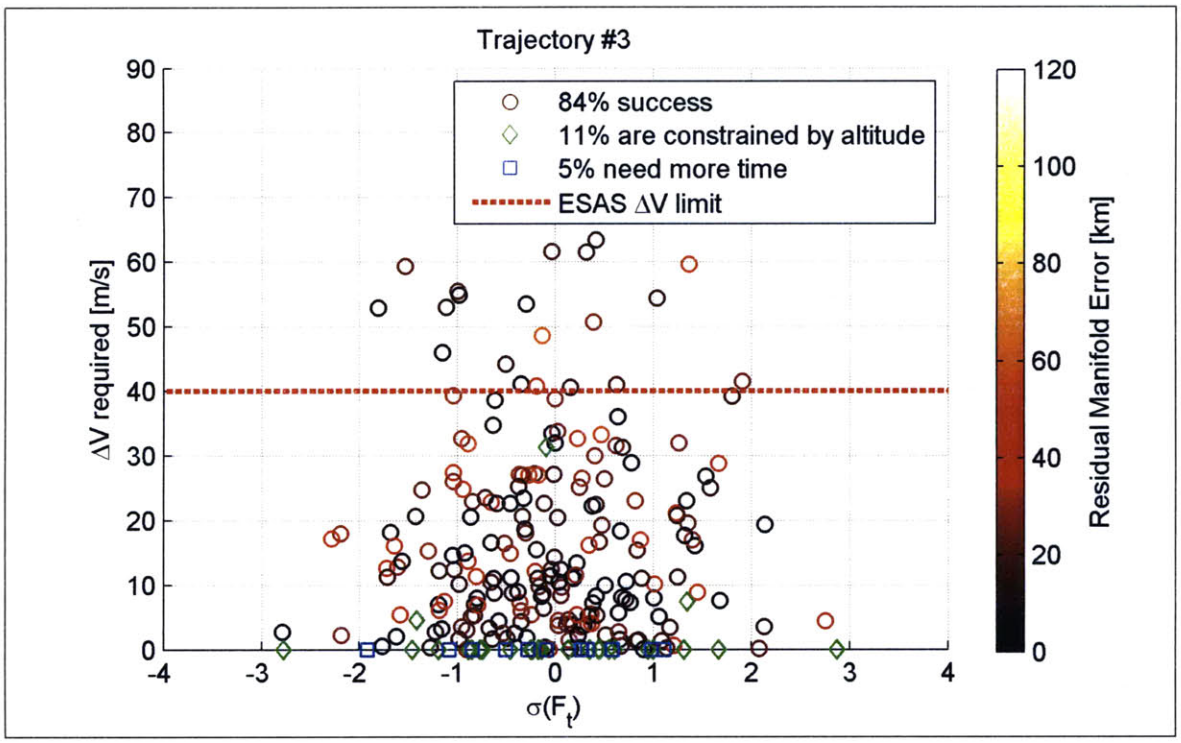

(e) Thruster force

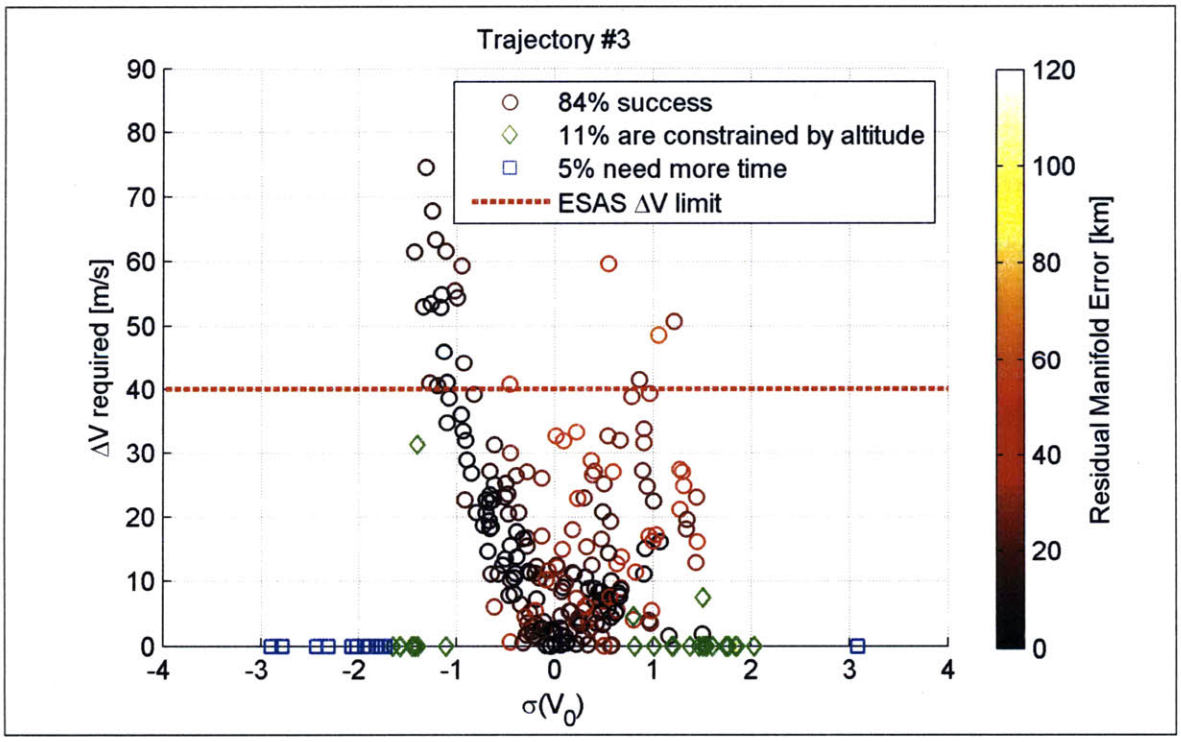

(f) Initial velocity

Figure 5-8: Scatter of ΔV required for trajectory #3 (cont'd)

from Reference [2]. The circles are colored corresponding to the residual manifold error at the end of the trajectory. The green diamonds are the trials that could not reach the target due the altitude constraint. Most of them show zero ΔV required because, despite the initial call to PEG returning a reasonable value, by the time the spacecraft reached the 100 km constraint it was no longer possible to perform the maneuver so none was attempted. A few green diamonds show a non-zero ΔV. These trials reached the altitude constraint and PEG still predicted success, but later in the trajectory it became apparent that the initial prediction was wrong due to the dispersions and will no longer reach the target, so the maneuver is stopped. The blue squares are trials that wouldn't have enough time to complete the necessary ΔV maneuver regardless of the altitude constraint.

For the most part there is very little correlation between the dispersed parameters and the ΔV required. There is however one very notable exception; that being the initial velocity perturbation in Figure 5-8f. For reference, one standard deviation of velocity perturbation is 75 $^m/_s$. There is a clear shape that defines the successes from the failures. It is somewhat shaped like a parabolic bowl opening to one side. The tilt of this bowl follows from the earlier results that demonstrated that it is cheaper to correct for undershooting trajectories than overshooting ones with an equal amount of error. This is shown in Figure 5-8f by the fact that it is easier to correct for positive perturbation when compared to negative perturbations because of the relationships between the initial conditions as shown in Equations (5.1) through (5.3). Even more striking is the apparent boundary separating the failures caused by the altitude constraint and those caused by a lack of time to perform the maneuver. This shows that the velocity perturbation is a system driver and must be minimized to guarantee complete success. Another trend in Figure 5-8f is that the more accurate trials (black circles) seem to bunch at the boundaries of the parabolic bowl. This is caused because these cases had a relatively low density perturbation which leads to the only other trend in Figure 5-8. That trend is shown for the atmospheric density perturbation in Figure 5-8a. It shows quite clearly that, irrespective of ΔV required, the more accurate trials are those with better knowledge of the actual of density. This

fact is intuitive but shows that having a relatively good knowledge of the atmospheric conditions is key to achieving good precision.

The results of Figure 5-8 are clear. Above all else, the precision of the state at the beginning of the skip phase needs to be as high possible to keep the ΔV required to a minimum. As stated in the discussion of the derivation of Equations (5.2) and (5.3), the velocity dispersion came from a set of Monte Carlo runs of a six degree-of-freedom version of the guidance algorithm discussed in Reference [10]. While it may not have been the final design of that guidance algorithm, the results of this analysis show that more work needs to be done before the ΔV can be brought to within the required amount. Beyond the velocity dispersion, it is also important to have good knowledge of the environment. Without a good knowledge of the density it is difficult to achieve a targeting precision less than 100 km. The remaining perturbed variables bear little correlation with the required ΔV to correct for the initial error or the precision of targeting the manifold. The trends (or lack thereof) are consistent throughout the different trajectories as seen in Appendix B.

The relationship between the residual manifold error and the atmospheric density dispersion can be clearly seen by switching the vertical and color axes in Figure 5-8a. This is shown in Figure 5-9 along with the equivalent version for the velocity dispersion. Only the successes are shown because clearly they are the only trials that reach the target and thus have a reasonable amount of residual manifold error. It is clear to see the effect of the dispersions on the residual manifold error. In fact, Figures 5-9a and 5-9b appear to give the dual of the relationship shown in Figures 5-8a and 5-8f. That is that the absolute value of the density dispersions give monotonically increasing residual error and the absolute value of the velocity dispersions give monotonically increasing values of required ΔV. The residual manifold error for each dispersed parameter and each trajectory is shown in Section B.2 of Appendix B. One should note that, as stated earlier, a large manifold miss does not mean that the spacecraft cannot achieve the desired landing target because the manifold is only a first order prediction of the capability of the final phase guidance.

What remains to be seen from this analysis is which trajectory is the best given

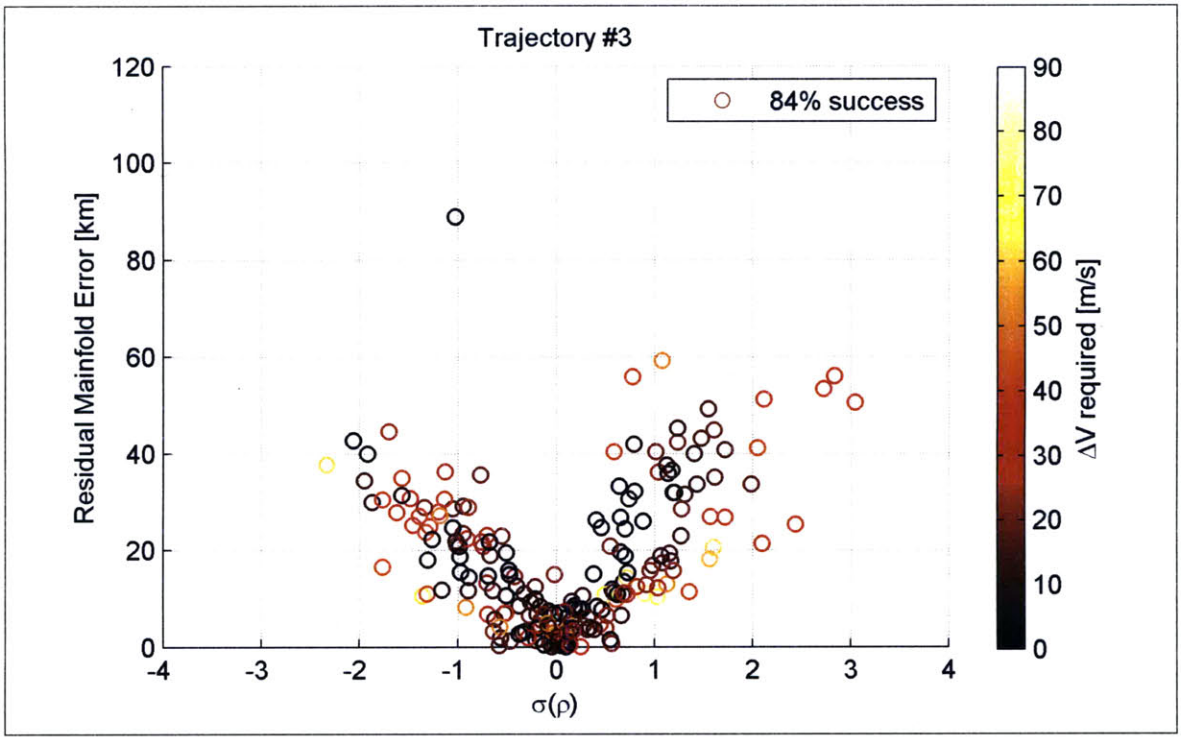

(a) Atmospheric density

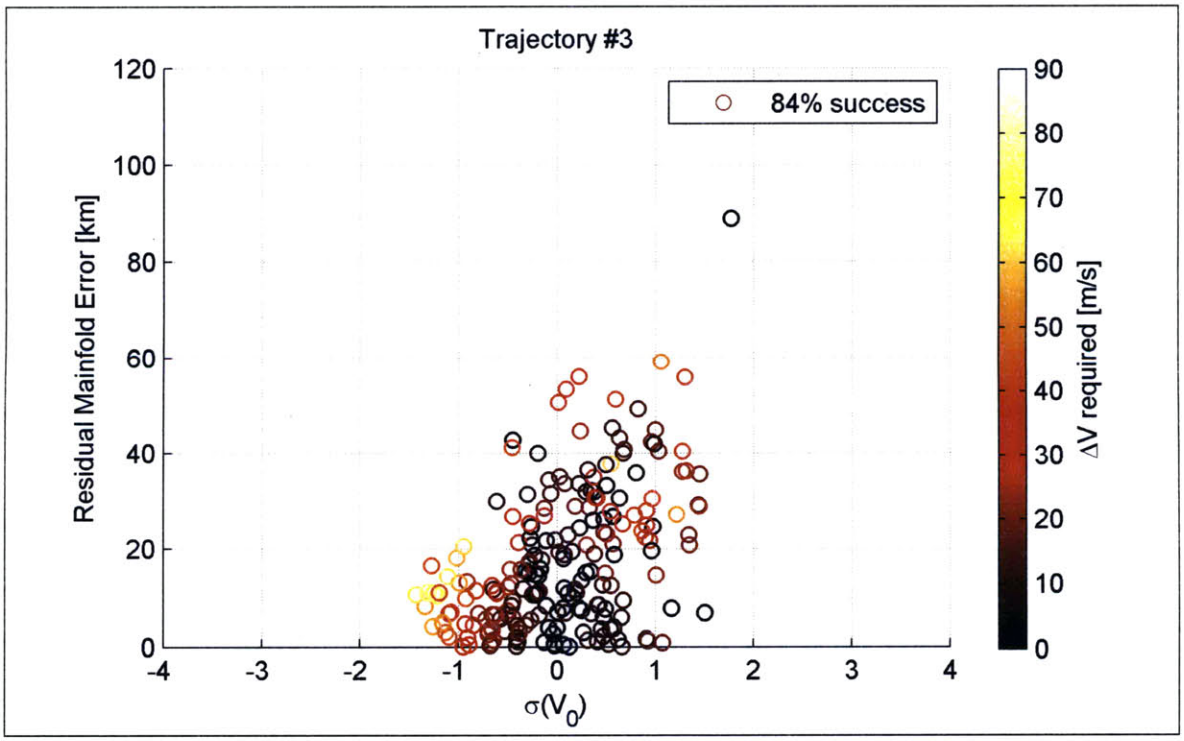

(b) Initial Velocity

Figure 5-9: Scatter of residual manifold error for trajectory #3

the current design of the CEV and the entry guidance algorithm. This answer can be found from the number of trials that successfully reached the target and used less ΔV than the limit. Based upon that fact alone, trajectory three is the winner by a narrow margin over trajectory two. It was stated before that given the number or trials, the margin of error is around a couple percent. Therefore, one could just as easily suggest trajectory two. What is clear from Figure 5-5 is that the high energy trajectory is the least desirable despite the results of Section 3.4 that suggested otherwise. One other option to explore is what would be required to turn some of the failures into successes given the current level of uncertainties and regardless of ΔV constraints. The ΔV constraint is artificially placed on the system based on a number of considerations that are well beyond the scope of this thesis. The most straightforward way to increase the amount of ΔV achievable for a given trajectory is to increase the thruster force. The amount of time available to perform a maneuver is relatively constant for a given trajectory so the force is the remaining variable. Increasing the thruster force will also have the effect of lowering the altitude constraint because more force is available to perform the reorientation maneuver. Therefore, increasing the thruster force effect will be twofold and even greater dispersions would be admissible. Unfortunately, deriving an altitude constraint is beyond the scope of this thesis so it will remain constant. Figure 5-10 shows how the success rate increases while increasing the thrust for trajectory two. Figure 5-10 shows that better success rates can be had with relatively small increases in thruster force. The upper bound on the success rate is determined by the number of trajectories that do not make it high enough to pass the altitude constraint and perform a ΔV burn (in this case that upper bound is 97.6 percent). These failures that were turned into success by more thruster force were trials that went above the 100 km altitude constraint but did not have enough time to generate enough ΔV with the original thrust provided. A greater amount of thrust enables guidance to create more ΔV in a shorter period of time. Also shown in Figure 5-10 are the effects of adding one or two more of the 100 lbf (445 N) thrusters that are currently on the CEV. The initial success rate is 85.6 percent. By adding one more thruster, the success rate jumps to 94.4 percent. By adding two more thrusters,

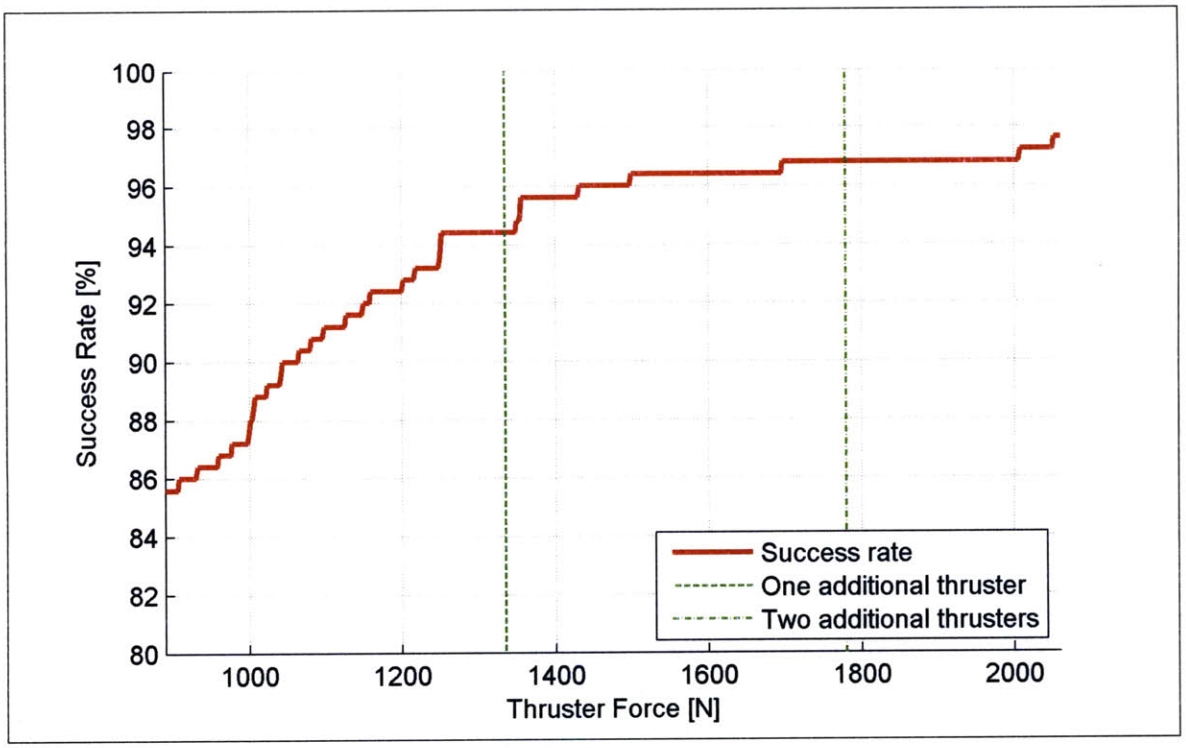

Figure 5-10: Success rate with increasing thruster force for trajectory #2

the success rate reaches 96.8 percent which is less than one percent from the upper bound achievable with a 100 km altitude constraint. A similar trend would also be present for the other trajectories.

Given the results of this section it is possible to make some firm conclusions regarding the design of the spacecraft presented in Reference [2] and the entry guidance algorithm in Reference [10]. The present configuration will not be acceptable for a crewed vehicle returning from the Moon performing skip trajectories. The success rate of a crewed vehicle needs to be well beyond the success rate presented here. Therefore, changes need to be made to the system. The spacecraft should be updated with larger thrusters or more thrusters of the size that is in the current design, irrespective of the amount of ΔV available. This will do many things to increase the success rate of the system. Larger thrusters will decrease the required ΔV across the board since less time is required to perform the maneuver. They will also reduce the altitude at which a maneuver can be performed which will allow for greater variation in the skip trajectory. This will also reduce the ΔV since the propulsive maneuver

will be started earlier in the skip phase. In addition to increasing the thrust, the entry guidance must be tuned to achieve more precise exit conditions. Given the extremely sensitive nature of a skip trajectory, the skip phase initial conditions must be met with a higher degree of precision than is currently done. It would also be beneficial to redefine the skip phase such that it begins when it is possible to perform the reorientation maneuver. This would give more time for the aerodynamic guidance to reach its target. Thus less time would be spent in the region between the initiation of the skip phase and the reorientation maneuver when no active guidance is being performed. As mentioned earlier, the lower energy trajectories result in more successes despite having less capability to correct for a given amount of error when compared to the higher energy trajectories because they achieve a higher maximum altitude.

Chapter 6

Conclusion

6.1 Summary

An analysis of the physics of the problem are presented through a study of the minimum impulsive ΔV required to target a downrange location or a manifold for varying amounts of initial range error. It was shown that undershooting trajectories are cheaper with respect to ΔV when compared to overshooting trajectories. It was also shown that the earlier a propulsive maneuver is performed the cheaper is. High energy trajectories (fast and shallow) were shown to have more ability to correct for a given amount of range error than low energy trajectories (slow and steep). The analysis was concluded by demonstrating a novel targeting method that aims for a locus of reentry conditions based upon the range-to-go to the landing target. This method was also shown to reduce the ΔV requirement for a given amount of error.

The groundwork for the propulsive guidance algorithm was presented and its components explained. This algorithm was initially tested for the span of trajectories examined above to show the effect of removing the impulsive assumption from the physics of the problem. It was shown that removing the impulsive assumption increases the ΔV required because the maneuver is now spread over a finite amount of time. An altitude constraint was added to simulate the effects of having a limited reorientation torque available due to the magnitude of the aerodynamic moments on the entry body. The robustness of the algorithm was tested on each trajectory by

performing a 250 trial Monte Carlo analysis while perturbing the atmospheric density, spacecraft mass, coefficient of lift, coefficient of drag, thruster force, and the initial speed. The initial speed was shown to have a direct relationship between the initial range error and the initial flight path angle. These relationships along with the speed dispersion were used to perturb the initial range error and flight path angle.

The result of the Monte Carlo analysis showed that the current implementation of the CEV to be inadequate for the purpose of bringing humans safely back from the Moon by performing an atmospheric skip entry. A number of design changes were suggested to improve the success rate of the mission. An increase of the ΔV allowance would compensate for some of the imprecision of the entry guidance scheme that was observed. Larger thrusters would reduce the amount of ΔV required for all the trajectories and allow some low flying trajectories to perform maneuvers because the amount of thrust also defines the altitude at which one can reorient. The system level definition of the skip phase could be changed so that it is defined at the point were the reorientation maneuver can be performed. This would also allow the entry aerodynamic guidance more time to accurately target the skip phase initial conditions. It was recommended that trajectory two be chosen as the prime target because it shows that best balance between the present capability and future designs that address the suggestions given above.

6.2 Future Work

A number of issues can and should be addressed in future studies of propulsive guidance for atmospheric skip entry trajectories. The first would be to improve the fidelity of the model. This can be done by including such eccentric effects that were neglected here like transitional and rarefied aerodynamics or a non-Newtonian gravitational field. The fidelity can also be improved by increasing the degrees of freedom of the model to include the rotational dynamics of the spacecraft. This would enable one to simulate the aerodynamic instability of the capsule at high altitudes, the reorientation maneuver, and find the precise altitude at which the reorientation maneuver

can be performed. Increasing the degrees of freedom would also enable one to study the effect of controlling the lift vector during the skip phase. This study should focus on examining if it is possible to direct the lift vector in a favorable way while in the correct orientation for the ΔV burn. Increasing the degrees of freedom will increase the physical accuracy of the model but will likely decrease the performance of the guidance algorithm.

Another avenue of future study is to improve the guidance algorithm itself. This can be done by improving the predictor by deriving an efficient method for computing an aerodynamic integral like the thrust and gravity integrals in PEG. It would also be beneficial to develop a technique to determine the optimum thrust direction dynamically. Improving the corrector could be done by using a quadratic interpolant to find the velocity to hit the target instead of a linear one.

Methods for mitigating the observed trends in the Monte Carlo analysis would help reduce the residual manifold targeting error. An in-depth study of the amount of thrust, ΔV allowance, and initial condition precision needed to guarantee a one hundred percent success rate would be very beneficial from a system design point of view. For completeness, this study should also include the entire entry phase guidance algorithm from the initialization of the first entry through the skip phase and to the end of the final phase. This will allow one to remove the linear relationships between the skip phase initial conditions as they will follow directly from the first entry. It will also enable one to better characterize the failures as it will be readily apparent which trials are not able to achieve the landing target which is the prime objective after all.

Appendix A

Impulsive ΔV Direction

The following figures document ΔV direction for the corresponding figures in Chapter 3. The solution for zero range error is singular and thus not shown.

A.1 Downrange Targeting

The ΔV directions corresponding to Figure 3-4 are shown below.

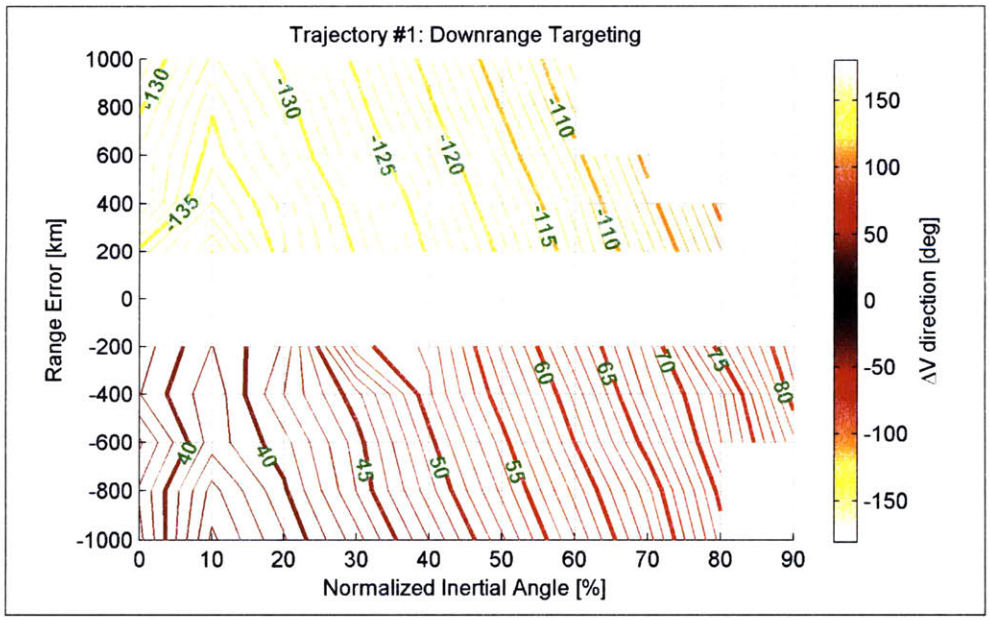

(a) Trajectory #1

Figure A-1: Direction of minimum impulsive ΔV to target a downrange location

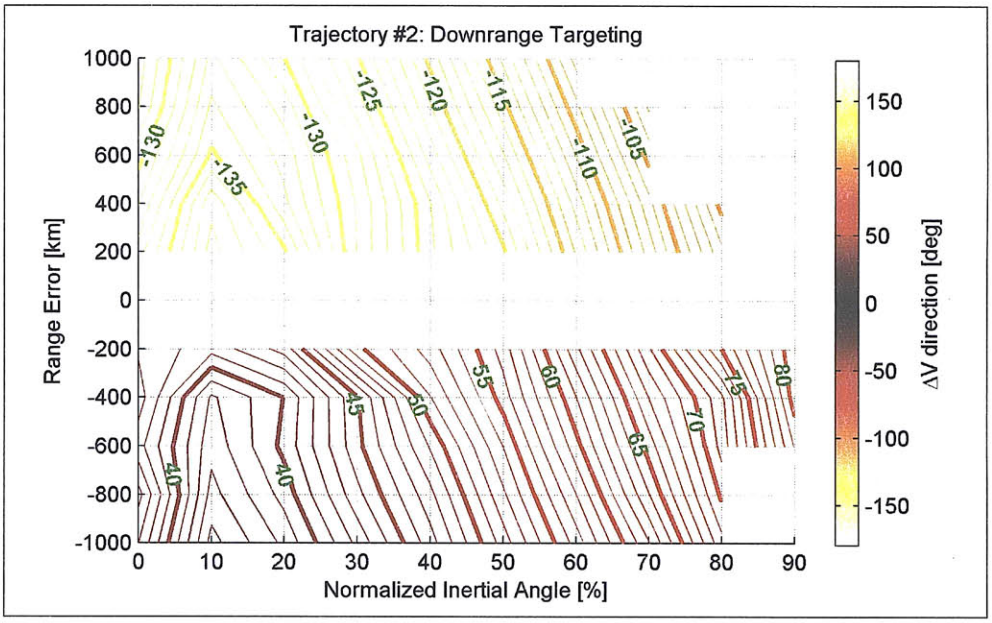

(b) Trajectory #2

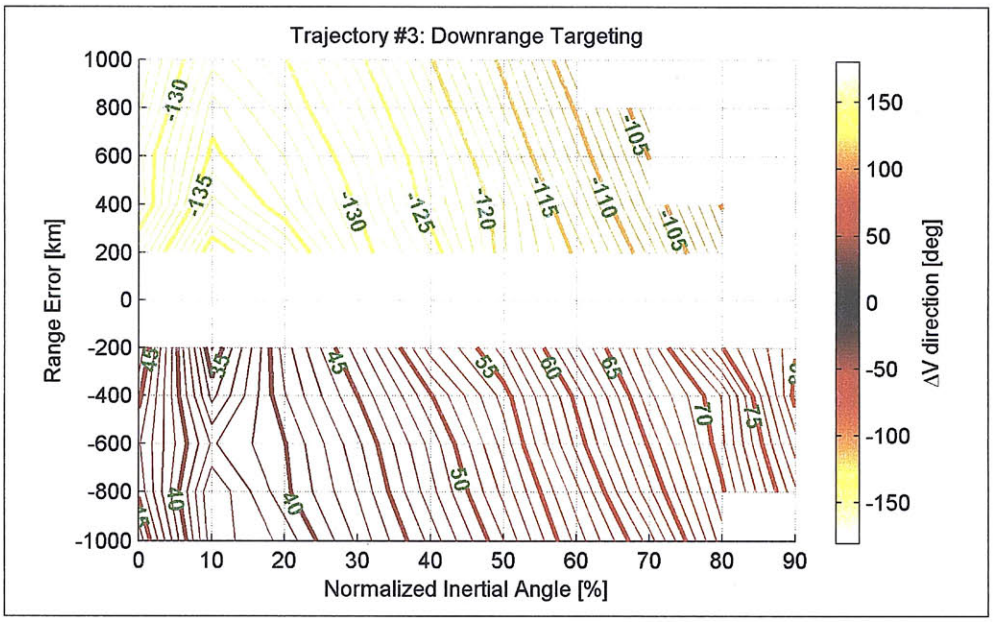

(c) Trajectory #3

Figure A-1: Direction of minimum impulsive ΔV to target a downrange location (cont'd)

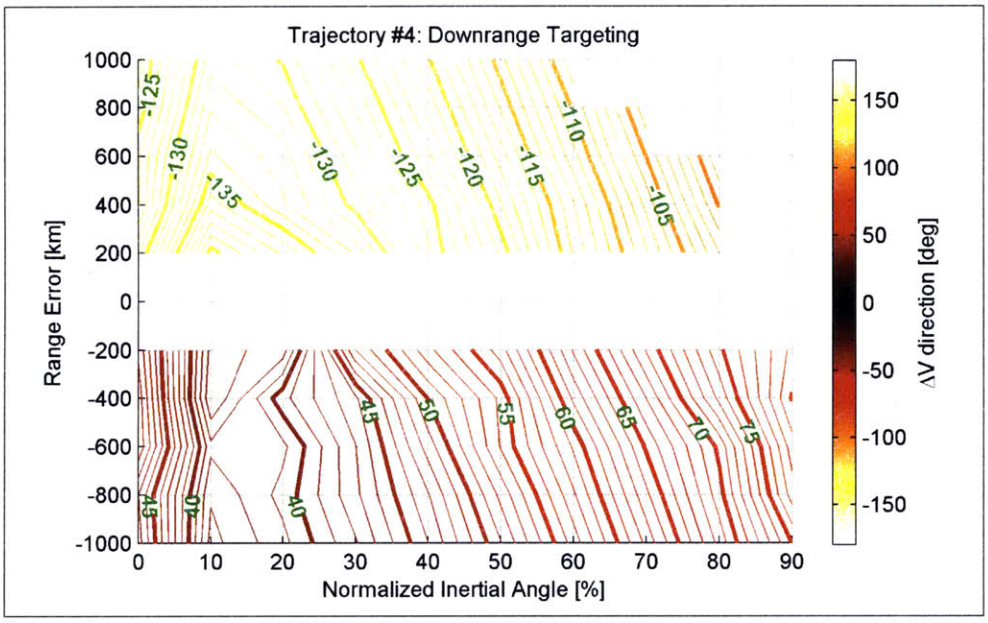

(d) Trajectory #4

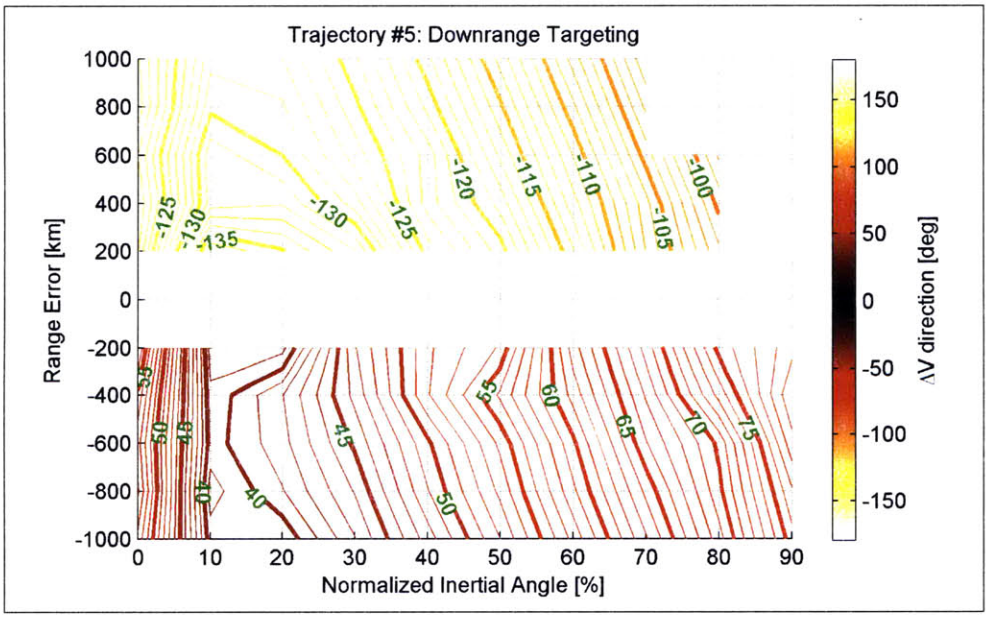

(e) Trajectory #5

Figure A-1: Direction of minimum impulsive ΔV to target a downrange location (cont'd)

A.2 Manifold Targeting

The ΔV directions corresponding to Figure 3-9 are shown below.

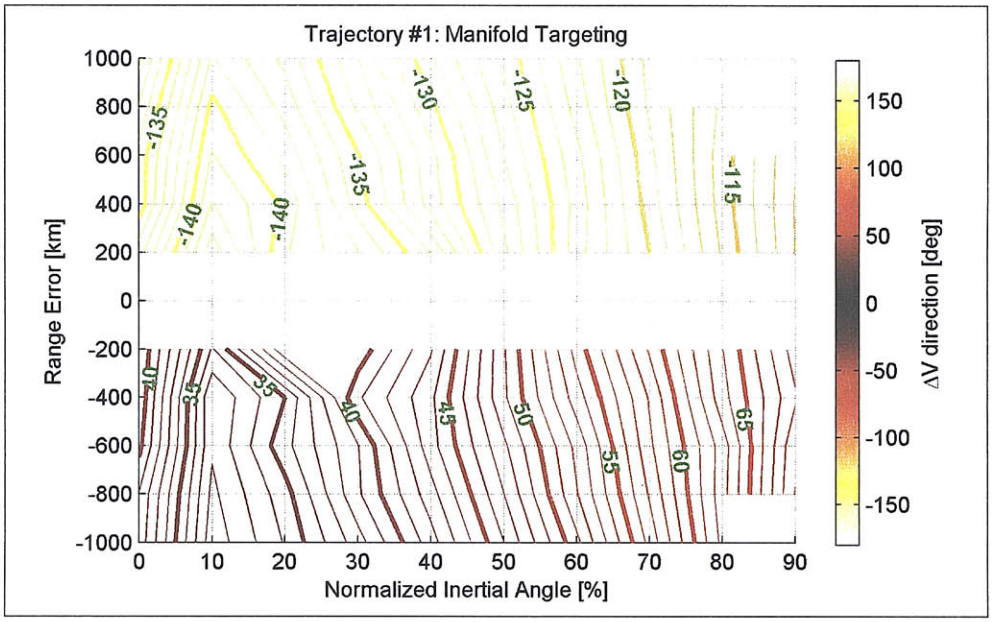

(a) Trajectory #1

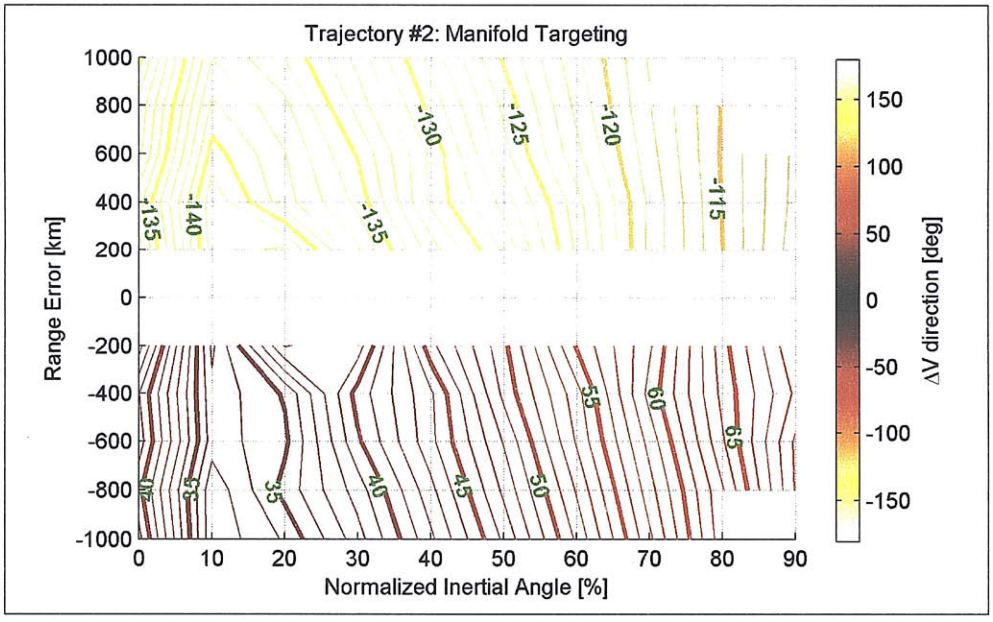

(b) Trajectory #2

Figure A-2: Direction of minimum impulsive ΔV to target a manifold

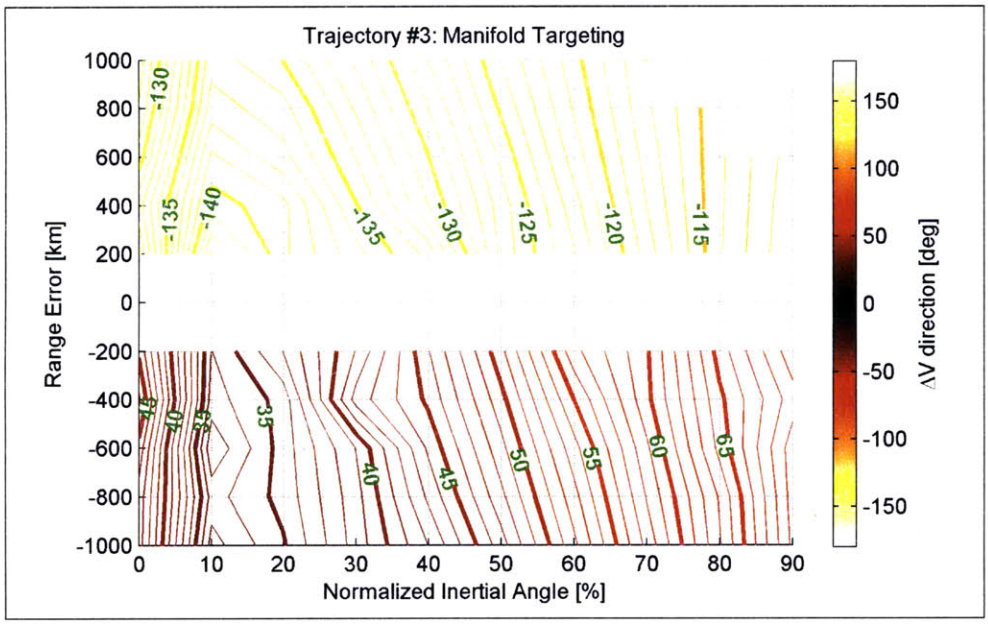

(c) Trajectory #3

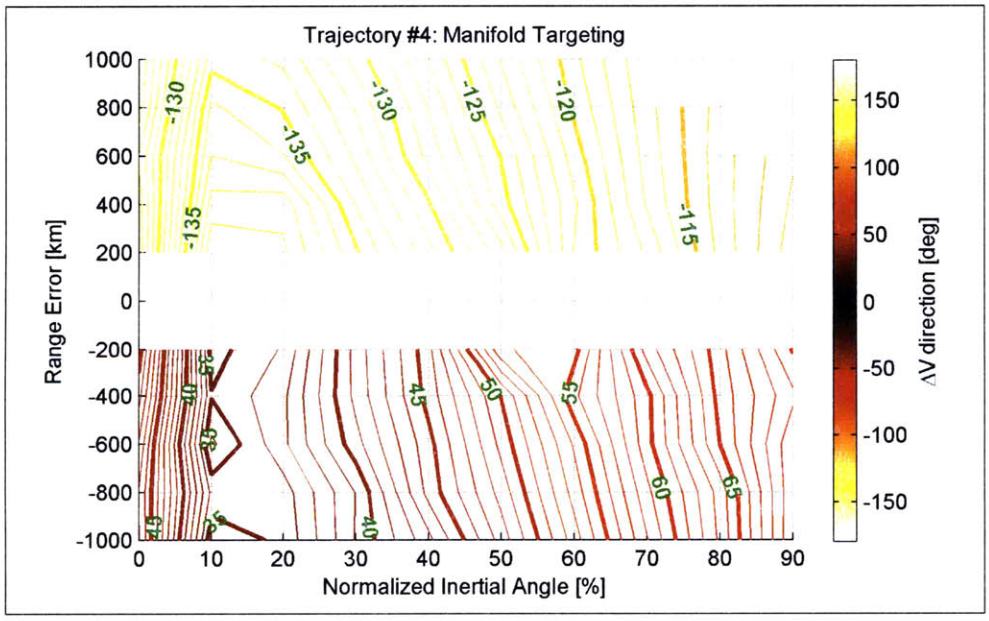

(d) Trajectory #4

Figure A-2: Direction of minimum impulsive ΔV to target a manifold (cont'd)

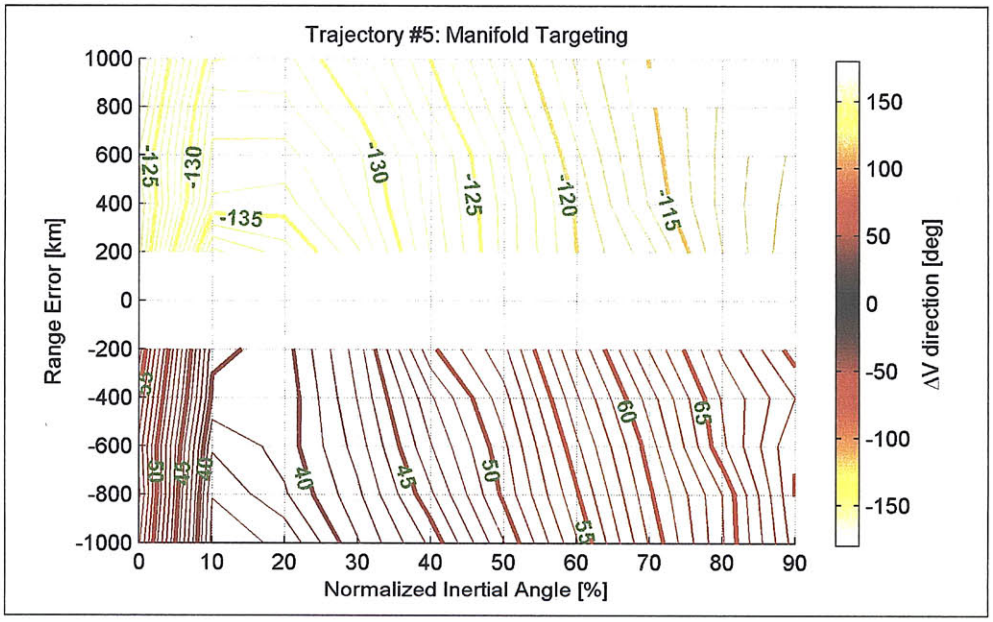

(e) Trajectory #5

Figure A-2: Direction of minimum impulsive ΔV to target a manifold (cont'd)

Appendix B

Dispersed Variables

The following figures document ΔV required to reach a target and the residual manifold targeting error as a function of the standard deviation of each perturbed variable for each trajectory. They are grouped by the perturbed variable to clearly show the the individual effect of perturbing that parameter.

B.1 Required ΔV Magnitude

The following figures show the relationship between the perturbed variable and the resulting ΔV required to correct for any errors.

B.1.1 Atmospheric Density

The atmospheric density was perturbed using a multiplier with a 3σ value of 30 percent.

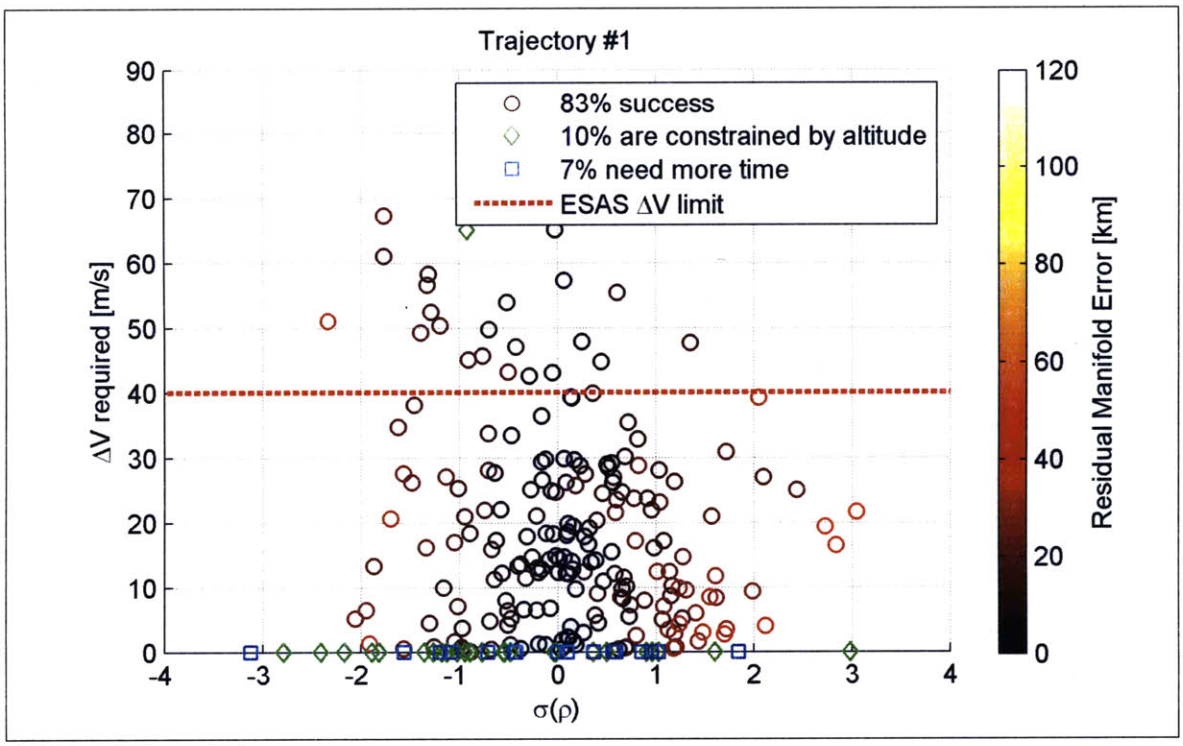

(a) Trajectory #1

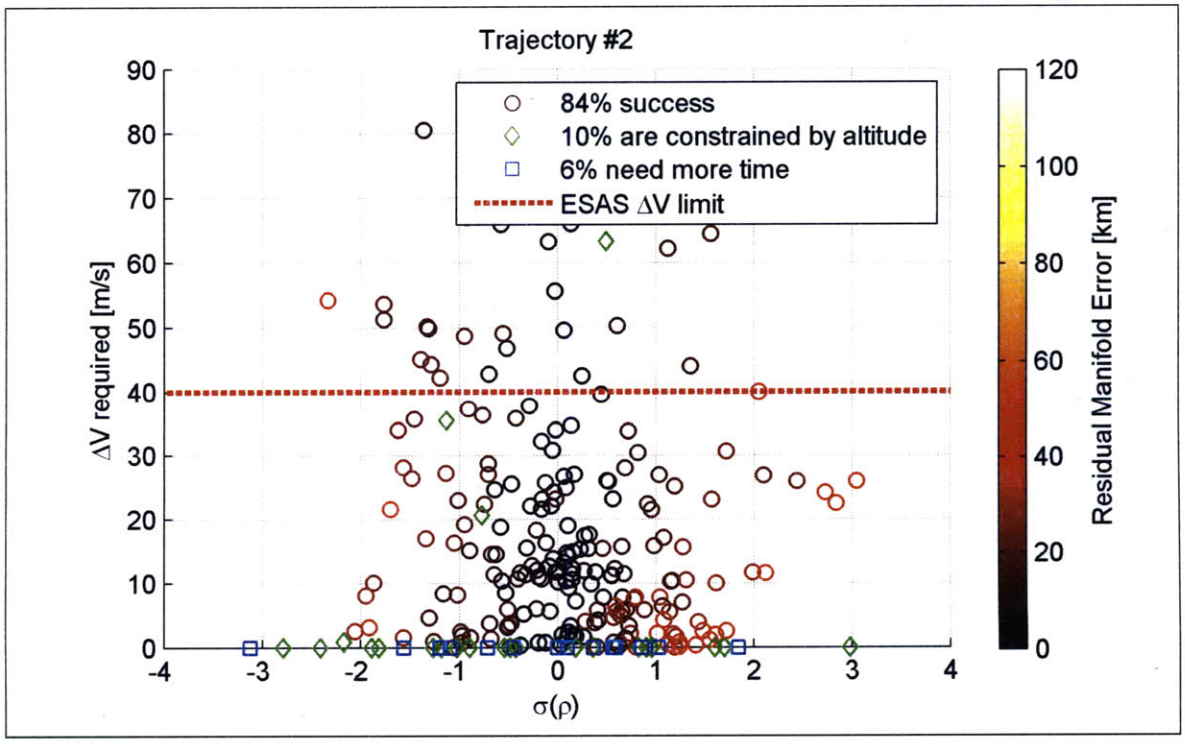

(b) Trajectory #2

Figure B-1: Scatter of ΔV required for a dispersed atmospheric density

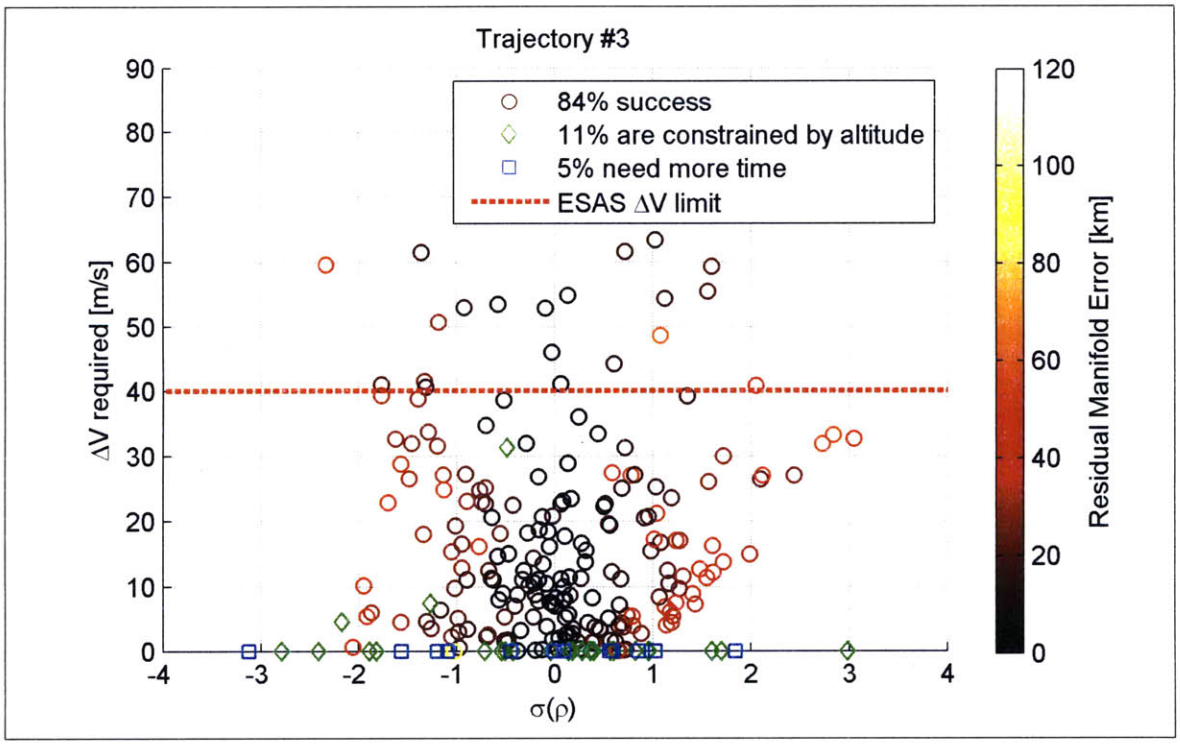

(c) Trajectory #3

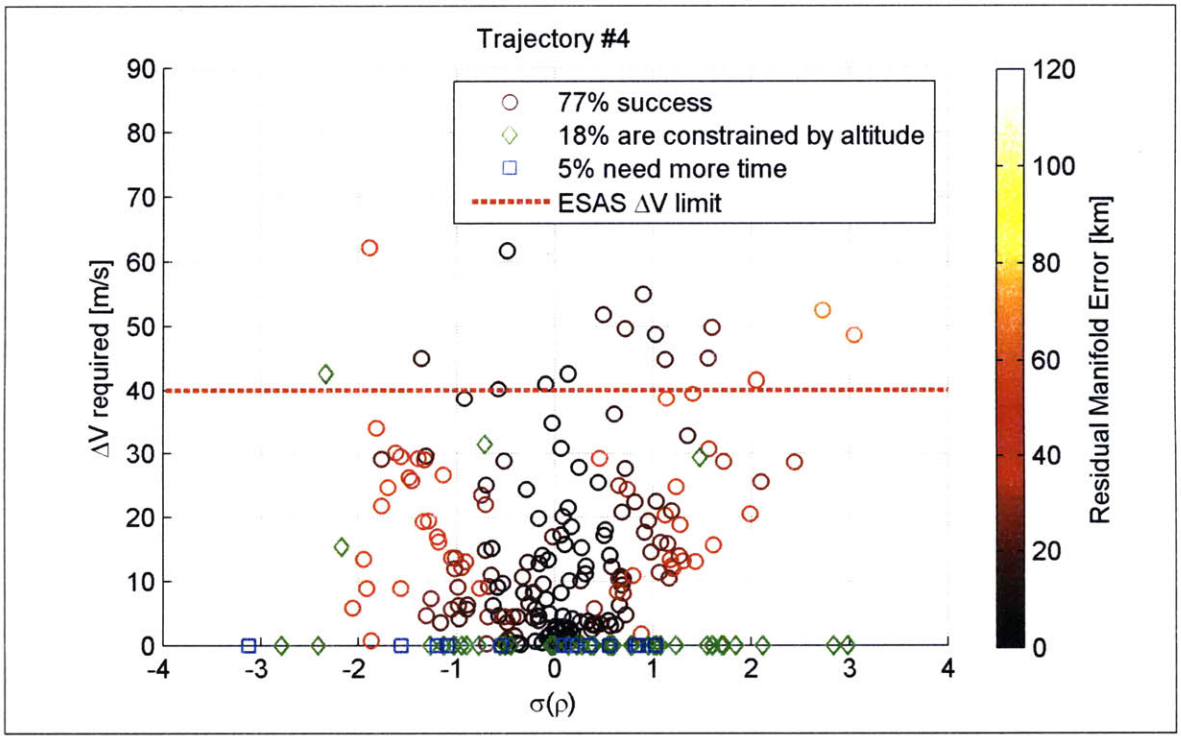

(d) Trajectory #4

Figure B-1: Scatter of ΔV required for a dispersed atmospheric density (cont'd)

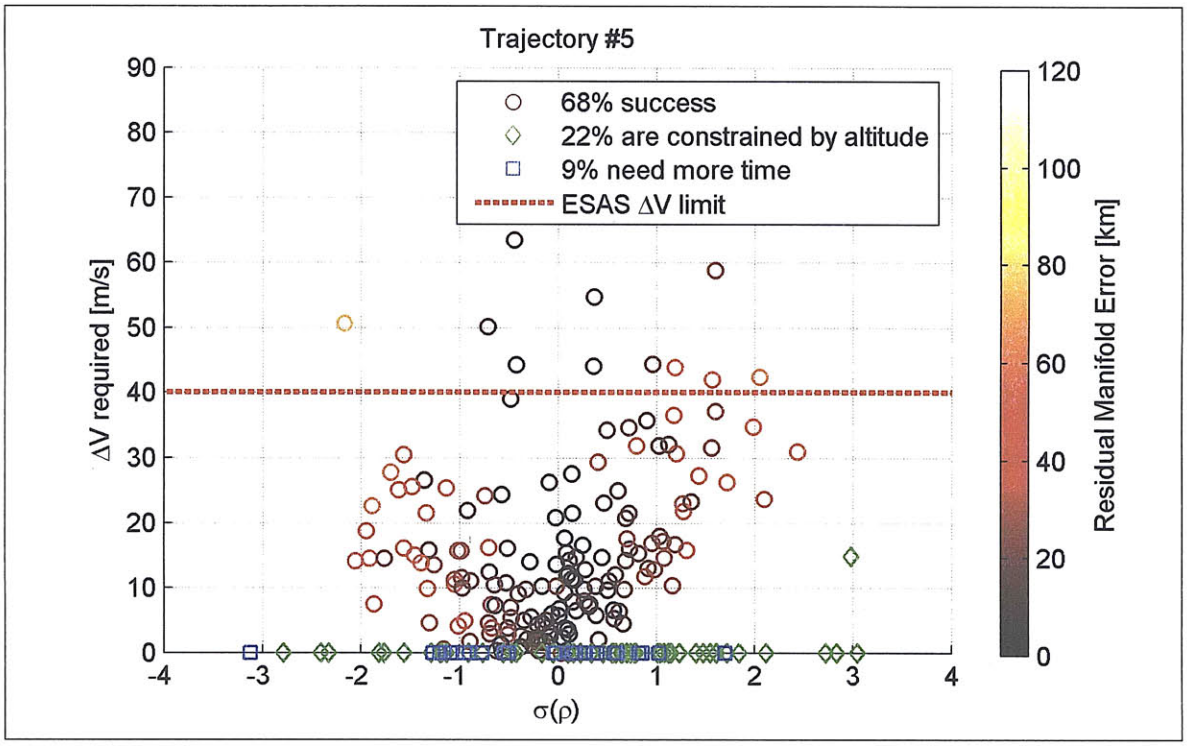

(e) Trajectory #5

Figure B-1: Scatter of ΔV required for a dispersed atmospheric density (cont'd)

B.1.2 Spacecraft Mass

The spacecraft mass was perturbed using a multiplier with a 3σ value of 5 percent.

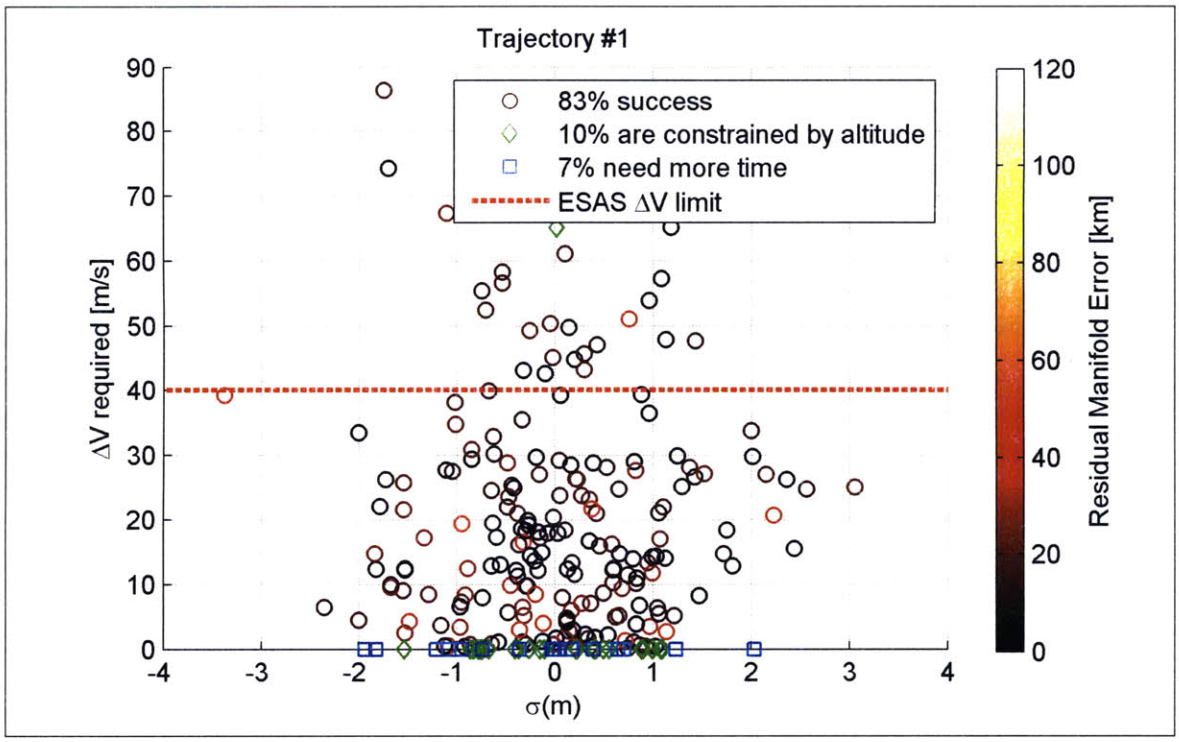

(a) Trajectory #1

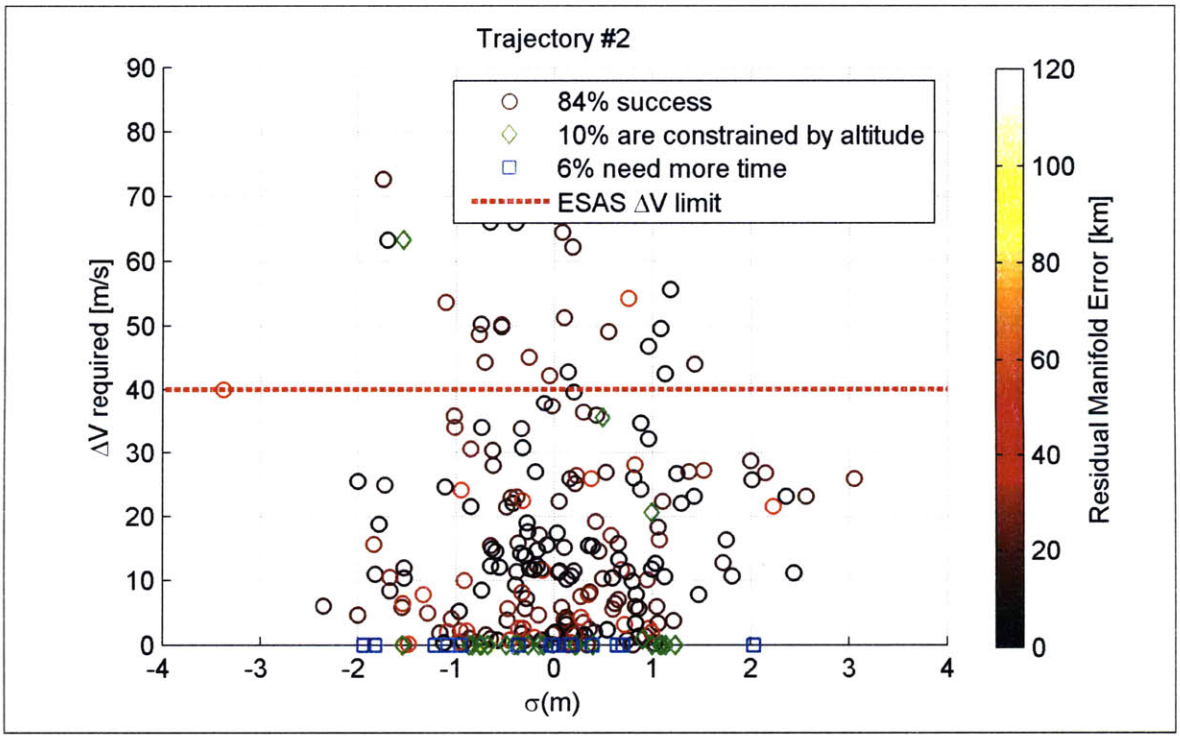

(b) Trajectory #2

Figure B-2: Scatter of ΔV required for a dispersed spacecraft mass

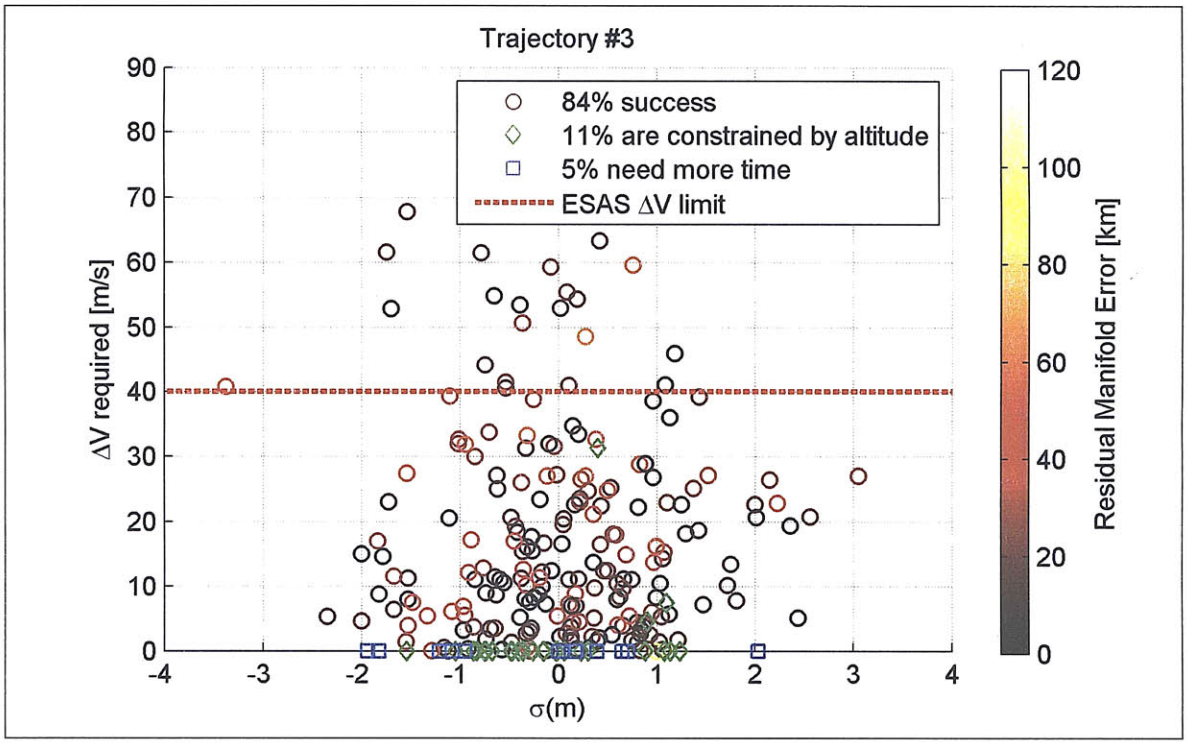

(c) Trajectory #3

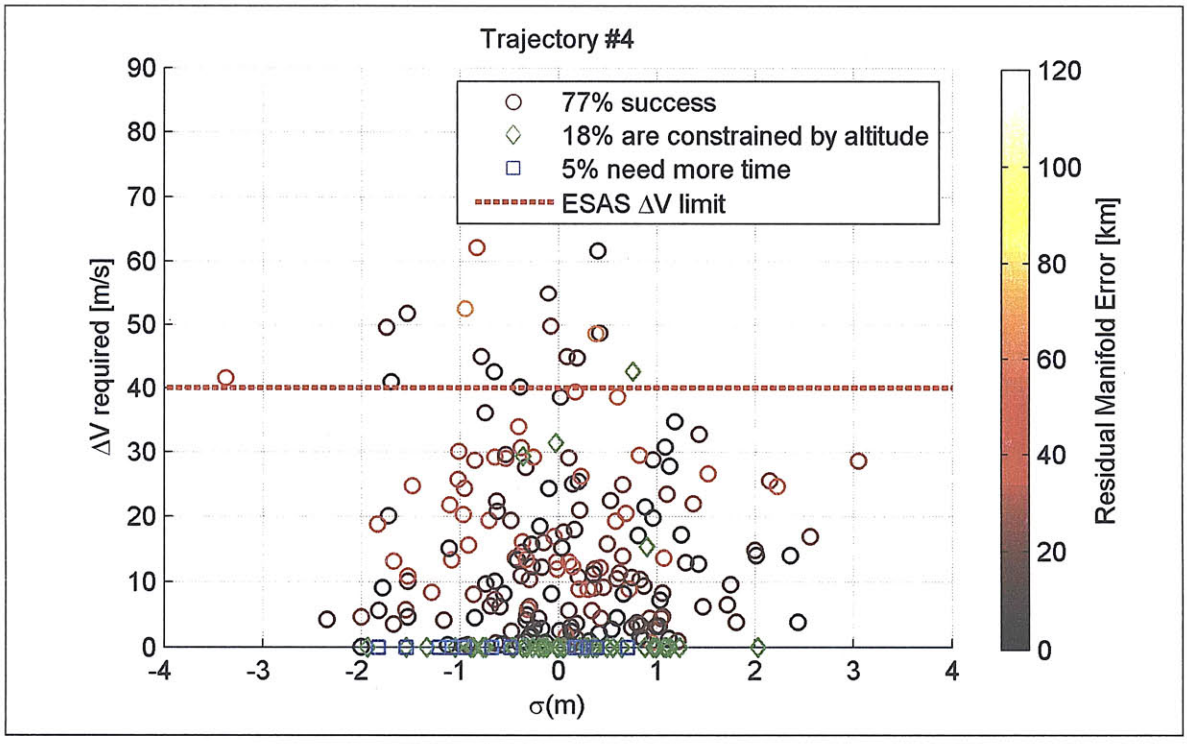

(d) Trajectory #4

Figure B-2: Scatter of ΔV required for a dispersed spacecraft mass (cont'd)

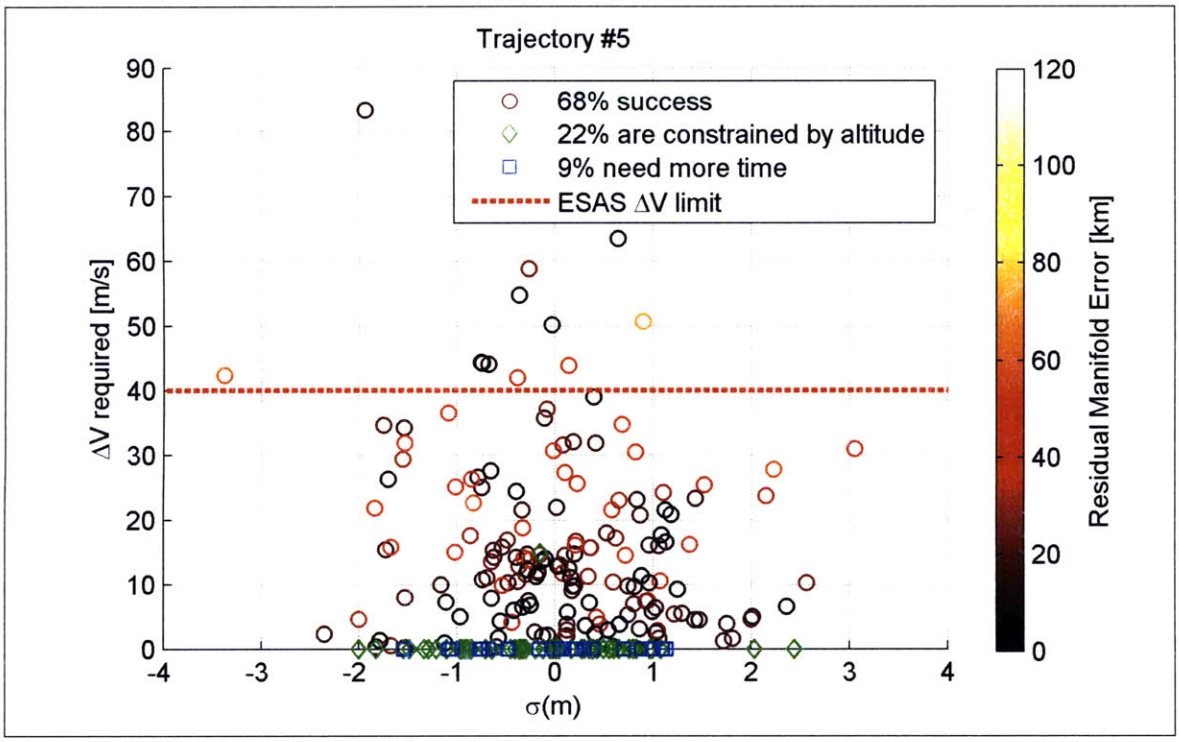

(e) Trajectory #5

Figure B-2: Scatter of ΔV required for a dispersed spacecraft mass (cont'd)

B.1.3 Spacecraft Lift Coefficient

The spacecraft lift coefficient was perturbed using a multiplier with a 3σ value of 10 percent.

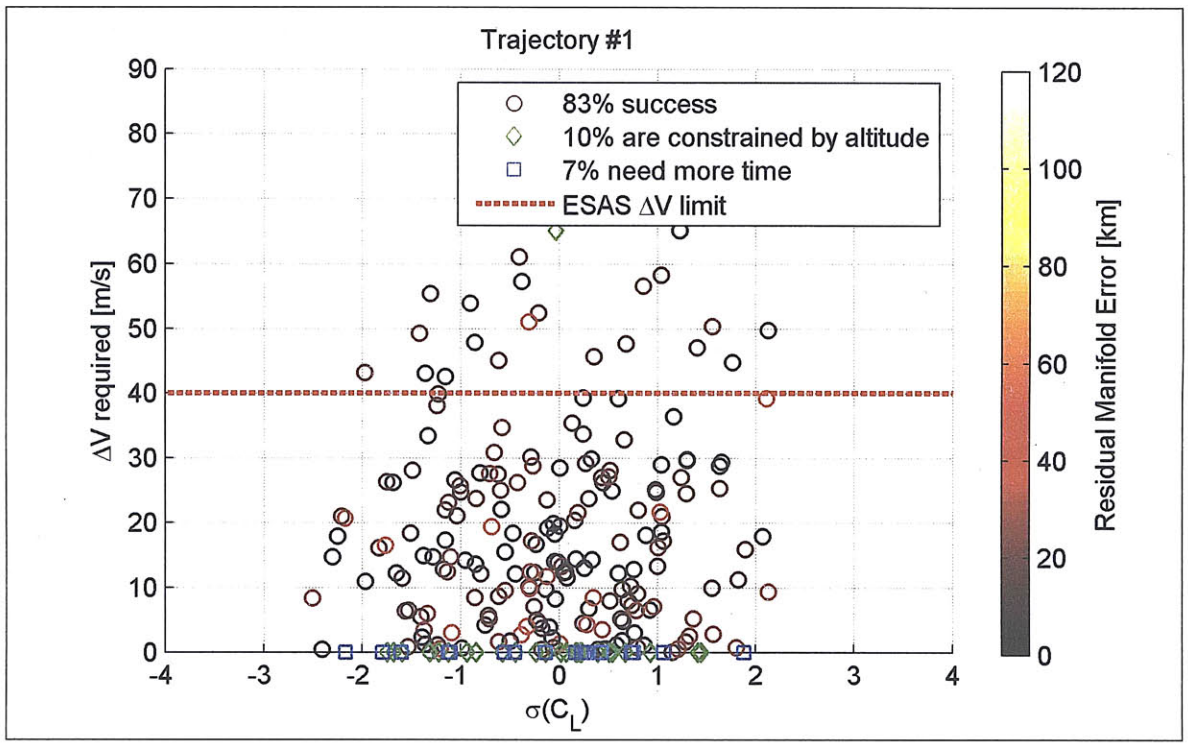

(a) Trajectory #1

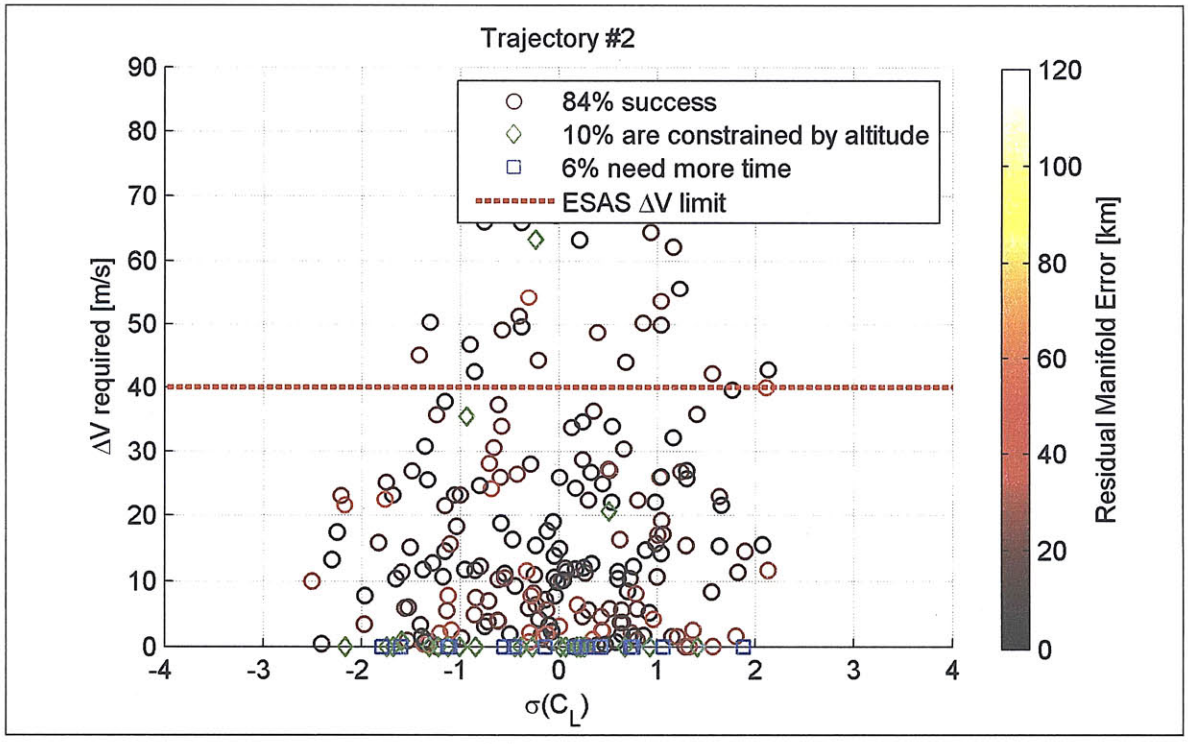

(b) Trajectory #2

Figure B-3: Scatter of ΔV required for a dispersed lift coefficient

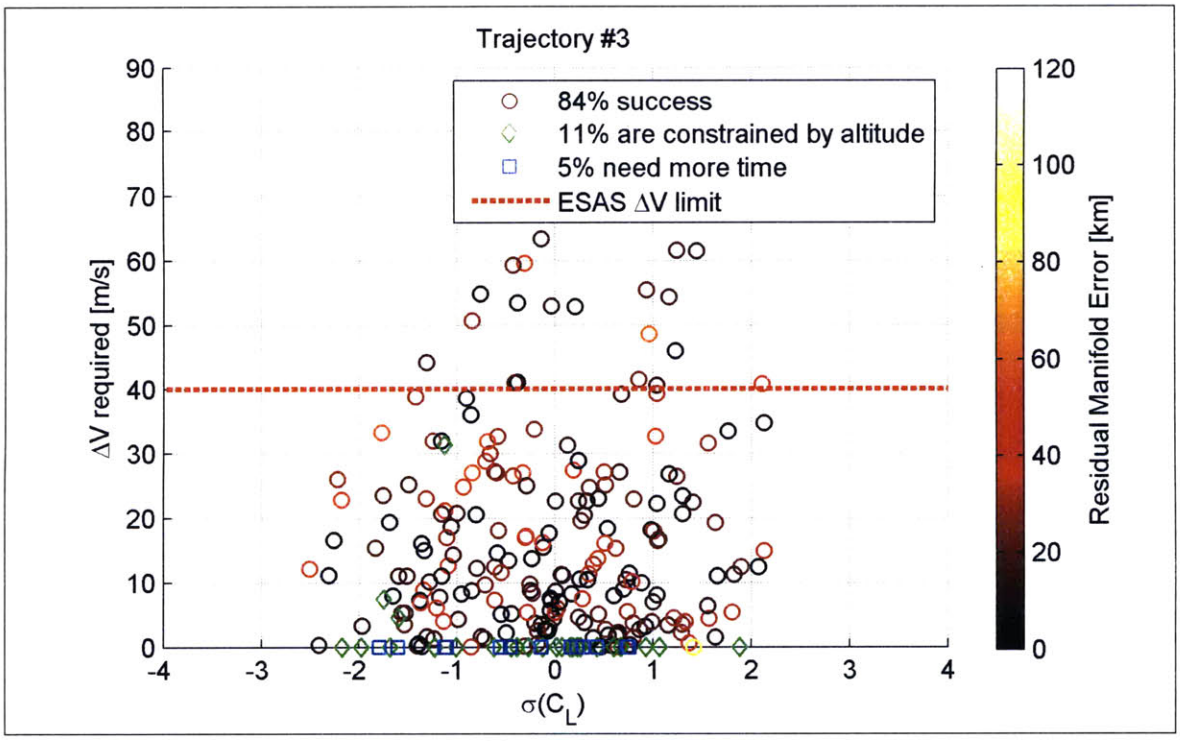

(c) Trajectory #3

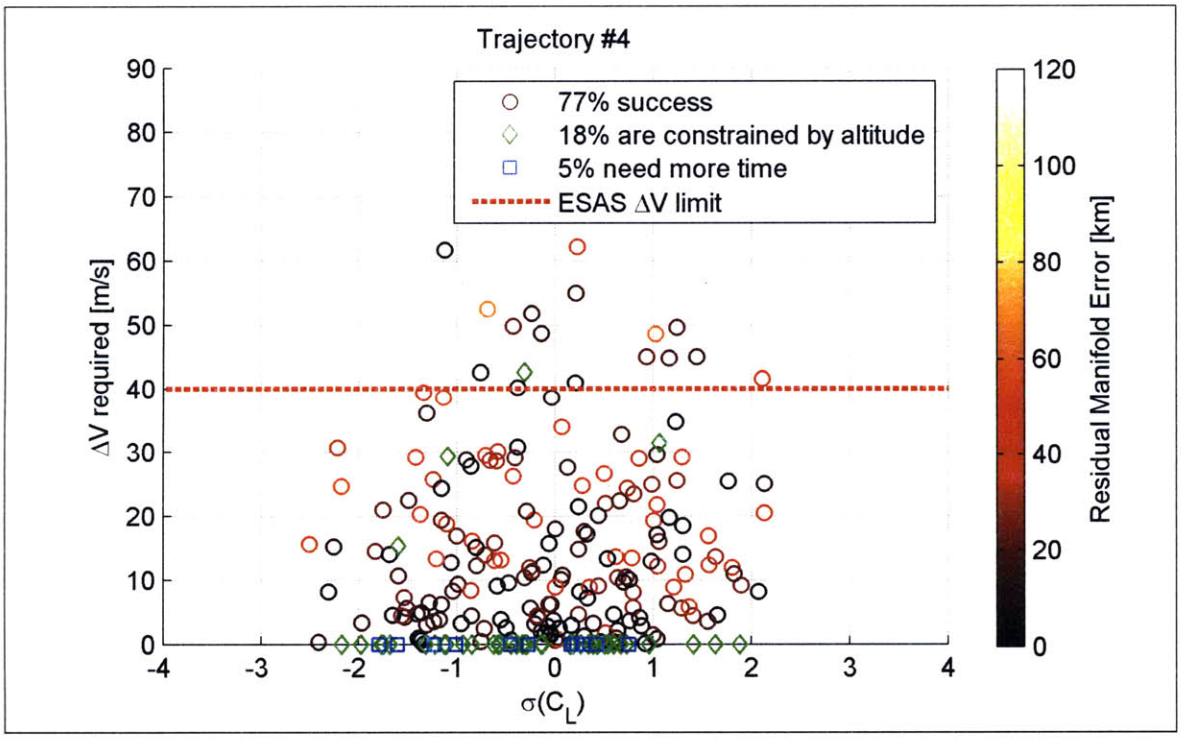

(d) Trajectory #4

Figure B-3: Scatter of ΔV required for a dispersed lift coefficient (cont'd)

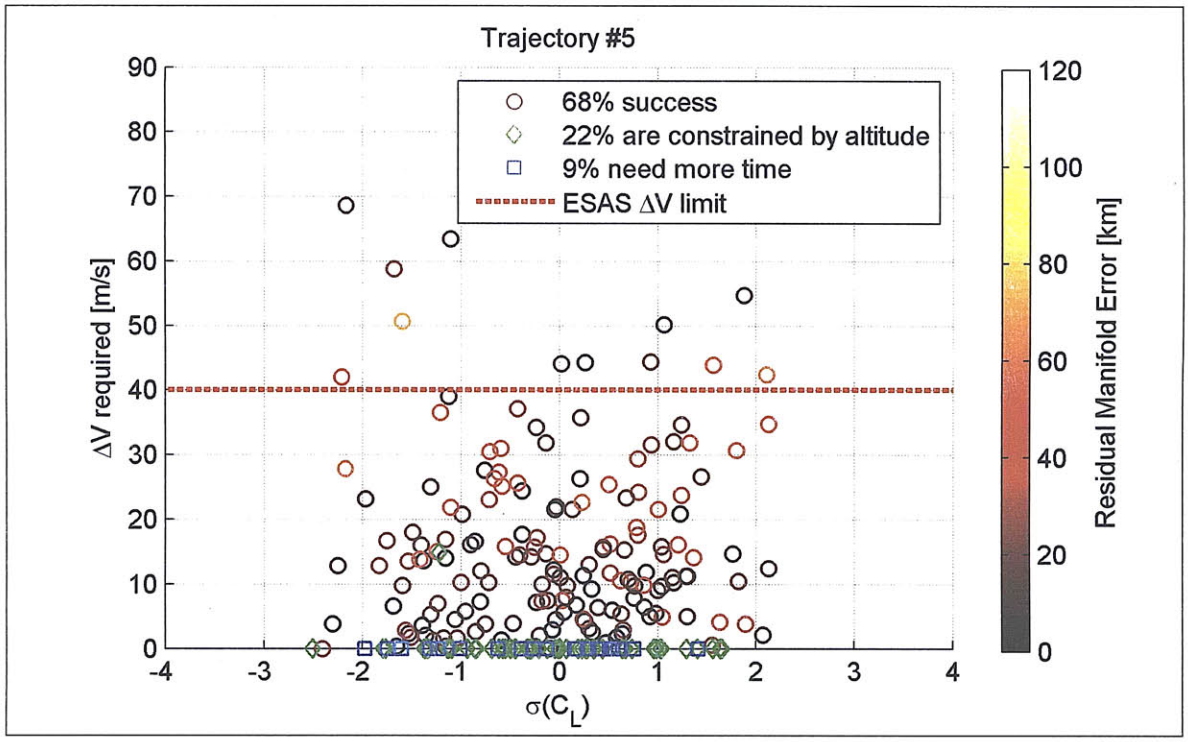

(e) Trajectory #5

Figure B-3: Scatter of ΔV required for a dispersed lift coefficient (cont'd)

B.1.4 Spacecraft Drag Coefficient

The spacecraft drag coefficient was perturbed using a multiplier with a 3σ value of 10 percent.

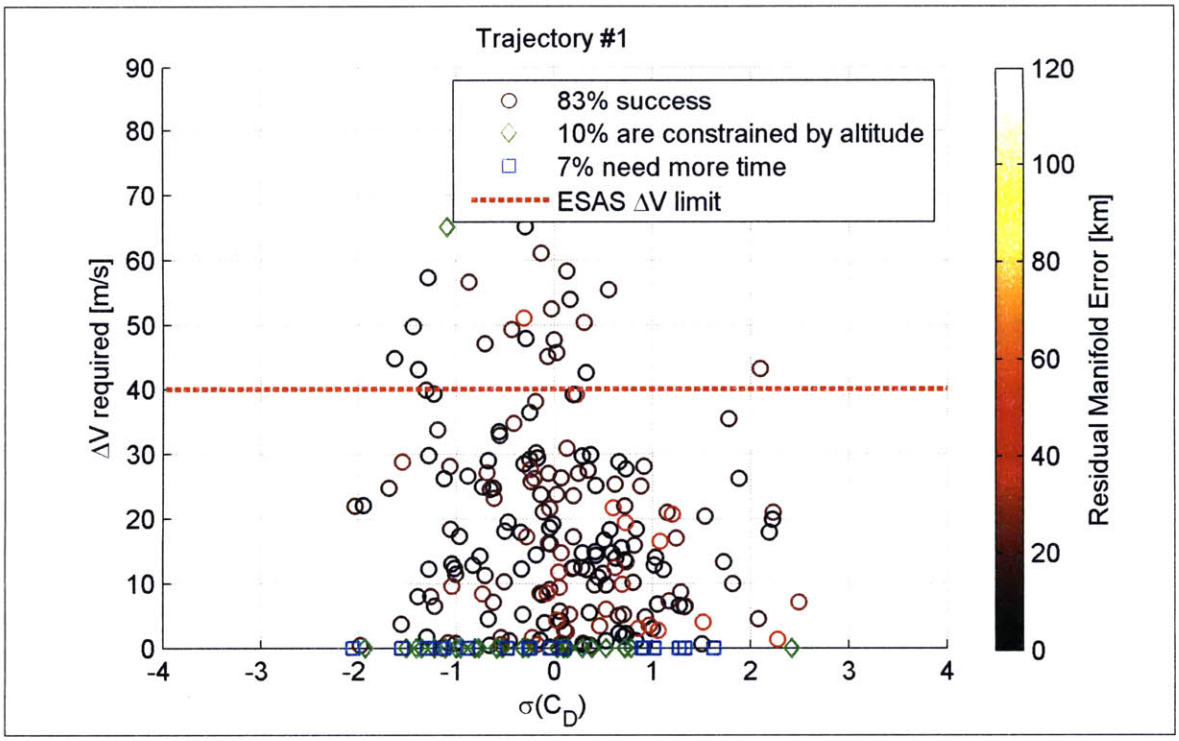

(a) Trajectory #1

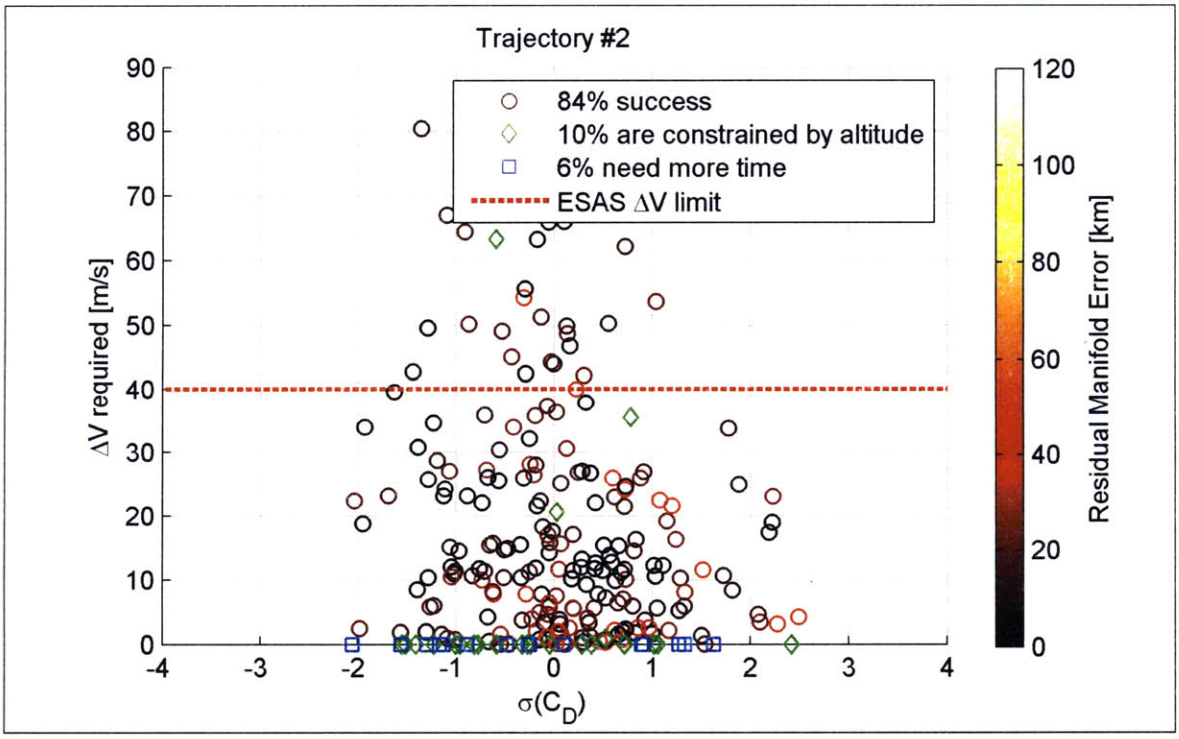

(b) Trajectory #2

Figure B-4: Scatter of ΔV required for a dispersed drag coefficient

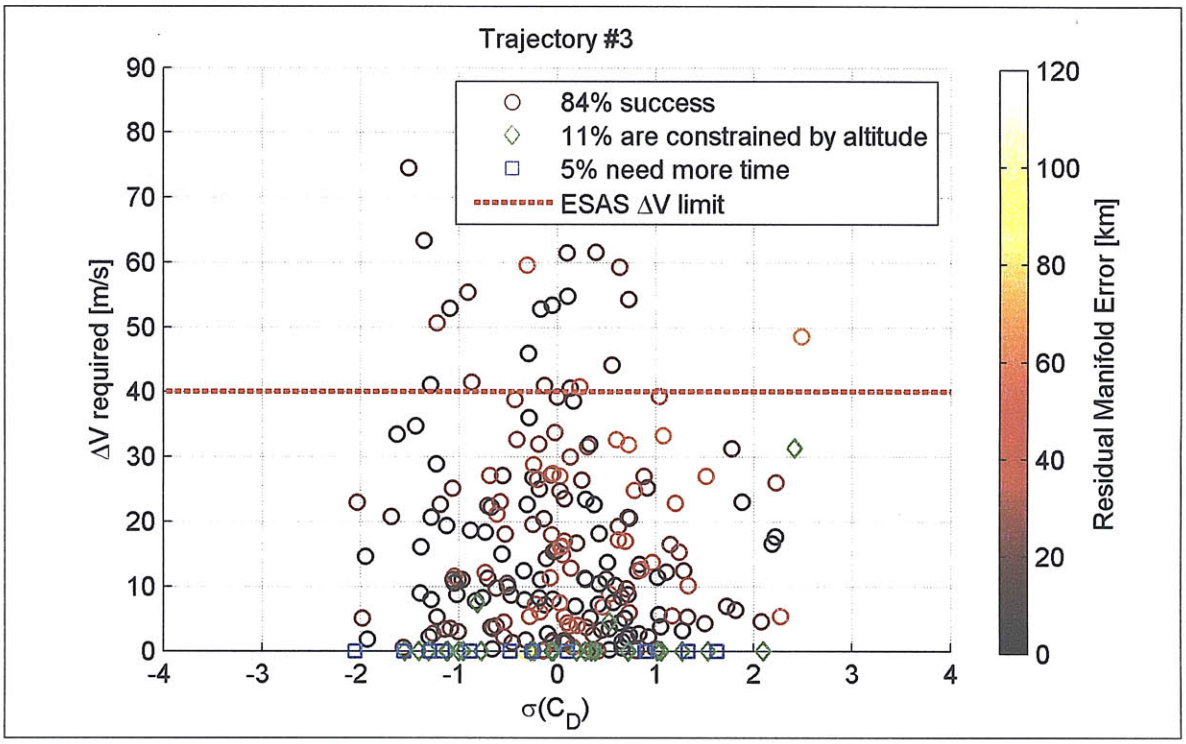

(c) Trajectory #3

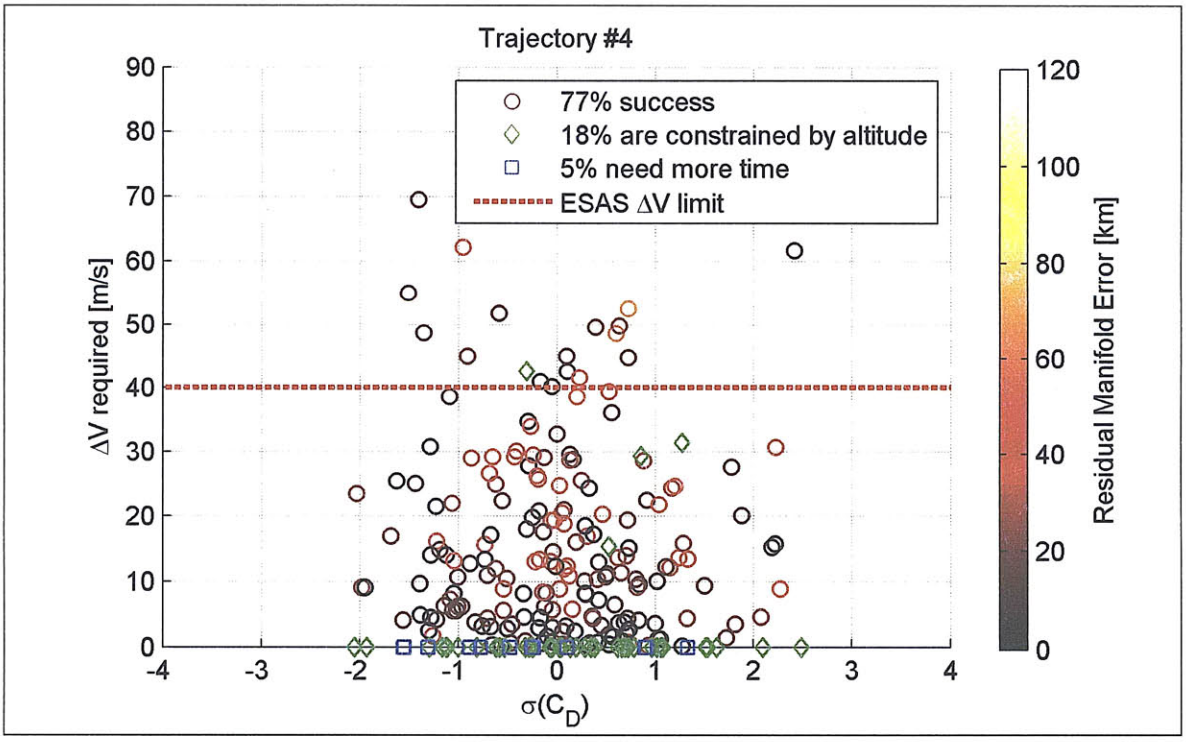

(d) Trajectory #4

Figure B-4: Scatter of ΔV required for a dispersed drag coefficient (cont'd)

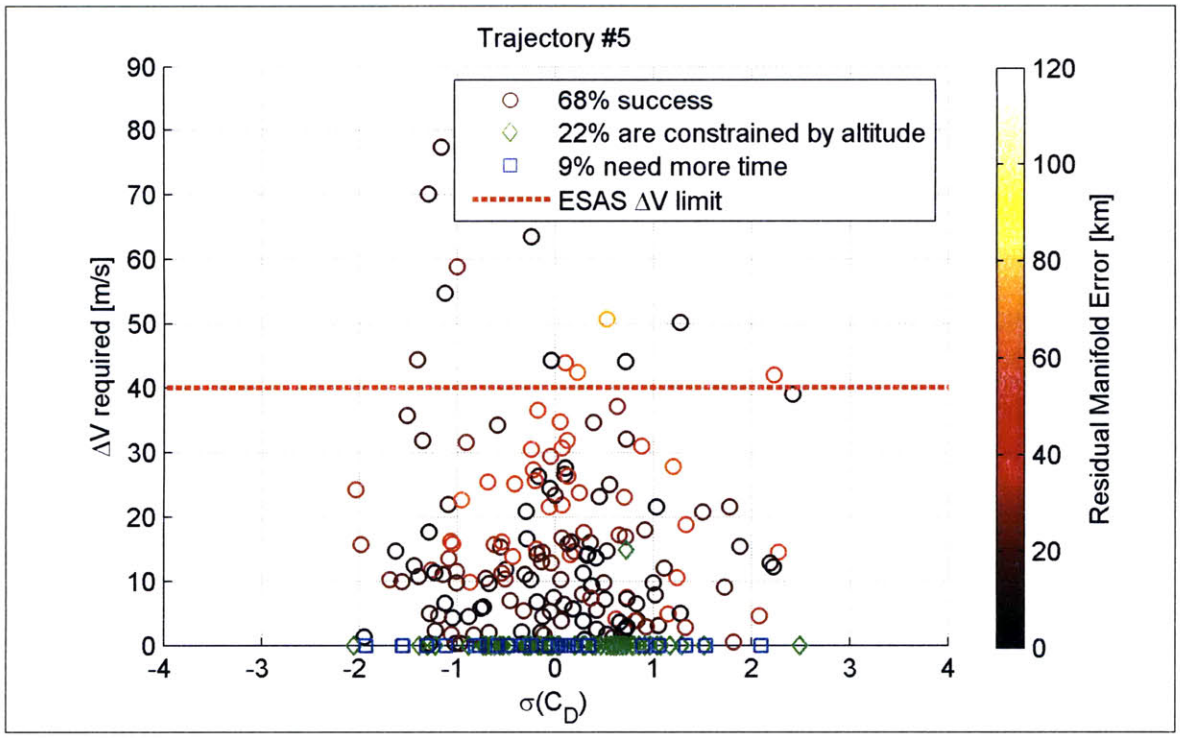

(e) Trajectory #5

Figure B-4: Scatter of ΔV required for a dispersed drag coefficient (cont'd)

B.1.5 Thruster Force

The thruster force was perturbed using a multiplier with a 3σ value of 3 percent.

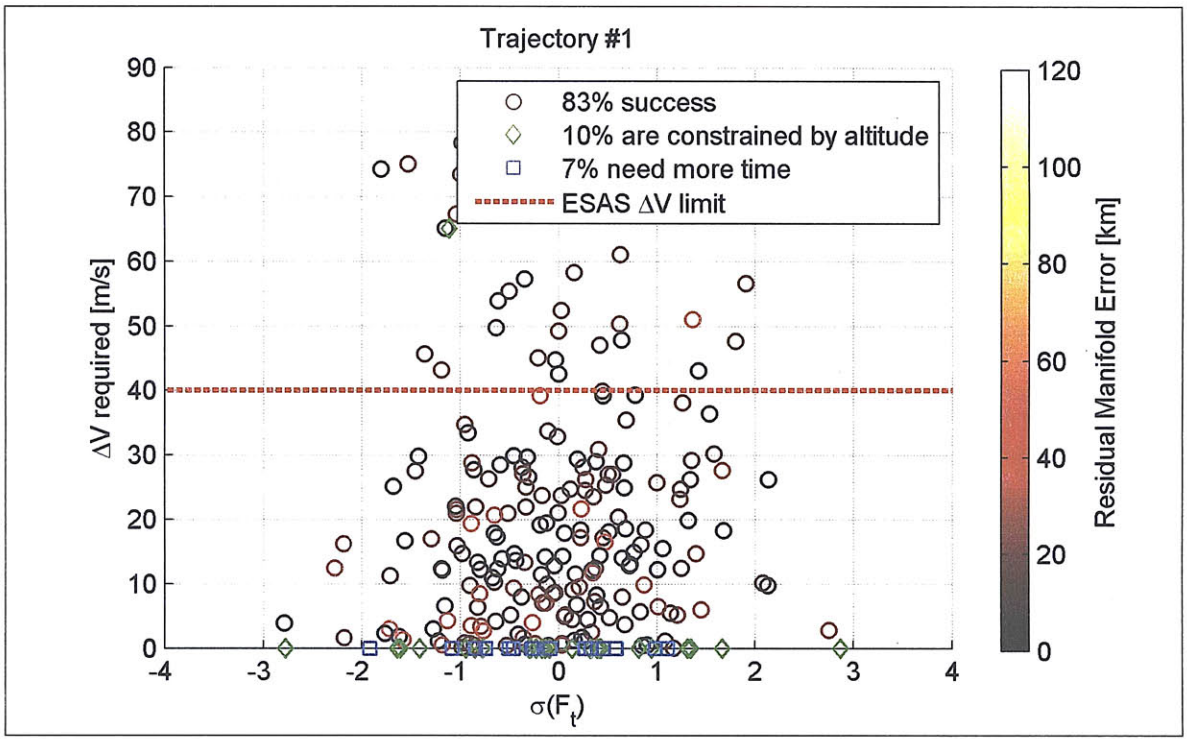

(a) Trajectory #1

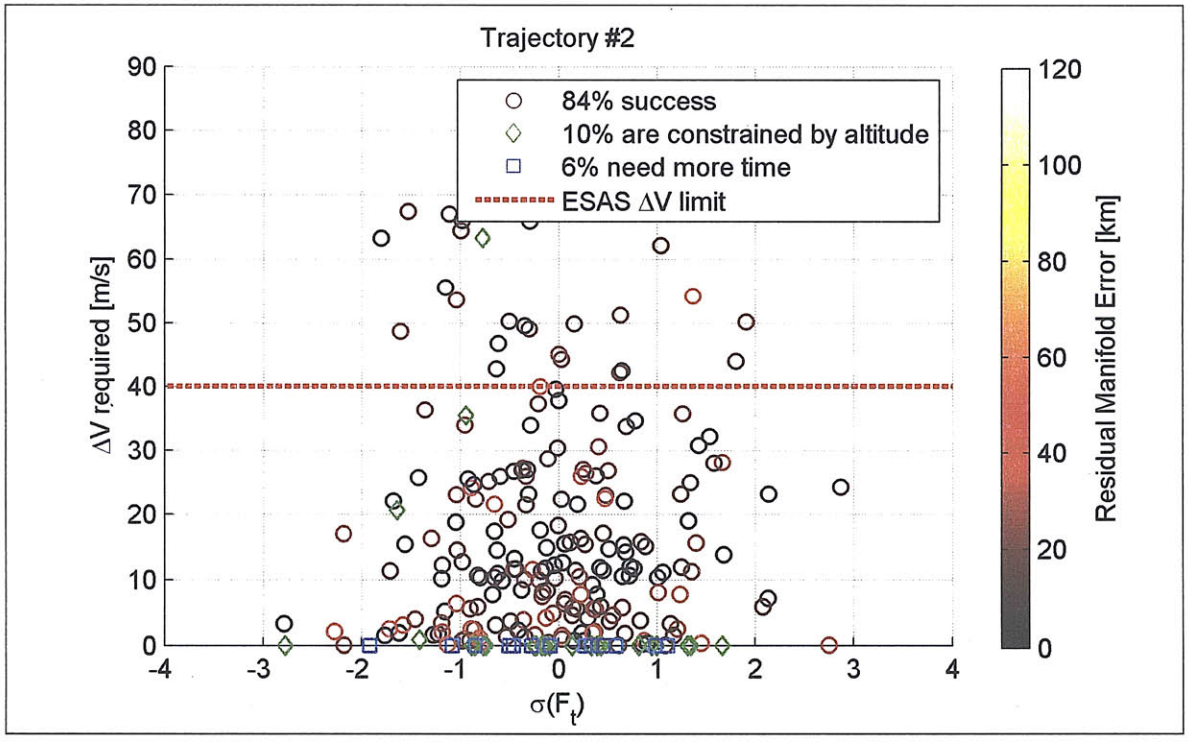

(b) Trajectory #2

Figure B-5: Scatter of ΔV required for a dispersed thruster force

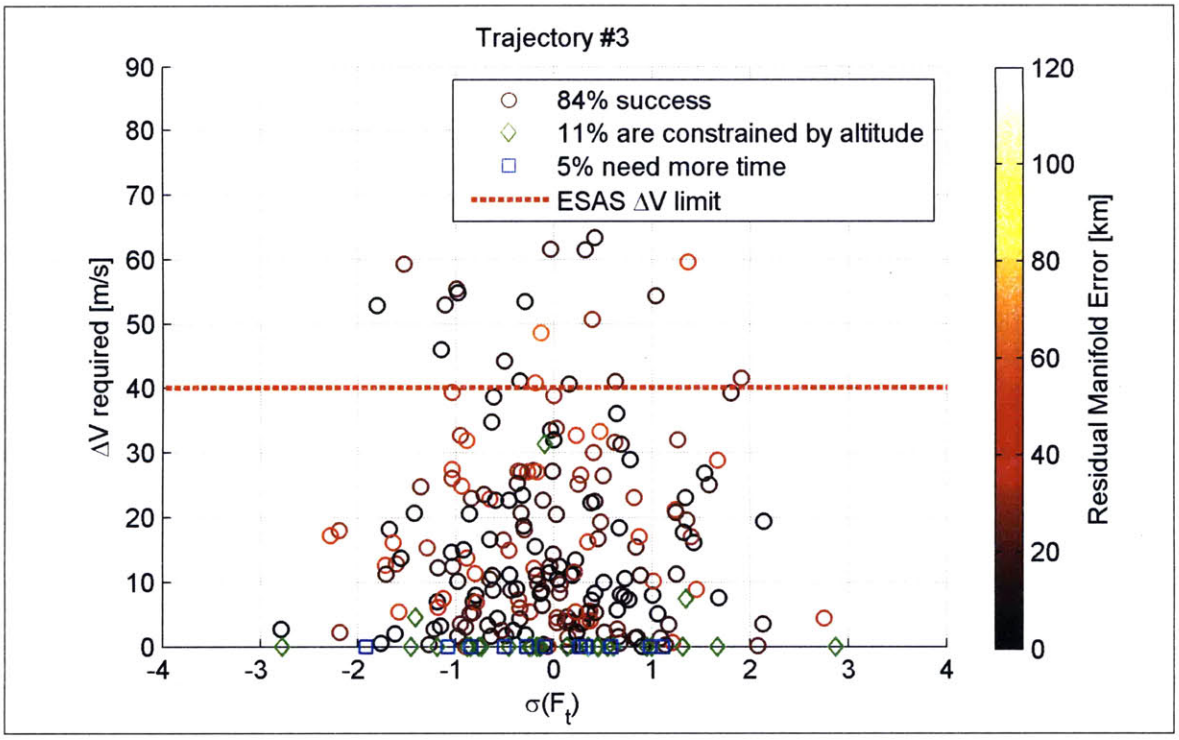

(c) Trajectory #3

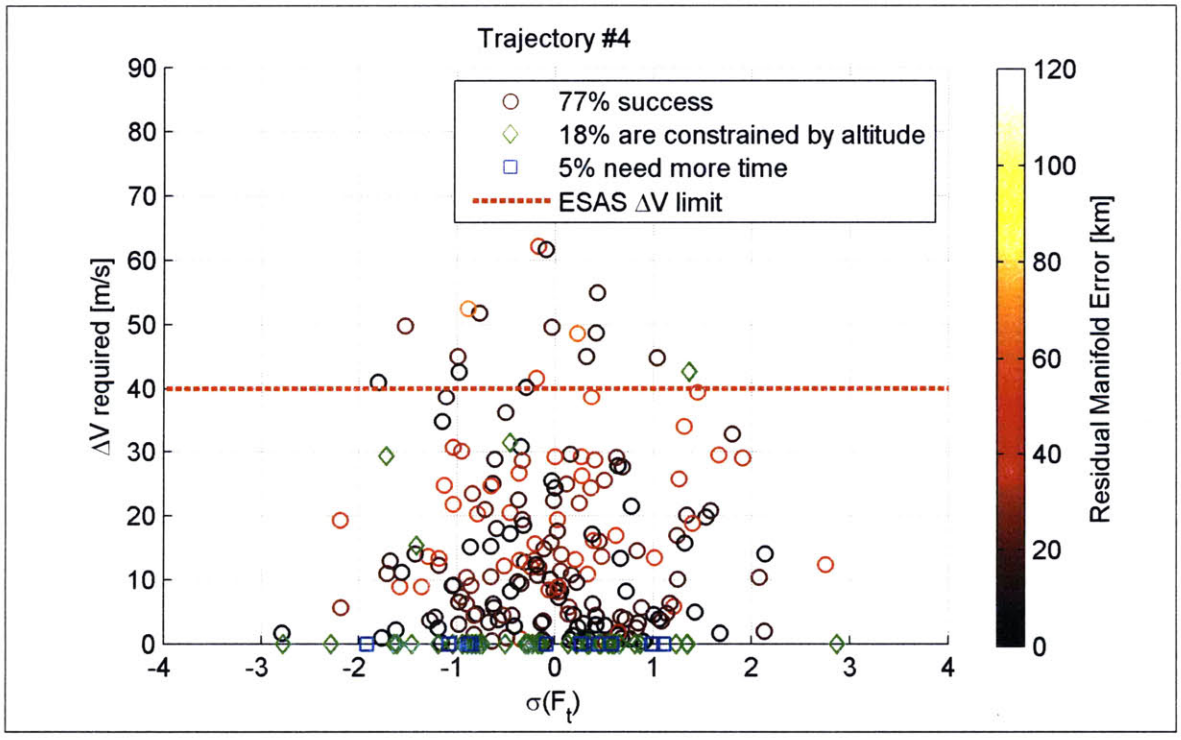

(d) Trajectory #4

Figure B-5: Scatter of ΔV required for a dispersed thruster force (cont'd)

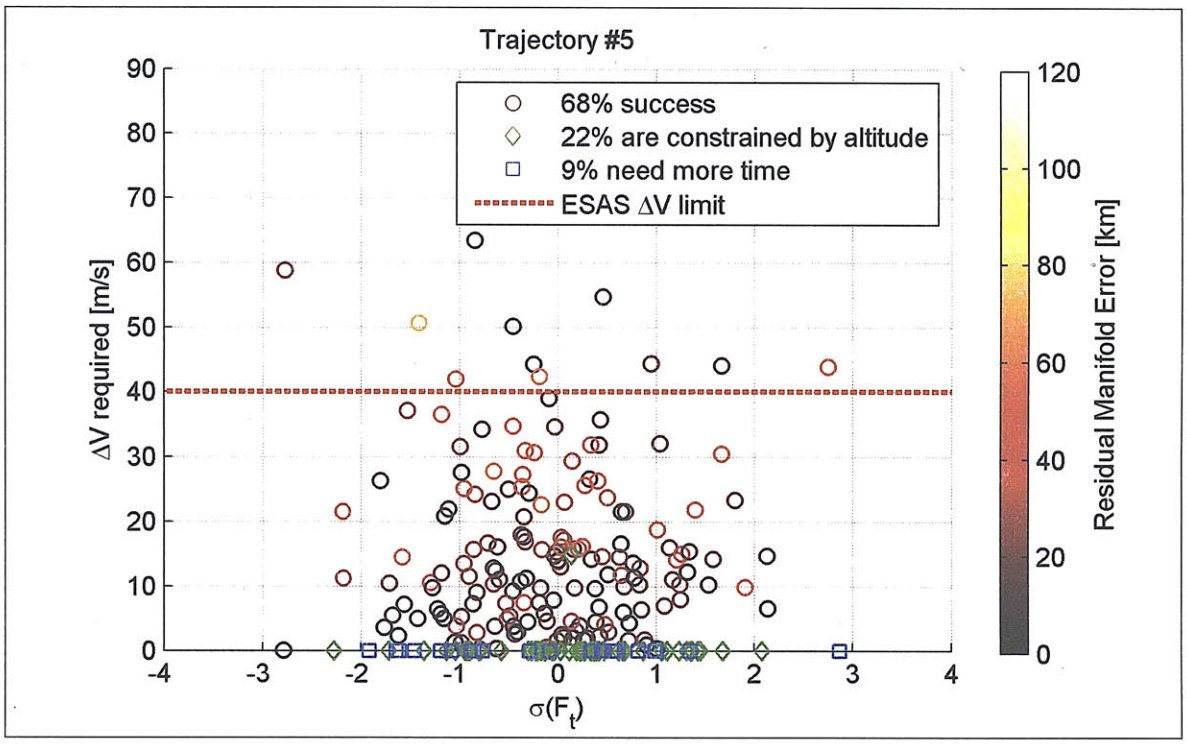

(e) Trajectory #5

Figure B-5: Scatter of ΔV required for a dispersed thruster force (cont'd)

B.1.6 Initial Velocity

The initial velocity was perturbed by using a mean value of those found in Table 3.1 for each respective trajectory with a 3σ value of 225 $^{m}/_{s}$.

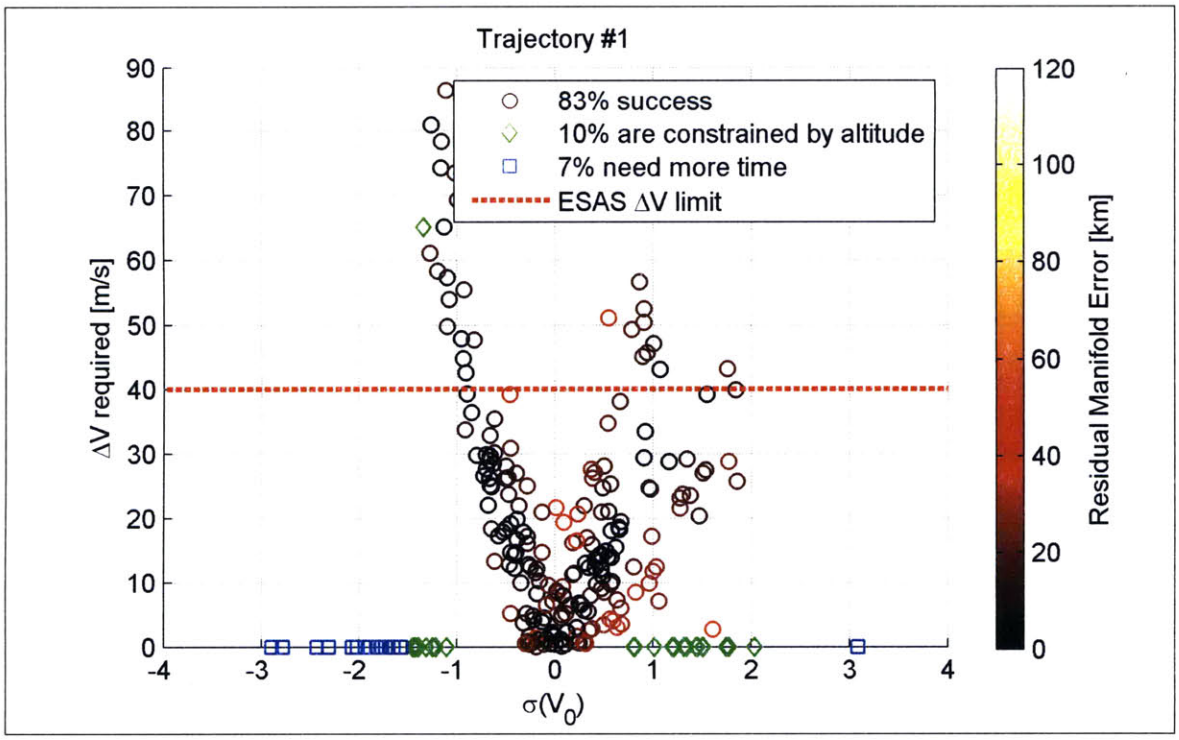

(a) Trajectory #1

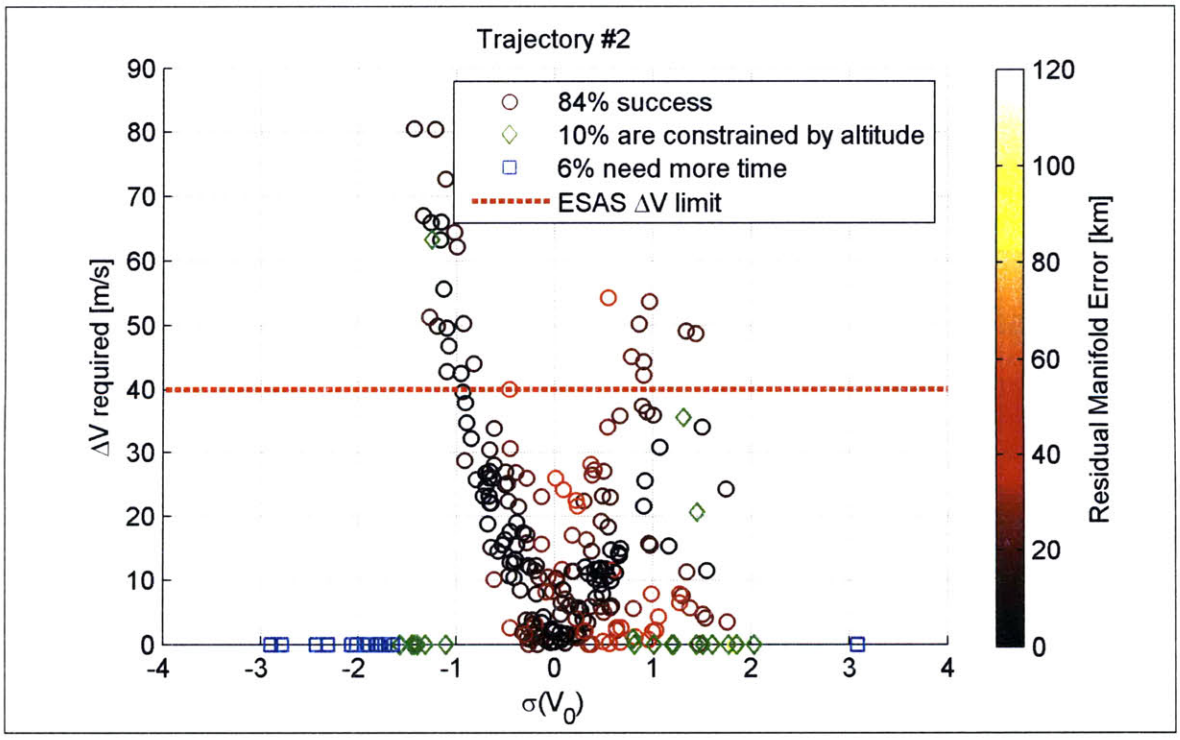

(b) Trajectory #2

Figure B-6: Scatter of ΔV required for a dispersed initial velocity

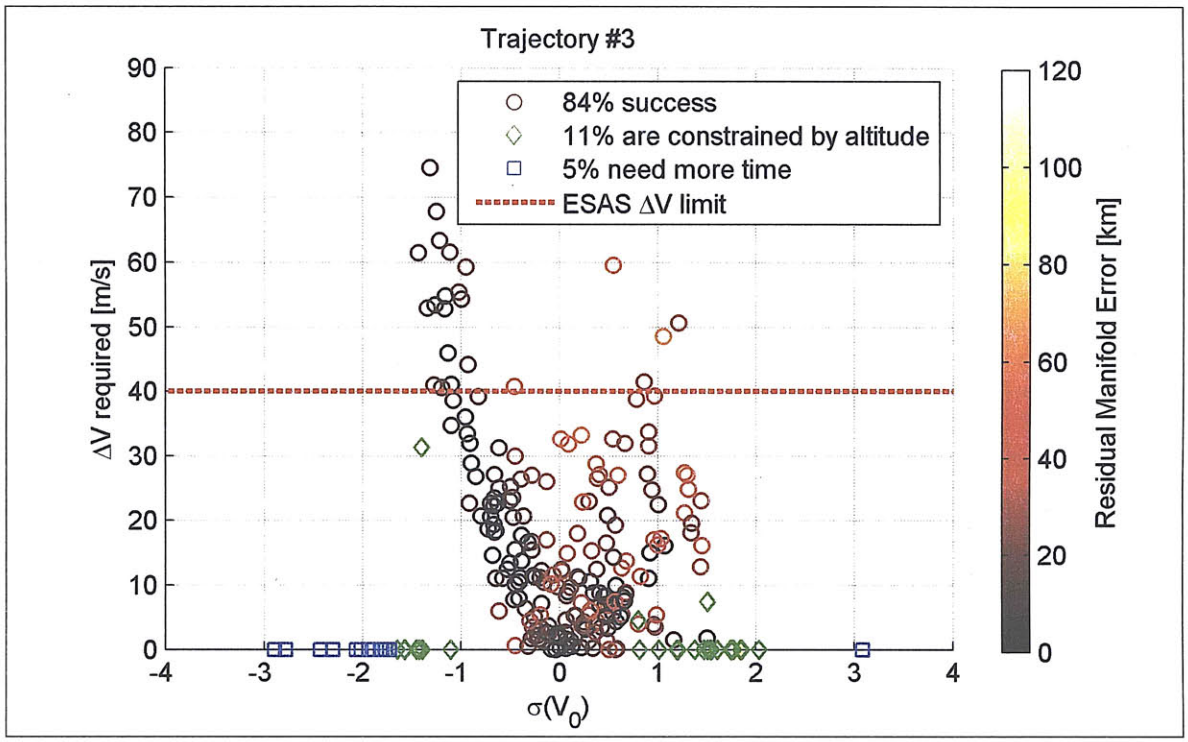

(c) Trajectory #3

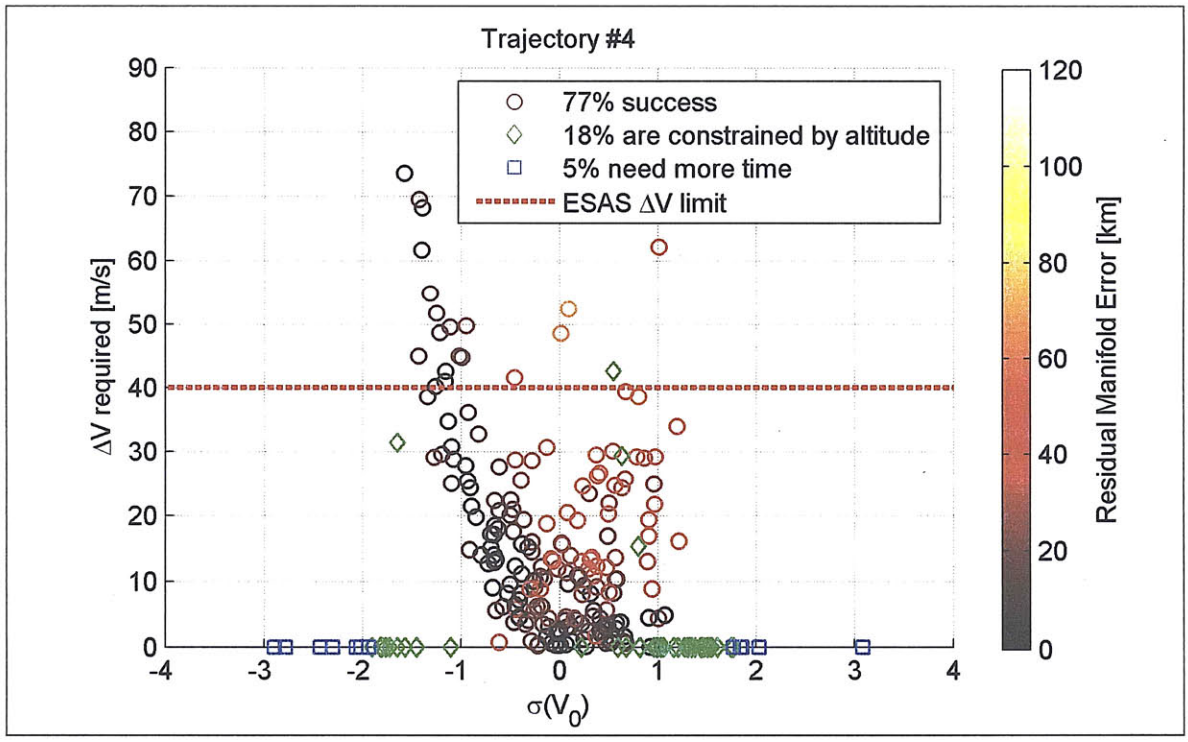

(d) Trajectory #4

Figure B-6: Scatter of ΔV required for a dispersed initial velocity (cont'd)

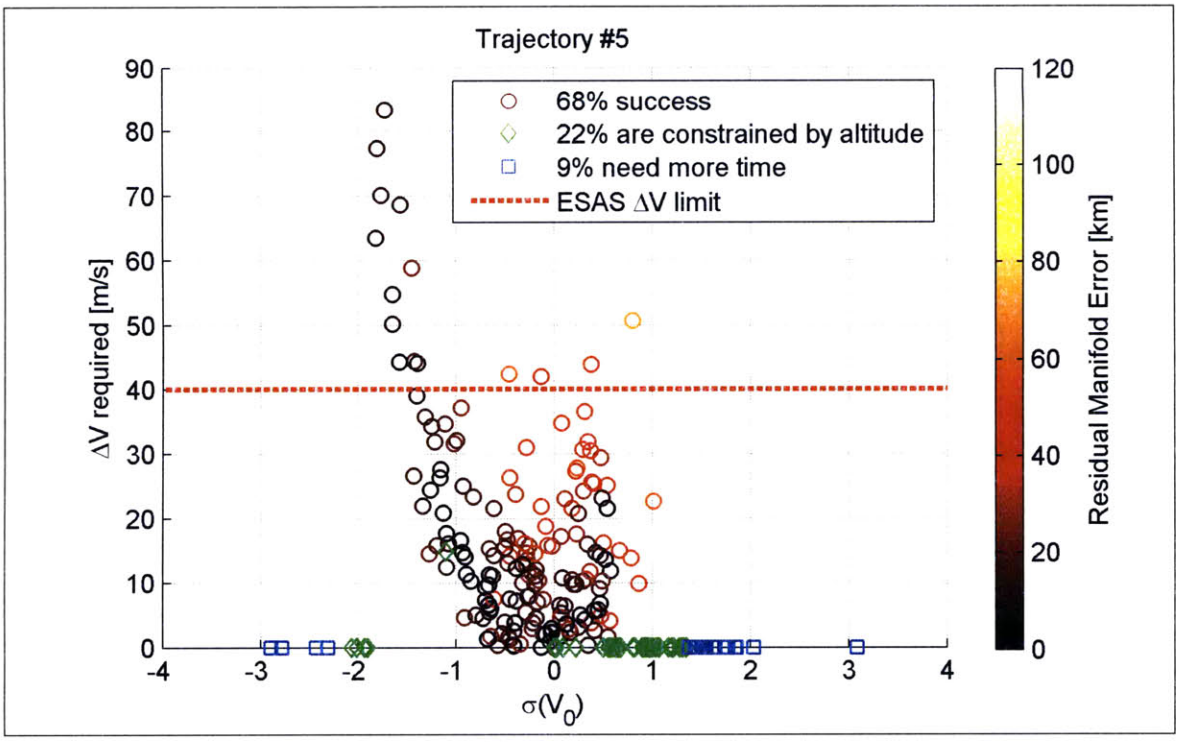

(e) Trajectory #5

Figure B-6: Scatter of ΔV required for a dispersed initial velocity(cont'd)

B.2 Residual Manifold Targeting Error

The following figures show the relationship between the perturbed variable and the residual manifold targeting errors.

B.2.1 Atmospheric Density

The atmospheric density was perturbed using a multiplier with a 3σ value of 30 percent.

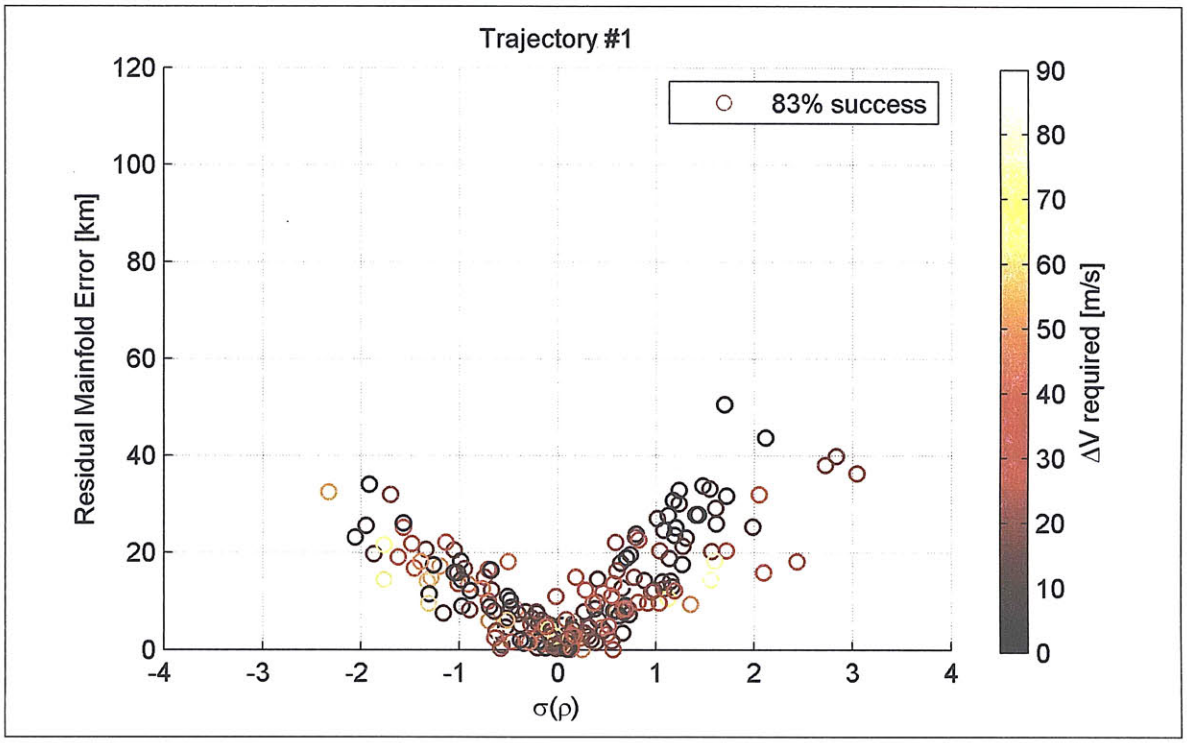

(a) Trajectory #1

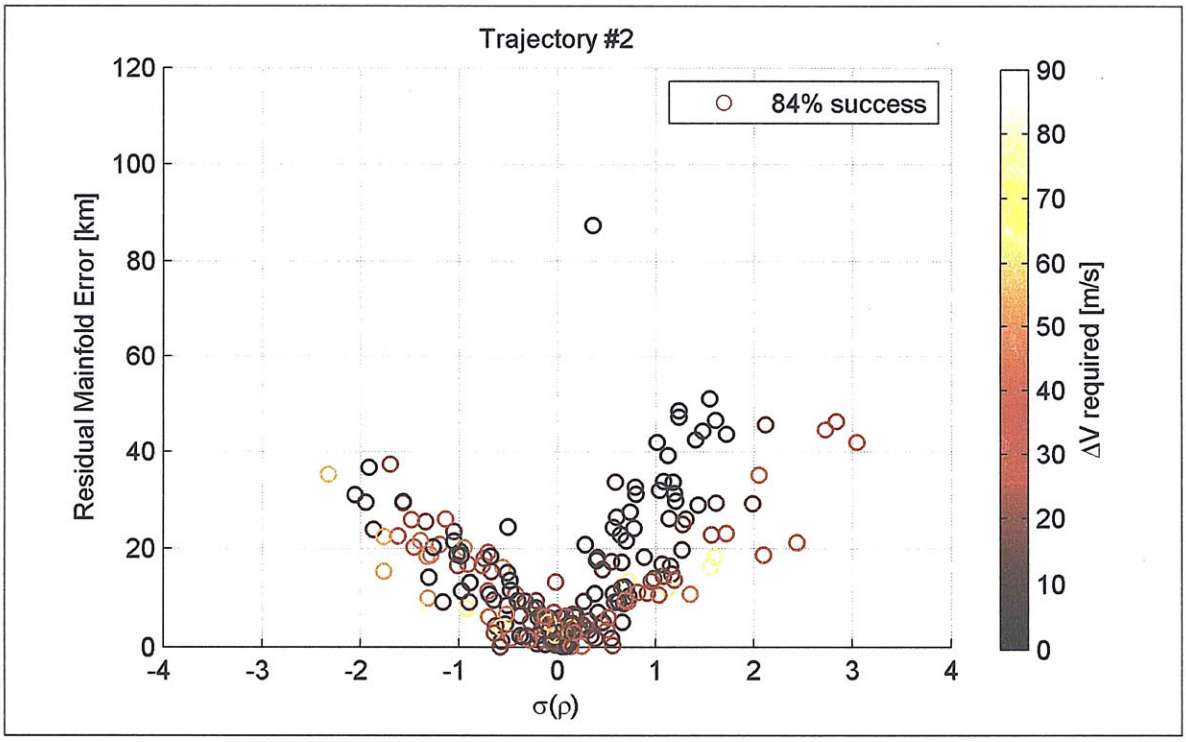

(b) Trajectory #2

Figure B-7: Scatter of residual error for a dispersed atmospheric density

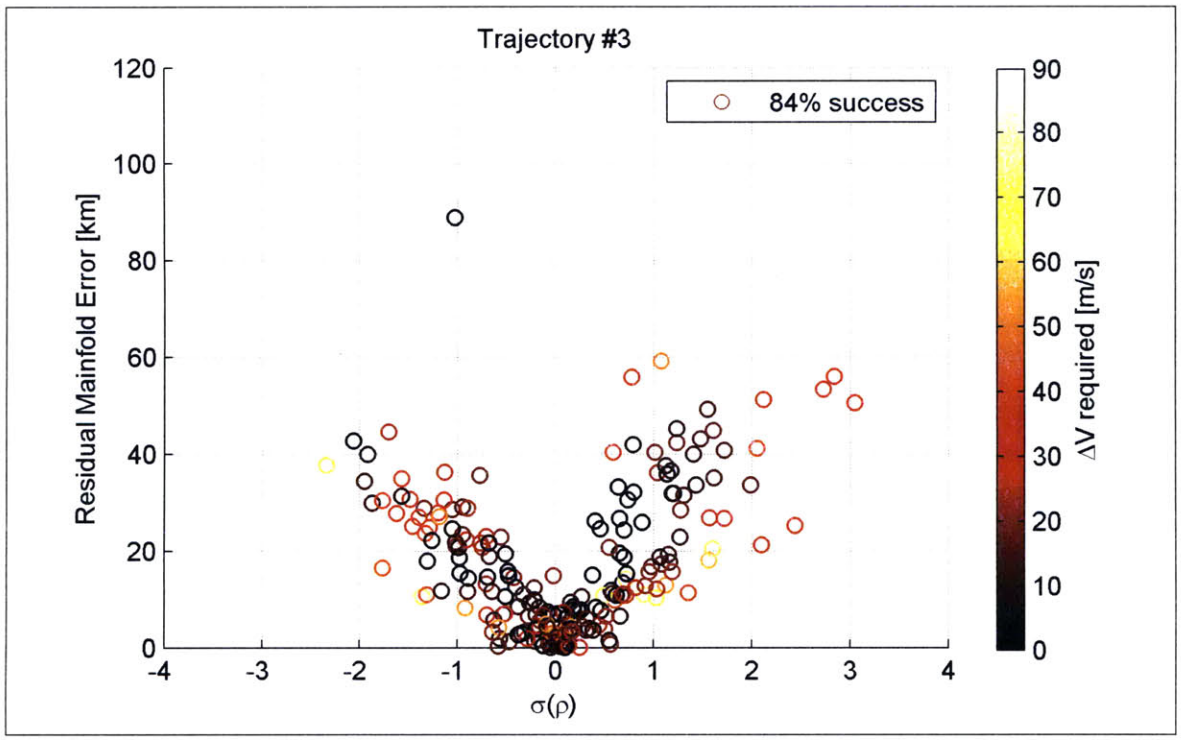

(c) Trajectory #3

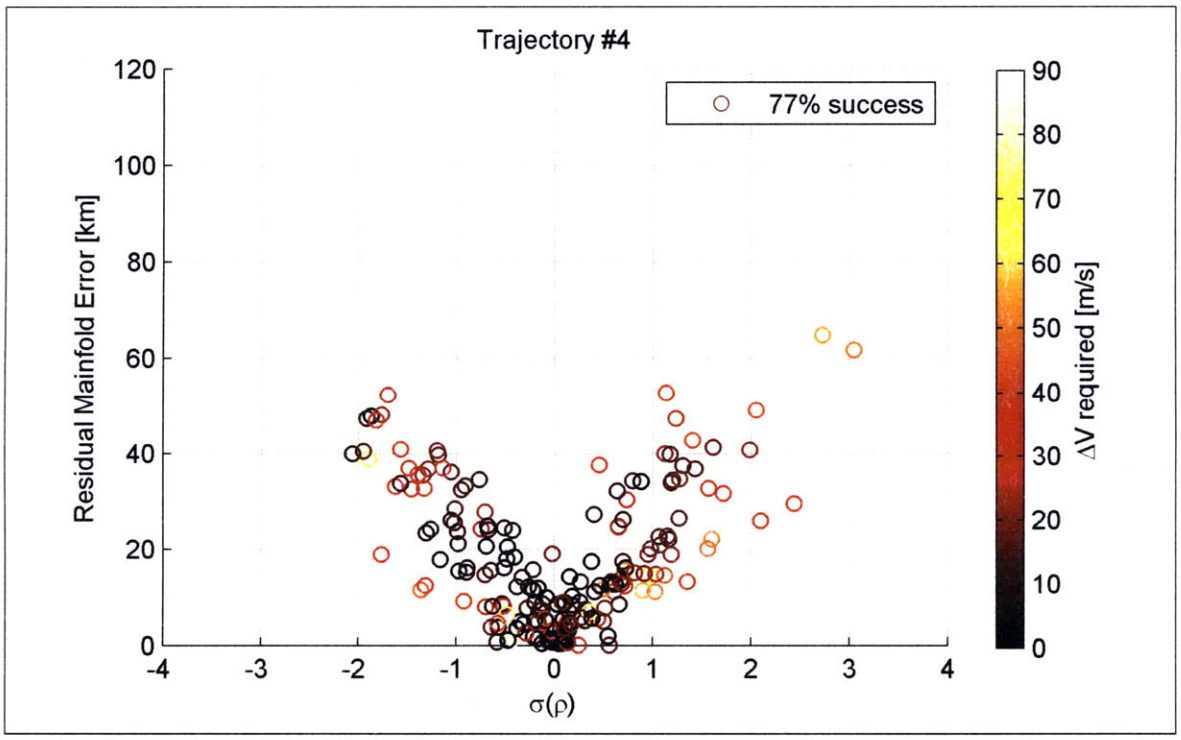

(d) Trajectory #4

Figure B-7: Scatter of residual error for a dispersed atmospheric density (cont'd)

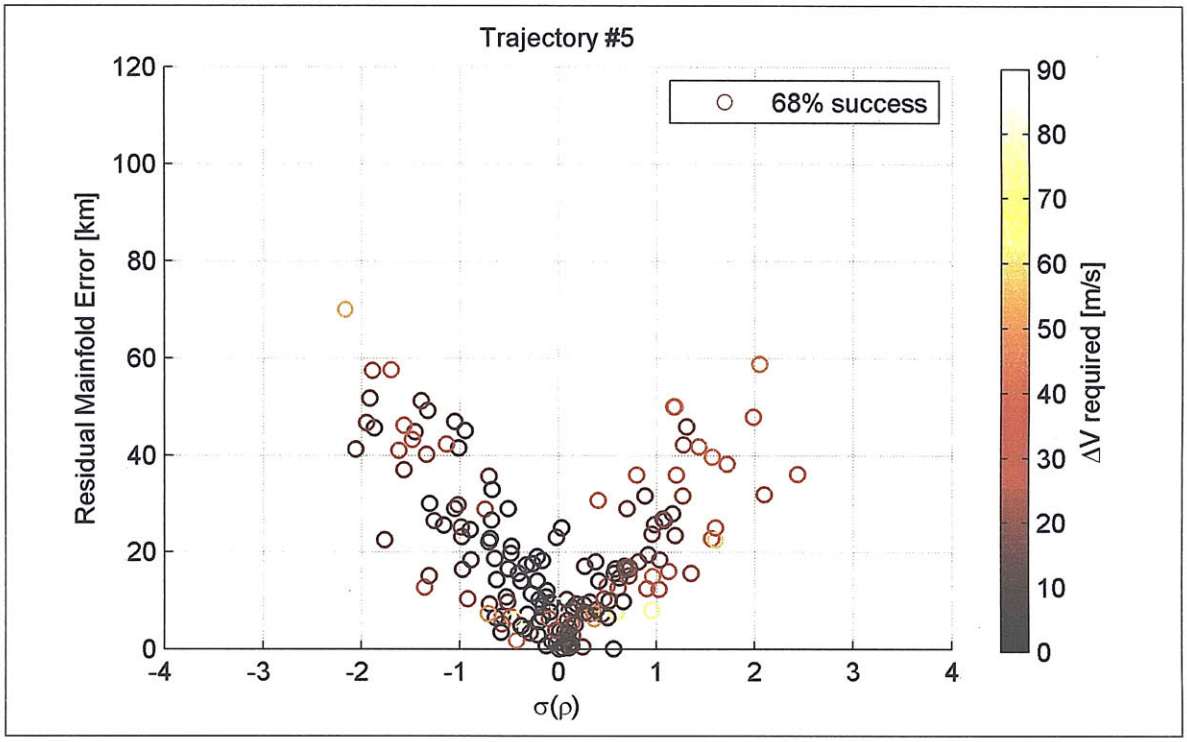

(e) Trajectory #5

Figure B-7: Scatter of residual error for a dispersed atmospheric density (cont'd)

B.2.2 Spacecraft Mass

The spacecraft mass was perturbed using a multiplier with a 3σ value of 5 percent.

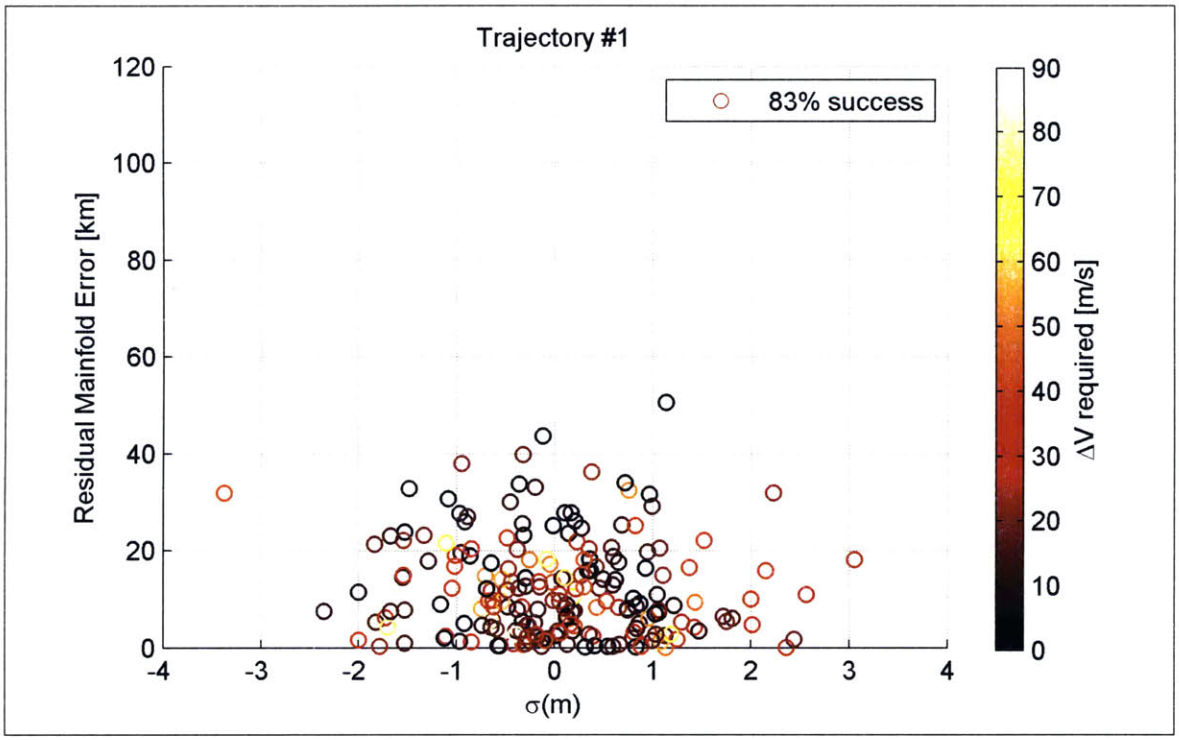

(a) Trajectory #1

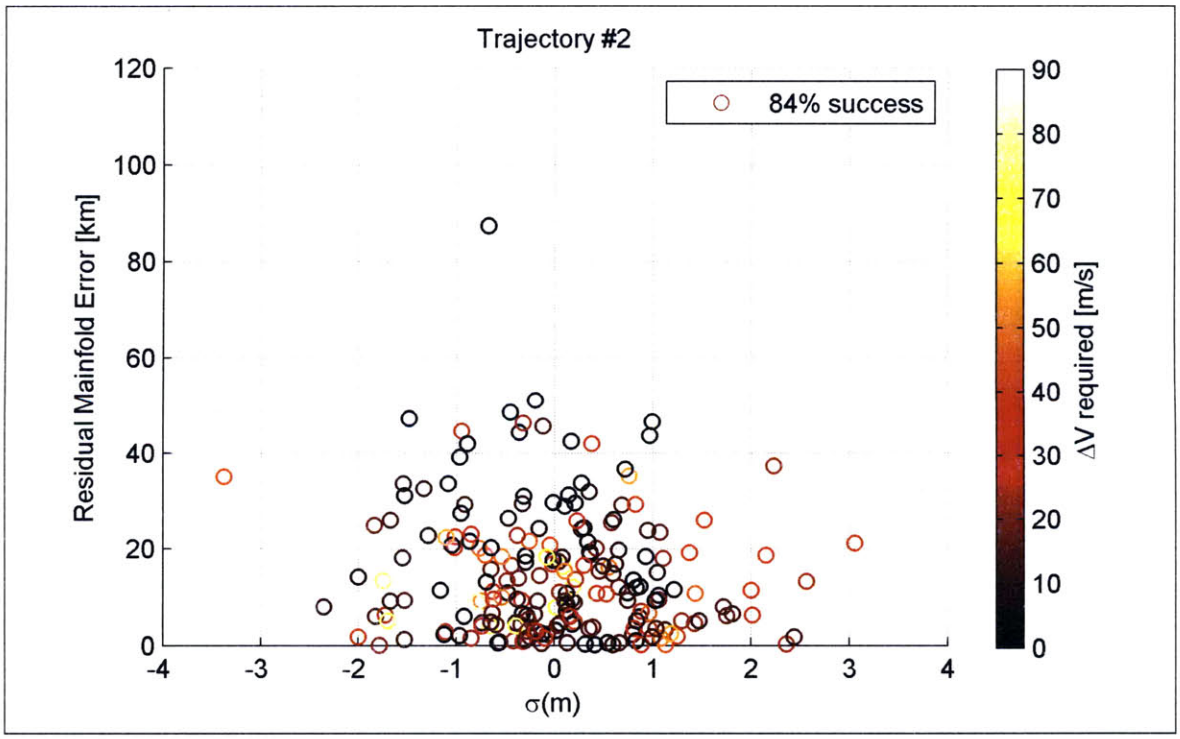

(b) Trajectory #2

Figure B-8: Scatter of residual error for a dispersed spacecraft mass

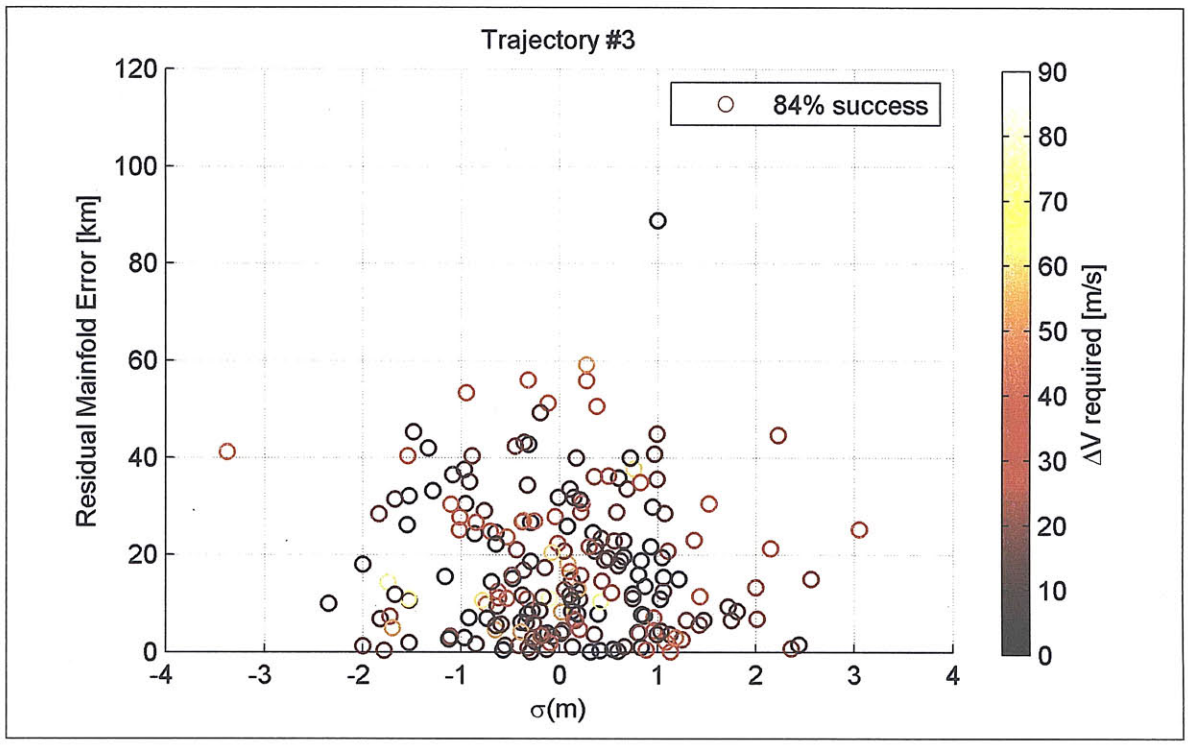

(c) Trajectory #3

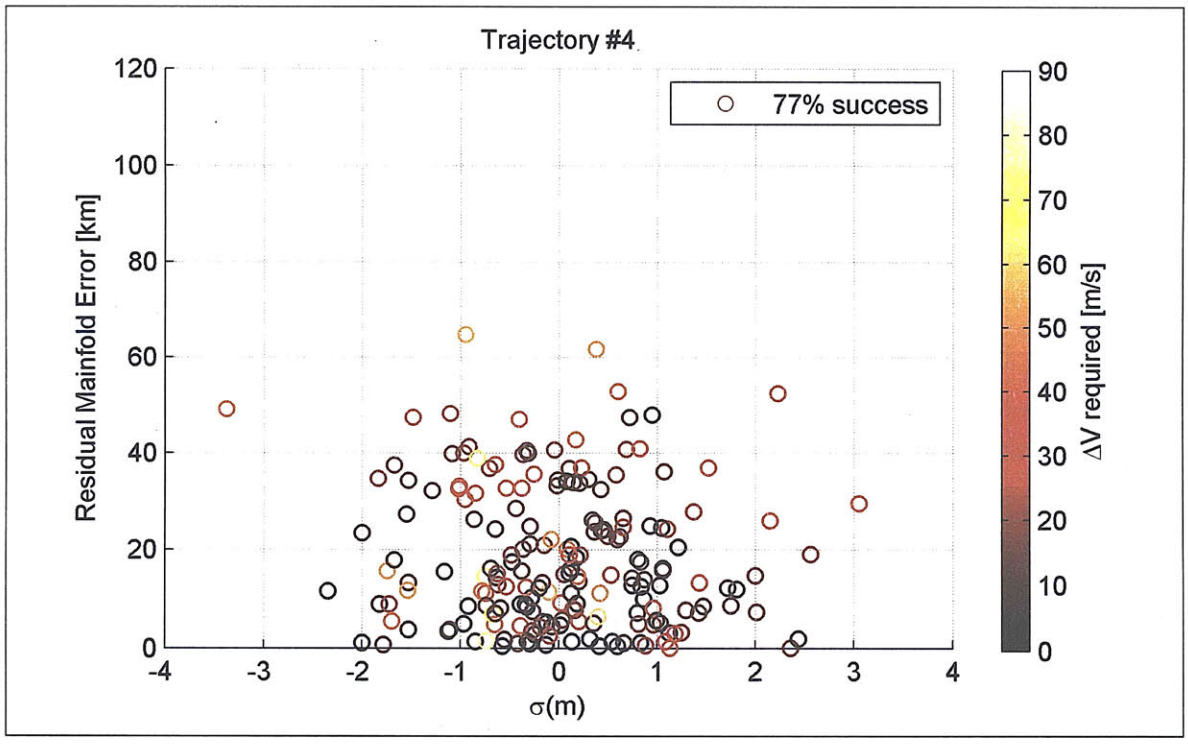

(d) Trajectory #4

Figure B-8: Scatter of residual error for a dispersed spacecraft mass (cont'd)

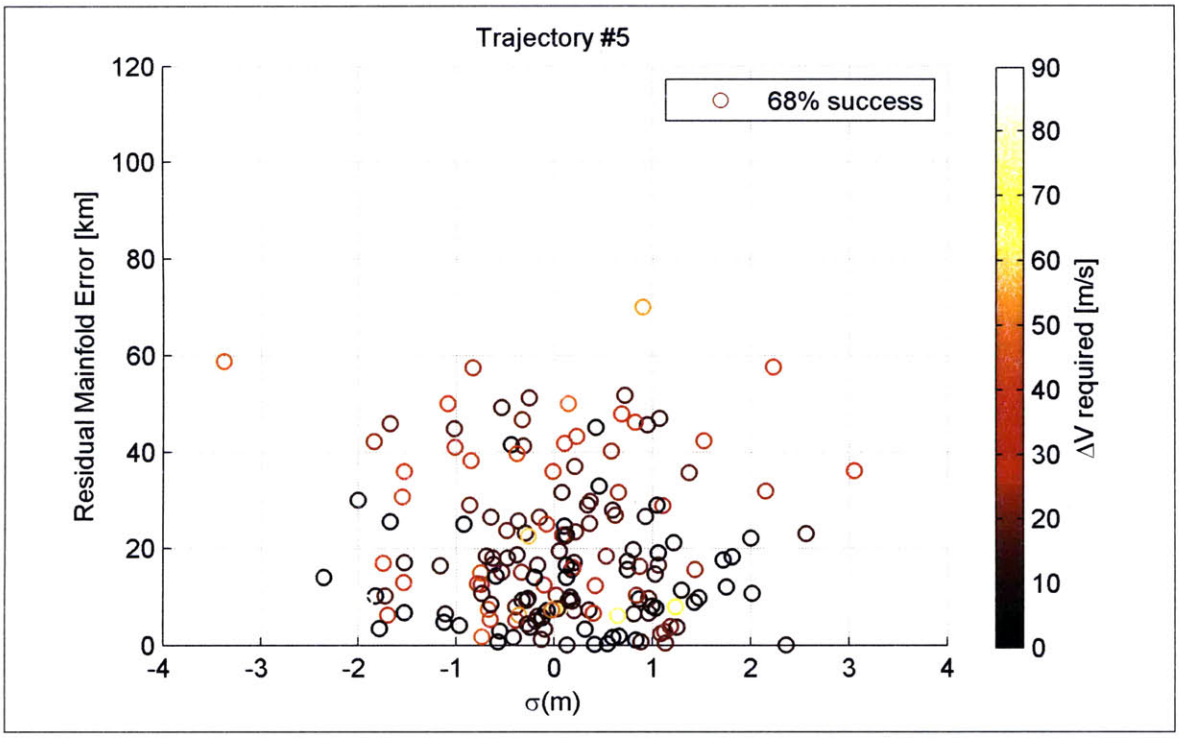

(e) Trajectory #5

Figure B-8: Scatter of residual error for a dispersed spacecraft mass (cont'd)

B.2.3 Spacecraft Lift Coefficient

The spacecraft lift coefficient was perturbed using a multiplier with a 3σ value of 10 percent.

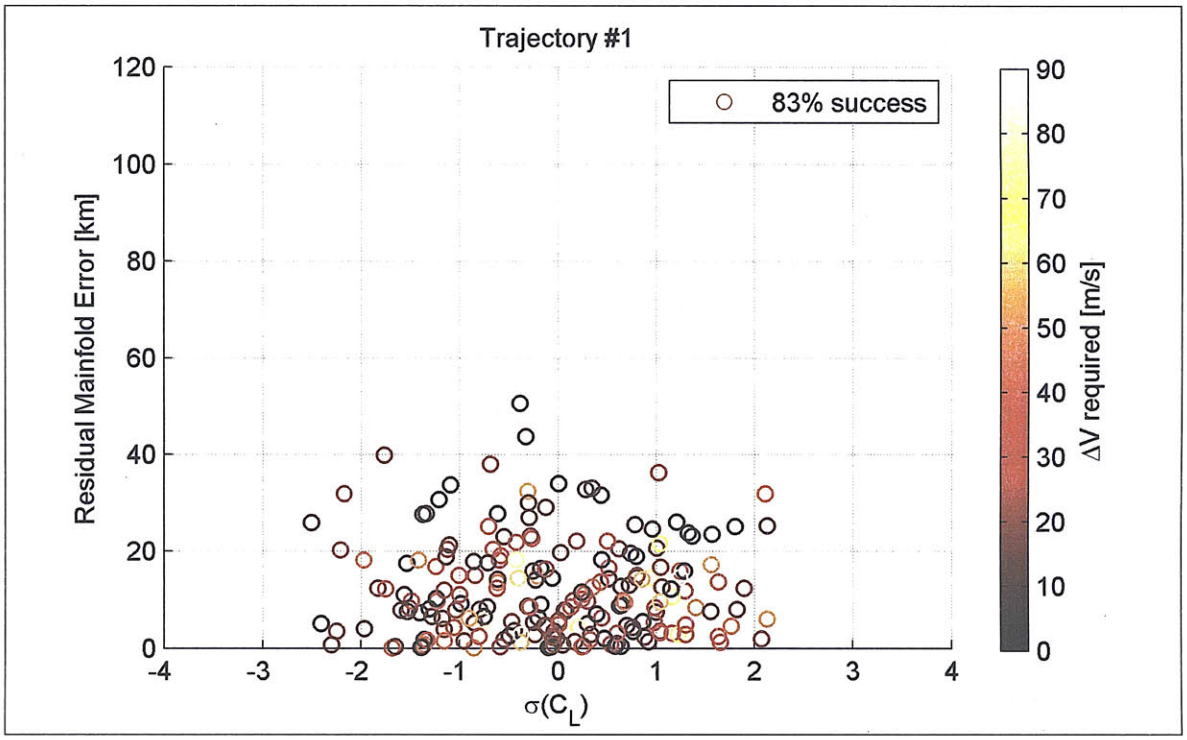

(a) Trajectory #1

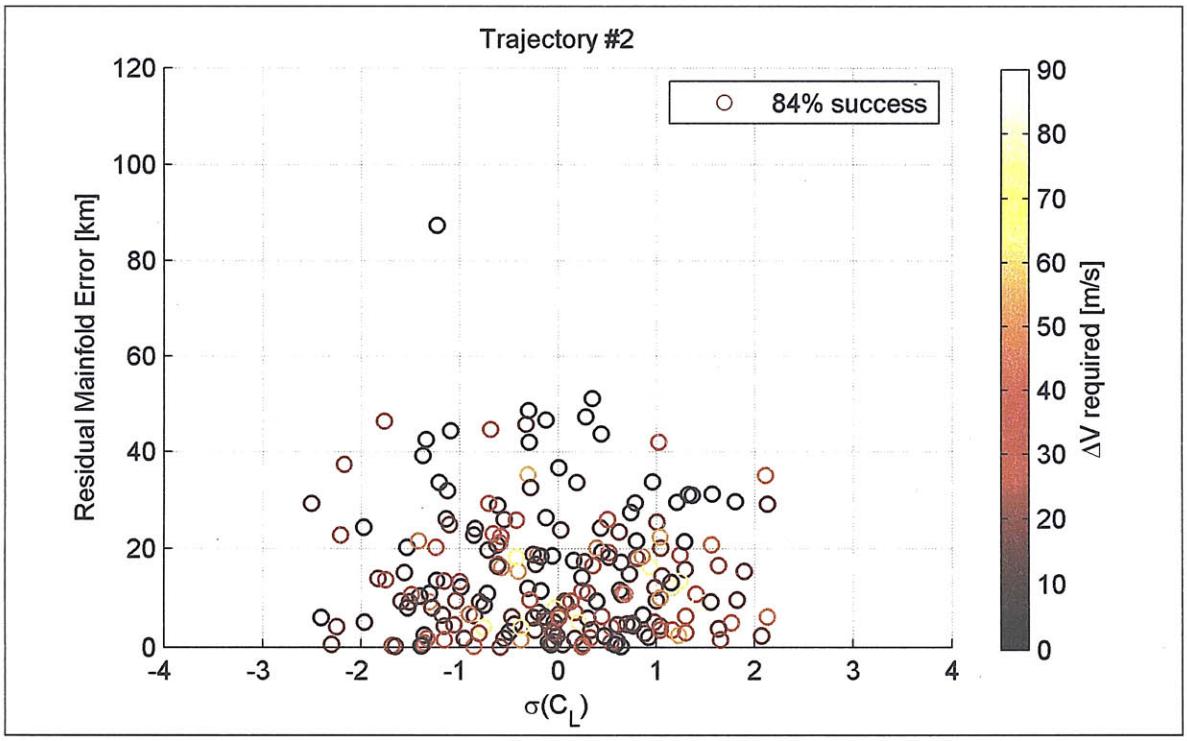

(b) Trajectory #2

Figure B-9: Scatter of residual error for a dispersed lift coefficient

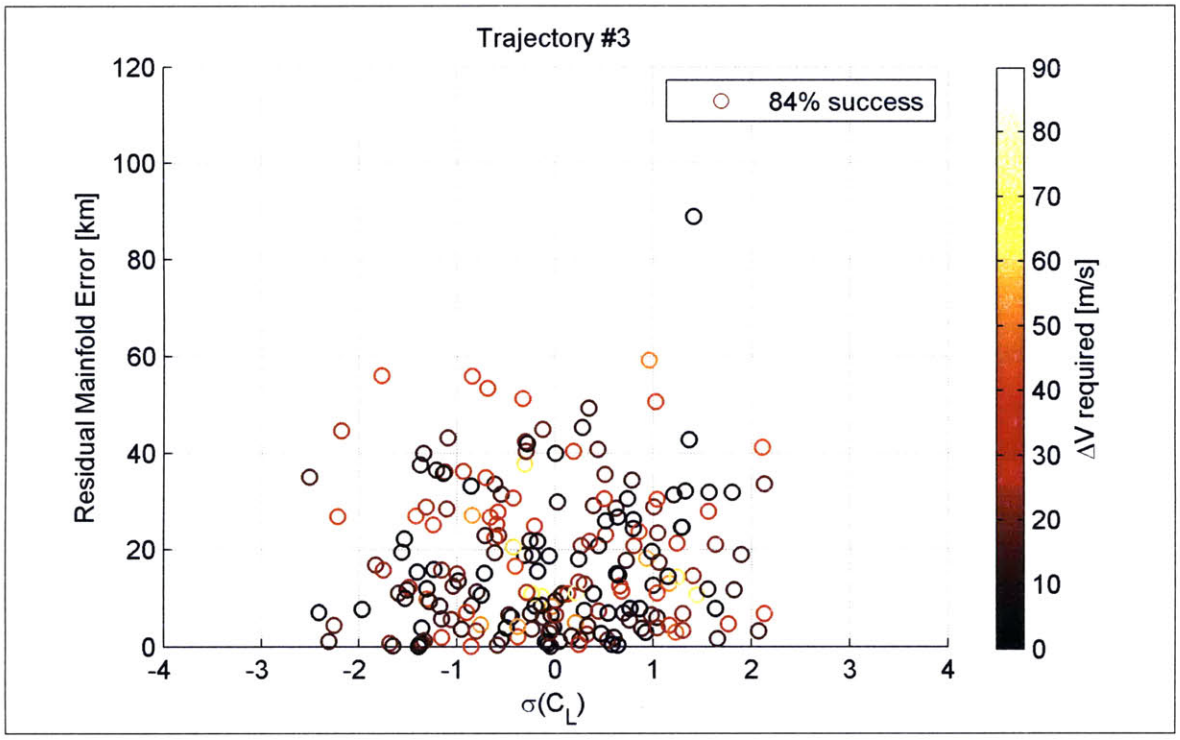

(c) Trajectory #3

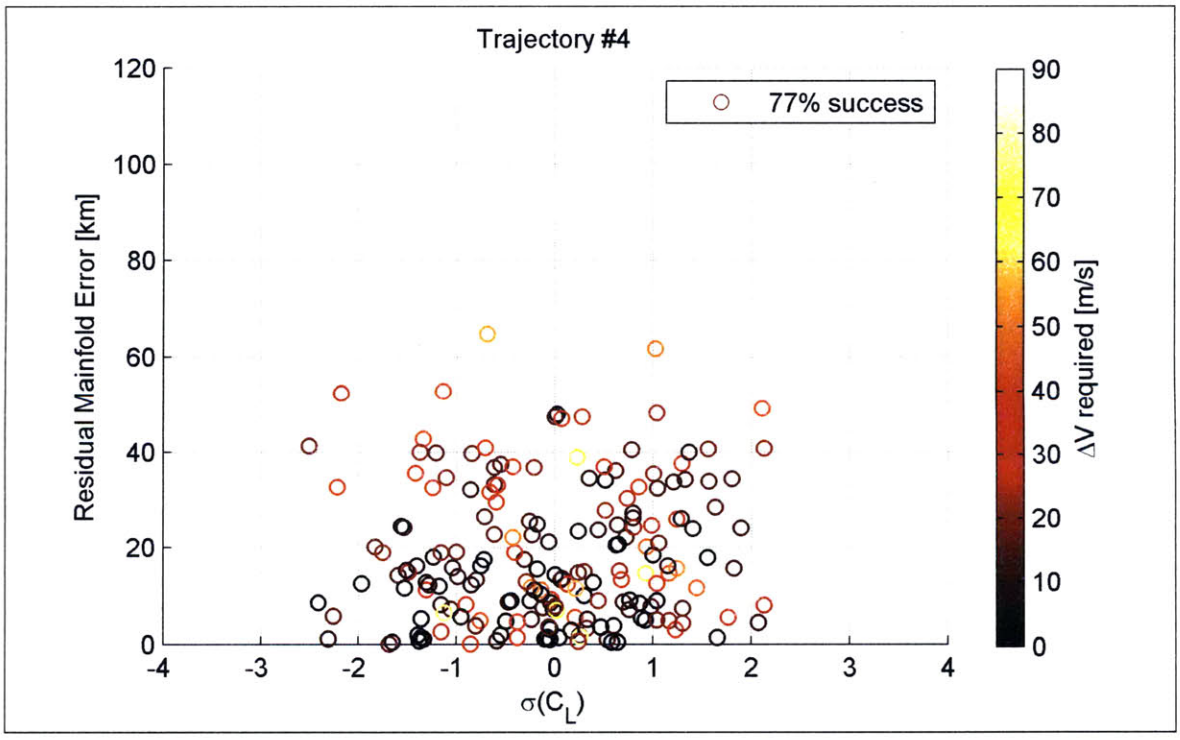

(d) Trajectory #4

Figure B-9: Scatter of residual error for a dispersed lift coefficient (cont'd)

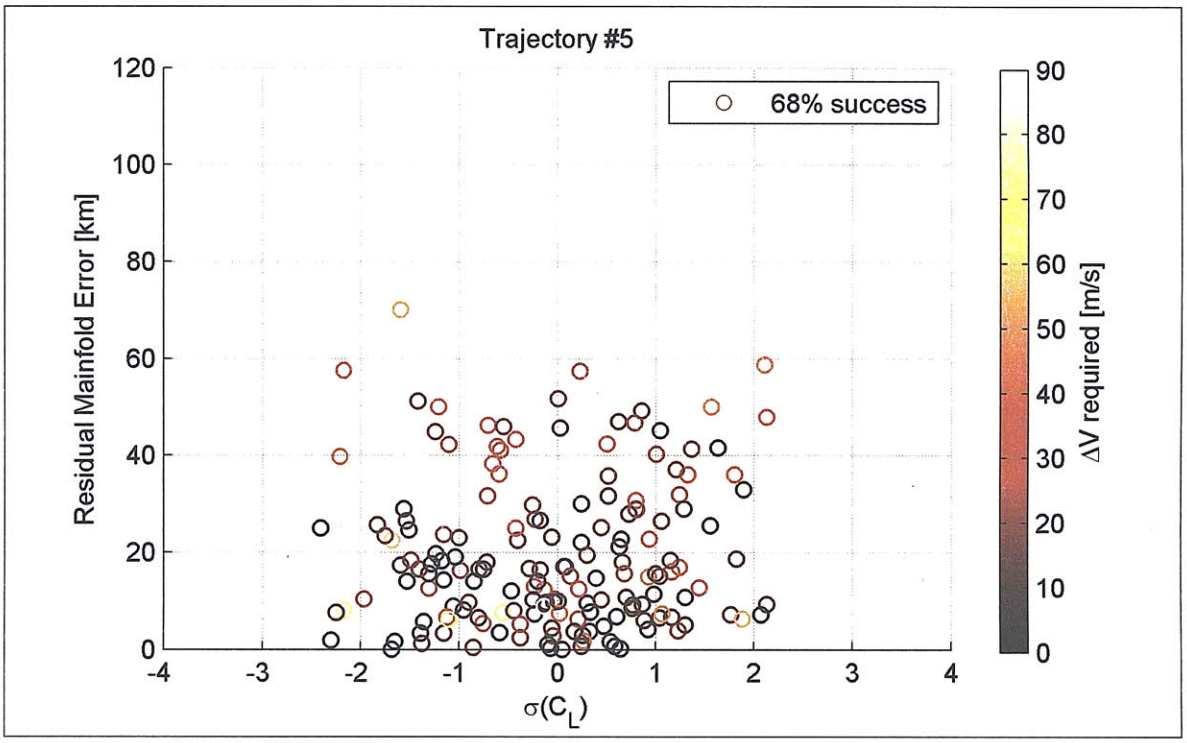

(e) Trajectory #5

Figure B-9: Scatter of residual error for a dispersed lift coefficient (cont'd)

B.2.4 Spacecraft Drag Coefficient

The spacecraft drag coefficient was perturbed using a multiplier with a 3σ value of 10 percent.

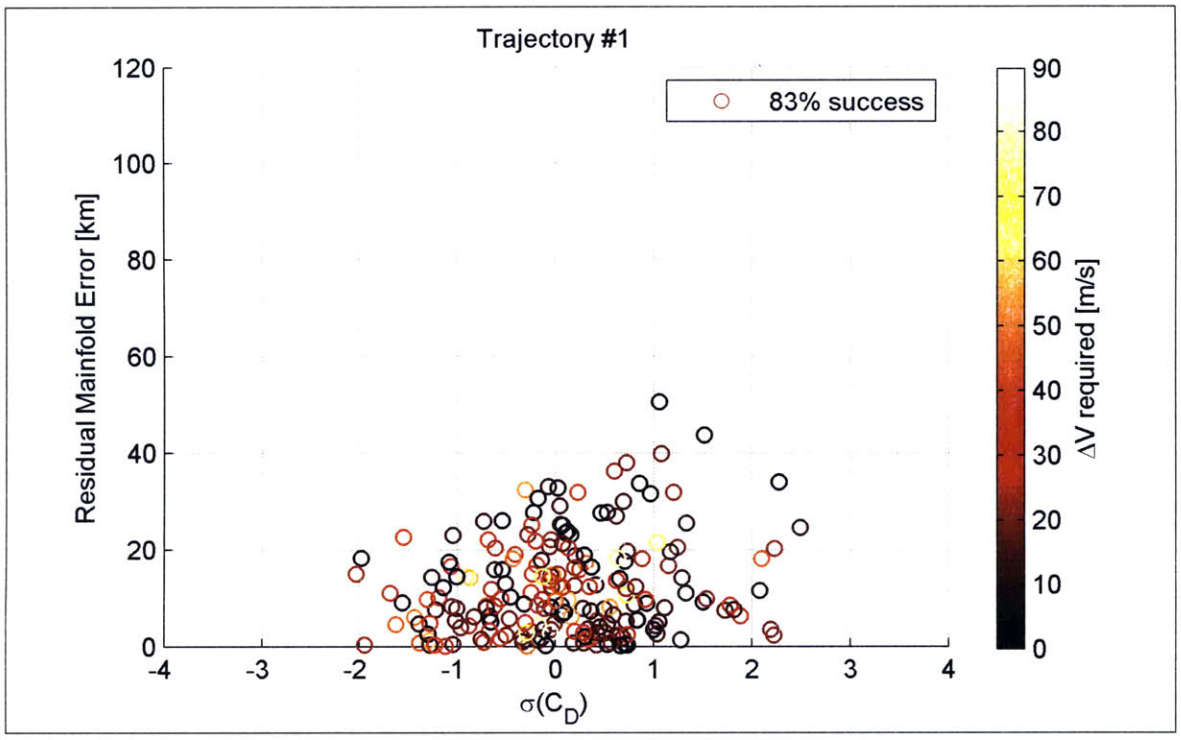

(a) Trajectory #1

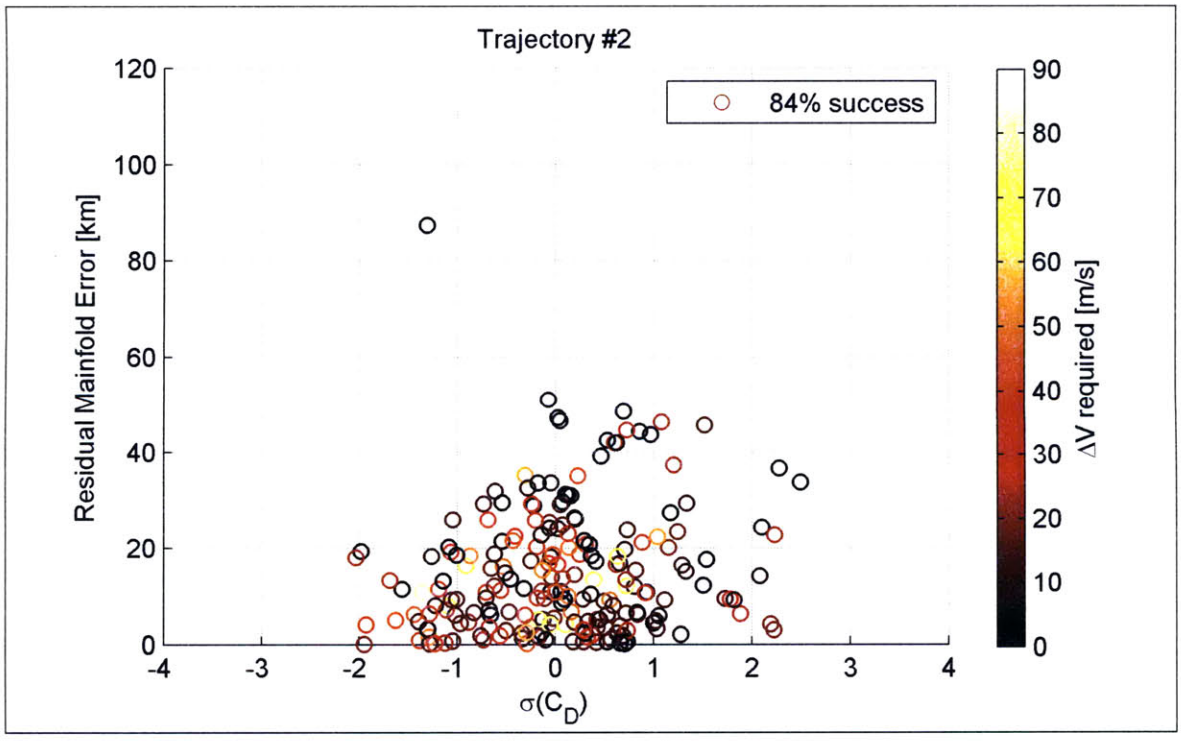

(b) Trajectory #2

Figure B-10: Scatter of residual error for a dispersed drag coefficient

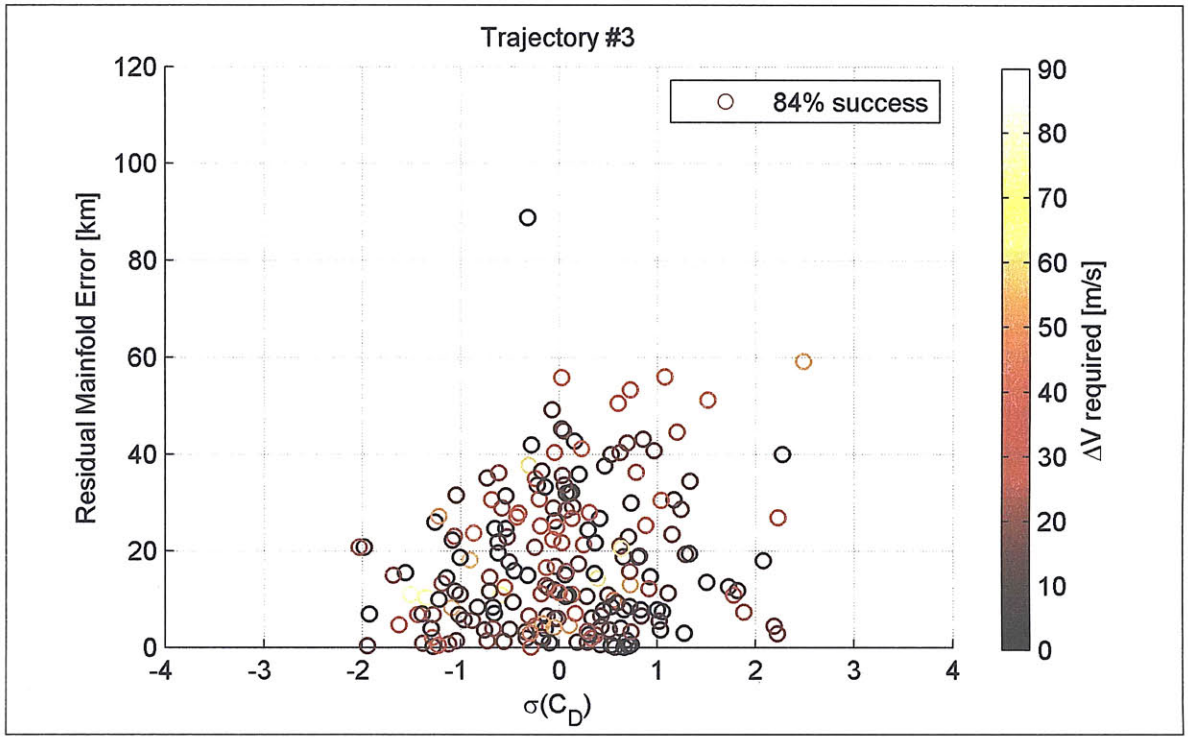

(c) Trajectory #3

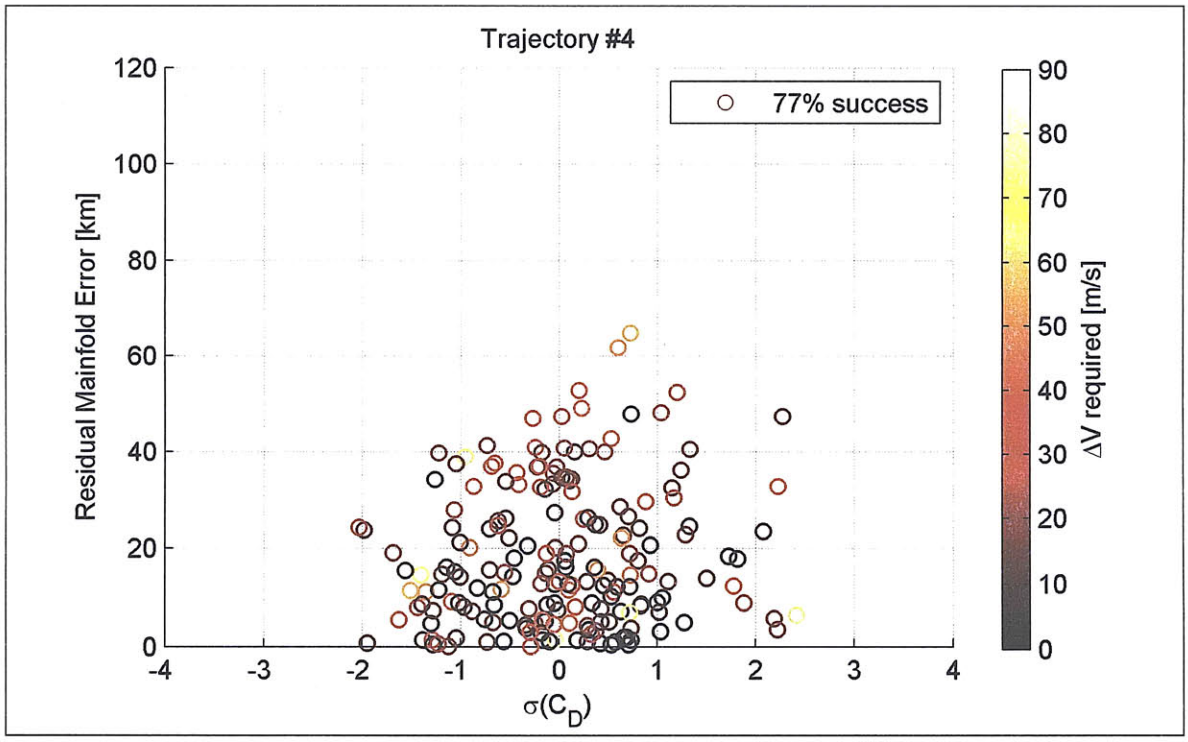

(d) Trajectory #4

Figure B-10: Scatter of residual error for a dispersed drag coefficient (cont'd)

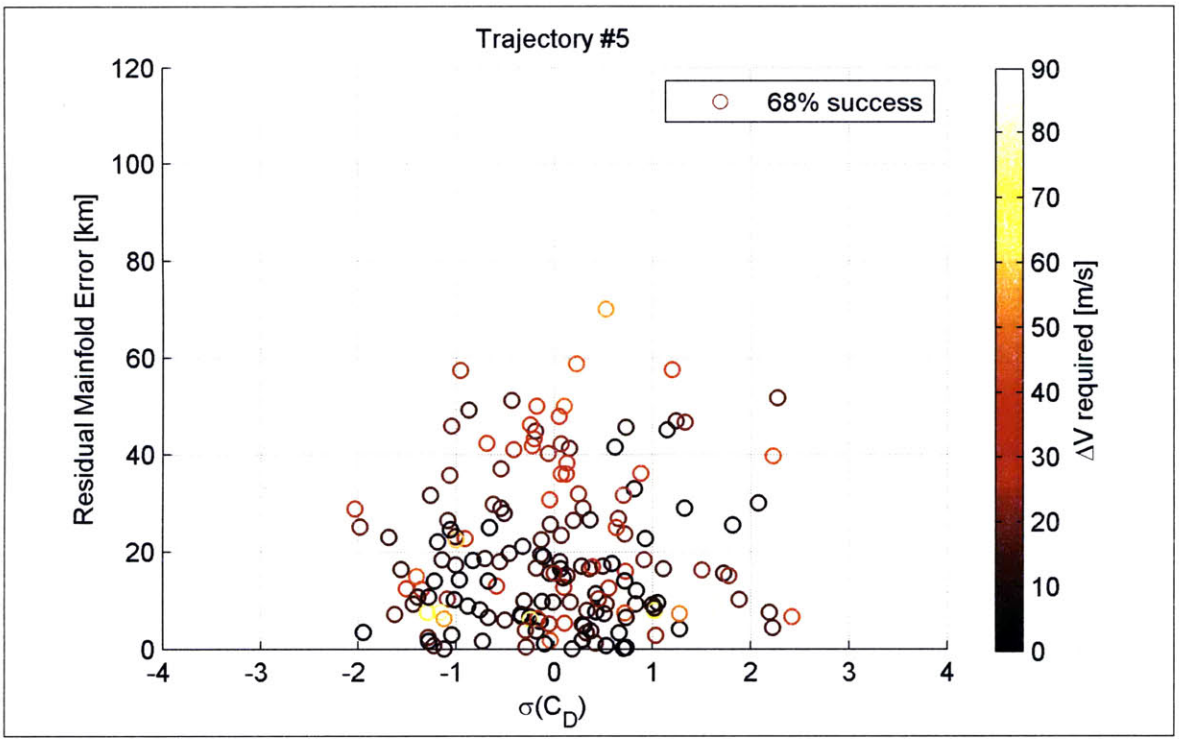

(e) Trajectory #5

Figure B-10: Scatter of residual error for a dispersed drag coefficient (cont'd)

B.2.5 Thruster Force

The thruster force was perturbed using a multiplier with a 3σ value of 3 percent.

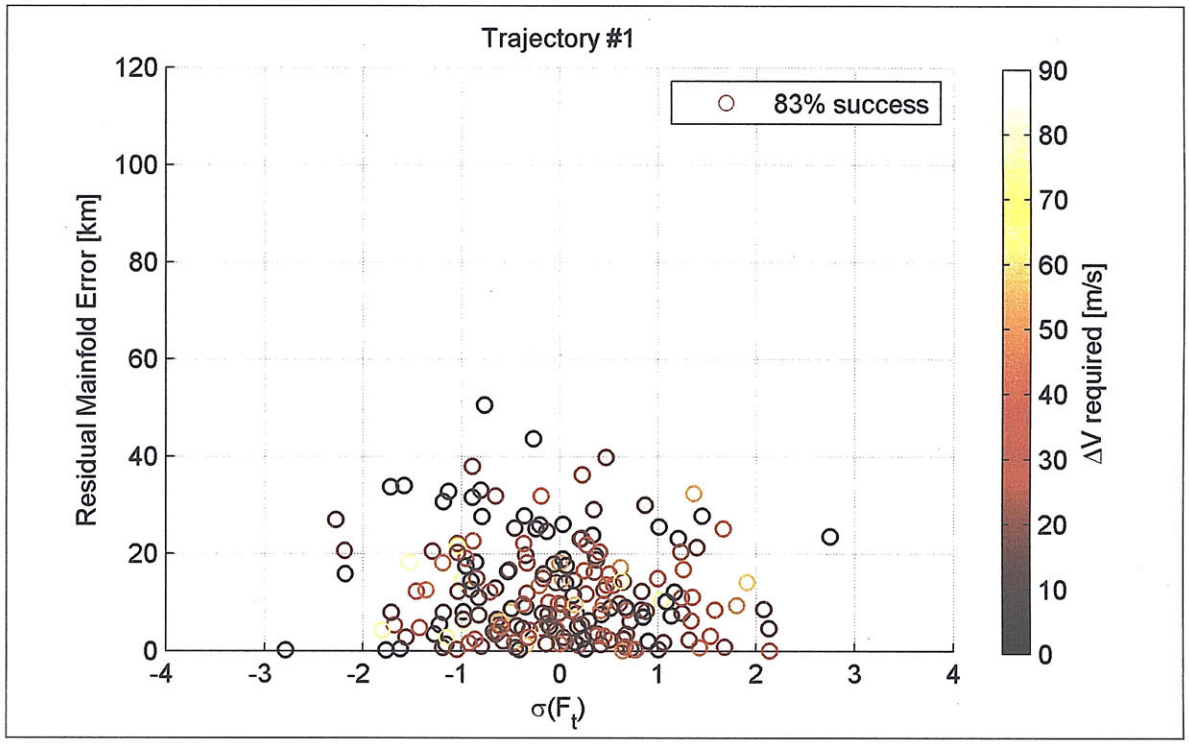

(a) Trajectory #1

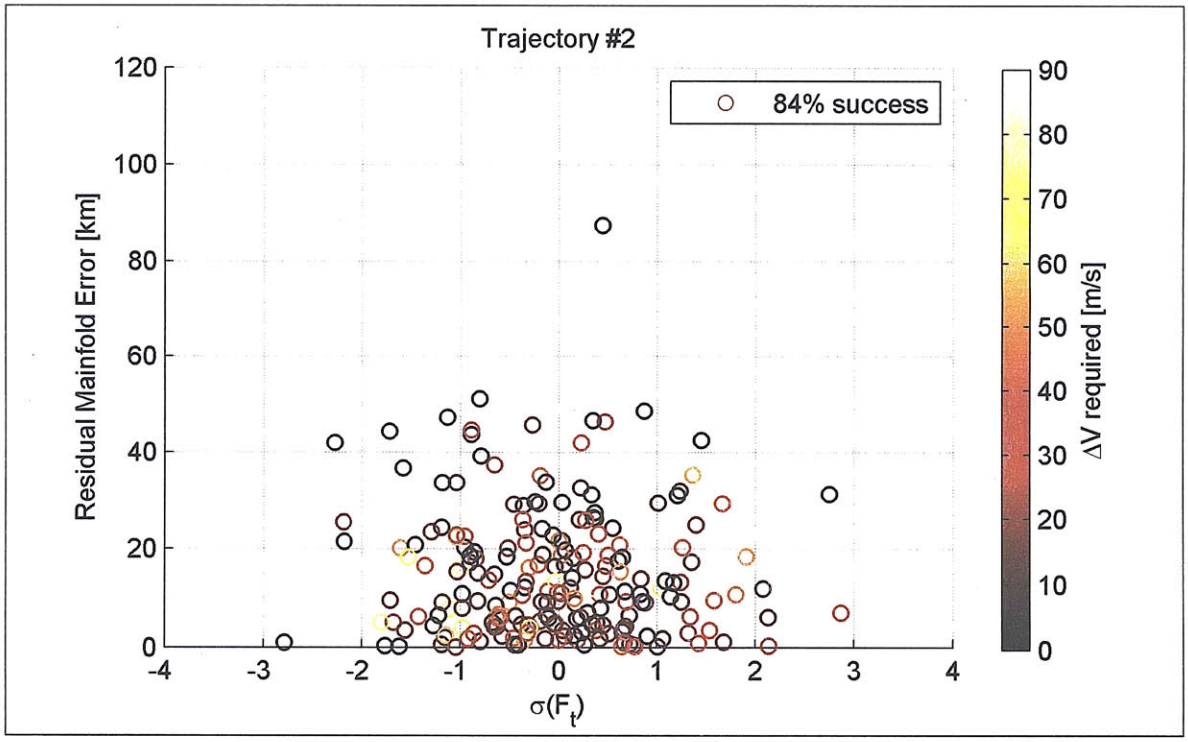

(b) Trajectory #2

Figure B-11: Scatter of residual error for a dispersed thruster force

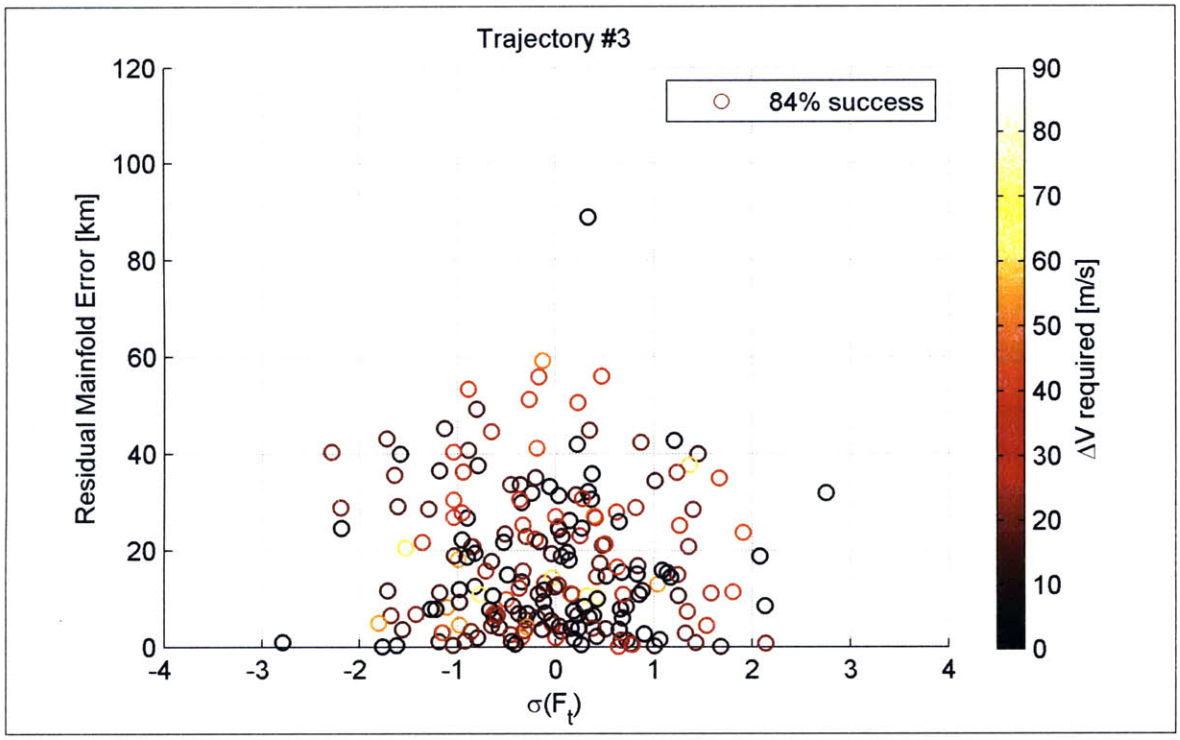

(c) Trajectory #3

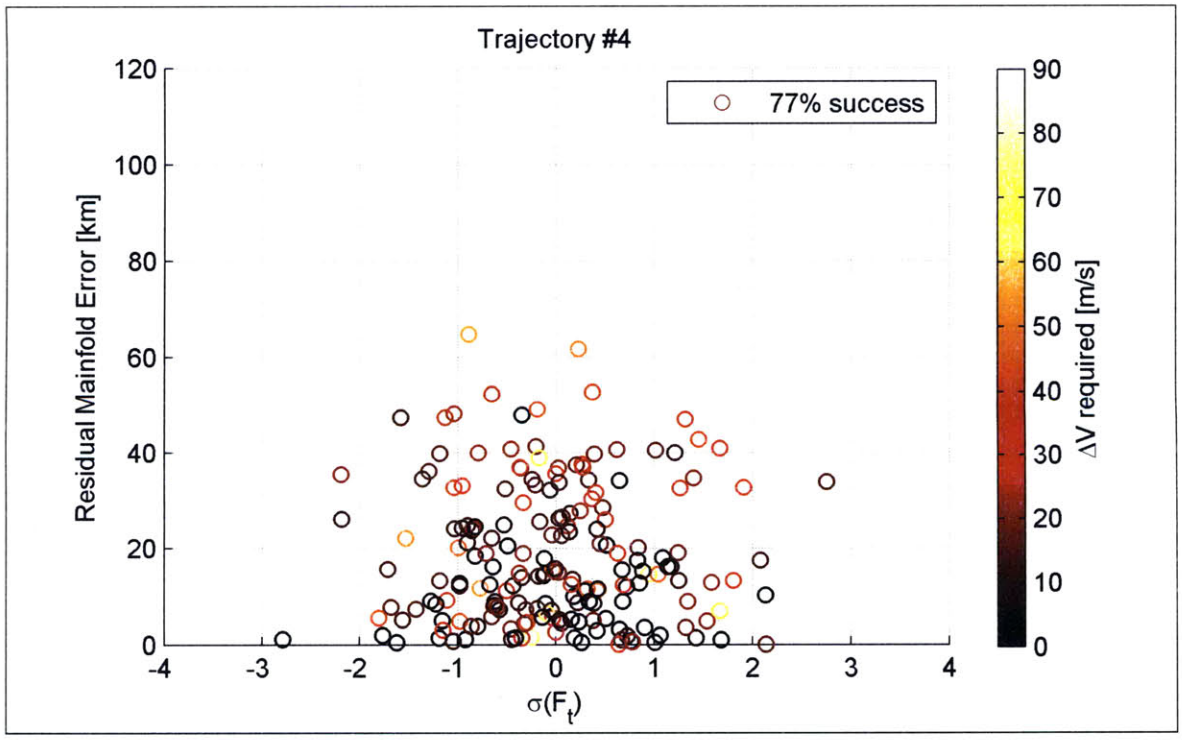

(d) Trajectory #4

Figure B-11: Scatter of residual error for a dispersed thruster force (cont'd)

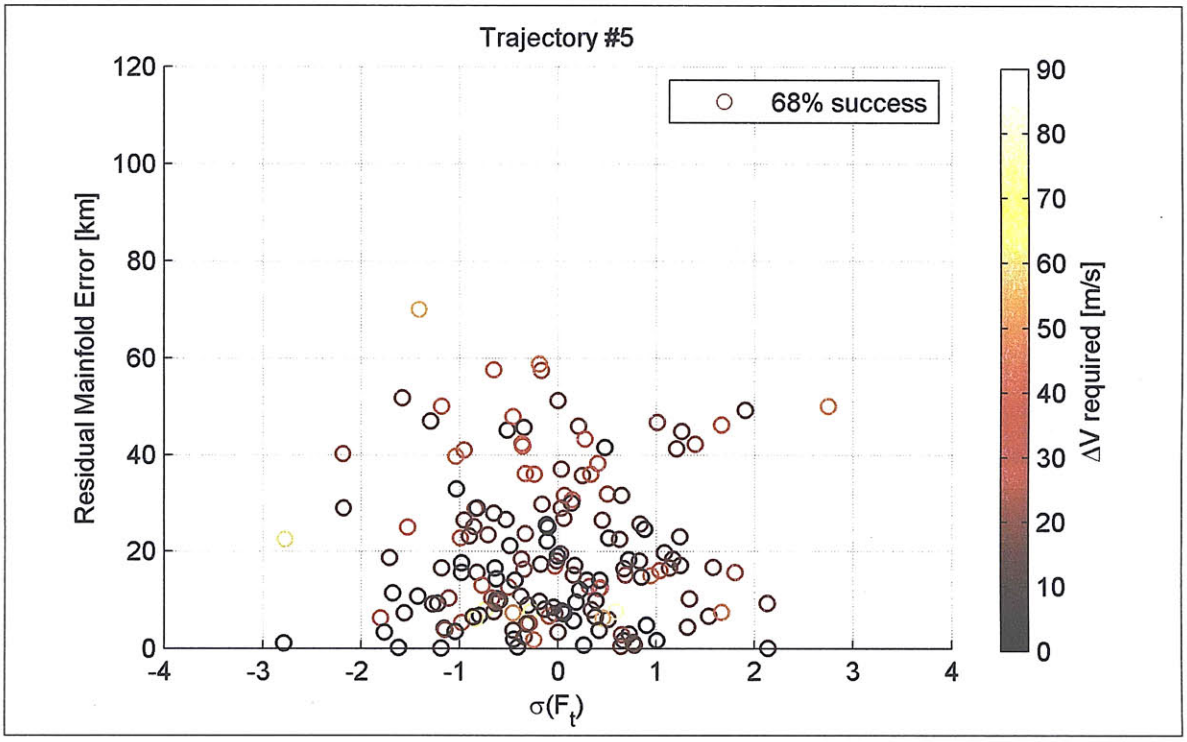

(e) Trajectory #5

Figure B-11: Scatter of residual error for a dispersed thruster force (cont'd)

B.2.6 Initial Velocity

The initial velocity was perturbed by using a mean value of those found in Table 3.1 for each respective trajectory with a 3σ value of 225 $^{m}/_{s}$.

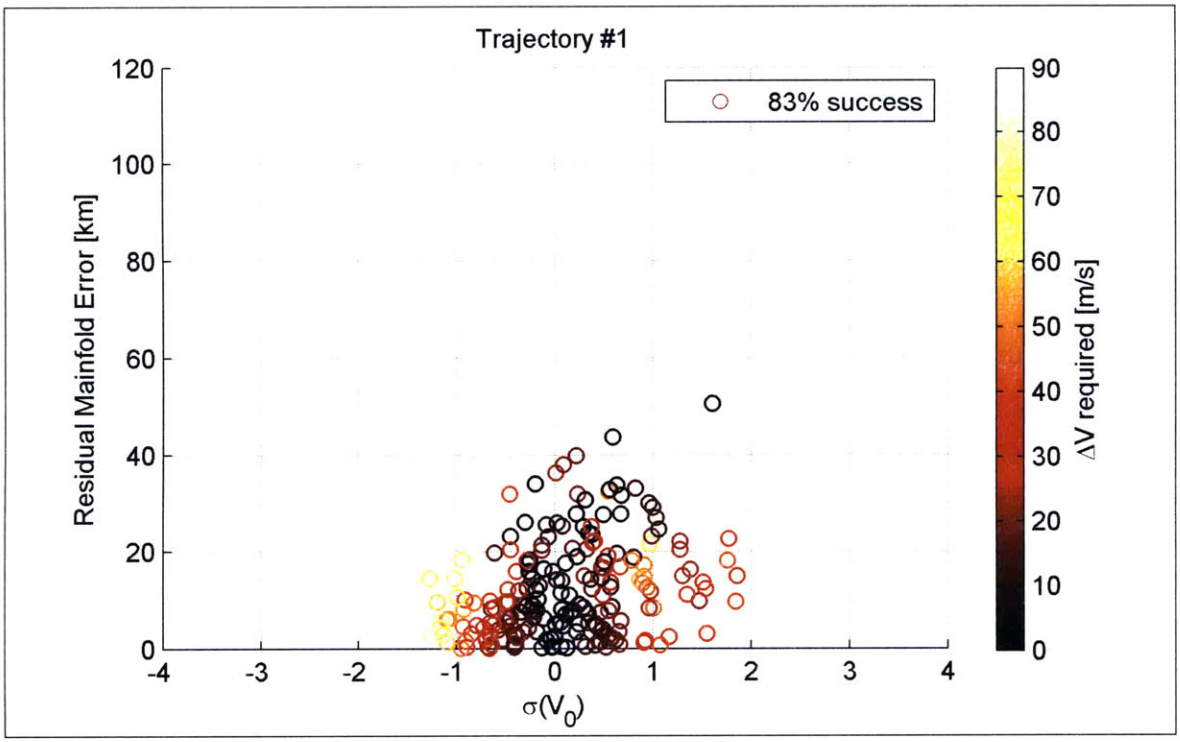

(a) Trajectory #1

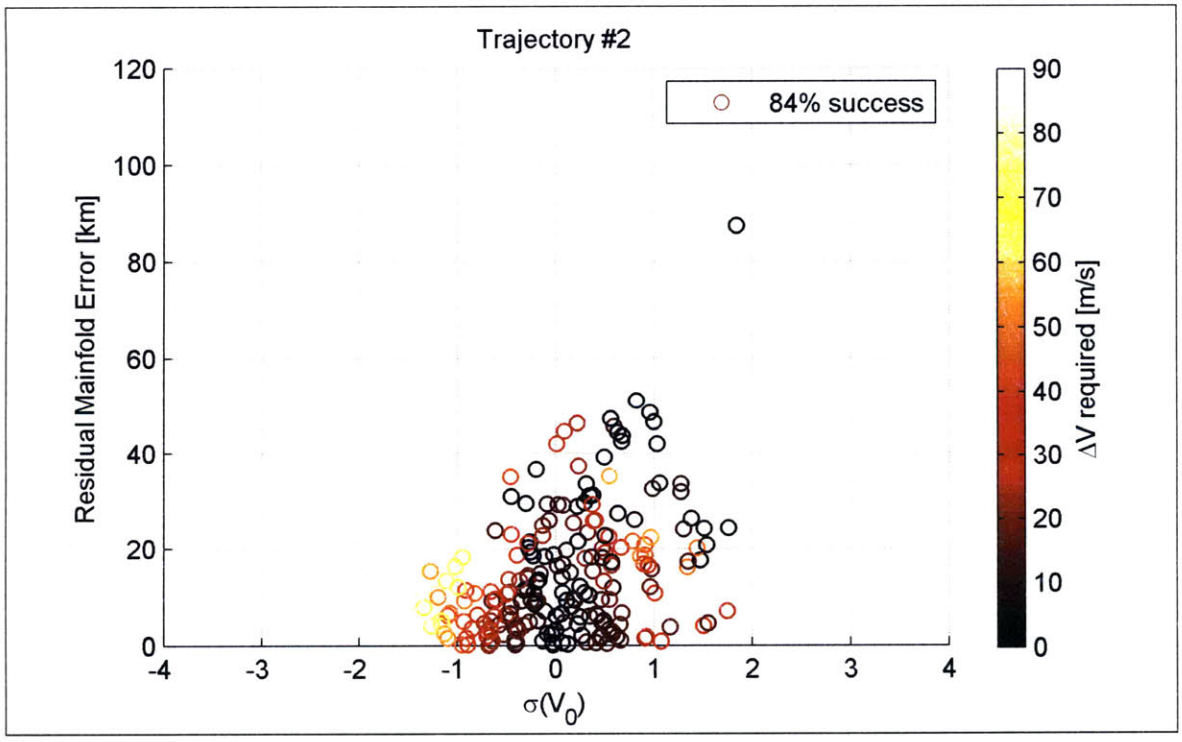

(b) Trajectory #2

Figure B-12: Scatter of residual error for a dispersed initial velocity

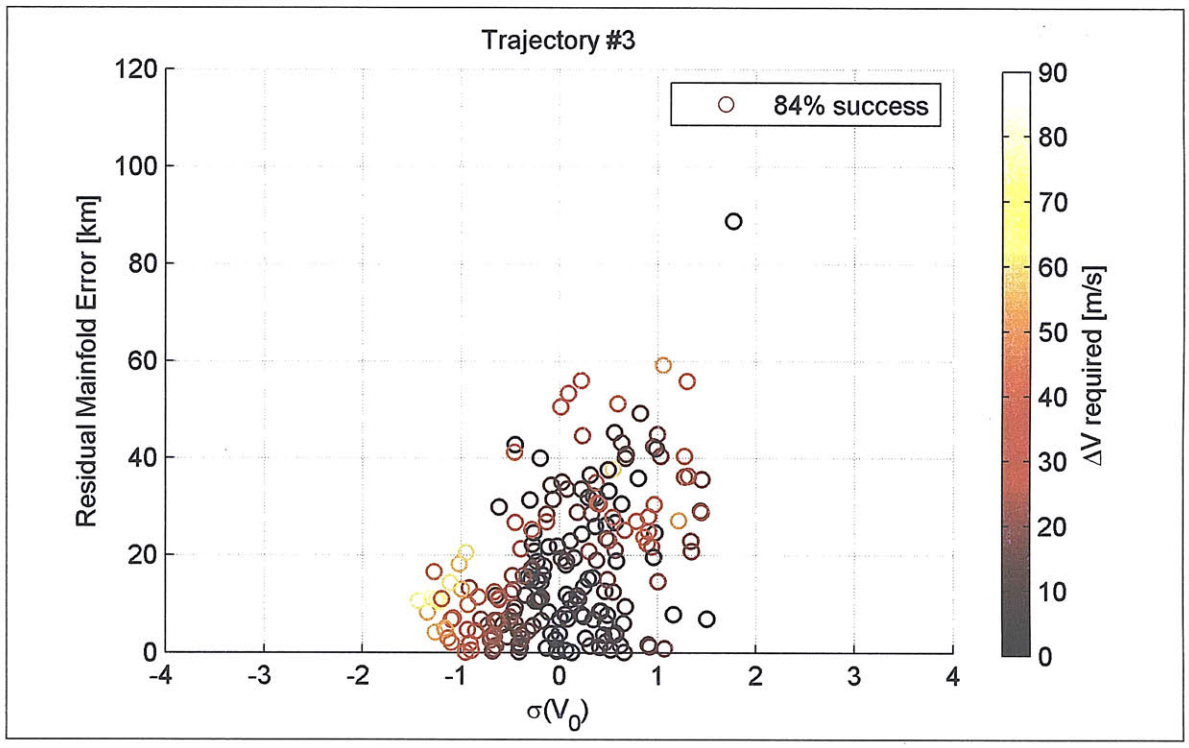

(c) Trajectory #3

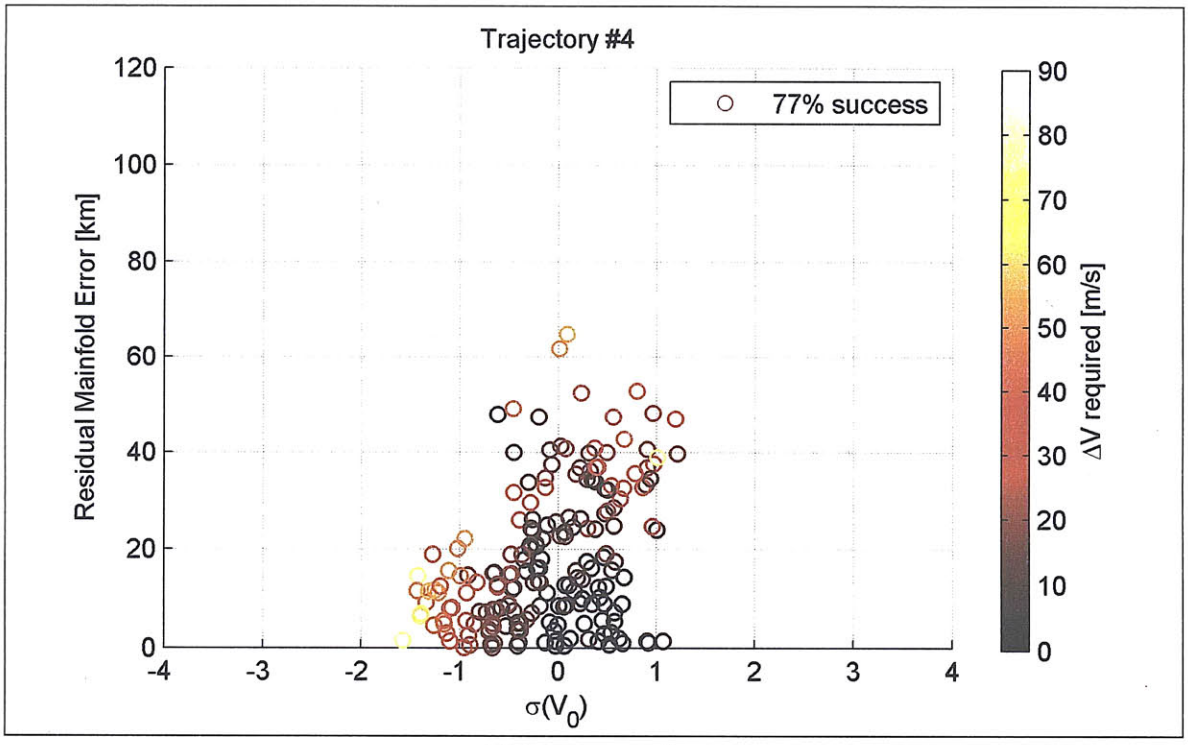

(d) Trajectory #4

Figure B-12: Scatter of residual error for a dispersed initial velocity (cont'd)

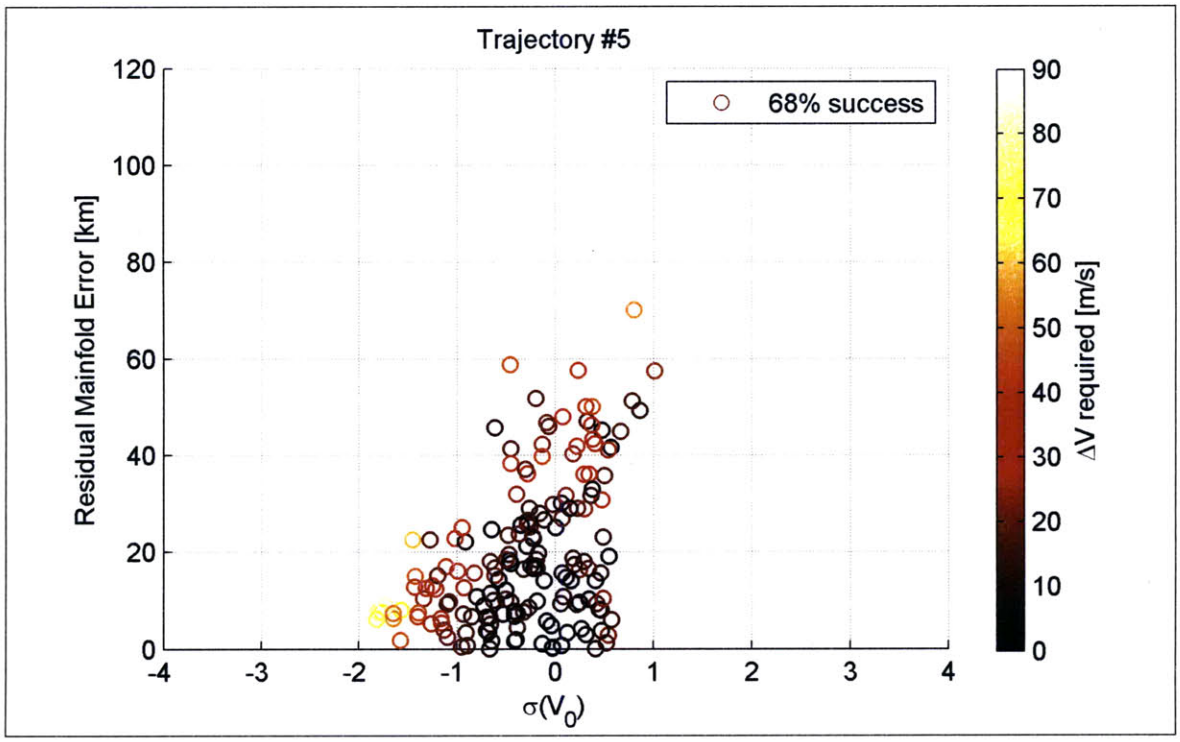

(e) Trajectory #5

Figure B-12: Scatter of residual error for a dispersed initial velocity(cont'd)

Bibliography

[1] "President Bush Announces New Vision for Space Exploration." http://www.whitehouse.gov/news/releases/2004/01/20040114-3.html, 14 Jan. 2004. *Accessed on 22 February 2006.*

[2] "NASA's Explorations Systems Architecture Study." NASA-TM-2005-214062, Nov. 2005.

[3] R. Morth, "Reentry Guidance for Apollo." Massachusetts Institute of Technology Instrumentation Laboratory: R-532, Jan. 1966.

[4] N. L. Johnson, *Handbook of Soviet Lunar and Planetary Exploration*, ch. 1, pp. 115–119. San Diego: American Astronautical Society, 1979.

[5] P. Clark, *The Soviet Manned Space Program*, ch. 4, pp. 39–40. New York: Salamander, 1988.

[6] A. L. Brichant, "Controlled Descent of Zond-6 from the Path Earth-Moon-Earth." Highlights of a column in *Pravda* #329, Moscow, 24 Nov. 1968. *Orignal author unknown, translated from Russian by listed.*

[7] B. Harvey, *The New Russian Space Programme*, ch. 3, pp. 120–122, 132–133. Chichester: John Wiley & Sons, second ed., 1996.

[8] M. L. Nagel, "*Ballistic Skip Guidance for Atmospheric Re-Entry*," Master's thesis, Air Force Institute of Technology, June 1973.

[9] K. D. Mease and F. A. McCreary, "Atmospheric Guidance Law for Planar Skip Trajectories," in *AIAA Atmospheric Flight Mechancis Conference*, (Snowmass, CO), pp. 408–415, 19–21 Aug. 1985. Paper #: AIAA-1985-1818.

[10] S. H. Bairstow, "*Reentry Guidance with Extended Range Capability for Low L/D Spacecraft*," Master's thesis, Massachusetts Institute of Technology, Feb. 2006.

[11] "U.S. Standard Atmosphere, 1962." DTIC Public STINET, Dec. 1962.

[12] R. H. Battin, *An Introduction to the Mathematics and Methods of Astrodynamics.* Reston, VA: AIAA, revised ed., 1999.

[13] R. L. McHenry, T. J. Brand, A. D. Long, B. F. Cockrell, and J. R. Thibodeau, "Space Shuttle Ascent Guidance, Navigation, and Control," *The Journal of the Astronautical Sciences*, vol. 27, pp. 1–38, Jan.-Mar. 1979.

[14] P. N. Springmann, "*Lunar Decent Using Sequential Engine Shutdown*," Master's thesis, Massachusetts Institute of Technology, Jan. 2006.

[15] S. A. Striepe, E. M. Queen, R. W. Powell, R. D. Braun, F. M. Cheatwood, J. T. Aguirre, L. A. Sachi, and D. T. Lyons, "An Atmospheric Guidance Algorithm Testbed for the Mars Surveyor Program 2001 Orbiter and Lander," in *AIAA Atmospheric Flight Mechancis Conference*, (Boston), 10–12 Aug. 1998. Paper #: AIAA-1998-4569.